

Tevatron-for-LHC Report: Top and Electroweak Physics

(The TeV4LHC-Top and Electroweak Working Group) C.E. Gerber,⁸ P. Murat,¹ T.M.P. Tait,¹⁰
D. Wackerth,¹⁶ A. Arbuzov,²⁴ D. Bardin,²⁴ U. Baur,¹⁶ J.A. Benitez,³ S. Berge,²⁶ S. Bondarenko,²⁴
E.E. Boos,¹⁴ M.T. Bowen,² R. Brock,³ V.E. Bunichev,¹⁴ J. Campbell,¹² F. Canelli,¹⁵ Q.-H. Cao,¹¹
C.M. Carloni Calame,^{28;35} F. Chevallier,¹⁷ P. Christova,²⁴ C. Ciobanu,⁹ S. Dittmaier,²⁵ L. V. Dudko,¹⁴
S.D. Ellis,² A.I. Etiennev,²⁰ F. Fiedler,⁶ A. Garcia-Bellido,² A. Giammanco,¹⁸ D. Glenzinski,¹
P. Golonka,^{30;31} C. Hays,^{22;34} S. Jadach,^{30;31} S. Jain,²¹ L. Kalinovskaya,²⁴ M. Krämer,²⁶ A. Lleres,¹⁷
J. Lück,¹⁵ A. Lucotte,¹⁷ A. Markina,¹⁴ G. Montagna,^{33;28} P.M. Nadolsky,¹⁰ O. Nicrosini,²⁸
F.I. Olness,²⁷ W. Płaczek,^{30;32} R. Sadykov,²⁴ V.I. Savrin,¹⁴ R. Schwienhorst,³ A.V. Sherstnev,¹⁴
S. Slabospitsky,¹⁹ B. Stelzer,⁵ M.J. Strassler,² Z. Sullivan,¹⁰ F. Tramontano,¹³ A. Vicini,^{36;29}
W. Wagner,¹⁵ Z. Was,^{30;31} G. Watts,² M. Weber,¹ S. Willenbrock,⁹ U.K. Yang,⁷ C.-P. Yuan,³ J. Zhu²³
¹ Fermilab, ² Univ. of Washington, ³ Michigan State Univ., ⁴ Univ. of Rochester,
⁵ Univ. of California, Los Angeles, ⁶ Ludwig-Maximilians-Universität München,
⁷ Univ. of Manchester, ⁸ Univ. of Illinois at Chicago, ⁹ Univ. of Illinois at Urbana-Champaign,
¹⁰ Argonne National Laboratory, ¹¹ Univ. of California, Riverside, ¹² Univ. of Glasgow,
¹³ Univ. di Napoli, ¹⁴ Moscow State Univ., ¹⁵ Univ. of Karlsruhe,
¹⁶ State Univ. of New York at Buffalo,
¹⁷ Laboratoire de Physique Subatomique & Cosmologie, Grenoble,
¹⁸ Université Catholique de Louvain, ¹⁹ Institute for High Energy Physics, Protvino, ²⁰ CEA-Saclay,
²¹ Univ. of Oklahoma, ²² Duke Univ., ²³ State Univ. of New York, Stony Brook, ²⁴ JINR Dubna,
²⁵ Max-Planck Institut für Physik (Werner-Heisenberg-Institut), ²⁶ RWTH Aachen ,
²⁷ Southern Methodist Univ., ²⁸ INFN - Sezione di Pavia, ²⁹ INFN - Sezione di Milano, ³⁰ CERN,
³¹ Institute of Nuclear Physics, Cracow, ³² Jagiellonian Univ., ³³ Univ. of Pavia, ³⁴ Oxford Univ.,
³⁵ Univ. of Southampton, ³⁶ Univ. of Milano

Abstract

The top quark and electroweak bosons (W and Z) represent the most massive fundamental particles yet discovered, and as such refer directly to the Standard Model's greatest remaining mystery: the mechanism by which all particles gained mass. This report summarizes the work done within the top-ew group of the Tevatron-for-LHC workshop. It represents a collection of both Tevatron results, and LHC predictions. The hope is that by considering and comparing both machines, the LHC program can be improved and aided by knowledge from the Tevatron, and that particle physics as a whole can be enriched. The report includes measurements of the top quark mass, searches for single top quark production, and physics of the electroweak bosons at hadron colliders.

Contents

1	Introduction	3
2	Measurement of the top quark mass	4
2.1	Introduction	4
2.2	Top Mass Determination at the Tevatron	6
2.3	Systematic Uncertainties	15
2.4	Top Mass Combination	20
2.5	Top Mass Expectations	22
2.6	Top Mass Determination at the LHC	23
2.7	Conclusions	33
3	Single Top Quark Physics	35
3.1	Introduction	35
3.2	Theory	35
3.3	Tevatron Single Top Quark Searches	83
3.4	LHC Single Top Quark Searches	99
3.5	From the Tevatron to the LHC	139
4	Precise predictions for \bar{W} boson observables	143
4.1	Introduction	143
4.2	Theoretical status	145
4.3	Description of higher-order calculations and MC programs	148
4.4	Results of a tuned comparison of HORACE, SANC and WGRAD2	153
4.5	Effects of multiple photon radiation	166
4.6	High-precision transverse momentum distributions in \bar{W} boson production	171
4.7	Estimate of theoretical uncertainties due to missing higher-order corrections	179
4.8	Experimental Uncertainties	180
4.9	Conclusion	183
5	Measurement of the W Mass	185
5.1	CDF Run 2 Measurement	185
6	Measurement of the \bar{W} Width	191
7	Summary	193

1 Introduction

The top quark and electroweak bosons (W and Z) represent the most massive fundamental particles yet discovered. Thus, they are not only the newest additions to the Standard Model (SM) of particle physics, but are also the most interesting because their large masses refer directly to the SM's greatest remaining mystery: the mechanism by which all particles gained mass. The $SU(2) \times U(1)$ gauge structure of SM is successful at describing all interactions, and is an essential ingredient for the theoretical consistency of the theory, but if the symmetry were exact it would require all particles to be massless. Thus, the symmetry must be spontaneously broken. In the SM itself this is defined by introducing a Higgs boson together with a potential that insures it has a non-zero expectation value in empty space. However, even if this assumption is correct, the Higgs has as yet eluded experimental observation, and it could be that the SM description is incomplete or even simply incorrect. Theoretical arguments related to the hierarchy of scales or triviality of the Higgs potential, further suggest that the SM description is at best a stand-in for some more natural explanation. Unravelling the details of the true nature of electroweak symmetry-breaking (EWSB) is one of the most pressing challenges awaiting particle physics.

The top and electroweak bosons, as the most massive objects in the SM, are those which felt the symmetry breaking the most profoundly. Thus, they must couple the most strongly to the agent of EWSB (be it a SM fundamental Higgs, or the result of some more plausible dynamics) and a detailed study of their properties represents an excellent chance to learn indirectly about EWSB itself. They are interesting in their own right and are produced copiously at both the Tevatron and the LHC. Thus, it is natural as run II of the Tevatron draws to a close, and the LHC era begins, to examine how well we can measure all of the quantities needed to describe these particles, and how the two machines may complement each other in our quest to explore EWSB through study of massive objects.

In addition to the interest in top and the electroweak bosons in their own right, they are also interesting "standard candles" that may allow us to understand the SM predictions at the LHC in the light of Tevatron data. It may be that the resolution of the EWSB dynamics involves new particles, and their observation as we probe the energy frontier may be more striking than deviations in the properties of top, W , or Z from SM predictions. If so, a key ingredient to observing these new states is that we be able to infer very precisely what the SM prediction for any given signature should be. Top and the electroweak bosons have signatures which can be extremely distinctive at hadrons colliders, including charged leptons, missing energy, hard jets, and massive resonances in distributions. Understanding how to predict signals involving these objects at the LHC can benefit from Tevatron data, and the Tevatron can provide a laboratory to test out analysis ideas in a better understood environment, before they become essential at the LHC.

This report is collection of both Tevatron results, and LHC predictions. The hope is that by considering and comparing both machines, the LHC program can be improved and aided by knowledge from the Tevatron, and that particle physics as a whole can be enriched by combining information from both machines. Subsequent chapters deal with measurement of the top quark mass, searches for single top quark production, and understanding the physics of the electroweak bosons at hadron colliders.

2 Measurement of the top quark mass

2.1 Introduction

Contributed by: T. Tait

The top quark mass is one of the fundamental parameters of the standard model (SM), related to the top's coupling to the Higgs by the tree level relationship $m_t = y_t v$. The top mass, like all SM fermion masses is a manifestation of the breaking of the electroweak symmetry from $SU(2)_L \times U(1)_Y$ to electromagnetism. As the heaviest fermion, the top felt this symmetry-breaking the most strongly, and thus is a natural laboratory to learn about the dynamics of the breaking. Thus, the hope is that precision measurements of the top quark will either confirm the SM's picture of electroweak breaking, or show deviations which will point the way to a more complete theory.

Even within the SM, the top's large mass implies that it is special. The large coupling of the Higgs boson to top inferred from the mass suggests that rates for processes involving both Higgs and top can be large. The top essentially determines the Higgs coupling to two gluons (induced by a loop of top quarks) and is significant in determining the coupling to two photons (complementing a loop of W bosons). The top mass is an essential input in determining the SM prediction for these processes. In addition, the top contribution to flavor-violating processes in the SM (such as bottom- or strangeness-number violating processes, which occur at loop level in the Standard Model) is usually dominant, because the large top mass disrupts the GIM mechanism and permits these processes to take place.

Perhaps the most famous role the top mass plays in the Standard Model is through the corrections to electroweak precision observables at loop level. The precision of experiments at LEP and SLAC is enough to be sensitive to loop contributions of the Higgs and top, and thus given the top mass measured at the Tevatron, the precision data can be used to predict the as yet unknown mass of the Higgs boson. The most important top mass dependence contribution to the Electroweak observables arises via the one-loop radiative correction term Δr [1], related to the W mass through the relation: $m_W^2 = \frac{2G_F \sin^2 \theta_w}{1 + \Delta r}$. Δr depends on the top mass via terms proportional to m_t^2/m_Z^2 , while the Higgs mass gives rise to terms proportional to $\log m_H/m_Z$: therefore, the dependence on the Higgs mass is much weaker than the dependence on the top mass and without a precise measurement of m_t , no information about m_H can be extracted. The current value of the top mass ($m_{\text{top}} = 172.7 \pm 2.9 \text{ GeV}/c^2$) [2] results in the following constraints on the Higgs boson mass: $m_H = 91^{+45}_{-32} \text{ GeV}/c^2$, $m_H < 186 \text{ GeV}/c^2$ at 95% C.L. limit. The allowed region in the (m_W, m_t) plane is displayed in Fig. 2.1.1, for different Higgs boson masses, in the SM and in the MSSM.

Even in theories beyond the Standard Model, the large top mass can imply a special role for top. In the minimal supersymmetric standard model (MSSM), the Higgs quartic interaction is determined from gauge couplings, and requires $m_H = m_Z$ at tree level. This would be largely ruled out by the LEP-II searches for the Higgs boson, if it were not for the quantum corrections from loops of the top quark – large because the large top mass implies strong coupling to the Higgs, the MSSM would be excluded by the null LEP search. As it is, the precise value of the top mass determines a preferred range of MSSM Higgs masses. As a further test of physics beyond the Standard Model, the top mass (along with the strong coupling constant) determines the SM prediction for the rate of $t\bar{t}$ production, and correlated measurements of the top mass and cross section thus test theories which contain new $t\bar{t}$ production mechanisms, or objects which decay like the top quark and thus can be confused in the top

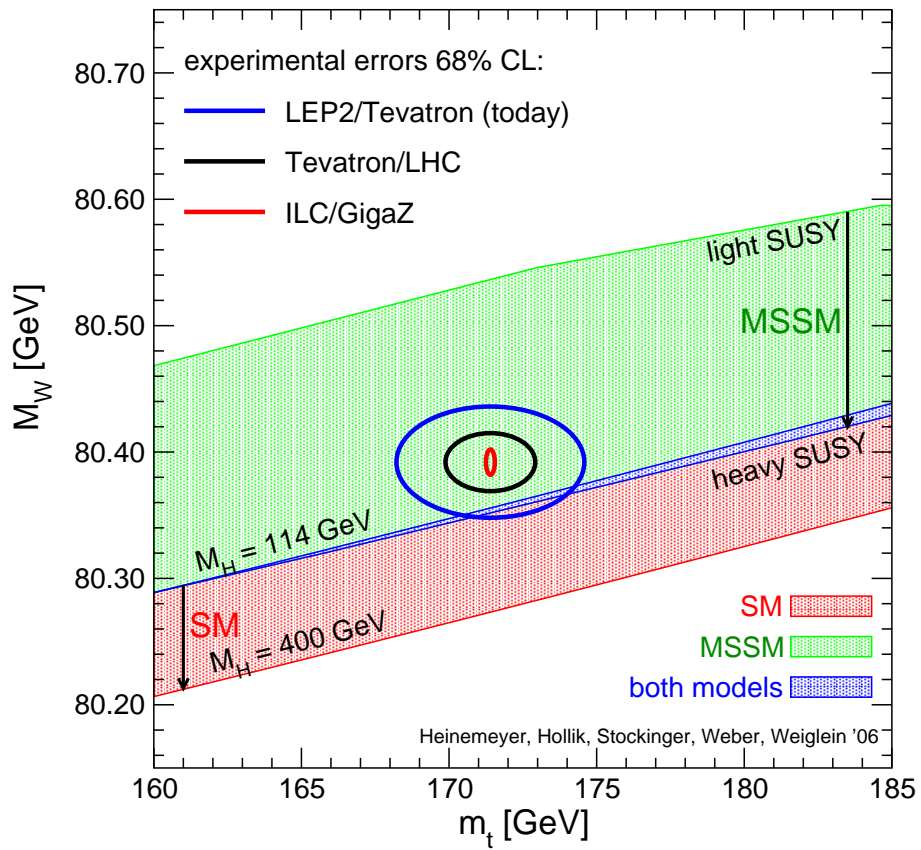


Fig. 2.1.1: Current experimental results for m_W and m_{top} , and expected accuracies at the next generation of colliders, compared with predictions obtained within the Standard Model and the MSSM [3].

event sample.

The following sections describe the methods used at the Tevatron to measure the top quark mass in the various channels, summarize the systematic uncertainties that dominate the results, and explain the techniques for combination of results. In addition, the expectation for the top mass measurement during Tevatron Run II, and the plans for the LHC are also included.

2.2 Top Mass Determination at the Tevatron

Introduction

Contributed by: C. Gerber

The top quark is pair-produced in $p\bar{p}$ collisions through quark-antiquark annihilation and gluon-gluon fusion. The Feynman diagrams of the leading order (LO) subprocesses are shown in Fig. 2.2.2. At Tevatron energies, the $q\bar{q} \rightarrow t\bar{t}$ process dominates, contributing 85% of the cross section. The $gg \rightarrow t\bar{t}$ process contributes the remaining 15%.

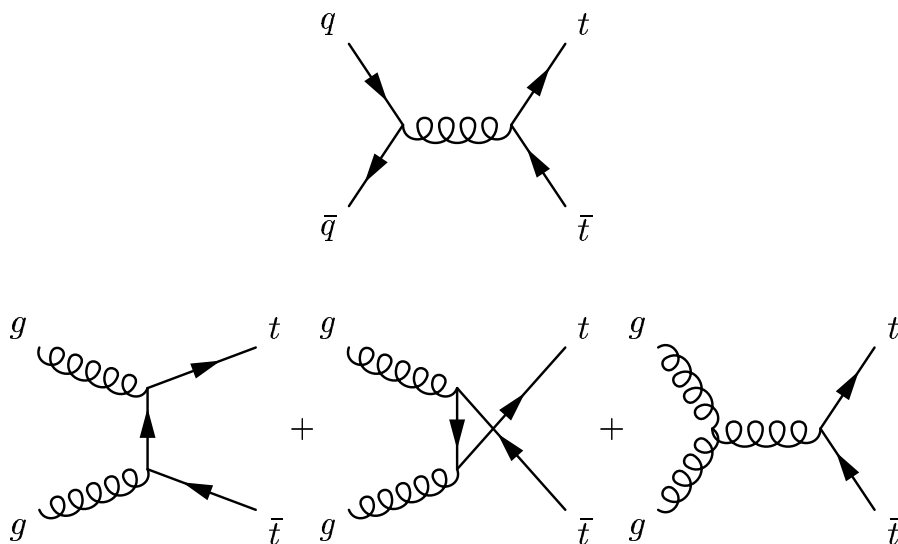


Fig. 2.2.2: Leading order Feynman diagrams for the production of $t\bar{t}$ pairs at the Tevatron.

Within the SM, the top quark decays via the weak interaction to a W boson and a b quark, with a branching fraction $\text{Br}(t \rightarrow W b) > 0.998$. The $t\bar{t}$ pair decay channels are classified as follows: the *dilepton channel*, where both W bosons decay leptonically into an electron or a muon ($e\bar{e}$, $\mu\bar{\mu}$, $e\bar{\mu}$); the *'+jets channel*, where one of the W bosons decays leptonically and the other hadronically (e +jets, μ +jets); and the *all-jets channel*, where both W bosons decay hadronically. A fraction of the leptons decays leptonically to an electron or a muon, and two neutrinos. These events have the same signature as events in which the W boson decays directly to an electron or a muon and are treated as part of the signal in the *'+jets channel*. In addition, dilepton events in which one of the leptons is not identified are also treated as part of the signal in the *'+jets channel*. Two b quarks are present in the final state of a $t\bar{t}$ event which distinguishes it from most of the background processes. As a consequence, identifying the bottom flavor of the corresponding jet can be used as a selection criteria to isolate the $t\bar{t}$ signal.

Template Method

Contributed by: U.-K. Yang

The template method relies on reconstructed distributions of the top quark mass from Monte Carlo for a wide range of mass values. The top quark mass is then extracted by comparing the reconstructed top quark mass distribution from data to the Monte Carlo mass templates using a likelihood fit.

In this method, the reconstructed top quark mass (m_t^{reco}) in each event is obtained by using kinematic constraints on the top quark decay products. We require that both t and \bar{t} have the same mass, and that two W particles have mass equal to 80.42 GeV (PDG value). For the $l+\text{jets}$ channel these constraints are sufficient to construct m_t^{reco} , even though the longitudinal momentum of the neutrino is not measured. For the dilepton channel these constraints are not sufficient due to the two missing neutrinos. We therefore have to assume some kinematic distributions based on the Standard Model when calculating the reconstructed top quark mass for each event.

Lepton+jet channel The $t\bar{t}$ events in the $l+\text{jets}$ channel are selected by requiring a high-pt lepton (electron or muon), large transverse missing energy (E_T^{miss}), and at least four jets. Even though kinematic constraints on the top pair system are sufficient to define all four vectors of the top quark decay products, we still need to figure out the correct jet-parton assignments. This task is very challenging, because the association between partons from the top quark decay and reconstructed jets is complicated by many processes, for instance parton shower, hadronization, and jet reconstruction. In addition, the observed jet energy is not precisely measured and additional jets are present in the event from initial and final state gluon radiation. Only 50% of the time the leading four jets contain four hard-scattered partons from the top quark decays. In this analysis we perform a kinematic χ^2 fit to choose the best assignment and to extract the reconstructed mass m_t^{reco} for each event. The χ^2 expression is given by:

$$\chi^2 = \sum_{i \in \text{4 jets}} \frac{(p_T^{i \neq \text{lepton}} - p_T^{i \text{ lepton}})^2}{\sigma_i^2} + \sum_{j \in \text{4 jets}} \frac{(p_j^{U E \neq \text{lepton}} - p_j^{U E \text{ lepton}})^2}{\sigma_j^2} + \frac{(M_{jj} - M_W)^2}{\sigma_W^2} + \frac{(M_{l\nu} - M_W)^2}{\sigma_W^2} + \frac{(M_{bjj} - M_t)^2}{\sigma_t^2} + \frac{(M_{b\nu} - M_t)^2}{\sigma_t^2};$$

where σ_l and σ_{jet} are the resolutions of the lepton and four leading jets, and $p_{xY}^{U E}$ and $p_{xY}^{L E}$ corresponds to the unclustered energy in the calorimeter. The jet energies are corrected to the parton-level. In each event there are 12 combinations for jet-parton assignment. We pick the combination with the lowest χ^2 as the best assignment. An additional requirement of $\sigma_{m_{\text{in}}}^2 < 9$ is found to give the best expected statistical uncertainty on the top quark mass. This requirement effectively rejects badly reconstructed $t\bar{t}$ events or background events).

Information from b tagging is very powerful in finding the correct combination. To improve the statistical power of the measurement, CDF divides the sample based on the number of tagged b jets (0, 1, and 2-tags) whereas D0 uses only events with tagged b jets. A typical reconstructed top mass distribution for signal Monte Carlo (178 GeV sample) is shown in Fig. 2.2.3. The blue histogram in the same figure shows the case for the correct jet-parton assignment. As can be observed, the resolution of the reconstructed mass is much better with more b -tagged jets.

The uncertainty in the jet energy scale is the dominant systematic error on the determination of the top quark mass. We use the dijet mass m_{jj} from hadronic W boson decay to reduce this error. The

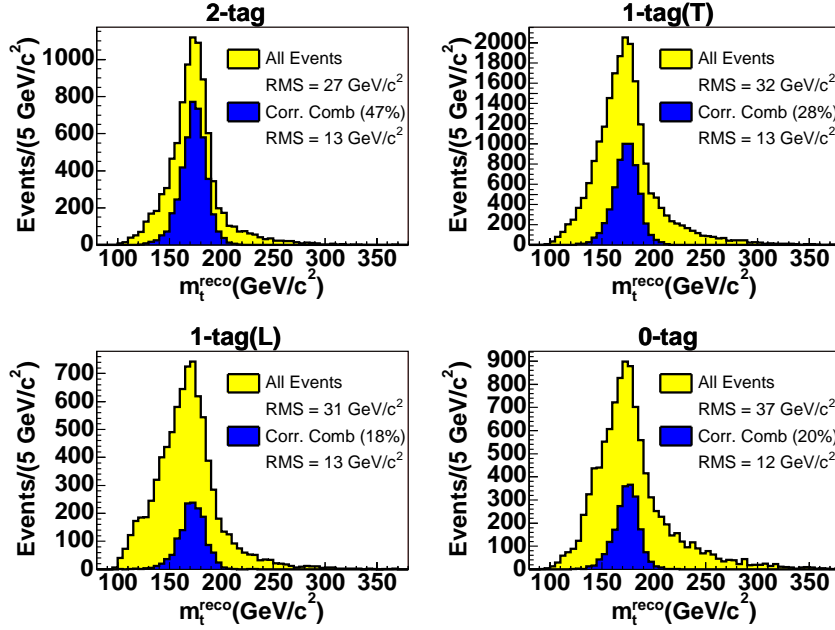


Fig. 2.2.3: The light histograms show the reconstructed top quark mass distribution for the $178 \text{ GeV} = c^2$ HERWIG $t\bar{t}$ sample, and the blue histogram for the correct jet-parton assignment.

quantity m_{jj} is sensitive to the jet energy scale but is relatively insensitive to the true top quark mass. Thus, we can calibrate the jet energy scale in situ while reconstructing the top quark mass. CDF has used both the m_{jj} templates and the a priori determination of \mathcal{JES} described in Sec. 2.3. All pairs of untagged jets are used to get the best sensitivity to the jet energy scale. Parameterized signal templates for the m_t^{reco} and m_{jj} are shown in Fig. 2.2.4. In the tagged samples, the size of backgrounds is small. Most of the background comes from W boson production associated with real heavy flavor jets, or associated jets with a misidentified b -jet (mistags), and QCD backgrounds due to fake leptons. Background templates for the $W + \text{jets}$ with heavy flavor production and mistags are obtained from ALPGEN Monte Carlo samples. The mistag template is also used for the QCD background, because the non-isolated lepton data (QCD enriched sample) shows a very similar shape to the mistag sample.

The reconstructed mass distribution from data is finally compared to parameterized signal templates for different values of top quark mass and jet energy scale, and background templates using an unbinned likelihood fit. Gaussian constraints on the prior jet energy scale and expected background rate are used. Thus, the likelihood fit to the data returns the number of signal events, the true top quark pole mass and the jet energy scale. This simultaneous fit to the top quark mass and the jet energy scale results in significant reduction of the total uncertainty as more data is added to the analysis because the dominant systematic uncertainty, the jet energy scale, is part of the statistical error. Currently, the template method used by both CDF and D0 treats all events equally regardless of the different mass resolution in each event. We might be able to improve the resolution on the top quark mass by introducing a weight to each event.

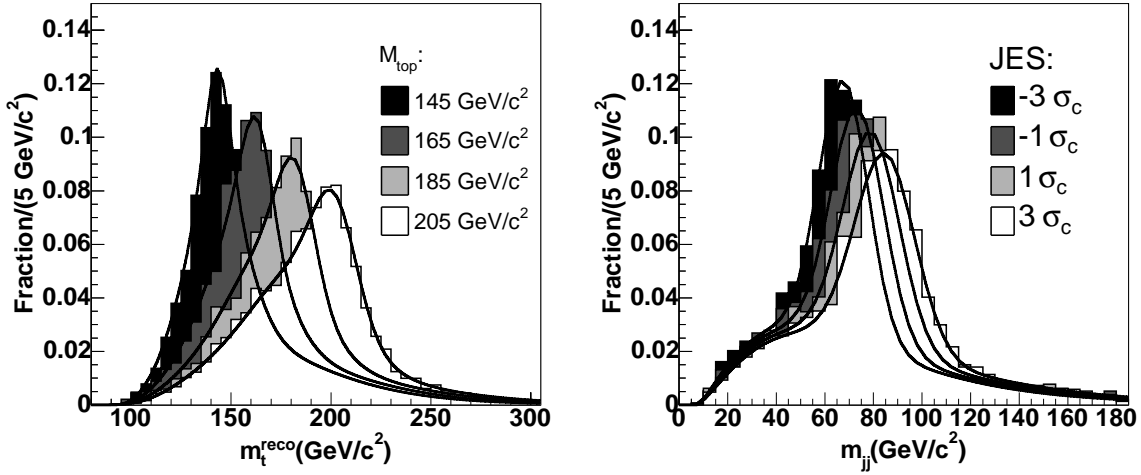


Fig. 2.2.4: [Left] Signal m_t^{reco} templates for 1-btag(T) sample are shown with top quark masses ranging from 145 GeV/c² to 205 GeV/c² and with JES set to 0. [Right] Signal m_{jj} templates for the 2-btag sample are shown with different values of the JES.

Dilepton channel Reconstruction of the top quark mass m_t^{reco} in the dilepton channel is difficult because much of the final state kinematic information is lost. The template method has to make kinematic assumptions on unconstrained variables, and obtain the probability distribution of the reconstructed top quark mass for each event. The most probable value of this distribution is taken as m_t^{reco} for each event. An unbinned likelihood fit is performed to parameterized signal and background templates to extract a top quark mass from data, like was done in the t -jets channel. CDF has developed three template methods, depending on the choice of the assumed kinematic distributions. The neutrino-weighting method (NWA) uses the distributions of the two neutrinos; the full kinematic method (KIN) uses the P_z of the $t\bar{t}$ system; and the neutrino-weighting method (PHI) uses the ϕ of the two neutrinos.

In the NWA method, we calculate m_t^{reco} for possible solutions for various values of the neutrinos. A probability for each solution (p) is given by the measured missing energy (E_T^{miss}) and its resolution (σ_x, σ_y).

$$p = \exp\left[-\frac{(E_T^{\text{miss}} - R_x - R_x)^2}{2\sigma_x^2}\right] \exp\left[-\frac{(E_T^{\text{miss}} - R_y - R_y)^2}{2\sigma_y^2}\right] :$$

The top quark mass that maximizes this probability is taken as m_t^{reco} for each event. The template method D0 has developed is similar, but the probability for each solution is based on the prediction of the matrix element.

Kinematic Methods

Contributed by: U.-K. Yang

In the previous section we have shown that the reconstructed top quark mass m_t^{reco} has a strong linear correlation with the true top quark mass. However, the method relies heavily on the calibration

Transverse Decay Length

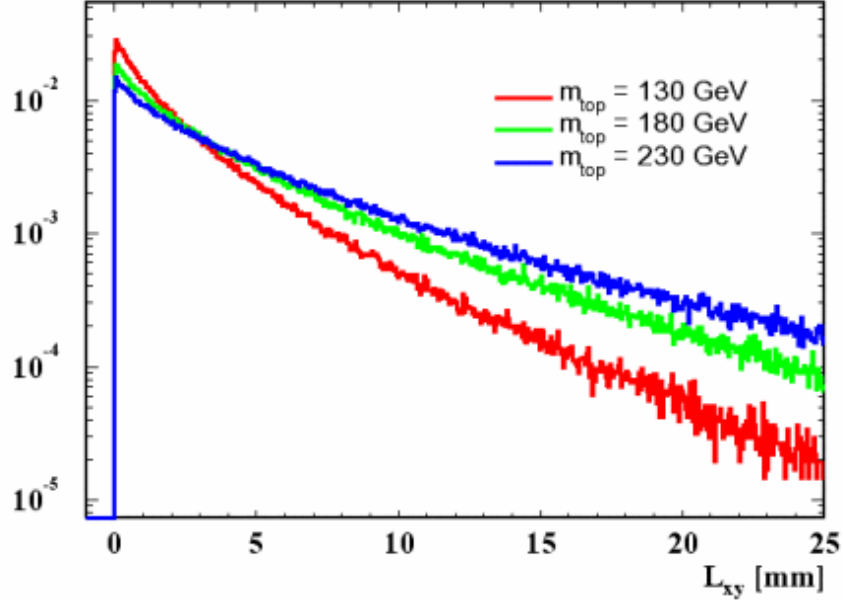


Fig. 2.2.5: The L_{xy} distributions for three different top mass values are shown.

of the jet energy scale. CDF has developed a novel method which uses the transverse decay length of b -hadrons from top decays to measure the top quark mass. This method avoids the jet energy scale uncertainty as it relies on measurements by the tracking system.

In the rest frame of the top quark, the boost factor (γ) to the b quark from the top decay can be written as

$$\gamma = \frac{m_t^2 + m_b^2 + m_W^2}{2m_t m_b} \approx 0.4 \frac{m_t}{m_b}$$

We can see that the top quark mass is strongly correlated with γ as long as the top quarks are produced at rest. At the Tevatron, top quarks are mostly produced nearly at rest given that the transverse momentum of the top quark is small compared to its mass. Thus, the average lifetime of the b hadrons can be used to extract the top quark mass. CDF used the transverse decay length of the b -hadrons (L_{xy}) as a measure of the lifetime of the b hadrons. Fig. 2.2.5 shows L_{xy} distributions for three different top quark masses. We can see that the L_{xy} distribution has good sensitivity to the top quark mass. Because this method requires only a tagged b -jet from top quark decays, events with three jets in the $4j$ are included. Dilepton events can be easily included in the method, which we plan to do in the near future.

The transverse decay length L_{xy} is obtained using the secondary vertex algorithm (SecVtx). Once SecVtx finds a secondary vertex, L_{xy} is calculated as the projection of the secondary vertex position to the jet axis. This method requires an efficient SecVtx algorithm and an accurate simulation of the L_{xy} , which has been tested using a heavy-flavor enriched data sample (mainly $b\bar{b}$). CDF finds good agreement in the average value of L_{xy} within 1.4% between data and simulated events. The average values of the L_{xy} distributions are calibrated for various true top quark mass values, including contributions from backgrounds. The top quark mass is obtained by a simple fit to the average value of L_{xy} from the data.

Currently the source of the largest systematic error at CDF comes from inaccurate simulation of L_{xy} including imprecise knowledge of b -hadron lifetimes.

Matrix Element Method

Contributed by: F. Canelli and F. Fiedler

Both CDF and D0 have implemented methods to extract the maximum possible information on the top quark mass from their limited $t\bar{t}$ event samples and thus minimize the (statistical and overall) error. In these measurements, a probability density as a function of the assumed top quark mass is calculated for each individual observed event by evaluating the differential cross-sections for production of top-antitop pairs of a given mass and for production of background events [4, 5]. The probability densities from all events are combined into one probability for the event sample, from which the value of the top quark mass is extracted. If the probability is calculated not only as a function of the assumed top quark mass, but also of the jet energy scale, both parameters can be measured simultaneously. Both CDF and D0 have reported a measurement in the l^+l^- jets channel using the matrix element (ME) method [6, 7]. In addition, CDF have applied the ME method to the dilepton channel [8, 9], and CDF have measured the top quark mass in the l^+l^- jets channel using the dynamical likelihood method (DLM) [10].

In general, the probability density P_{evt} for one event to be observed in the detector can be expressed as the sum of probability densities P_{sgn} for signal and P_{bkg}^i for n background processes as

$$P_{\text{evt}} = f_{\text{sgn}} P_{\text{sgn}} + \sum_{i=1}^n f_{\text{bkg}}^i P_{\text{bkg}}^i \quad (2.2.1)$$

Here, f_{sgn} is the signal fraction of the event sample, and the f_{bkg}^i denote the fractions of events from the background sources, where $f_{\text{sgn}} + \sum_{i=1}^n f_{\text{bkg}}^i = 1$. The probability density for a given partonic final state to be produced in the hard scattering process is proportional to the differential cross-section d_{hs} of the corresponding process. The differential cross-section for $t\bar{t}$ production will depend on the assumed top quark mass. To obtain the differential cross-section in $p\bar{p}$ collisions, the differential cross-section for the hard scattering process has to be convoluted with the parton density functions (PDF) of the proton and antiproton. The finite detector resolution is taken into account via a convolution with transfer functions (TF) that describe the detector response. These transfer functions are derived from Monte Carlo simulated events.

For a measured event x , the signal probability density as a function of assumed top quark mass m_t becomes

$$P_{\text{sgn}}(x; m_t) = \frac{1}{N} \sum_{\text{com } b_{q_1} b_{q_2} \bar{q}_1 \bar{q}_2 \bar{q}_3 \bar{q}_4} \int_{\text{av}} d\alpha_1 d\alpha_2 f_{\text{PDF}}(\alpha_1) f_{\text{PDF}}(\alpha_2) d_{\text{hs}}(y; m_t) \text{TF}(x; y) \quad (2.2.2)$$

(similarly for the backgrounds). Here, $d_{\text{hs}}(y; m_t)$ denotes the differential hard scattering cross-section for $t\bar{t}$ production, and $\text{TF}(x; y)$ is the probability to observe x in the detector when y was produced. A sum over all flavors (flav) of colliding partons has to be performed, including the relevant PDFs. The integration is over the entire 6-particle phase space of all possible partonic final states y that could have led to the event x , and over the momentum fractions α_i of the colliding partons inside the proton/antiproton. The integration is performed numerically, and assumptions on the detector response (e.g. good lepton

momentum resolution compared to the jet energy resolution) allow to reduce the dimension of the integration space. The quantity N ensures that the probability is normalized. The sum over jet-parton assignments (comb) is discussed below.

The event selection for the $\ell^+\ell^-$ jets analyses (ME and DL) requires an energetic isolated charged lepton (electron or muon), missing transverse energy, and exactly four hadronic jets. The reconstructed jets in the detector cannot be assigned unambiguously to the partons described by the differential cross-section. Without the identification of b jets, there are 24 possible assignments of jets to partons. In events with identified b jets, this number (and also the fraction of background events) is reduced. For the ME measurement in the dilepton channel, events with two energetic charged leptons, missing transverse energy, and two hadronic jets are selected, which amounts to 2 possible jet-parton assignments per event. All relevant possibilities for assignment of jets to partons are taken into account as indicated in Eq. (2.2.2).

In the D0 and CDF ME measurement in the $\ell^+\ell^-$ jets channel, $t\bar{t}$ production is described with the leading order matrix element, and $W^+ + \text{jets}$ background is described using matrix-elements from subroutines of the Vecbos Monte Carlo generator, while QCD multijet background is not handled explicitly in the probability calculation. Jet and charged lepton angles as well as electron energies are assumed to be well-measured in the probability calculation. A likelihood function is determined for the event sample as a function of top quark mass, jet energy scale, and of the parameter f_{sgn} defined in Eq. (2.2.1). The event selection and jet energy scale are taken into account in the normalization of the signal probability, and the background probability normalization is determined such that the parameter f_{sgn} reproduces the $t\bar{t}$ fraction in the event sample. The top quark mass and jet energy scale are then determined in a fit to the likelihood.

For the CDF ME measurement in the dilepton channel, also the leading order matrix element is used. The background considered for this measurement are Drell-Yan production with extra jets, W pairs with jets, and single W production with jets one of which is misidentified as a lepton. So far, the jet energy scale uncertainty is treated as an external error.

In the dynamical likelihood (DL) technique used by the CDF collaboration in the $\ell^+\ell^-$ jets channel, the integration over all possible partonic final states is performed with a Monte Carlo technique, where the mass of the leptonically decaying W boson is generated according to the Breit-Wigner form, and parton energies according to a transfer function. Backgrounds are then not treated explicitly in the likelihood calculation; instead, the measured top quark mass is corrected for the effect of presence of background in the event sample.

Ideogram Method

Contributed by: M. Weber

As in the Matrix Element analyses a likelihood is calculated for each event as a function of the assumed top quark mass taking into account all possible jet assignments and the probability that the event was signal or background. The approach is very similar to a technique, which was used by the DELPHI experiment [11, 12, 13, 14, 15] to extract the mass of the W boson at LEP. As in the Matrix Element method the likelihood is described as a convolution of a physics function and the detector resolution. The difference, however, is that in the ideogram method a kinematic constrained fit is used to describe

the detector resolution, and the physics function is simplified to a relativistic Breit-Wigner describing the average of the invariant masses of the supposed top and anti-top quark that were produced in the event. The ME methods are based on matrix element integrations which require significant computing resources. The approximations of the signal and background probability functions used in the ideogram method result in approximately a factor 1000 faster processing times. This is a major technical advantage of the ideogram method especially considering running an analysis multiple times for systematics evaluation and parameter optimization. The probability P_{evt} is the same as for the Matrix Element methods in equation 2.2.1. P_{sgn} and P_{bkg} are functions of the full set of observables that characterize the event \mathbf{x} . The event observables \mathbf{x} can be divided in two groups. One set was chosen to provide good separation between signal and background events while minimizing the correlation with the mass information in the event. These topological variables are used to construct a discriminant D . The other event information used is the mass information x_t from the constrained kinematic fit, which will give the sensitivity to the top mass. The variables used in the low-bias discriminant D are the same as developed in Run I [16]. The first variable $x_1 = E_T$ is the missing transverse energy. The second variable $x_2 = A$ is the aplanarity, which is the least eigenvalue of the laboratory normalized momentum tensor of the jets and the W boson. $x_3 = \frac{H_{T2}}{H_k}$ measures the event centrality, where H_k is the scalar sum of p_{Tj} of the jets, isolated lepton, and the neutrino. H_{T2} is the sum of the p_{Tj} of the jets excluding the leading jet. $x_4 = \frac{R_{jj}^{\text{min}} E_T^{\text{lesserj}}}{E_W^T}$ is a measure of the jet separation folded together with the transverse energy of the reconstructed W . R_{ij} is the least distance in \sqrt{s} space between any two of the four leading jets. E_T^{lesserj} is the smaller of the two jets E_T 's. The transverse energy of the W is defined as the sum of p_{Tj}^1 and p_{Tj} . For each variable x_i we determine the probability density functions s_i for $t\bar{t}$ signal and b_i for W + jets background from MC. We assume these to be nearly uncorrelated and we write $s = \prod_i s_i^{w_i}$ and $b = \prod_i b_i^{w_i}$. With the weights w_i slightly adjusted away from unity for $x_{1,2,3,4}$ the correlation to the top quark mass was nullified. A discriminant D is built from $s(\mathbf{x})$ and $b(\mathbf{x})$ as:

$$D(\mathbf{x}) = \frac{s(\mathbf{x})}{s(\mathbf{x}) + b(\mathbf{x})}$$

We do use a parametrized form for D where the ratios $s(x_i)/b(x_i)$ were parametrized with polynomial fits¹. The fitted mass information x_t is a set of kinematic variables, calculated from a constrained kinematic fit to the reconstructed jets, lepton and missing transverse energy. The procedure explained in section 2.3 corrects the measured jets for the portion of the showers which spread outside the jet cone, but not for any radiation outside the cone. We do further correct the jet energies to that of the fragmented partons in the MC. To derive this correction we use MC events where the jets could be matched to the partons of the $t\bar{t}$ decay and compare the jet energy to the parton energy information from the MC. The constrained fit technique is the same as used in the D0 Run I template mass analysis [16]. The fit is performed by minimizing a χ^2 defined as:

$$\chi^2 = (\mathbf{x} - \mathbf{x}_M) G (\mathbf{x} - \mathbf{x}_M)^T \quad (2.2.3)$$

where \mathbf{x}_M is a vector of measured variables, \mathbf{x} is a vector of fitted variables, and G is the inverse error matrix of the measured quantities. G^{-1} is taken to be diagonal. The χ^2 is minimized subject to the

¹Additional transformations to the x_i s before the fit were done for the functions to be better approximated by polynomials: $x_1^0 = \exp[-(m_{ax}(0; \sqrt{\frac{3(x_1 - (16 \text{ eV})^2)}{2}}))]$, $x_2^0 = \exp(-11x_2)$, $x_3^0 = \ln(x_3)$, $x_4^0 = \frac{1}{x_4}$.

kinematic constraints $m(t \rightarrow l b) = m(t \rightarrow q \bar{q})$, $m(l) = M_W$ and $m(q \bar{q}) = M_W$. The minimization algorithm uses the method of Lagrange Multipliers; the nonlinear constraint equations are solved using an iterative technique. The fitted mass m_{fit} and its uncertainty σ_{fit} are taken at the minimum of the χ^2 . For every event we run the kinematic fitter for each of the 12 possible permutations i of assigning the 4-momenta of the reconstructed jets to the partons ($b \bar{q} q$). The W -boson mass constraint on the leptonic side can result in a twofold ambiguity on the neutrino longitudinal momentum p_z . Both cases are considered and the fit is repeated for each initial guess. To good approximation D and x_t are uncorrelated, and the P_{sgn} and P_{bkg} probabilities can be written as the product of a probability to observe a value D and a probability to observe x_t :

$$P_{\text{sgn}}(x; m_{\text{top}}) = P_{\text{sgn}}(D) P_{\text{sgn}}(x_t; m_{\text{top}}) \quad (2.2.4)$$

and

$$P_{\text{bkg}}(x) = P_{\text{bkg}}(D) P_{\text{bkg}}(x_t) \quad (2.2.5)$$

The normalized probability distributions of the D discriminant for signal $P_{\text{sgn}}(D)$ and background $P_{\text{bkg}}(D)$ are obtained from Monte Carlo simulation. The permutations are weighted using weights w_i , which estimate the relative probability for a certain jet permutation to be the correct one. The relative probability of each jet assignment w_i purely depends on the χ^2_i for the corresponding fit and is calculated as $w_i = \exp(-\frac{1}{2} \chi^2_i)$. The signal term in Eq. 2.2.4 is calculated as

$$P_{\text{sgn}}(x_t; m_{\text{top}}) = \sum_{i=1}^{\chi^2_{24}} w_i \int_{100}^{300} G(m_i; m^0; \sigma_i) BW(m^0; m_t) dm^0 \quad (2.2.6)$$

and the background term:

$$P_{\text{bkg}}(x_t) = \sum_{i=1}^{\chi^2_{24}} w_i BG(m_i) \quad (2.2.7)$$

The signal term consists of the compatibility of the solution with a certain value of the top mass, taking into account the estimated mass resolution σ_i for each jet permutation. This is given by a convolution of a Gaussian resolution function $G(m_i; m^0; \sigma_i)$ describing the experimental resolution with a relativistic Breit-Wigner $BW(m^0; m_t)$, representing the expected distribution of the average of the two invariant masses of the top and anti-top quark in the event, for a top mass m_t .

For the background term a weighted sum $BG(m_i)$ is used, where $BG(m)$ is the shape of the mass spectrum obtained from W +jets in MC simulation with all entries weighted according to the permutation weight w_i assigned to each solution. The Breit-Wigner and other permutation signal shape are normalized to unity on the integration interval: 100 to 300 GeV. This interval was chosen large enough not to bias the mass in the region of interest. Since each event is independent the combined likelihood for the whole sample is calculated as the product of the single event likelihood curves:

$$L_{\text{sam p}}(m_t; f_{\text{sgn}}) = \prod_j L_{\text{evt j}}(m_t; f_{\text{sgn}})$$

This likelihood is maximized with respect to the top mass m_t and the estimated fraction of signal in the sample f_{sgn} .

2.3 Systematic Uncertainties

Contributed by: F. Canelli, F. Fiedler, M. Weber, and U.-K. Yang

Systematic uncertainties arise from the modeling of physics processes and from the simulation of the detector. These two sources are described in the two following sections.

Physics Modeling

Signal Modeling: When $t\bar{t}$ events are produced in association with a jet, the additional jet can be misinterpreted as a product of the $t\bar{t}$ decay. Such events are present in the simulated events used for the calibration of the method. We tuned the initial and final state gluon radiations in PYTHIA by using the transverse momentum of Drell-Yan events and extrapolated to the Q^2 region of the $t\bar{t}$ production. Uncertainties on the extra jets are estimated based on this tuning. The difference between $t\bar{t}$ cross-sections calculated at leading and next-to-leading order is also used to estimate abundance of such events. To assess the uncertainty in the modeling of these effects, their fraction is varied in the simulation. Also, the relative cross-section of the processes $g\bar{g} \rightarrow t\bar{t}$ and $q\bar{q} \rightarrow t\bar{t}$ is varied.

Background Modeling: The main background in the lepton+jets channel is due to the production of jets in association with a leptonically decaying W . In order to study the sensitivity of the measurement to the choice of background model, the factorization scale of $Q^2 = m_W^2 + \sum_j p_{T,j}^2$ used in the modeling of W +jets events is replaced by $Q^2 = p_{T,j}^2$.

PDF Uncertainty: To study the systematic uncertainty on the top mass due to the choice of PDF used to simulate signal and background events, the variations provided with the next-to-leading-order PDF set CTEQ6M [17] are used. The result obtained with each of these variations is compared with the result using the default CTEQ6M parametrization. The difference between the results obtained with the CTEQ and MRST PDF sets is taken as another uncertainty. Finally, the value of α_s is varied. All errors are added in quadrature.

Bottom Fragmentation and Semileptonic Decays: The estimate of the jet energy scale from a priori information and from $W \rightarrow jj$ decays do not give direct information on the b -jets energy scale. The b -jets can behave differently from gluon and light quark jets because of their different fragmentation models, more abundant semi leptonic decays and different color flow in $t\bar{t}$ events than W -daughter jets. However, we find that a major uncertainty on the b -jet energy scale comes from common features of the generic jets. We study simulated $t\bar{t}$ events with different fragmentation models for b -jets due to the choice of the model.

The reconstructed energy of b -jets containing a semileptonic bottom or charm decay is in general lower than that of jets containing only hadronic decays. This can only be taken into account for jets in which a soft muon is reconstructed. Thus, the fitted top quark mass still depends on the semileptonic b and c decay branching ratios. They are varied within the bounds given by the LEP results [18].

Jet Energy Scale

Since the measurement of the top quark mass requires the determination of the four-momenta of quarks which relies on the reconstruction of hadronic jets resulting from fragmentation, the dominant systematic uncertainty comes from our measurements of the jet energies.

At CDF and D0, jets are observed as clustered energy depositions in the calorimeters. Both experiments use a cone algorithm defined with a radius of $R_{\text{jet}}=0.4$ and $R_{\text{jet}}=0.5$ for CDF and D0, respectively. Measured jet energies are corrected to best describe particle jets or partons energies. The accurate modeling of the detector response as well as a good understanding of the fragmentation process is an essential requirement for these corrections.

In the following, we describe the corrections to the measured jet energy and the determination of the overall jet energy scale in CDF and D0. A more detailed explanation can be found in [19, 20] and [21].

The overall jet energy scale is the dominant systematic uncertainty on top quark mass measurements in the lepton+jets channel unless it is determined simultaneously (“in situ”) with the top quark mass from the same event sample. Both CDF and D0 have shown such analyses with a simultaneous measurement of the top quark mass and overall jet energy scale. But even for such an in situ calibration, systematic errors still arise from the possible dependence of the jet energy scale on the energy itself or on the position in the calorimeter.

CDF Jet Energy Scale CDF uses the Monte Carlo simulation to determine the jet energy scale allowing to correct an energy range from 8 GeV to 600 GeV. Therefore, the major task involved in the determination of the jet energy scale is the tuning and validation of the detector simulation as well as of the physics modeling used in the simulation.

Before corrections are derived, the energy scale for the electromagnetic calorimeter is set using electrons from the decay $Z \rightarrow e^+ e^-$ and the energy scale for the hadronic calorimeter is set to the test-beam scale of 50 GeV/c charged pions.

The corrections are divided in different levels to allow many different analyses in different groups to use them and to create an experiment-wide definition of jet energies. Firstly, measured jets are corrected for all instrumental effects to a particle-level jet which corresponds to the sum of the momenta of the hadrons, leptons, and photons within the jet cone. Particle-level jets are then corrected to parton level energies.

Since the simulation is used to correlate a particle jet to a calorimeter jet a detailed understanding of the detector is needed. The simulation is tuned to model the response of the calorimeter to single particles by comparing the calorimeter energy measurement, E , to the particle momentum, p , measured in tracking detectors. Here, measurements based on both test beam and CDF data taken during Run II are used. The calorimeter simulation is most reliable in the central part of the calorimeters since the tracking coverage in the forward regions is limited. Therefore, the forward calorimeter jet response is calibrated with respect to the central, to flatten out the jet response versus the jet polar angle. This procedure also corrects for the lower response in poorly instrumented regions of the calorimeters. After tuning the simulation to the individual particles response and achieving a jet response independent of the polar angle, calorimeter jets are corrected to a particle jet, i.e. they are corrected for the central

calorimeter response. Since the correction is derived from simulation, it is also important to ensure that the multiplicity and momentum spectrum of particles in the data is well reproduced by the simulation.

A further correction is made for pile-up of additional $p p$ interactions. This pile-up can lead to an overestimate of the jet energy if particles produced in the additional interactions happen to overlap with those produced in the hard scattering process. Similarly, the jet energy is also corrected for particles from the underlying event, i.e. interactions from spectator quarks and initial state QCD radiation.

Since the jet cone is of finite size some particles originating from the initial parton may escape from the jet cone either in the fragmentation process or due to parton radiation. The out-of-cone energy is measured in MC events. Depending on the analysis different corrections are used. For matrix element based analyses these corrections correspond to the transfer functions. Here, the full shape of the mapping between particle jets and parton energies is used. The template analysis uses an average correction of this mapping also obtained from \sqrt{s} HERWIG MC.

The original parton transverse energy is estimated by correcting the jet for all the above effects:

$$p_T^{\text{parton}} = (p_T^{\text{jet}} \cdot C_{\theta} \cdot C_{M I}) \cdot C_{Abs} \cdot C_{UE} + C_{OOC} = p_T^{\text{particle}} \cdot C_{UE} + C_{OOC} \quad (2.3.8)$$

where p_T^{parton} is the transverse momentum of the parent parton the procedure is aimed at, p_T^{jet} is the transverse momentum measured in the calorimeter jet, p_T^{particle} is the transverse momentum of the particle jet. The different factors in the corrections are: C_{θ} , “ θ -dependent” correction, ensures homogeneous response over the entire angular range; $C_{M I}$, “Multiple Interaction” correction, is the energy to subtract from the jet due to pile-up of multiple $p p$ interactions in the same bunch crossing; C_{Abs} , “Absolute” correction, is the correction of the calorimeter response to the momentum of the particle jet. Particle jets can be compared directly to data from other experiments or theoretical predictions which include parton radiation and hadronization. C_{UE} and C_{OOC} , the “Underlying Event” and “Out-Of-Cone” corrections, correct for parton radiation and hadronization effects due to the finite size of the jet cone algorithm that is used. Note that the C_{UE} and C_{OOC} corrections are independent of the experimental setup, i.e. the CDF detector environment. All the correction factors are determined as a function of the jet transverse momentum but they apply to all components of the four-momentum of the jet.

Various cross-checks using different physics processes (γ +jet, Z +jet, W +jet) are done to validate the universality of the procedure and verify the systematic uncertainties.

The systematic uncertainties take into account any differences observed between the data and the simulation and possible systematic biases in the procedure used to determine the corrections. Data and Monte Carlo are compared in every step of the correction procedure, and the uncertainties are added in quadrature. The final systematic error on the jet energy scale is shown in Fig. 2.3.6. The total systematic uncertainty on the jet energy scale varies between 8% at low jet p_T and 3% at high jet p_T . The systematic uncertainties are largely independent of the corrections applied and mostly arise from the modeling of jets by MC simulation and from uncertainties in the calorimeter response to single particles.

For $p_T > 60$ GeV/c the largest contribution arises from the absolute jet energy scale which is limited by the uncertainty of the calorimeter response to charged hadrons. A further reduction of the systematic uncertainties can be achieved by improving the tuning of the simulation, and by including *in situ* single track data which recently became available, replacing test beam data used so far in the momentum region 7-20 GeV/c and probably beyond.

At low p_T the largest uncertainty arises from the out-of-cone energy which can be improved by

further studying differences between the data and the predictions of PYTHIA and HERWIG, and by optimizing the fragmentation and underlying event model of both generators.

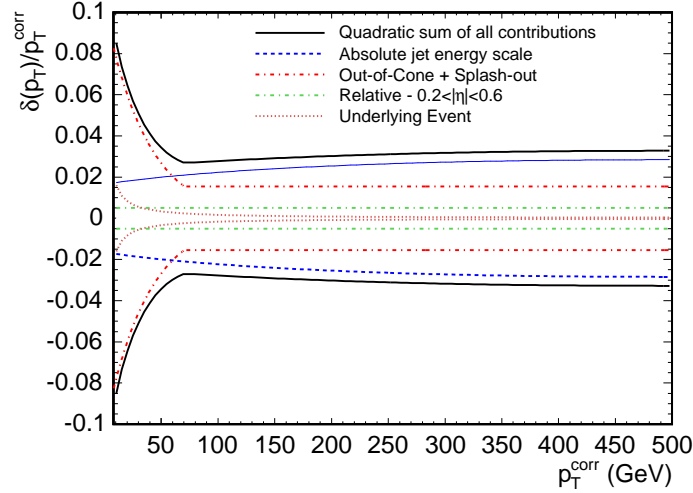


Fig. 2.3.6: CDF jet energy scale systematic uncertainties as a function of the corrected jet p_T in $0.2 < |j| < 0.6$.

D0 Jet Energy Scale The measured energy of a reconstructed jet is given by the sum of energies deposited in the calorimeter cells associated with the jet by a cone algorithm. Several mechanisms cause this energy estimate to deviate from the energy of the particle level jet:

Energy Offset: Energy in the clustered cells which is due to noise, underlying event, multiple interactions, energy pile-up, and uranium noise lead to an offset E_0 (R ; η ; L) of jet energies. E_0 is determined from energy densities in minimum bias events.

Calorimeter Response: Jets consist of different particles (mostly photons, pions, kaons, protons and neutrons), for which the calorimeter response is different. Furthermore, the calorimeter responds slightly non-linearly to particle energies. The response $R_{jet}(E_{jet}^{m eas}; \eta)$ is determined with $+jets$ events requiring transverse momentum balance. The photon scale is measured independently with high precision in $Z \rightarrow e e$ events.

Showering Corrections: Not all particles deposit their energy within the jet cone. The fraction $R_{cone}(R; E_{jet}^{m eas}; \eta)$ deposited inside the cone of radius $R = \frac{p_T}{\sqrt{(\Delta\eta)^2 + (\Delta\phi)^2}}$ is obtained from jet energy density profiles.

Consequently, the corrected particle level jet energy E_{jet}^{corr} is obtained from the measured reconstructed jet energy $E_{jet}^{m eas}$ as

$$E_{jet}^{corr} = \frac{E_{jet}^{m eas} - E_0}{R_{jet} R_{cone}} \quad (2.3.9)$$

The offset energy E_0 is defined as the energy contribution to a jet that is not associated with the hard scattering process. Contributions to the offset come from electronic noise, uranium noise, pile-up, and energy from additional interactions underneath the interesting physics process. The shaping time of

the D0 calorimeter readout electronics is longer than the bunch crossing time of 396 ns, so the signal from an earlier bunch crossing may contribute to the energy of the jet under consideration. The offset energy is measured from minimum bias events, which are defined as events triggered by the condition that the luminosity counters on both sides of the interaction point are hit. As a cross-check, the contribution from noise and pile-up is also measured from events without a hard interaction.

As in Run I, D0 uses the missing E_T projection fraction method to measure the calorimeter response from the p_T imbalance in back-to-back γ +jet events [21]. For an ideal detector, the photon transverse momentum p_T and the transverse momentum of the hadronic recoil p_T^{had} are balanced. However, because the calorimeter response to photons, R_γ , and hadronic jets, R^{had} , is different, an overall transverse momentum imbalance is observed:

$$R_\gamma p_T + R^{\text{had}} p_T^{\text{had}} = \cancel{p_T} \quad (2.3.10)$$

The missing transverse momentum $\cancel{p_T}$ is corrected for the electromagnetic calorimeter response R_γ , which is determined from the position of the mass peak in $Z^0 \rightarrow e^+e^-$ events. After that, the hadronic response is obtained as

$$R^{\text{had}} = 1 + \frac{\cancel{p_T}^{\text{corr}}}{(p_T)^2} \quad (2.3.11)$$

In events with one photon and exactly one jet, the jet response can be identified with the hadronic response. The jet response is determined as a function of jet energy and pseudorapidity, and an additional correction is applied for jets in the region between the central and endcap calorimeter cryostats.

Part of the jet energy may be deposited outside the jet cone because of the finite lateral shower width and because charged particles may be bent outside the cone by the magnetic field. This effect is measured from energy density profiles of jets. Because gluon emission and fragmentation processes also contribute to the energy density profile measurement, these effects are corrected for using Monte Carlo simulation.

Additional corrections are needed to reconstruct the energy of a jet containing an identified semimuonic decay of a bottom or charm hadron. The expected energy that the muon deposited in the calorimeter is subtracted from the jet energy, and the muon momentum and the average neutrino momentum added. The average neutrino momentum has been obtained from simulated events and is calculated as a function of the momentum of the muon and its transverse momentum relative to the jet axis.

In each event, the missing transverse momentum is adjusted according to the jet energy scale factors applied to all jets in the event.

The measurement technique for the top quark mass is calibrated using Monte Carlo simulated events. Consequently, the ratio between data and Monte Carlo of the jet energy scale and the associated uncertainty are the relevant quantities for the top quark mass measurement. Because the dependence of the jet energy scale on jet energy and pseudorapidity is not necessarily the same in data and Monte Carlo, this ratio will depend on jet energy and pseudorapidity as well. In measurements of the top quark mass at D0, these dependences are taken from the γ +jet measurement. The overall data/Monte Carlo scale factor, JES , is either taken from the γ +jet measurement as well, or determined “in situ” simultaneously with the top quark mass in measurements using lepton+jets $t\bar{t}$ events.

The jet energy scale for b jets may be different from that for light quark jets. If the relative b /light quark jet energy scale is different in data from that in the simulation, then the measurement of the top

quark mass is affected. The uncertainty on this double ratio is estimated by varying the ratio of the calorimeter response to hadrons and electrons, and by varying the b quark fragmentation model. In addition, the double ratio is cross-checked with b -jet events where the jet is tagged by the presence of a secondary vertex.

If the overall JES factor is determined simultaneously with the top quark mass, the statistical error on the latter increases by a factor of about 1.5. The uncertainty on the energy dependence of the jet energy scale measurement from b -jet events contributes a systematic error to the top quark mass measurement of 250 MeV [7]. Currently, the largest systematic uncertainty on the top quark mass measurement with in situ JES calibration comes from the knowledge of the b /light quark jet energy scale ratio. This systematic error is about 1 GeV.

2.4 Top Mass Combination

Contributed by: D. Glenzinski

A world average top quark mass, M_t , is obtained by combining the various Tevatron measurements. The average is performed by the Tevatron Electroweak Working Group (TevEWWG) with working members from both the CDF and D0 Collaborations. The most recent combination is described in detail in reference [22] and includes preliminary CDF and D0 measurements using about 350 pb^{-1} of Run II data. A summary of the methodology is given in this section.

The combination takes into account all statistical and systematic correlations. Measurements of M_t in the lepton+jets (l+j), di-lepton (dil), and all-jet (all-j) channels from both CDF and D0 are combined using the analytic BLUE method [23, 24] and cross-checked using a numerical χ^2 minimization. The experiments supply the inputs and the TevEWWG, in collaboration with the experts from the experiment, specifies the error categories. The definition of error categories is driven by the categories of uncertainties considered and their correlations. For example, in an effort to more accurately account for the JES uncertainties correlated between the experiments, the JES is broken into several sub-categories. The error categories are discussed in detail below.

At present, each experiment evaluates the associated systematic uncertainties independently, often times using different techniques. These differences can effect the weight a particular input carries, and thus the world average M_t as a result. While at the present time these differences affect the average M_t at the level of $100 \text{ MeV} = \sigma$ or less, the TevEWWG will focus on more accurately determining the intra-experiment correlations as the precision of the combination continues to improve. For example, by specifying the methodology to use when quantifying particular classes of systematic uncertainties (e.g. the Signal Modeling, Background Modeling, and JES uncertainties). These discussions have already begun, although there is nothing concrete to report at this time. Once LHC results become available, the precision on the world average M_t may be such that these same specifications may also be important when including the new LHC results. Thus it will be important to document any common methodologies used.

The following error categories are used when performing the M_t combination:

Statistical: The statistical uncertainty, calibrated to correspond to 68% coverage using pseudo-experiments to study the r.m.s. of the resulting pull distribution.

Signal Modeling: This includes modeling uncertainties related to ISR, FSR, PDF, and α_{QCD} variations

in $\tau\tau$ events.

Background Modeling: This includes modeling uncertainties related to fragmentation, Q^2 , and normalization variations in background events.

Monte Carlo Generator: This includes comparisons of fit biases introduced when using different Monte Carlo generators to simulate $\tau\tau$ events. This arguably double-counts some of the uncertainty in the "Signal Modeling" category and may be revised as we gain further confidence in the methodologies and variations used to quantify those modeling uncertainties.

Fit: This includes uncertainties from limited Monte Carlo statistics, and other possible (small) residual biases related to the specific techniques used to determine M_τ for a given input.

Uranium Noise: Includes uncertainties specific to D0 Run I results which account for effects of noise in the Uranium calorimeter on the jet energy determination.

In-Situ JES: This is the uncertainty from the JES as determined using the mass of *in situ* $W \rightarrow q\bar{q}$ decays. At this time this determination is completely statistics dominated and is thus treated as uncorrelated between CDF and D0.

JES Modeling: This includes modeling uncertainties from fragmentation and out-of-cone showering variations which affect the determination of corrections necessary to estimate the original parton energy from the measured jet energy.

JES B-jet Modeling: This includes modeling uncertainties specific to B-jets and includes fragmentation, color flow, and b-decay branching fraction variations.

JES B-jet Response: This includes uncertainties arising from differences in the e/h ratio between light-quark-jets and B-jets and is specific to D0 Run II.

JES Relative Response: This includes uncertainties arising from uncertainties associated with the p_T -dependent corrections made to flatten the calorimeter response as a function of pseudo-rapidity.

JES Calibration: This includes uncertainties arising from the limited statistics of the calibration and control samples used to determine several components of the JES corrections.

The techniques used to quantify these uncertainties are described in detail in Section 2.3 above. The eight M_τ measurements presently included in the combination are summarized in Table 2.4.1². Note that the CDF Run II determination in the lepton+jets channel uses both the *in situ* $W \rightarrow q\bar{q}$ mass and the external calibrations to determine the JES. In order to accurately account for the correlations with other inputs that measurement is recorded as two separate inputs with the JES components of the uncertainty appropriately divided while the remaining statistical and systematic uncertainties are taken to be 100% correlated. The combination of these two inputs yields the same statistical, systematic, and total uncertainty as the original measurement.

In the combination, the categories of uncertainty discussed above are assumed to have the following correlations among the various inputs:

The Statistical, Fit, and *in situ* JES uncertainties are taken to be uncorrelated among all inputs.

The Uranium Noise and JES Relative Response uncertainties are taken to be 100% correlated among all inputs from the same experiment, but uncorrelated between the experiments.

²The inputs listed in Table 2.4.1 are the same as those used in reference [22]. Since then the two CDF Run II measurements have been finalized and published [25][26] with small improvements to some of systematic uncertainties. However, these improvements have not yet been included in a new Tevatron combined M_τ .

The JES uncertainties from B-jet Response and Calibration are taken to be 100% correlated among all inputs from the same experiment and data-taking period (ie. Run I or Run II) and uncorrelated otherwise.

The Background uncertainties are taken to be 100% correlated across all inputs in the same final-state (ie. all-j, l+j, or dil), regardless of experiment or data-taking period, and uncorrelated otherwise.

The Signal, Monte Carlo, JES Modeling, and JES B-Jet Modeling uncertainties are taken to be 100% correlated across all inputs.

The resulting global correlation coefficients are given in Table 2.4.2 and yield a world average

$$M_{\tau} = 172.7 \pm 2.9 \text{ GeV} \quad (2.4.12)$$

with a $\chi^2_{\text{dof}} = 6.5/7$, corresponding to a χ^2 probability of 49%. The total uncertainty of 2.9 GeV is the quadrature sum of a Statistical uncertainty of 1.7 GeV , a total JES uncertainty of 2.0 GeV , a Signal uncertainty of 0.9 GeV , a Background uncertainty of 0.9 GeV , a Uranium Noise uncertainty of 0.3 GeV , a Fit uncertainty of 0.3 GeV , and a Monte Carlo uncertainty of 0.2 GeV . The inputs and the combined M_{τ} are all shown together in Fig. 2.4.7 while the pulls and weights of each input are given in Table 2.4.3. The issue of negative weights, as observed in this case for one of the inputs, is discussed in detail in reference [23] and arises when the correlation coefficient is comparable to the ratio of the total uncertainties between two measurements.

2.5 Top Mass Expectations

Contributed by: D. Glenzinski

Using the new Run II measurements as a basis, some simple extrapolations have been performed in order to roughly estimate what the future sensitivity of the Tevatron combined M_{τ} might be. The present Run II results each use approximately 350 pb^{-1} , a factor of 15-20 less than the expected data set at the end of Run II. It is important to note that at present the JES uncertainty is effectively the weighted average of the *in situ* JES with the quadrature sum of the remaining JES uncertainties so that as the data sets increase the *in situ* determination will improve and will eventually come to dominate the JES uncertainty. Initial studies indicate that the total JES uncertainty will fall to approximately 1.5 GeV per experiment with 1 fb data-sets (each) and to 1.0 GeV per experiment for data-sets exceeding 4 fb each. Even under the conservative assumption that *only* the Statistical and *in situ* JES uncertainties improve (proportional to $1/\sqrt{N}$) with increasing data-sets while all other uncertainties are fixed, the ultimate Tevatron combined sensitivity should readily fall below $M_{\tau} < 2 \text{ GeV}$. Figure 2.5.8 shows how the total uncertainty in the l+j channel for CDF is expected to evolve. For this extrapolation the expected statistical uncertainties have been estimated by performing Monte Carlo pseudo-experiments at several luminosity points, assuming the Standard Model $t\bar{t}$ production cross-section, and assuming the signal and background acceptances do not change with the increasing instantaneous luminosity necessary to meet the Run II delivered luminosity goals. With these conservative assumptions, CDF alone with this single channel alone is expected to do better than the original TDR estimates for the CDF combined sensitivity [27]. Using extrapolations for the other inputs with the same conservative assumptions and repeating the combination using the same error categories and correlations discussed above predict an ultimate Tevatron combined sensitivity of $M_{\tau} = 1.5 \text{ GeV}$ for data-sets of 4 fb collected per

	Run I Published					Run II Preliminary			
	CDF			D0		CDF			D0
	all-j	l+j	dil	l+j	dil	(l+j) _i	(l+j) _e	dil	l+j
Result	186.0	176.1	176.4	180.1	168.4	173.5	165.3	169.5	
Signal	1.8	2.6	2.8	1.1	1.8	1.1	1.5	0.3	
Background	1.7	1.3	0.3	1.0	1.1	1.2	1.6	0.7	
Generator	0.8	0.1	0.6	0.0	0.0	0.2	0.8	0.0	
Fit	0.6	0.0	0.7	0.6	1.1	0.6	0.6	0.6	
Ur. Noise	0.0	0.0	0.0	1.3	1.3	0.0	0.0	0.0	
Sub-total	2.7	2.9	3.0	2.1	2.7	1.7	2.4	1.0	
JES <i>in situ</i>	0.0	0.0	0.0	0.0	0.0	4.2	0.0	0.0	3.3
Model	3.0	2.7	2.6	2.0	2.0	0.0	2.0	2.2	0.0
B-Model	0.6	0.6	0.8	0.7	0.7	0.6	0.6	0.8	0.7
B-Resp.	0.0	0.0	0.0	0.0	0.0	0.0	0.0	0.0	0.9
Rel-Resp.	4.0	3.4	2.7	2.5	1.1	0.0	2.3	1.4	0.0
Calib.	0.3	0.7	0.6	0.0	0.0	0.0	0.0	0.0	0.0
JES Total	5.0	4.4	3.9	3.3	2.4	4.3	3.1	2.7	3.5
Syst Total	5.7	5.3	4.9	3.9	3.6	4.6	3.5	3.6	3.6
Statistical	10.0	5.1	10.3	3.6	12.3	2.7	6.3	3.0	3.0
Total	11.5	7.3	11.4	5.3	12.8	4.1	7.3	4.7	4.7

Table 2.4.1: The inputs for the most recent world average M_t combination [22]. All values are in $G \sqrt{s} = c^2$. The CDF Run II measurement in the l+j channel is specially treated as described in the text. The total uncertainties are the quadrature sum of the individual uncertainties listed.

experiment. It should be noted that at present, as discussed above in Section 2.3, several systematic uncertainties are limited by the statistics of the samples used to quantify them. Thus it is reasonable to expect that these, too, will improve with time to yield an even better Tevatron combined sensitivity.

2.6 Top Mass Determination at the LHC

Contributed by: A.I. Etienvre, A. Giammanco

Introduction

At the LHC, the top quark will be produced mainly in pairs through the hard process $gg \rightarrow t\bar{t}$ (90%) and $q\bar{q} \rightarrow t\bar{t}$ (10%); the corresponding cross-section, at the next-to-leading order, is equal to 796^{+94}_{-91} pb; therefore, we expect roughly 8 million $t\bar{t}$ pairs to be produced with 100 days at low luminosity (corresponding to an integrated luminosity of 10 fb^{-1}).

In order to ensure a similar contribution to the indirect measurement of the Higgs mass, the precision on m_W and m_t must fulfill the following relation: $m_t \approx 0.710^2 m_W$. At LHC, we expect to reach an accuracy of $15 \text{ MeV}/c^2$ on m_W and $1 \text{ GeV}/c^2$ on m_t . With these precision measurements, the relative precision on a Higgs boson mass of $115 \text{ GeV}/c^2$ would be of the order of 18% [28]. The various

		Run I Published					Run II Preliminary			
		CDF			D0		CDF			D0
		all-j	l+j	dil	l+j	dil	(l+j) _i	(l+j) _e	dil	l+j
CDF I	all-j	1.00								
CDF I	l+j	0.32	1.00							
CDF I	dil	0.19	0.29	1.00						
D0 I	l+j	0.14	0.26	0.15	1.00					
D0 I	dil	0.07	0.11	0.08	0.16	1.00				
CDF II	(l+j) _i	0.04	0.12	0.06	0.10	0.03	1.00			
CDF II	(l+j) _e	0.35	0.54	0.29	0.29	0.11	0.45	1.00		
CDF II	dil	0.19	0.28	0.18	0.17	0.10	0.06	0.30	1.00	
D0 II	l+j	0.02	0.07	0.03	0.07	0.02	0.07	0.08	0.03	1.00

Table 2.4.2: The matrix of global correlation coefficients between the M_t measurements of Table 2.4.1 using the error categories and assuming the correlations described in the text.

		Run I Published					Run II Preliminary			
		CDF			D0		CDF			D0
		all-j	l+j	dil	l+j	dil	(l+j) _i	(l+j) _e	dil	l+j
Pull		+1.19	+0.51	-0.48	+1.67	-0.34	+0.28	-1.11	-0.86	
Weight [%]		+1.0	-0.2	+1.1	+18.8	+2.1	+36.0	+8.0	+33.3	

Table 2.4.3: The pull and weight of each input from Table 2.4.1 in the Tevatron combined M_t determination using the global correlation coefficients given in Table 2.4.2.

methods developed to measure the top mass at the LHC are explained, together with their advantages, their disadvantages, and their corresponding systematic errors.

Systematic Uncertainties

For the top mass analyses presented here, performed within ATLAS or CMS, several systematic uncertainties have been estimated. The main sources of errors, common to several analyses, are briefly described below.

Jet energy scale When the top quark is reconstructed via its hadronic decay ($t \rightarrow Wb \rightarrow jjb$), the accuracy of the measurement of its mass relies on a precise knowledge of the energy calibration for both light jets and b-jets. The energy of the two light jets can be calibrated precisely event by event using an in-situ calibration based on the W mass constraint [29], while the b-jet energy scale has to be calibrated independently : therefore, their contributions to systematic errors are always estimated separately.

A jet energy scale calibration at the level of 1% , for both light jets and b-jets, should be reached at LHC : the corresponding errors on the top mass measurement given below correspond to this level of precision. The estimation of an absolute jet energy scale uncertainty has been carried out applying

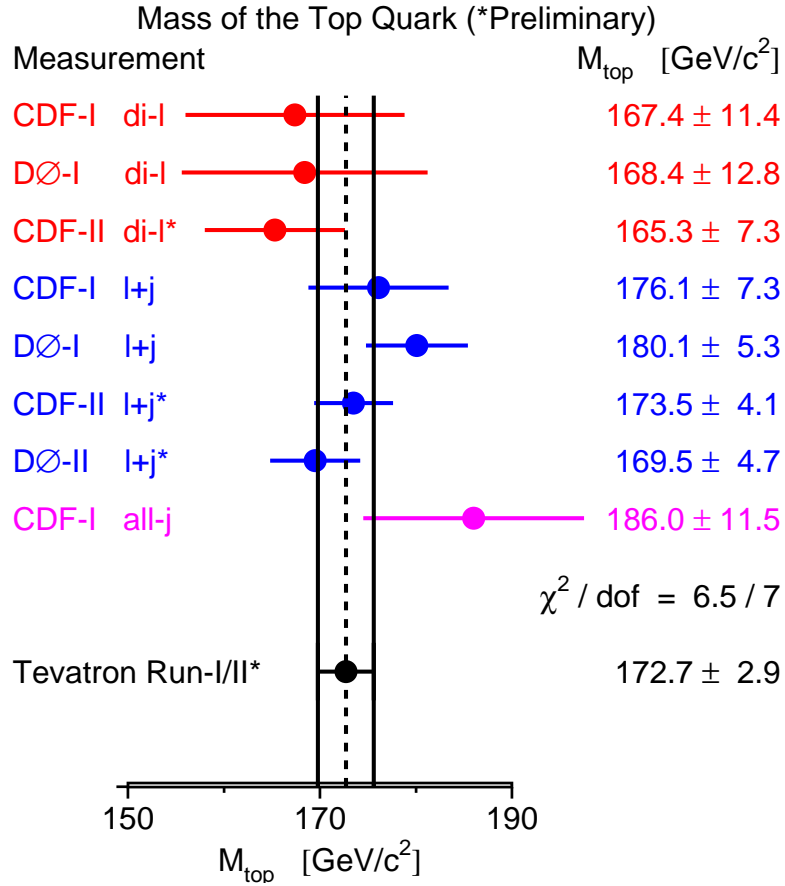


Fig. 2.4.7: The inputs for the Tevatron combined M_t combination and the resulting world average top quark mass, obtained as described in Section 2.4.

different miscalibration coefficients to the reconstructed jet energies ; a linear dependence has been observed.

Initial and final state radiation The presence of initial state radiation (ISR) of incoming partons and final state radiation (FSR) from the top decay products has an impact on the top mass measurement. In order to estimate the uncertainty due to these radiations, the top mass has been determined with ISR (FSR) switched on, at the generator level, and ISR (FSR) switched off. The systematic uncertainty on the top mass is taken to be 20 % of the corresponding mass shifts : this should be a conservative estimate, assuming that ISR and FSR are known at a level of order of 10 % [30].

b-quark fragmentation The systematic error due to an imperfect knowledge of the b-quark fragmentation has been estimated by varying the Peterson parameter of the fragmentation function (equal to -0.006) within its experimental uncertainty (0.0025) : the consecutive shift on the top mass is taken as the systematic error on the top mass.

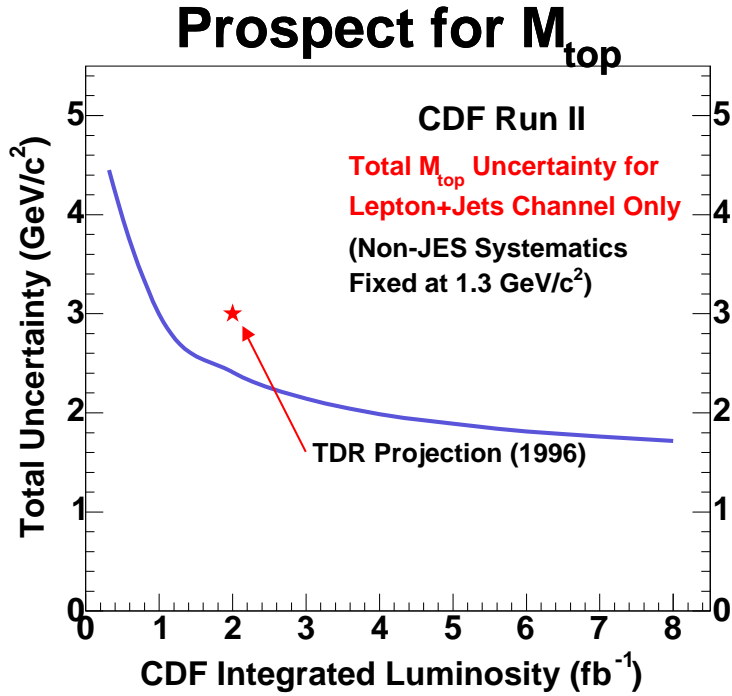


Fig. 2.5.8: The total uncertainty on the top quark mass for the CDF lepton+jets channel, extrapolated to larger data-sets using the assumptions described in Section 2.5 and based on the methodology described in reference [25].

Background The background of the top quark reconstruction is dominated by wrong combinations in $t\bar{t}$ events themselves (FSR, wrong association of the W to the corresponding b-jet,...). Varying the background shape and size in the fitting procedure of the top mass distribution gives access to the resulting uncertainty on the top mass measurement.

Top mass measurement in the lepton + jets channel

The lepton plus jets channel will provide a large and clean sample of $t\bar{t}$ events and is probably the most promising channel for an accurate measurement of the top mass. The main backgrounds are summarized in Table 2.6.4, with their corresponding cross sections and expected number of events at 10 fb^{-1} . Before any selection, the signal over background ratio is of the order of 10^{-4} . Events are selected by requiring one isolated lepton (electron or muon) with $p_T > 20 \text{ GeV}/c$ and $j-j > 2.5$, $E_T^{\text{miss}} > 20 \text{ GeV}/c^2$, and at least 4 jets with $p_T > 40 \text{ GeV}/c$ and $j-j > 2.5$, of which two of them are required to be tagged as b-jets. Jets used for these analysis are reconstructed with a $R = 0.4^3$ cone algorithm. After these cuts, S/B becomes much more favorable : $S/B \sim 30$.

Top mass measurement using the hadronic top decay ([31], [32], [33], [34]) The top mass is estimated here from the reconstruction of the invariant mass of a three-jet system : the two light jets from the W and one of the two b-jets. The determination of this combination of three jets proceeds in two steps : the choice of the two light jets, and the choice of the b-jet associated to the reconstructed hadronic W.

³ $R = \sqrt{r^2 + z^2}$

Process	Cross section (pb)	Number of events @ 10 fb ⁻¹ (millions)
Signal	250	2.5 millions
bb ! l + jets	2.2 10 ⁶	22 10 ³
W + jets ! l + jets	7.8 10 ³	78
Z + jets ! l + jets	1.2 10 ³	12
W W ! l + jets	17.1	0.17
W Z ! l + jets	3.4	0.034
Z Z ! l + jets	9.2	0.092

Table 2.6.4: Main backgrounds to the lepton (l = e, μ) + jets $t\bar{t}$ signal.

Events kept after the selection described above have at least two light jets above a given threshold on their transverse momentum. In a first step, we select the hadronic W candidates in a mass window of $5 m_{jj}$ around the peak value of the distribution of the invariant mass of the light jet pairs, made with events with only two light jets (m_{jj} is the width of this distribution).

In order to reduce the incidence of a light-jet energy mis-measurement (due to the energy lost out of cone) on the precision of the top mass measurement, an in-situ calibration of these jets is performed, through a χ^2 minimization procedure ([29], [32]). This minimization is applied event by event, for each light-jet pair combination. The expression of χ^2 , given by equation (2.6.13), is the sum of three terms : the first (and leading) one corresponds to the constrain of the jet pair invariant mass m_{jj} to the PDG W mass (m_W) ; the others correspond to the jet energy correction factors, c_i ($i = 1;2$), to be determined by this minimization (σ_i ($i = 1;2$) is the resolution on the light jet energy).

$$\chi^2 = \frac{(m_{jj}(c_1; c_2) - m_W)^2}{\sigma_W^2} + \frac{(E_{j1}(1 - c_1))^2}{\sigma_1^2} + \frac{(E_{j2}(1 - c_2))^2}{\sigma_2^2} \quad (2.6.13)$$

The χ^2 is minimized, event by event, for each light jet pair ; the light jet pair $j_1; j_2$ corresponding to the minimal χ^2 is kept as the hadronic W candidate. This minimization procedure also leads to the corresponding energy correction factors $c_1; c_2$. The hadronic W is then reconstructed with the light jets chosen by this χ^2 minimization.

Several methods have been investigated to choose the b-jet among the two candidates, and the one giving the highest purity has been kept : the b-jet associated to the hadronic W is the one leading to the highest p_T for the top.

The reconstructed three jets invariant mass is shown in Fig. 2.6.9: the mass peak (176.1 ± 0.6 GeV/ c^2) is in reasonable agreement with the generated value (175 GeV/ c^2); the width is equal to 11.9 ± 0.7 GeV/ c^2 . The overall efficiencies and purities, with respect to lepton + jets events, are summarized in Table 2.6.5: we expect with this method 64,000 events at 10 fb⁻¹, corresponding to a statistical error equal to 0.05 GeV/ c^2 .

The dominant remaining background to lepton + jets $t\bar{t}$ events comes from W + jets events. The contribution to the top mass measurement is negligible : the values of the mass peak (176.1 ± 0.6 GeV/ c^2 for signal only, 176.2 ± 0.6 GeV/ c^2 for signal plus background) and of the width (11.9 ± 0.7 GeV/ c^2 for signal, 12.1 ± 0.7 GeV/ c^2 for signal plus background) are identical.

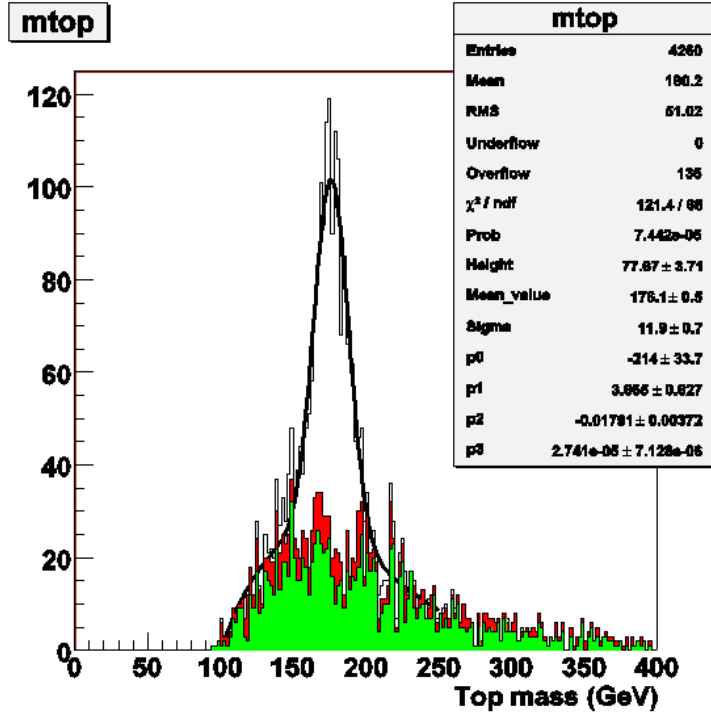


Fig. 2.6.9: Top mass distribution, with the contribution from wrong W combinations, in green, and, in red, from wrong b-jet associations. This analysis has been performed using the MC@NLO generator and the full simulation of the ATLAS detector.

	Efficiency (%)		b purity (%)		W purity (%)		Top purity (%)	
full mass window	2.70	0.005	56.0	0.9	63.2	0.9	40.5	0.9
mass window within $3 m_{top}$	1.82	0.04	69.1	0.8	75.8	0.8	58.6	0.8

Table 2.6.5: Total efficiency and W, b and top purity of the final selected events (MC@NLO, full simulation of the ATLAS detector), with respect to lepton (electron, muon) + jets events

Top mass measurement using a kinematic fit [32] An alternative method for the top mass measurement in the lepton plus jets channel consists in reconstructing the entire $t\bar{t}$ final state, in order to reduce the systematic error due to FSR. The hadronic part is reconstructed in a similar way to the previous section. The leptonic side can not be directly reconstructed due to the presence of the undetected neutrino, but can be estimated in three steps :

$$p_z(\nu) = E_T^{miss}$$

$p_z(\nu)$ is obtained by constraining the invariant mass of the lepton-neutrino system to the PDG mass value : this kinematic equation leads to two $p_z(\nu)$ solutions

the remaining b-jet is associated to the reconstructed W

The top mass determination is performed through a kinematic fit, relying on a χ^2 based on mass constraints ($m_{jj} = m_W^{PDG} = m_{l\nu}$; $m_{jjb} = m_{lb}$) and kinematic constraints (energy and direction of leptons and jets can vary within their resolutions). The minimization of this χ^2 is performed event by

event, for the two p_z () solutions : the one giving the lower ΔR^2 is kept. The top mass is determined as the linear extrapolation of $m_{\text{top}}(\Delta R^2)$ for $\Delta R^2 = 0$.

With an efficiency equal to 1.1 % , we expect with this method 26 000 events at 10 fb^{-1} , corresponding to a statistical error equal to $0.1 \text{ GeV}/c^2$. This analysis has been performed using a fast simulation of the ATLAS detector, and will be checked with a full simulation.

Top mass measurement using large p_T top events ([32] [35]) Thanks to the large amount of $t\bar{t}$ events produced at LHC, a subsample of lepton + jets $t\bar{t}$ events, where the top quarks have a p_T greater than $200 \text{ GeV}/c$, can be studied. The interest of such events is that the top and the anti-top are produced back-to-back in the laboratory frame, so that their daughters will appear in distinct hemispheres of the detector : therefore, the combinatorial background should be strongly reduced.

Because of the high p_T (top), the three jets in one hemisphere tend to overlap. To overcome this problem, the top quark is reconstructed in a large calorimeter cone (R in $[0.8 - 1.8]$), around the top quark direction.

A strong dependence of the reconstructed top mass with the cone size has been observed and can be attributed to the Underlying Events (UE) contribution, evaluated to 45 MeV in a 0.1×0.1 calorimeter tower with the full simulation of the ATLAS detector. After UE subtraction, the top mass is independent of the cone size, but lower than the generated top mass by 25% , as can be seen in Fig. 2.6.10. A mass scale recalibration, based on the hadronic W, is then applied and leads to an average top mass value consistent with the generated value (see Fig. 2.6.10).

With an efficiency equal to 2% with respect to this subsample, we expect with this method 3600 events at 10 fb^{-1} , corresponding to a statistical error equal to $0.2 \text{ GeV}/c^2$.

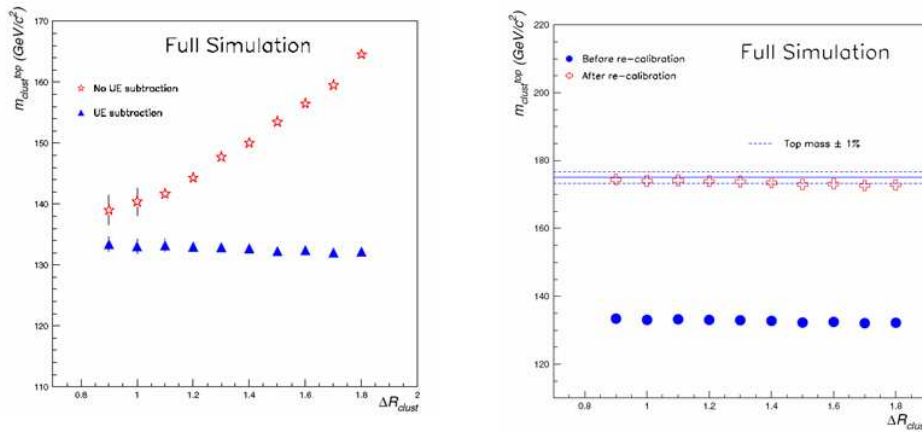


Fig. 2.6.10: Fitted top mass reconstructed in a large calorimeter cluster as a function of the cluster size, for a subsample of events with $p_T(\text{top}) > 200 \text{ GeV}/c$, before and after UE subtraction, on the left. The plot on the right shows the effect of the mass scale recalibration. This analysis has been performed using the PYTHIA generator for signal, and the full simulation of the ATLAS detector.

Systematic uncertainties on the top mass measurement in the lepton + jets channel The systematic uncertainties on the top mass measurement are summarized in Table 2.6.6, for the three methods explained above. It is possible to get rid of the error due to the light jet energy scale thanks to the in-situ calibration ; the dominant contribution comes from the FSR and the b-jet energy scale.

Source of uncertainty	Hadronic top m_{top} (GeV/c ²)	Kinematic fit m_{top} (GeV/c ²)	High p_T top sample m_{top} (GeV/c ²)
Light jet energy scale (1 %)	0.2	0.2	
b-jet energy scale (1 %)	0.7	0.7	
b-quark fragmentation	0.1	0.1	0.3
ISR	0.1	0.1	0.1
FSR	1.	0.5	0.1
Combinatorial background	0.1	0.1	
Mass rescaling			0.9
UE estimate (10 %)			1.3
Total	1.3	0.9	1.6
Statistical error	0.05	0.1	0.2

Table 2.6.6: Systematic errors on the top mass measurements, in the lepton + jets channel, for the three methods described above.

Top mass measurement in leptonic final states with J/ψ ([36], [37])

A last top mass determination can be carried out in the lepton+jets channel where a J/ψ arises from the b-quark associated to the leptonic decaying W (Fig. 2.6.11). The large mass of the J/ψ induces a strong correlation with the top mass, as will be shown below. Although the overall branching ratio ($5.5 \cdot 10^{-4}$) is low, this analysis starts to be competitive with more traditional mass measurements already with the first 20 fb^{-1} . This measure is expected to have an excellent resolution because of the very clean experimental reconstruction of the lepton three-vectors. In the analysis presented in [37], in order to increase the available statistics, no attempt is made to correctly pair the J/ψ to the lepton, when two isolated leptons are present: the top mass is extracted from the full distribution containing the combinatorial background.

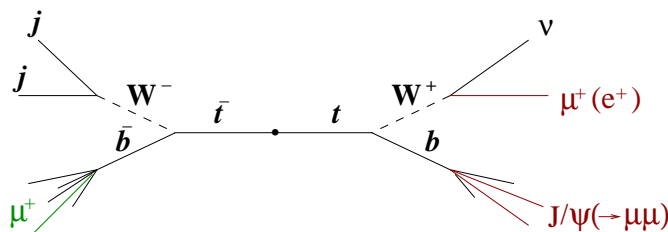


Fig. 2.6.11: Diagram of the $t\bar{t}$ decay to semi-leptonic final state with J/ψ .

Events are triggered using the inclusive lepton trigger. In events passing the trigger thresholds a J/ψ is searched for by looking for same-flavour, opposite-sign leptons with invariant mass in the range $[2.8, 3.2] \text{ GeV}/c^2$ and forming an angle greater than 2° and lower than 35° . If a J/ψ is found in an event, the isolated lepton with the highest p_T and higher than $20 \text{ GeV}/c$ is considered as the lepton

candidate from the \bar{W} decay. To reduce the background from non-top processes, the total scalar sum of the transverse jet momenta is required to be greater than 100 GeV/c. This cut is not applied if two isolated leptons are found, in order to preserve dileptonic $t\bar{t}$ events. If the flavour of the two leptons is the same, an explicit Z veto is applied (removing events where the pair has invariant mass within 6 GeV/c² of the Z mass). To further reduce soft background and make the analysis less sensitive to systematic effects involving soft QCD, the cut on the transverse momentum of the isolated lepton is brought to 40 GeV/c.

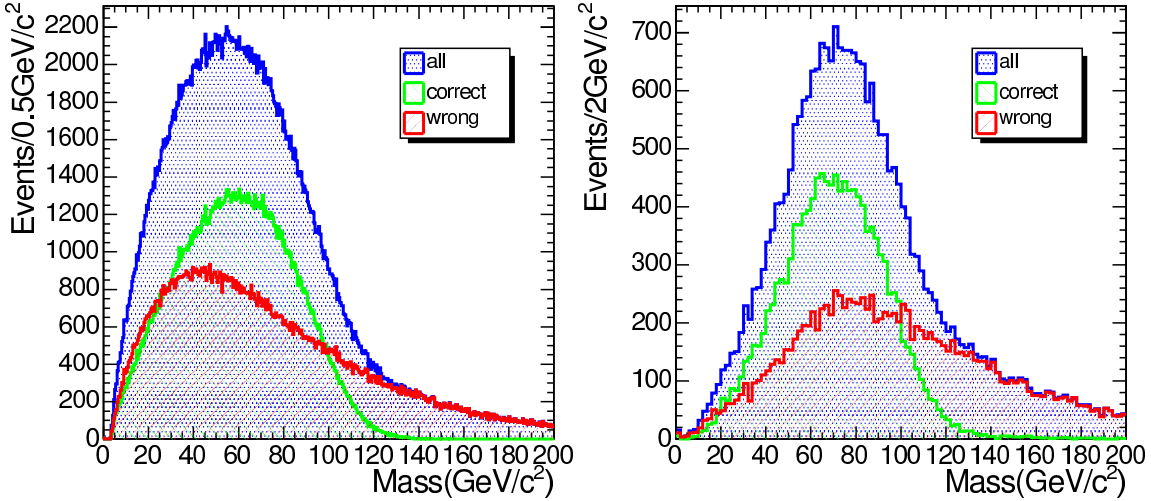


Fig. 2.6.12: Lepton- J/ψ invariant mass for $m_t = 175 \text{ GeV}/c^2$ with 1 fb^{-1} integrated luminosity, at generator level (left) and after full detector simulation and reconstruction (right).

The observable most sensitive to the top mass is the position of the maximum of the three-lepton mass distribution, shown in Fig. 2.6.12. Its correlation to the top mass and the statistical error are shown in Fig. 2.6.13.

A statistical error of around 1.2 GeV/c² is expected after the first 20 fb⁻¹, and the systematic error, dominated by theory, is lower than 1.5 GeV/c² (only 0.5 GeV/c² of which come from instrumental uncertainties). This analysis reduces to a minimum those systematics which are expected to dominate in more traditional estimations of the top mass, especially the ones from direct reconstruction, like the jet energy scale and the b-tagging efficiency. Therefore a reduction of the uncertainty on m_t is expected when combining this to the direct measurements.

Top mass measurement in the dilepton channel [32], [38]

The dilepton channel is very clean, with a lower contribution of combinatorial background, but it can only provide an indirect top mass measurement, because of the presence of two undetected neutrinos in the final state. Events are selected requiring two leptons of opposite charge, with $p_T \geq 20 \text{ GeV}/c$ and $j_j \geq 2.5$, an $E_T^{\text{miss}} \geq 40 \text{ GeV}$ and 2 b-jets with $p_T \geq 25 \text{ GeV}/c$ and $j_j \geq 2.5$. After this selection, the ratio of signal over background is around 10.

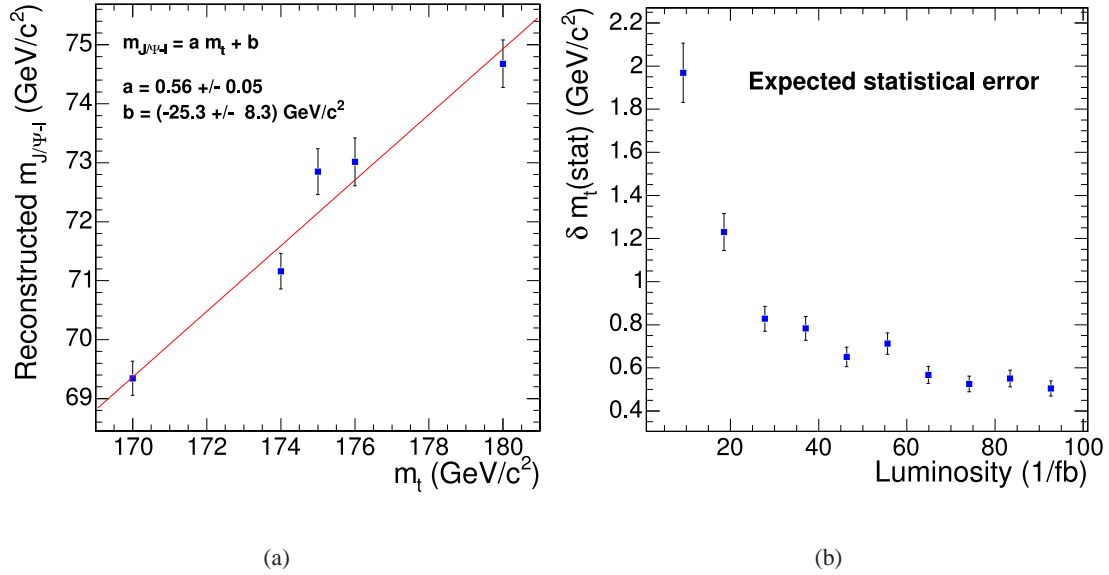


Fig. 2.6.13: Correlation between the reconstructed J/ψ mass and the generated top quark mass (left), and expected statistical error as a function of integrated luminosity (right). This study has been performed with a fast simulation of the CMS detector [33].

The final state reconstruction relies on a set of six equations for the six unknown components of momenta of neutrino and antineutrino, based on kinematic conservation laws and assuming a given top mass value. This set of equations can provide more than one solution; then, weights are computed from kinematic Monte Carlo distributions of three variables ($\cos \theta_{\text{top}}$, E_{ν} and $E_{\bar{\nu}}$), and the solution corresponding to the highest weight is kept. This weight is computed for several input top masses, and the top mass estimator corresponds to the maximum mean weight.

With an efficiency of 6.5 %, 20 000 events are expected at 10 fb^{-1} . The statistical error on the top mass measurement is negligible ($0.04 \text{ GeV}/c^2$). The systematic error, equal to $1.7 \text{ GeV}/c^2$, is dominated by the uncertainty on the parton distribution function ($1.2 \text{ GeV}/c^2$).

Top mass measurement in the all hadronic channel ([32], [38])

The main advantage of this channel is a full kinematic reconstruction of both sides, and its main disadvantage is the huge QCD multijet background : before any selection, the ratio of signal over background is very low (10^{-8}). Events are selected requiring at least six jets with $p_{\text{T}} \geq 40 \text{ GeV}/c$, and $j_j \geq 3$, and at least two b-jets with $p_{\text{T}} \geq 40 \text{ GeV}/c$, and $j_j \geq 2.5$. The final state reconstruction proceeds in two steps : first, the choice of the two light jets pairs to form the two W bosons is performed through the minimization of a χ^2 based on the W mass constraint. Both W candidates are then associated to the right b-jet minimizing a χ^2 based on the equality of the top masses on both sides. In order to improve the signal over background ratio, the analysis can be restricted to a sample of high p_{T} ($> 200 \text{ GeV}/c$) top and anti-top : this ratio is finally favorable ($S/B \sim 18$).

The top mass distribution is displayed in Fig. 2.6.14. The overall efficiency, within the 130-200 GeV/c^2

top mass window, is equal to 0.08%, corresponding to 3300 events at 10 fb^{-1} , and a statistical error equal to $0.18 \text{ GeV}/c^2$. The systematic error, of the order of $3 \text{ GeV}/c^2$, is dominated by the contribution of FSR ($2.8 \text{ GeV}/c^2$).

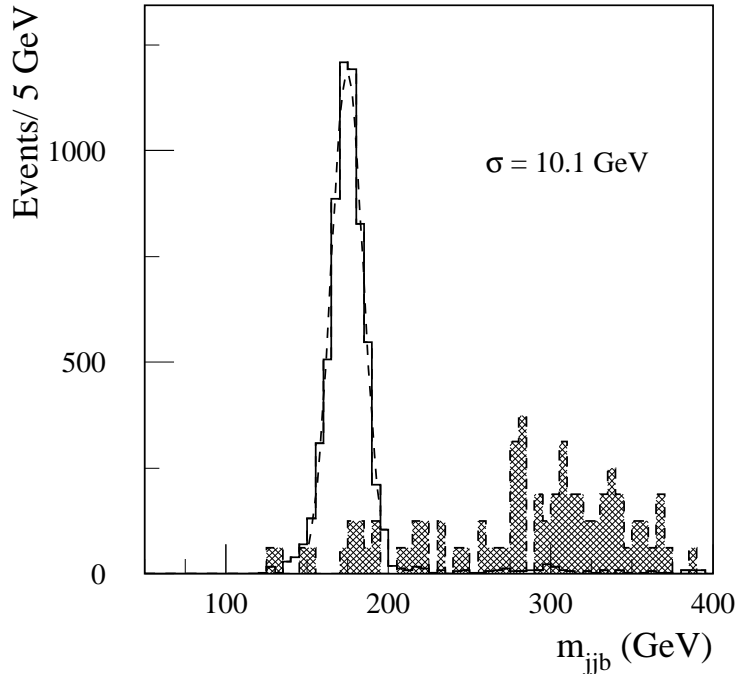


Fig. 2.6.14: Top mass distribution in the all hadronic channel, for the high p_T top sample. The shaded area corresponds to the remaining QCD background. This study has been performed with a fast simulation of the ATLAS detector [32].

2.7 Conclusions

Contributed by: F. Canelli, A.I. Etienne, and D. Glenzinski

Impressive improvements have been achieved in the latest top-quark mass measurements at the Tevatron. All the decay channels have explored new techniques to address their major uncertainties and as a consequence all measurements in all channels are currently systematic dominated. There are still some improvements which are believed will be important. In the all-jets channel it is possible to make an in-situ measurement of the JES. This could result in a measurement with the same precision as the those in the lepton+jets channel. Once these channels have an in-situ JES measurement the remaining uncertainty on the jet energy scale in all the channels will predominantly arising from the uncertainty on b-jets. We expect to reduce the uncertainty on this jet energy scale using $Z \rightarrow b\bar{b}$ events. Currently there has been some progress on extracting an uncertainty from this sample but the understanding of the overwhelming background has been difficult. We expect to have this done in the next year. This will be more important for the dilepton channel, where an in-situ determination of the JES is not possible. In the future we plan to combine different methods of analysis in the same channel. We have done this previously in the dilepton channel and obtained a significant improvement in the sensitivity since each method uses different information from the same dataset. We would like to do this in all the channels.

The remaining systematic uncertainties should be revisited by both experiments. These will soon be the uncertainties dominating the top- quark mass measurements. Currently the list of these uncertainties used by D0 and CDF is different and we don't have a common way of applying them. In the near future we should agree upon the best way to classify and calculate these uncertainties. Finally, there needs to be a quantitative study of the effects of Color Reconnection and other final state interactions. Monte Carlo generators which include these effects for $p p \rightarrow t \bar{t}$ interactions are only recently becoming available. All these improvements will get us to a precision of less than 1.5 GeV.

At the LHC, various top mass measurement methods have been investigated, in all decay channels of the top quark. The very large sample of $t \bar{t}$ events that will be accumulated will allow a precision measurement after only one year of data taking at low luminosity (10 fb^{-1}): the statistical error on the top mass is negligible in all these methods except the method involving leptonic final states with $J=0$. These analyses are differently sensitive to the various sources of systematic uncertainties: therefore, this will allow reliable cross-checks between the various methods. The top quark mass should be measured at LHC with a precision of the order of $1 \text{ GeV}/c^2$, in the lepton plus jets channel.

In all cases we need to be aware of physics limitations from Monte Carlo or analysis approaches which would prevent us from reaching the levels of expected precision as soon as possible so that we can mitigate their effects.

3 Single Top Quark Physics

3.1 Introduction

Contributed by: C. Ciobanu and R. Schwienhorst

The existence of the top quark was established in top quark pair events produced via the strong interaction [39, 40], where quark-antiquark annihilation or gluon-gluon fusion leads to top-antitop pairs. The Standard Model (SM) also allows for the top quark to be produced singly rather than in pairs via the electroweak charged current interaction, a mode typically referred to as single-top quark production. At the time of this report, the single-top production mode is yet to be observed experimentally. Current searches at the Tevatron CDF and DØ experiments are nearing in on this production mode as datasets in excess of 1 fb^{-1} are being accumulated. At the LHC, it is expected that the three different production modes of single-top quark production can be observed individually.

Studying single-top quark production at hadron colliders is important for a number of reasons. First, a measurement of the production cross section provides the only direct measurement of the total top quark decay width and the CKM matrix element $|V_{tb}|^2$, without having to assume three quark generations or CKM matrix unitarity. Second, measuring the spin polarization of single-top quarks and can be used to test the V-A structure of the top quark electroweak charged current interaction. Third, the presence of various new SM and non-SM phenomena may be inferred by observing deviations from the predicted rate of the single-top signal and by comparing different production modes. Fourth, the single-top quark final state presents an irreducible background to several searches for SM or non-SM signals, for example Higgs boson searches in the associated production channel.

This report is intended as a guide to the current issues in single-top quark physics at hadron colliders. Section 3.2 presents a theoretical perspective on single-top quark production. Studies of single-top quark production at next-to-leading-order (NLO) are presented, followed by discussions of Monte Carlo modeling and its agreement with NLO results as well as strategies for choosing event variables to optimize the signal-background separation. Section 3.3 presents the experimental challenges faced by single-top quark searches at the Tevatron. Recent studies from the CDF and DØ Collaborations are described, along with sensitivity projections for the remainder of Run II at the Tevatron. Section 3.4 presents the experimental perspective from the LHC point of view. The connection between LHC and Tevatron single top searches are discussed in Section 3.5.

3.2 Theory

Overview

Contributed by: T. Tait and S. Willenbrock

At the Tevatron and the LHC, top quarks are mostly produced in pairs, via the strong processes $q\bar{q} \rightarrow t\bar{t}$ (dominant at the Tevatron) and $gg \rightarrow t\bar{t}$ (dominant at the LHC). However, there are also a significant number of top quarks that are produced singly, via the weak interaction. There are three separate single-top-quark production processes, which may be characterized by the virtuality of the W boson (of four-momentum q) in the process:

t -channel: The dominant process involves a spacelike W boson ($q^2 < 0$), as shown in Fig. 3.2.15(a) [41, 42, 43]. The virtual W boson strikes a b quark in the proton sea, promoting it to a top quark. This process is also referred to as W -gluon fusion, because the b quark arises

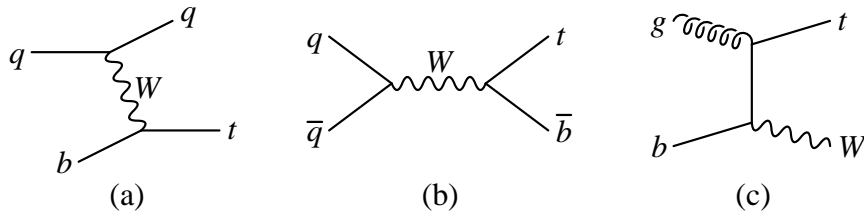


Fig. 3.2.15: Feynman diagrams for single-top-quark production in hadron collisions: (a) t -channel process; (b) s -channel process; (c) associated production (only one of the two diagrams for this process is shown).

from a gluon splitting to $b\bar{b}$

s -channel: If one rotates the t -channel diagram such that the virtual W boson becomes timelike, as shown in Fig. 3.2.15(b), one has another process that produces a single top quark [44, 45]. The virtuality of the W boson is $q^2 = (m_t + m_b)^2$.

Associated production: A single top quark may also be produced via the weak interaction in association with a real W boson ($q^2 = M_W^2$), as shown in Fig. 3.2.15(c) [46, 47]. One of the initial partons is a b quark in the proton sea, as in the t -channel process.

The total cross sections for these three single-top-quark production processes, calculated at next-to-leading-order in QCD, are listed in Table 3.2.7, along with the cross section for the strong production of top-quark pairs. Of the single-top processes, the t -channel process has the largest cross section; it is nearly one third as large as the cross section for top-quark pairs at both the Tevatron and the LHC. The cross section for the s -channel process is less than half that of the t -channel process at the Tevatron, and is more than an order of magnitude less than the t -channel process at the LHC. The W t process is negligible at the Tevatron, but is significant at the LHC, with a cross section intermediate between the t -channel and s -channel cross sections.

The cross sections for single-top production are all known at next-to-leading-order in QCD, and have been calculated with increasing sophistication over the years, such that they are now all available as differential cross sections. The s -channel process has very little theoretical uncertainty [48, 49, 50, 51, 52, 53, 54], and the total cross section is even known to next-to-next-to-leading order (in the large N limit) [55]. The theoretical uncertainty is larger for the dominant t -channel process [56, 57, 49, 50, 52, 53, 58, 54]. The W t process is also known at next-to-leading order [47, 59, 53, 60], and requires some care to separate out the large contribution from $t\bar{t} \rightarrow t\bar{t} + W$ [61, 47, 60]. Phenomenological studies of single-top production have also been carried out with increasing sophistication [62, 63, 52, 64, 65, 66].

Within the standard model, there are several reasons for studying the production of single top quarks at the Tevatron and the LHC. First, the cross sections for single-top-quark processes are proportional to $|V_{tb}|^2$. These processes provide the only known way to directly measure V_{tb} . In contrast, the observed fact that $\text{BR}(t \rightarrow W b) \approx 1$ [68] only tells us that $V_{tb} \approx \sqrt{V_{ts}^2 + V_{td}^2}$. If there are just three generations of quarks, as favored by precision electroweak data, then we already know $V_{tb} = 0.9990 \pm 0.0002$ at 90% CL [69]. In this case single-top production may be regarded as a test of the standard model, including the generation of the b -quark sea from gluon splitting.

Another reason for studying single-top production is that it these processes are backgrounds to

(pb)	Tevatron	LHC
t -channel	1.98	246
s -channel	0.88	10.6
$W t$	0.14	68
$t\bar{t}$	6.7	860

Table 3.2.7: Total cross sections (pb) for single-top-quark production and top-quark pair production at the LHC, for $m_t = 175$ GeV. The next-to-leading-order t -channel and s -channel cross sections are from Ref. [52]. The next-to-leading-order cross section for the $W t$ process is from Ref. [60] (adjusted for $m_t = 175$ GeV). The next-to-leading-order cross section for $t\bar{t}$ production is from Ref. [67] (Tevatron) and Ref. [30] (LHC).

other signals. For example, single-top-quark events are backgrounds to some signals for the Higgs boson [60, 70, 71, 72]. Thus it is important to have a good understanding of single top both theoretically and experimentally. Single top will also serve a testing ground for important theoretical tools needed to correctly model Higgs physics. For example, if no signal of physics beyond the Standard Model is manifest in single top production, the t -channel production mode will serve to constrain the bottom quark parton distribution function, important for Higgs production from initial states including heavy quarks. Just as in the weak boson fusion mode of Higgs production, the t -channel mode also contains a t -channel W exchange and the associated forward tagging jets, and thus single top represents an experimental insight into a key characteristic of the Higgs signal.

A third reason is that single top quarks are produced with nearly 100% polarization, due to the weak interaction [46, 73, 74, 75]. This polarization serves as a test of the $V-A$ structure of the top-quark charged-current weak interaction.

Single top is also interesting beyond the standard model. New physics can influence single-top-quark production by inducing non-standard weak interactions [73, 76, 77, 78, 79, 80, 81, 82], via loop effects [83, 84, 85, 86, 87, 88], or by providing new sources of single-top-quark events [78, 81, 84, 89, 90, 91, 92, 93]. The three modes of single top production each respond quite differently to different realizations of physics beyond the Standard Model [81]. The s -channel mode is very sensitive to an exotic charged boson which couples to top and bottom. Because the exchanged particle is time-like, there is the possibility (if it is heavier than the top) that it can be produced on-shell, resulting in a large enhancement of the cross section. On the other hand, while a FCNC interaction (such as $Z-t-c$) would allow new s -channel processes such as $q\bar{q} \rightarrow Z \rightarrow t\bar{c}$, these are difficult to extract from backgrounds, because there is no longer a final state b quark that can be tagged. So the experimentally measured s -channel cross section would not include the FCNC events. Specific theories which predict an enhancement of the s -channel rate are theories with a W^0 [94, 95, 96, 97, 98, 99] or charged Higgs, both of which can result in s -channel rates different from the SM by factors of few at either Tevatron or LHC [81, 100, 101].

The t -channel mode is insensitive to heavy charged bosons. The reason for this is that the t -channel exchange results in a space-like momentum, which never can go on-shell, and thus the amplitude for the heavy particle is always suppressed by the mass of the heavy boson, $\propto 1/M_B^2$. However, the FCNC processes can have a drastic effect on the t -channel mode. Because they involve new interactions between the top quark, a boson ($\gamma, Z, g, \text{ or } H$), and one of the light quarks, (c or u), the t -channel mode can

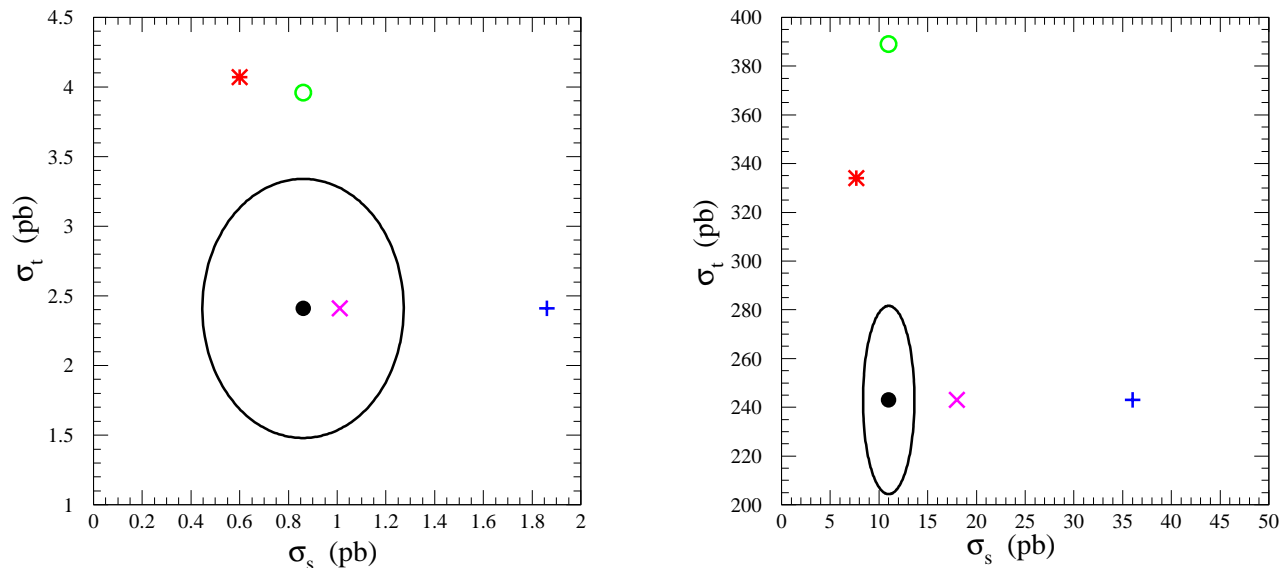


Fig. 3.2.16: Single top cross sections in the s - and \bar{t} -channels in the SM (including theoretical and expected statistical uncertainties) and a few models of physics beyond the SM, at the Tevatron run II and LHC (from Ref. [81]).

be enhanced. For example, in the case of a Z - $\bar{t}c$ interaction there is the process $qc \rightarrow \bar{q}t$ with a Z exchanged. The fact that high energy proton collisions contain more c quarks than b quarks further enhances the new physics contribution compared to the SM piece.

The $\bar{t}W$ mode is more or less insensitive to new bosons, because the W is manifest in the final state. From this line of thinking, we see that all three modes are really complimentary views of the top quark, and thus measured separately they provide more information than would be obtained by lumping them together into a singular single top process. This point is emphasized (at Tevatron run II and LHC) for a few different models in Fig. 3.2.16, where we also show the SM predictions, and some estimates for the theoretical and statistical uncertainties in the s - and \bar{t} -channels.

Next-to-Leading Order Corrections to Single Top Quark Production and Decay

Contributed by: Q.-H. Cao, R. Schwienhorst, J.A. Benitez, R. Brock, C.-P. Yuan

In a few recent papers [50, 51, 58], we first developed methods for calculating the next-to-leading (NLO) order QCD corrections to the production and decay of the top quark in the s - and \bar{t} -channel single-top events produced at hadron colliders, and then studied the implication of NLO corrections to the phenomenology of single-top physics at the Tevatron Run-II. In this section, we first briefly review the method of our calculations and then summarize the main results of our phenomenological studies.

Method of Calculations We adopted the phase space slicing method with one cut-off scale to organize the NLO calculations [102, 103, 104]. When the invariant mass of the two colored partons in the $2 \rightarrow 3$ tree level production processes is smaller than some theoretical cutoff scale $p_{\text{min}}^{\text{in}}$, collinear and/or soft singularities are taken care of using the dimensional regularization method, and they are canceled by similar singularities in the $2 \rightarrow 2$ virtual processes after redefining the normalized parton distribution functions (PDF). For the remaining phase space region of the $2 \rightarrow 3$ processes, we numerically evaluate the final state parton distributions. By this way, we calculate the differential distributions of final state partons in the production processes, including both $2 \rightarrow 2$ and $2 \rightarrow 3$ kinematics. A similar procedure was also adopted to handle the decay of top quark via $t \rightarrow b\bar{W}(\rightarrow l\bar{\nu}_l)(g)$ at the NLO in QCD. Again, the soft singularities cancel among the virtual and real gluon emission contributions and there is no remaining collinear singularity after integrating out the sliced regions of phase space that correspond to soft and/or collinear singularities in the tree level process $t \rightarrow b\bar{W}(g)$. In our calculation, we have ignored the bottom quark mass, for its contribution to the matrix element is negligible in single-top processes. In order to obtain the fully spin-correlated matrix elements, we take the complete set of Feynman diagrams for the production and decay of top quark in single-top processes with effective form factors obtained from summing up both virtual and real emission contributions (coming from the sliced phase space regions with the invariant mass of a set of two external partons less than $p_{\text{min}}^{\text{in}}$). We have also introduced a new method in our calculation which is called the modified narrow width approximation. In contrast to taking the usual narrow width approximation to approximate the internal top-quark propagator by a delta-function, so as to take the top quark width to be exactly equal to zero, we have generated a Breit-Wigner resonance distribution of top quark mass according to its predicted SM total decay width at NLO. We then use that generated mass to calculate the production and decay matrix elements in order to respect gauge invariance and to clearly separate the production and decay contributions beyond Born level. By doing so, we are able to generate differential distributions of final state particles where the reconstructed top quark invariant mass peaks around the true value of the top quark mass, and with a Breit-Wigner shape whose width is the top quark total decay width. Hence, it improves the prediction of NLO calculations in some kinematic distributions.

Phenomenology of s- and t-channel Single Top Quark Events at NLO Although all the results of our studies regarding the phenomenology of s- and t-channel single-top events predicted by our NLO calculations have been published in Refs. [50, 51, 58], it is useful to summarize a few key findings from our studies in this section.

In order to calculate the fully differential cross sections at NLO and compare to experimental data, we have to impose kinematic cuts on the final state partons. Moreover, if the number of signal events is large, then one would like to impose a tight kinematic cut to further suppress the backgrounds. However, in some cases, such as the single-top search at the Tevatron in Run II, the signal rate is not large. It is thus not desirable to impose a tight kinematic cut because that would not only suppress the background rate but also the signal rate and thus not improve the signal significance compared to imposing a loose kinematic cut. Furthermore, we must define a jet as an infrared-safe observable. In our studies, we adopt the cone-jet algorithm [105], as explained in Ref. [51, 58]. More specifically, we adopt the E-scheme cone-jet approach (4-momenta of particles in a cone are simply added to form a jet) with radius $R = \sqrt{\frac{p_T^2}{p_T^2 + \Delta^2}}$ in order to define b, q and possibly extra $g, q, \text{ or } b$ jets, where Δ and Δ are the

separation of particles in the pseudo-rapidity η and the azimuthal angle ϕ , respectively. For reference, we shall consider both $R = 0.5$ and $R = 1.0$. The same R -separation will also be applied to the separation between the lepton and each jet.

Below, we discuss a few aspects of the single-top phenomenology studies based on our calculations for the Tevatron in Run II, a 1.96 TeV $p\bar{p}$ collider. Here, we take $m_t = 178$ GeV and $M_W = 80.33$ GeV.

Kinematic Acceptance The kinematic cuts imposed on the final state objects are:

$$\begin{aligned}
 p_T^l &= 15 \text{ GeV} \quad ; \quad |\eta_j| \leq \eta_j^{\text{max}} ; \\
 E_T^l &= 15 \text{ GeV} \quad ; \\
 E_T^j &= 15 \text{ GeV} \quad ; \quad |\eta_{jj}| \leq \eta_j^{\text{max}} ; \\
 R_{lj} &= R_{\text{cut}} \quad ; \quad R_{jj} = R_{\text{cut}} ;
 \end{aligned} \tag{3.2.14}$$

where the jet cuts are applied to both the b - and light quark jets as well as any gluon or antiquark jet in the final state. η_j^{max} (and η_l^{max}) denotes the maximum value in magnitude of the charged lepton (and jet) rapidity. The minimum transverse energy of the lepton and jets is chosen to be 15 GeV. Each event is furthermore required to have at least one charged lepton and two jets passing all selection criteria. The cut on the separation in R between lepton and jets as well as between different jets is given by R_{cut} . In Table 3.2.8, we show the s - and t -channel single-top production cross sections (in femtobarns), including the top quark decay branching ratio $\text{Br}(t \rightarrow b\bar{W})$ ($\text{Br}(t \rightarrow e)$), as well as acceptances at leading order (LO) and NLO for several sets of cuts. We apply the E_T cuts listed in Eq. (3.2.14) and study three separate sets of values:

1. loose cuts with small R_{cut} : $\eta_l^{\text{max}} = 2.5$, $\eta_j^{\text{max}} = 3.0$, and $R_{\text{cut}} = 0.5$,
2. loose cuts with large R_{cut} : $\eta_l^{\text{max}} = 2.5$, $\eta_j^{\text{max}} = 3.0$, and $R_{\text{cut}} = 1.0$,
3. tight cuts with small R_{cut} : $\eta_l^{\text{max}} = 1.0$, $\eta_j^{\text{max}} = 2.0$, and $R_{\text{cut}} = 0.5$.

As clearly illustrated in Table 3.2.8, the acceptance for single-top signal events is sensitive to the applied kinematic selections. A larger value for R_{cut} reduces the acceptance significantly mainly because more events fail the lepton-jet separation cut. With tight cuts, LO and NLO acceptances are almost the same. By contrast, with loose cuts, LO and NLO acceptances are quite different. The important lesson here is that with a loose cut, to keep most of the signal events, the acceptance for NLO kinematics cannot be accurately modeled with a multiplicative K -factor (to scale the inclusive cross section from LO to NLO).

	s-channel				t-channel			
	[fb]		Accept. (%)		[fb]		Accept. (%)	
	LO	NLO	LO	NLO	LO	NLO	LO	NLO
(1)	22.7	32.3	73	64	65.6	64.0	66	61
(2)	19.0	21.7	61	46	56.8	48.1	57	46
(3)	14.7	21.4	47	45	31.1	34.0	31	32

Table 3.2.8: The s - and t -channel single-top production cross sections (in fb) and acceptance at the Tevatron in Run II under various scenarios. The decay branching ratio $\text{Br}(t \rightarrow b\bar{W})$ ($\text{Br}(t \rightarrow e)$) is included.

Top Quark Reconstruction In order to identify single-top signal events and to test the polarization of the top quark by studying spin correlations amongst the final state particles, we need to reconstruct the top quark in each single top event. To do so, we need to first identify the b -jet and reconstruct the W boson from the top decay. In Table 3.2.9, we show the efficiency of finding the correct b -jet (b) in two different algorithms: the best-jet algorithm and the leading b -tagged jet algorithm. The “best-jet” is defined to be the b -tagged jet which gives an invariant mass closest to the true top mass when it is combined with the reconstructed W boson after determining the longitudinal momentum p_z of the neutrino from the W decay. The leading b -tagged jet algorithm picks the leading b -tagged jet as the correct b -jet to reconstruct the top quark after combining with the reconstructed W boson. As shown in Refs. [51, 58], we find that the best-jet algorithm shows a higher efficiency (about 80%) in picking up the correct b -jet than the leading-jet algorithm (about 55%) for s -channel single-top events. On the other hand, for t -channel single-top events, the leading b -tagged jet algorithm picks up the correct b -jet with a higher efficiency, about 95% for inclusive 2-jet events and 90% for exclusive 3-jet events. The reason that the leading b -tagged jet algorithm works well in exclusive 3-jet t -channel single-top events is that there are distinct kinematic differences between b and b -jets. In Fig. 3.2.17, we show the inclusive b - and b -jet E_T distributions in t -channel single-top events. To reconstruct the top quark in signal events, we also need to reconstruct the W boson, which is done with the help of a mass constraint: $M_W^2 = (p_1 + p)^2$. Which of the two-fold solutions in p_z is chosen depends on the b -jet algorithm we use. In the case of the best-jet algorithm, we find that the one with the smaller magnitude gives the best efficiency in W boson reconstruction. In the case of leading b -tagged jet algorithm however, we use the top quark mass constraint $M_t^2 = (p_b + p_1 + p)^2$ to pick up the best p_z value. The efficiency for picking up the correct p_z value (p_z), at LO and NLO, respectively, is presented in Table 3.2.9.

	best-jet algorithm			leading b -tagged jet algorithm		
	s -channel	t -channel		s -channel	t -channel	
	incl. 2-jet	incl. 2-jet	excl. 3-jet	incl. 2-jet	incl. 2-jet	excl. 3-jet
b	80%	80%	72%	55%	95%	90%
	70%			84%		

Table 3.2.9: Efficiencies of identifying correct b -jet (b) and picking up correct p_z (p_z) in both the best-jet algorithm and the leading-jet algorithm.

Top Quark Polarization Although the top quark is produced via the left-handed charged current, there is no reason to believe that the helicity basis will give the best description of the top quark spin. Choosing an appropriate basis could maximize spin correlation effects. Two definitions for the polarization have been studied in the literature for s -channel processes, differing by the reference frame used to define the polarization: one calculation uses the helicity basis, another the so-called “optimal” basis [106, 107]. Both work in the top quark rest frame, but they have different reference axis for the top quark spin, cf. Fig. 3.2.18. In the more common helicity basis the top quark spin is measured along the top quark direction of motion in the center-of-mass (c.m.) frame which is chosen as the frame of the (reconstructed top quark, non-best-jet) system after event reconstruction. In the optimal basis (beamline basis) we can maximize the spin correlations by taking advantage of the fact that the top quark produced through the

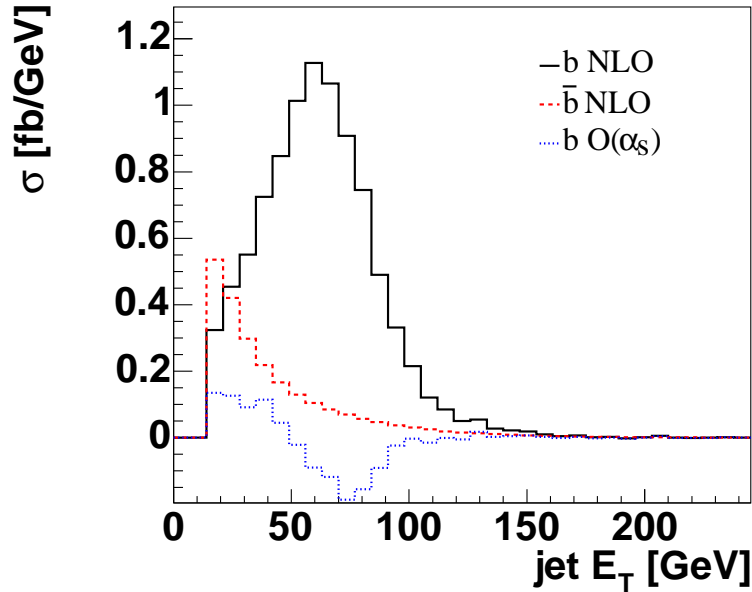


Fig. 3.2.17: Transverse momentum of the b - and b -jets in the t -channel single-top process. The dotted curve shows the $\mathcal{O}(\alpha_s)$ correction to the b -jet E_T distribution.

s -channel single top quark processes is almost 100% polarized along the direction of the d -type quark.

When studying the top polarization in helicity basis, the c.m. frame needs to be reconstructed in order to define the top quark momentum. Due to additional jet radiation, the determination of the c.m. frame at NLO is more complicated than at the Born-level. The additional radiation will also blur the spin correlation, and the degree of reduction depends on the chosen reference frame. Therefore, choosing the appropriate frame will reduce this effect. In this study, two options for reconstructing the c.m. frame are investigated:

1. $t\bar{b}(j)$ -frame: the c.m. frame of the incoming partons. This is the rest frame of all the final state objects (reconstructed top quark and all other jets). In exclusive two-jet events, this frame is the same as that at the Born-level, i.e. reconstructed from summing over momentum of the top quark and non-best-jet. In exclusive three-jet events, this frame is reconstructed by summing over the 4-momenta of top quark, non-best-jet, and the third-jet from the parton level calculation.
2. $t\bar{b}$ -frame: the c.m. frame of the top quark and non-best-jet. In this case, even in the exclusive three-jet events, the reference frame is constructed by summing over only the 4-momenta of the top quark and non-best-jet. Note that this differs from the $t\bar{b}(j)$ -frame only in exclusive three-jet events.

To better quantify the top quark polarization, it is useful to define the degree of polarization D of the top quark. This is given as the ratio

$$D = \frac{N_- - N_+}{N_- + N_+}; \quad (3.2.15)$$

where N_- (N_+) is , the number of left-hand (right-hand) polarized top quarks in the helicity basis.

Similarly, in the optimal basis, $N_- (N_+)$ is the number of top quarks with polarization against (along) the direction of the anti-proton three momentum in the top quark rest frame. Based on the degree of polarization D , we can easily get the spin fractions F_- as:

$$\begin{aligned} F_- &= \frac{N_-}{N_- + N_+} = \frac{1 - D}{2}; \\ F_+ &= \frac{N_+}{N_- + N_+} = \frac{1 + D}{2}; \end{aligned} \quad (3.2.16)$$

Note that $F_- (F_+)$ is the fraction of left-handed (right-handed) polarized top quarks in the helicity basis. Similar, in the optimal basis, $F_- (F_+)$ is the fraction of top quarks with polarization against (along) the direction of the anti-proton three momentum in the top quark rest frame. In Table 3.2.10, we show the prediction on the top quark polarization in s -channel single-top events at the LO and NLO for various choices of polarization basis and c.m. frame of the hard-scattering parton system where the polarization of the top quark is defined. One important observation is that the measured value of the degree of polarization of the top quark strongly depend on the algorithm for reconstructing the top quark in s -channel single-top events. For example, at the parton level with known identity of every final state particle, and before imposing any kinematic selection, the optimal basis gives the largest degree of polarization, but after event reconstruction it gives almost the same prediction as the helicity basis.

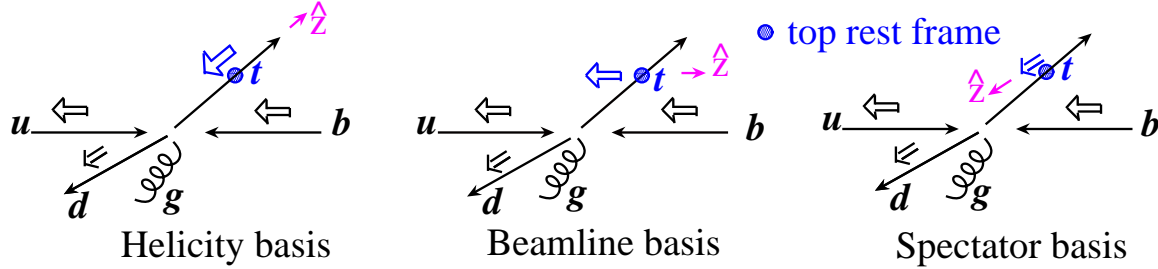


Fig. 3.2.18: Illustration of the three choices for the top quark spin basis. The circle denotes the top quark rest frame and the blue arrows denote the top quark spin direction.

In t -channel single-top events, the most studied polarization bases are the helicity basis, the beamline basis, and the so-called “spectator” basis [74]. In the more commonly used helicity basis, the top quark spin is measured along the top quark direction of motion in the c.m. frame which is chosen as the frame of the (reconstructed top quark, spectator jet) system after event reconstruction. In the beamline basis, the top quark spin is measured along the incoming proton direction. In the spectator basis we can maximize spin correlations by taking advantage of the fact that the top quark produced through the t -channel single top processes is almost 100% polarized along the direction of the spectator quark. In the discussion below, we will examine the polarization of single top quark events in these three bases.

As same as the s -channel study, two options for reconstructing the c.m. frame in the helicity basis are investigated:

1. $\text{tq}(j)$ -frame: the c.m. frame of the incoming partons. This is the rest frame of all the final state objects (reconstructed top quark and all others jets). In exclusive two-jet events, this frame is the

		D		F	
		LO	NLO	LO	NLO
Helicity basis:	Parton($\bar{t}b(j)$ -frame)	0.63	0.54	0.82	0.77
	Parton($\bar{t}b$ -frame)	0.63	0.58	0.82	0.79
	Recon. ($\bar{t}b(j)$ -frame)	0.46	0.37	0.73	0.68
	Recon. ($\bar{t}b$ -frame)	0.46	0.37	0.73	0.68
Optimal basis:	Parton	-0.96	-0.92	0.98	0.96
	Recon.	-0.48	-0.42	0.74	0.71

Table 3.2.10: Degree of polarization D and polarization fraction F , for inclusive two-jet s -channel single top quark events, at the parton level (Parton) and after event reconstruction (Recon.). Here, F corresponds to F^- in the helicity basis for left-handed top quarks and to F_+ in the optimal basis for top quarks with polarization along the direction of anti-proton three momentum, respectively. The $\bar{t}b(j)$ frame in the helicity basis denotes the c.m. frame of the incoming partons while $\bar{t}b$ frame denotes the rest frame of the reconstructed top quark and b quark.

same as the c.m. frame at the Born-level, i.e. reconstructed from summing over momentum of the top quark and spectator jet. In exclusive three-jet events, this frame is reconstructed by summing over the 4-momenta of top quark, spectator jet, and the third-jet from our parton level calculation.

2. $\bar{t}q$ -frame: the c.m. frame of the top quark and spectator jet. In this case, even in exclusive three-jet events, the reference frame is constructed by summing over only the 4-momenta of the top quark and spectator jet. Note that this differs from the $\bar{t}q(j)$ -frame only in exclusive three-jet events.

In Table 3.2.11, we present our results for inclusive two-jet events at the parton level before selection cuts and after the loose set of cuts and event reconstruction. Our study shows that the helicity basis (using the $\bar{t}q$ -frame) and the spectator basis are equally good to study the top quark polarization. Unlike the s -channel process in which the W^- -boson is not perfectly reconstructed in the best-jet algorithm and thus the polarization measurement is significantly degraded after event reconstruction, using the leading b -tagged jet and the top mass constraint gives excellent final state reconstruction in the t -channel process, and the degree of top quark polarization is only somewhat degraded after event reconstruction.

Single-Top Events as Background to Higgs Search The s -channel single top quark process also contributes as one of the major backgrounds to the SM Higgs searching channel $q\bar{q} \rightarrow W^- H$ with $H \rightarrow b\bar{b}$. In this case it is particularly important to understand how the $\mathcal{O}(\alpha_s)$ corrections change kinematic distributions around the Higgs mass region.

Because of the scalar property of the Higgs boson, its decay products b and \bar{b} have symmetric distributions. Fig. 3.2.19 shows the invariant mass distribution of the (b -jet, \bar{b} -jet) system. For a Higgs signal, this invariant mass of the two b -tagged jets would correspond to a plot of the reconstructed Higgs mass. Thus, understanding this invariant mass distribution will be important to reach the highest sensitivity for Higgs boson searches at the Tevatron. The figure shows that at $\mathcal{O}(\alpha_s)$, the invariant mass distribution not only peaks at lower values than at Born level, it also drops off faster. This change in shape is particularly relevant in the region focused on by SM Higgs boson searches of $80 \text{ GeV} < m_{b\bar{b}} < 140 \text{ GeV}$ which is also at the \mathcal{E}_b level. In particular, the NLO contribution from the decay of top quark, while small in its

		D		F	
		LO	NLO	LO	NLO
Helicity basis:	Parton($t\bar{q}(j)$ -frame)	0.96	0.74	0.98	0.87
	Parton($t\bar{q}$ -frame)	0.96	0.94	0.98	0.97
	Recon.($t\bar{q}(j)$ -frame)	0.84	0.73	0.92	0.86
	Recon. ($t\bar{q}$ -frame)	0.84	0.75	0.92	0.88
Spectator basis:	Parton	-0.96	-0.94	0.98	0.98
	Recon.	-0.85	-0.77	0.93	0.89
Beamline basis:	Parton	-0.34	-0.38	0.67	0.69
	Recon.	-0.30	-0.32	0.65	0.66

Table 3.2.11: Degree of polarization D and polarization fraction F for inclusive two-jet t -channel single top quark events, at the parton level (Parton) before cuts and after selection cuts and event reconstruction (Recon.). Here, F corresponds to F in the helicity basis for left-handed top quarks and to F_+ in the spectator and beamline bases for top quarks with polarization along the direction of the spectator-jet and proton three momentum, respectively. Also, the $t\bar{q}(j)$ -frame in the helicity basis denotes the c.m. frame of the incoming partons, while the $t\bar{q}$ -frame denotes the rest frame of the top quark and spectator jet.

overall rate, has a sizable effect in this region of the invariant mass and will thus have to be considered in order to make reliable background predictions for the Higgs boson searches.

Other kinematic distributions are also changing in shape when going from Born-level to $\mathcal{O}(\alpha_s)$. Fig. 3.2.20 shows the distribution of $\cos\theta$ for the two b -tagged jets, where θ is the angle between the direction of a b -tagged jet and the direction of the $(b\text{-jet}, b\text{-jet})$ system, in the rest frame of the $(b\text{-jet}, b\text{-jet})$ system. Experiments cannot distinguish between the b - and the \bar{b} -jets, we therefore include both the b -jet and the \bar{b} -jet in the graph. This distribution is generally flat at Born-level, with a drop-off at high $\cos\theta$ due to jet clustering effects, and a drop-off at negative $\cos\theta$ due to kinematic selection cuts. The $\mathcal{O}(\alpha_s)$ corrections change this distribution significantly and result in a more forward peak, similar to what is expected in Higgs boson production. In other words, a flatter $\cos\theta$ distribution in s -channel single-top events makes it more difficult to separate $W H$ events from the s -channel single top background in an experimental analysis.

Connection to Higgs Boson Searches at the LHC One of the most important tasks at the CERN Large Hadron Collider (LHC) is to find the Higgs boson, denoted as H . It has been shown extensively in the literature that the Higgs boson production mechanism via weak gauge boson fusion is an important channel for Higgs boson searches. Furthermore, to test whether it is a SM Higgs boson after the discovery, one needs to determine the coupling $H V V$, where V denotes either W or Z , by measuring the production rate of $q\bar{q}(V V) \rightarrow H q\bar{q}$ via the weak boson fusion processes. In order to suppress the large background rates, one usual trick is to tag one of the two forward-jets resulting from emitting a vector boson V which produces the Higgs boson via $V V \rightarrow H$. Prior to the discovery of Higgs boson, one can learn about the detection efficiency for forward jets from studying the s -channel single-top process. This is because in the s -channel single-top process, the forward jet also results from emitting a W boson which interacts with the b quark from the other hadron beam to produce the heavy top quark. As pointed out in Ref. [42], in the effective- W approximation, a high-energy t -channel single top quark

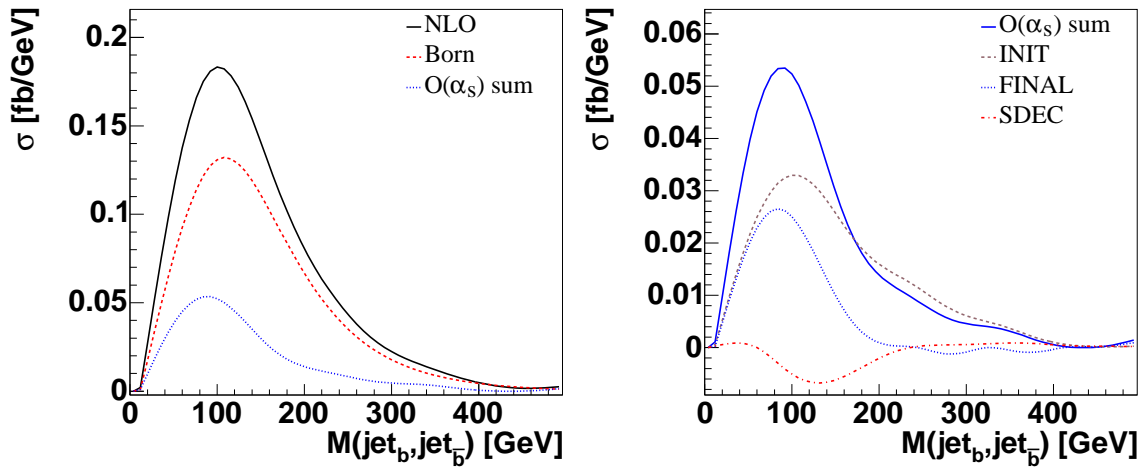


Fig. 3.2.19: Invariant mass of the (b-jet, b-jet) system after selection cuts, comparing Born-level to $O(\alpha_s)$ corrections. In the legend, INIT, FINAL and SDEC denotes the contributions from initial state, final state and top quark decay corrections, respectively.

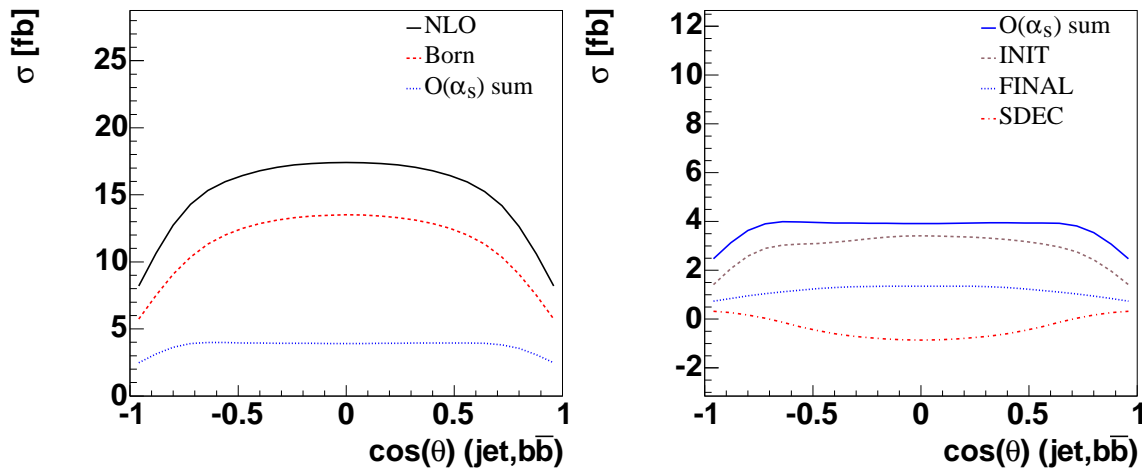


Fig. 3.2.20: Angular distance $\cos \theta$ between a b-tagged jet and the (bjet, bjet) system after selection cuts, comparing Born-level to $O(\alpha_s)$ corrections.

event is dominated by a longitudinal W boson and the b quark fusion diagram. It is the same effective longitudinal W boson that dominates the production of a heavy Higgs boson at high energy colliders via the W -boson fusion process. For a heavy SM Higgs boson, the longitudinal W boson fusion process dominates the Higgs boson production rate. Therefore, it is also important to study the kinematics of the spectator jet in t -channel single top quark events in order to have a better prediction for the kinematics of Higgs boson events via the $W W$ fusion process at the LHC.

The unique signature of the t -channel single top process is the spectator jet in the forward direction, which can be utilized to suppress the copious backgrounds, such as $W b\bar{b}$ and $t\bar{t}$ production. Studying the kinematics of this spectator jet is important in order to have a better prediction of the acceptance for t -channel single top quark events and of the distribution of several important kinematic variables. Below, we discuss the impact of NLO QCD corrections on the kinematic properties of the spectator jet. Here, we again concentrate on Tevatron Run II phenomenology and show in Fig. 3.2.21 the pseudo-rapidity distribution of the spectator jet at LO and NLO for comparison.

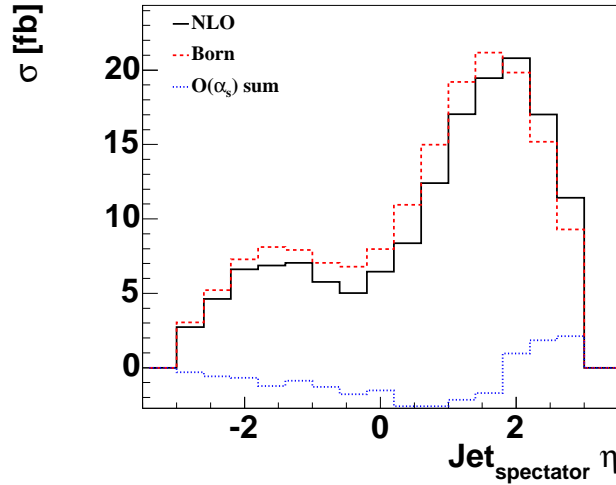


Fig. 3.2.21: Pseudo-rapidity η of the spectator jet in t -channel single-top events produced at the Tevatron in Run II, after imposing kinematic selection cuts, comparing Born-level to $\mathcal{O}(\alpha_s)$ corrections.

The pseudo-rapidity distribution of the spectator jet is asymmetric at the Tevatron for being a $p\bar{p}$ collider [42]. In order to produce a heavy top quark decaying to a positively charged lepton, the valence quark from the proton is most important, implying that the light quark will tend to move in the proton direction. We define the positive z -direction to be the proton direction in the laboratory frame, thus the pseudo-rapidity of the spectator jet will tend to be positive. Similarly, the spectator jet in an anti-top quark event produced from the t -channel process at the Tevatron will preferably be at a negative pseudo-rapidity due to the large anti-up quark parton distribution inside the antiproton. The $\mathcal{O}(\alpha_s)$ corrections shift the spectator jet to even more forward pseudo-rapidities due to additional gluon radiation. However, since the $\mathcal{O}(\alpha_s)$ corrections are small compared to the Born-level contribution, the spectator jet pseudo-rapidity distribution only shifts slightly. As Fig. 3.2.22 shows, the LIGHT and HEAVY contributions have almost opposite behavior (LIGHT and HEAVY denote $\mathcal{O}(\alpha_s)$ contributions originating from the

light and heavy quark line QCD corrections in the \bar{t} -channel single top process. The former shifts the spectator jet to even higher pseudo-rapidities, while the latter shifts it more to the central rapidity region. This behavior is due to two different effects, as illustrated in Fig. 3.2.22(b), in which “PA” denotes that the light quarks come from the proton while the bottom quarks from the anti-proton and vice versa for “AP”. After separating the contributions by whether the light quark is from the proton or the antiproton, it can be seen that the HEAVY corrections shift the proton contribution down and the antiproton contribution up due to the slight change in acceptance caused by the additional jet. The LIGHT corrections show the opposite tendency. For the TDEC contribution, originating from the top quark decay, all corrections have similar shapes and the sum of them leaves the spectator jet pseudo-rapidity unchanged, as expected. After summing the negative soft-plus-virtual corrections with the real emission corrections, we obtain the result shown in Fig. 3.2.21, which shows that the $\mathcal{O}(\alpha_s)$ correction shifts the spectator jet even further to the forward direction.

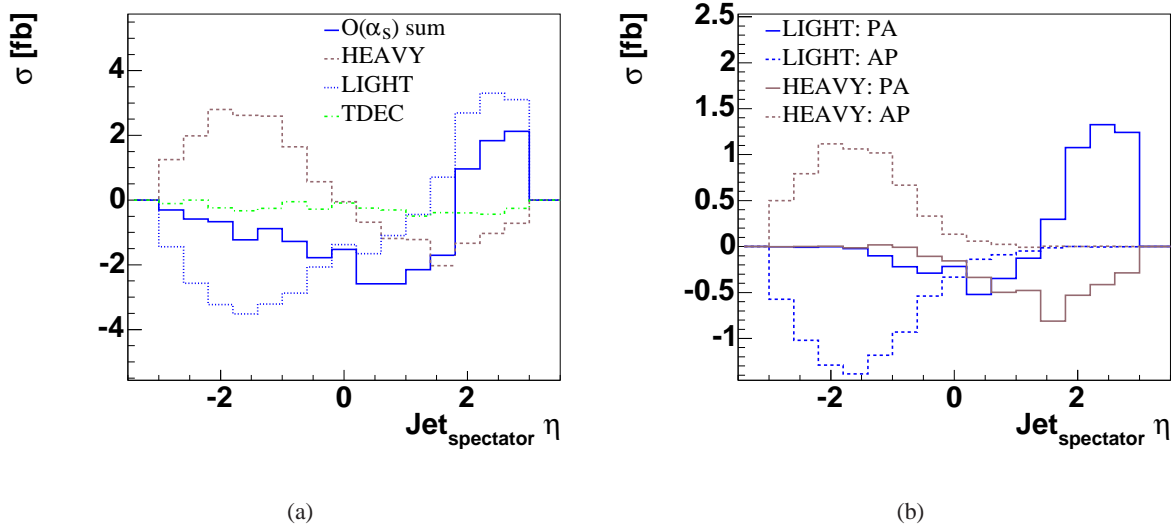


Fig. 3.2.22: Each individual contribution of the $\mathcal{O}(\alpha_s)$ corrections to the spectator jet pseudo-rapidity, summed (a), separately for the case when the incoming up-type quark is from the proton and anti-proton (b). Here, “PA” and “AP” denotes the initial state light quark originating from proton and anti-proton, respectively. In the legend, HEAVY, LIGHT and TDEC denotes contributions from NLO corrections to the heavy quark line, light quark line and decay of top quark, respectively.

Besides its forward rapidity, the spectator jet also has large transverse momentum. Since it comes from the initial state quark after emitting the effective W boson, the transverse momentum peaks around $M_W = 2$. By comparison, the third jet is most often much softer, we can thus use p_T of the jet to identify the spectator jet when considering exclusive three-jet events.

Summary Based on a NLO calculation to consistently include corrections to the production and decay of the top quark in the s - and \bar{t} -channel single-top processes, we perform a phenomenology study for the Tevatron Run-II. We find that:

1. When using loose kinematic cuts to maximize the acceptance of single-top signal events, the full

NLO kinematics have to be studied. Applying a constant K -factor with LO kinematics does not reproduce the actual NLO distributions.

2. In order to reconstruct the top quark in single-top events, the best-jet algorithm works better in the s -channel process, while the leading b -tagged jet algorithm works best in the t -channel process.
3. NLO corrections can largely change some kinematic distributions and spin correlations. After event reconstruction with kinematic selection cuts, we find that the degree of top quark polarization is about the same in the optimal basis and the helicity basis ($t\bar{b}$ -frame) for the s -channel process. For the t -channel process, the helicity basis (the $t\bar{q}$ -frame) gives almost the same prediction as the spectator basis.
4. To accurately model the s -channel single-top background in searches for Higgs boson production via $W H$ associated production, one has to use NLO kinematics to model the decay of the top quark in single-top events. This is because the LO top decay kinematics underestimate the s -channel single-top rate as a background for Higgs searches.
5. Studying the detection efficiency of the forward light quark jet (the spectator jet) in t -channel single-top events can help us optimize the detection efficiency in searches for the Higgs boson produced via weak gauge boson fusion processes at the LHC. We find that the NLO corrections to the light quark line in t -channel single-top events tend to shift the spectator jet to even more forward rapidities. Hence, the NLO effect is important for determining the coupling of $H V V$ by measuring the $V V \rightarrow H$ production rate.

ACKNOWLEDGMENTS The work of C.-P. Y. was supported in part by the U. S. National Science Foundation under award PHY-0244919.

Single top production and decay at next-to-leading order

Contributed by: J. Campbell and F. Tramontano

In this section, we report on the recent calculations of all single top processes at next-to-leading order and their inclusion in the Monte Carlo program MCFM [53, 60]. The implementation of these processes includes the leptonic decays of the top quark (with full spin correlations) as well as the effects of gluon radiation in the decay of the top quark. The inclusion of these effects allows for the application of cuts on all the decay products and thus a better comparison with experimental studies.

The lowest order processes which we consider are s -channel production,

$$u + d \rightarrow t + b \quad (3.2.17)$$

$$\downarrow \quad + e^+ + b$$

t -channel production,

$$b + u \rightarrow t + d \quad (3.2.18)$$

$$\downarrow \quad + e^+ + b$$

and single top production in association with a W boson which also decays leptonically,

$$b + g \rightarrow W + t \rightarrow e + b \quad (3.2.19)$$

At the Tevatron only the processes in Eqs. (3.2.17) and (3.2.18) can be observed. At the LHC top quarks can be produced copiously in all channels, with a significant amount of events from the associated channel, Eq. (3.2.19). Thus the study of single top events passes from the search for their observation at the Tevatron to their study as a significant source of background events in new physics searches at the LHC. We note that at the Tevatron, the rates for the production of an anti-top quark in any of these modes are identical to those for a top quark. At the LHC, the cross sections for top and anti-top production in the s and \bar{t} channels differ. In contrast, the rate for $W^+ t$ is the same as that for $W^- \bar{t}$ due to the equality of the perturbatively-derived b and \bar{b} distribution functions.

All of these processes have previously been considered extensively at leading order, but the first serious approximation in QCD is obtained by including $\mathcal{O}(\alpha_s)$ radiative corrections. Such next-to-leading order calculations can give important information about the choice of factorization and renormalization scales. In addition, it is only at next-to-leading order that we obtain accurate predictions of event rates which are sensitive to the structure of jets in the final state. Such NLO calculations have so far been available only for the case where the decays of the top quark (and the W boson, in the case of associated production) are not included [48, 56, 57, 49, 52, 108, 59].

First we describe the inclusion of radiative corrections with reference to the s -channel process, although a similar procedure is followed for the other two processes. In general, the real and virtual radiative corrections fall into two categories. The first type is radiation in the production stage of the top quark and the second corresponds to radiation associated with its decay. Examples of diagrams in each category are depicted in Figure 3.2.23, where the double bar indicates the separation of production and decay stages.

In order to make this separation in a gauge-invariant way, the double bar represents a top quark which is on its mass shell. Thus every diagram has exactly one top quark which is on its mass shell and diagrams without an on-shell top quark are suppressed by Γ_t/m_t where Γ_t and m_t are the width and mass of the top quark. In this procedure, we have neglected the interference between radiation in the production and decay stages, both in the real and virtual contributions. An example of such an interference term in the virtual contribution is shown in Fig. 3.2.24. The physical argument for neglecting these terms is based on the characteristic time scale for the production and the decay of the top quark [109, 110, 111]. For the production, this time scale is of order $1/m_t$ while for the decay it is $1/\Gamma_t$. In general, this suggests that radiation in the production and decay stages is separated by a large time and the interference effects are expected to be of order Γ_t/m_t . In both total cross sections and in distributions of selected observables, there is evidence that this is indeed the case [112, 113].

The implementation of the cancellation of soft and collinear singularities between the real and the virtual contributions is performed using the dipole subtraction method [114, 115, 116]. For the case of single top production we have a massive quark in the final state, so in fact we have implemented a generalization of this scheme as suggested in [117]. We have also extended these results to include a tunable parameter which controls the size of the subtraction region, as originally proposed in [118, 119].

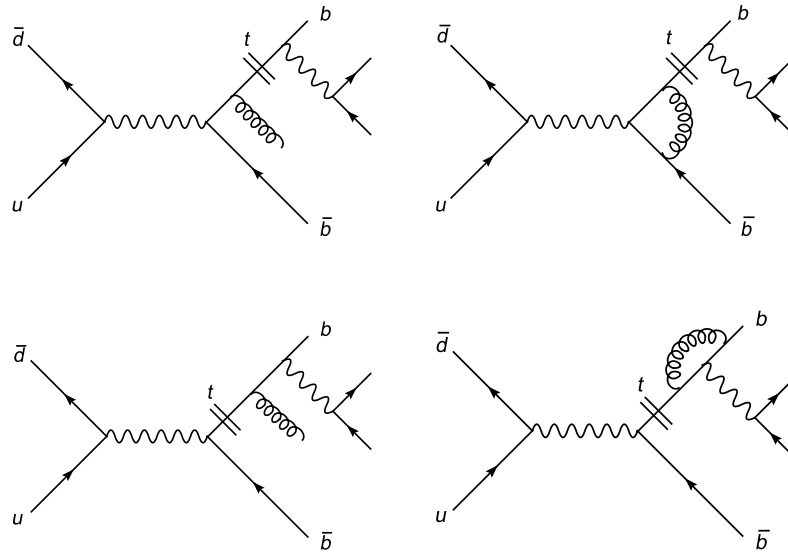


Fig. 3.2.23: Real and virtual radiation in the production and decay stages of s -channel single top production. The double bar indicates the on-shell top quark.

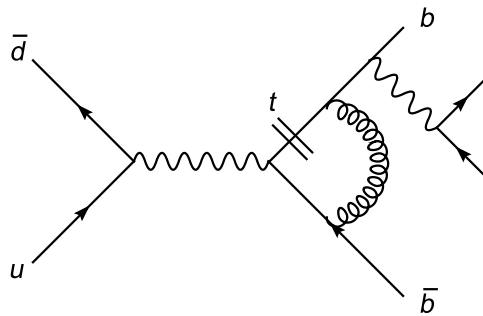


Fig. 3.2.24: An example of a diagram that is not included, in this case interference between virtual radiation in the production and decay stages.

Further details may be found in Ref. [53]. In order to deal with radiation in the decay stage of the process we have developed a specialized subtraction procedure, which can be applied to the decay of the top quark in any process. We will briefly describe this procedure here.

We begin by constructing a counter-term for the process,

$$t \rightarrow W + b + g; \quad (3.2.20)$$

which has the same soft and collinear singularities as the full matrix element. This counter-term takes the form of a lowest order matrix element multiplied by a function D which describes the emission of soft or collinear radiation,

$$\mathcal{M}(\dots; p_t; p_W; p_b; p_g) \approx \mathcal{M}_0(\dots; p_t; \tilde{p}_W; \tilde{p}_b) D(p_t, p_g; p_b, p_g; m_t^2; m_W^2); \quad (3.2.21)$$

In the region of soft emission, or in the region where the momenta p_g and p_b are collinear, the right hand side of Eq. (3.2.21) has the same singularity structure as the full matrix element. The lowest order matrix element \mathcal{M}_0 in Eq. (3.2.21) is evaluated for values of the momenta p_W and p_b modified to absorb the four-momentum carried away by the gluon, and subject to the momentum conservation constraint, $p_t = p_W + p_b$. The modified momenta denoted by a tilde are also subject to the mass-shell constraints, $\tilde{p}_b^2 = 0$ and $\tilde{p}_W^2 = p_W^2$. The latter condition is necessary in order that the rapidly varying Breit-Wigner function for the W is evaluated at the same kinematic point in the counterterm and in the full matrix element. We define \tilde{p}_W by a Lorentz transformation, $\tilde{p}_W = \Lambda p_W$ fixed in terms of the momenta p_W and p_t . Because \tilde{p}_W and p_W are related by a Lorentz transformation the phase space for the subsequent decay of the W is unchanged.

The required transformation defining \tilde{p}_W lies in the plane of the vectors p_t and p_W , with the transformed momentum of the b quark fixed by $\tilde{p}_b = p_t - \tilde{p}_W$. The full details of the transformation, subtraction term and integrated form of the dipole can be found in Ref. [60].

In the calculation of the real radiative corrections to the associated W t process, a further complication arises. The difficulty stems from diagrams in which the additional radiated parton is a b quark, such as the ones illustrated in Figure 3.2.25. Both of these diagrams produce a final state consisting of a W , an on-shell top quark and a b quark. However, diagram (b) contains a resonant t propagator and represents the production of a $t\bar{t}$ pair with the subsequent decay of the t into the W and b quark. Therefore the contribution from diagrams such as this, when integrated over the total available phase space, can be much larger than the lowest order W t cross section (an order of magnitude at the LHC).

Rather than using an invariant mass cut [63], or subtracting the problematic resonant contribution [47] we instead utilize an approach which is more suited to our Monte Carlo implementation which includes decays. Using the b -quark PDF, we already include all contributions such as diagram (a) of Fig. 3.2.25 up to a p_T of the b -quark equal to the factorization scale, p_F . In order to ensure the validity of the collinear approximation used in the derivation of the b -PDF [120], we should choose $p_F \gg (m_W + m_t) = 465$ GeV. When a b quark is observed with a p_T above p_F then the doubly resonant diagrams (such as (b) of Fig. 3.2.25) dominate. In this region of phase space, the $t\bar{t}$ process is therefore more appropriate. Thus, in order to disentangle these two processes, we perform our calculation of the W t process by applying a veto on the p_T of the additional b quark that appears at next-to-leading order. For the results presented here, we have chosen this veto to occur at 50 GeV. In doing so, the result

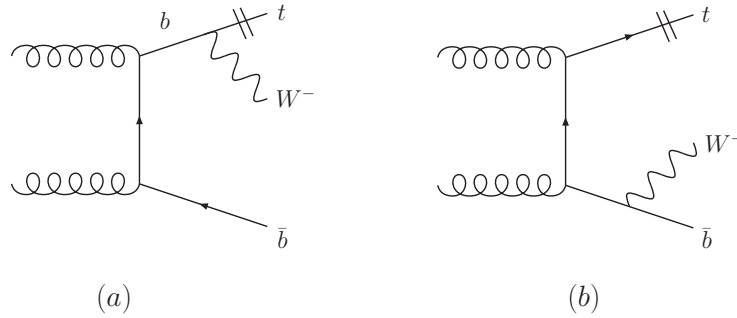


Fig. 3.2.25: Diagrams present in the real corrections to $W^+ \tau$ production which involve an additional b quark. The double bars indicate the on-shell top quark which subsequently decays into $W^+ b$. Diagram (b) contains a resonant τ propagator, while (a) does not.

Table 3.2.12: LO and NLO cross sections (in picobarns) for each channel of single top-quark production at the Tevatron and LHC, for $m_\tau = 175$ GeV. Cross sections are evaluated with CTEQ6L1 ($\alpha_s(M_Z) = 0.130$) and CTEQ6M ($\alpha_s(M_Z) = 0.118$) PDFs [17], using scales of m_τ for the s - and t -channel processes and 50 GeV for $W \tau$.

Process [pb]	Tevatron		LHC	
	LO	NLO	LO	NLO
s -channel	0.582	0.872	7.27	10.4
t -channel	1.75	1.92	237	245
$W \tau$	0.104	0.143	61.3	68.7

for the diagrams represented in Figure 3.2.25 remains at the level of a few percent of the lowest order cross section and, for simplicity, the doubly resonant diagrams can even be omitted.

The methods that we have described have been implemented in the Monte Carlo program, MCFM, allowing us to make predictions for kinematic distributions in all channels. As a simple example of our simulation of these single top processes, we first compare the leading order and NLO cross sections for each of the channels in Table 3.2.12. These cross sections are calculated for a top mass of 175 GeV and use the CTEQ6 set of structure functions. Both the s -channel and $W \tau$ processes can receive sizeable corrections at NLO, with the cross-sections increasing by around 40–50% at the Tevatron. In contrast, the t -channel process receives only mild corrections at both colliders. As well as the normalization of the cross section changing, its dependence upon the factorization and renormalization scales can also be significantly reduced at next-to-leading order. This is illustrated in Figure 3.2.26, where we show the effect of varying these scales on the $W \tau$ cross-section. The renormalization and factorization scales are varied separately by a factor of two, with the other scale kept fixed at $\mu_0 = 50$ GeV. The LO and NLO cross sections are each normalized to their central values. One can see that there is a great reduction in the dependence of the cross section on each of these scales. If both scales are varied together, the scale

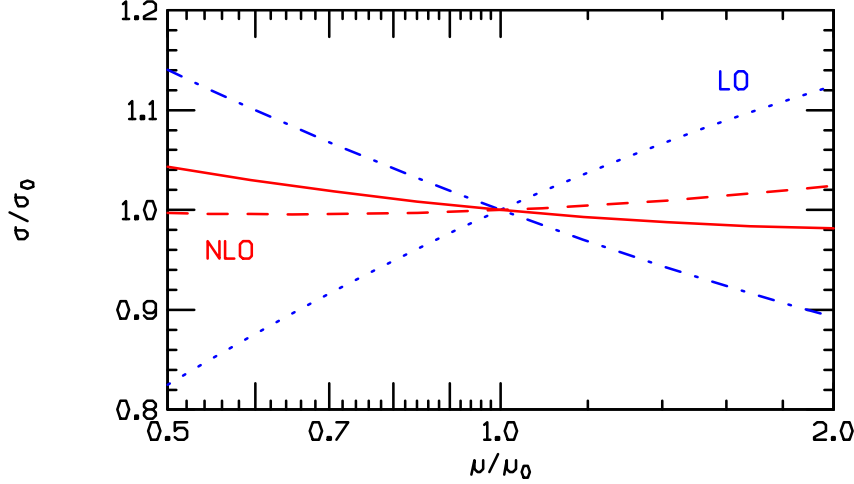


Fig. 3.2.26: Scale dependence of the cross section for $W \tau$ production at the LHC, as described in the text. Factorization scale dependence is shown by a dotted curve at LO and a dashed curve at NLO. Renormalization scale dependence is shown by a dot-dashed curve at LO and a solid curve at NLO.

dependence from each individually practically cancels, even at leading order. Thus one might incorrectly assume that the cross section is well predicted at leading order, when this is clearly not the case.

We now consider the search for single top processes at the Tevatron where, as mentioned earlier, only the s - and t -channel cross sections can possibly be observed. However, much of the lessons learned at the Tevatron will be applicable for the observation of the top quark in the $W \tau$ channel at the LHC. We shall consider the signal for single top production to be the presence of a lepton, missing energy and two jets, one of which is tagged as a b -jet. With this signal, the largest background comes from the process $W b\bar{b}$ with further substantial contributions when a charm quark is mis-tagged as a b in $u s \rightarrow W u c$ and from other mis-tagged $W + 2$ jet events. Smaller background contributions result from $t\bar{t}$ and $W Z$ production.

Most of these processes can be calculated to NLO in MCFM, with cuts designed to reproduce the ones used in the experimental searches at CDF and D0. To that end, we have used the cuts,

$$p_T^e > 20 \text{ GeV}; \quad j^e j < 1:1; \quad E_T > 20 \text{ GeV}; \quad (3.2.22)$$

on the leptons and missing transverse energy, as well as,

$$p_T^{\text{jet}} > 15 \text{ GeV}; \quad j^{\text{jet}} j < 2:3; \quad R > 1:0; \quad (3.2.23)$$

on the jets, which have been clustered using the k_T algorithm. Lastly, in order to reduce the background from events that do not contain a top quark, we apply a cut on the reconstructed mass of the ' $b + l + \cancel{E}$ '-system, $140 < m_{bl} < 210 \text{ GeV}$. Using these cuts, we have calculated the distribution of the variable H_T , the sum of the lepton p_T , missing transverse energy and jet transverse momenta. This can be useful for selecting single-top events from the large backgrounds, as indicated in Figure 3.2.27 where we show the distribution of the signal and the sum of all background processes, under some assumptions about mis-tagging and efficiencies [53]. Although the single top processes represent a large fraction of the

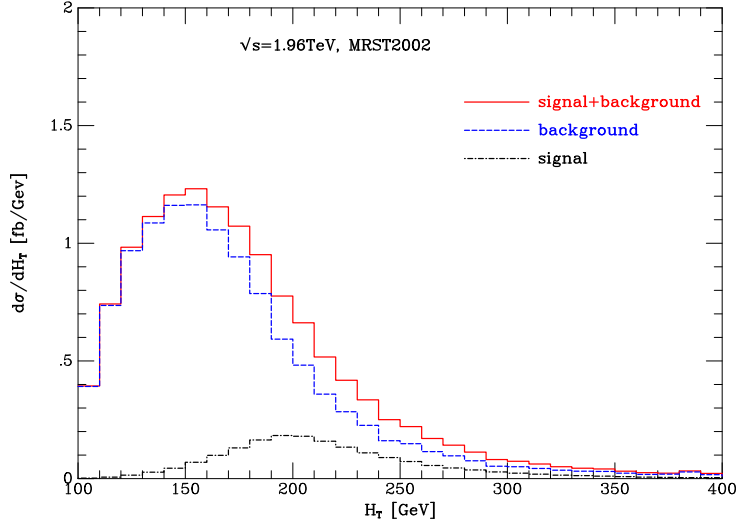


Fig. 3.2.27: The H_T distributions of signal (s - and t -channel single top production), background and signal plus background at the Tevatron.

events in the region of large H_T , searches using this distribution as a key are heavily reliant on accurate predictions of the shapes and normalization of the signal and backgrounds. Since almost all of these are now known at next-to-leading order, this information can be used to refine current analyses.

As a final example of the utility of our calculations we consider a rather different role that single top production can take at the LHC. In the search for an intermediate mass Higgs boson, of mass $155 < m_H < 180$ GeV, the $W \tau$ process can be a significant background when trying to observe Higgs production via gluon fusion [121],

$$g + g \rightarrow H \rightarrow W^- + W^+ + e^+ + e^- \quad (3.2.24)$$

The significant missing energy in the signal process means that the Higgs mass peak cannot be fully reconstructed, so that accurate predictions for all backgrounds are imperative. Here we do not detail all aspects of the study that we have performed (for further details, see Ref. [60]), but merely draw attention to the conclusions. A useful observable for discriminating between the signal and $W \tau$ background is the opening angle in the transverse plane between the leptons from the W decays, $\Delta\phi$. As shown in Figure 3.2.28, the leptons in the signal are predominantly produced with only a small opening angle, while the $W \tau$ background tends to produce them mostly back-to-back. One can see that this statement is weakened at NLO since the $W \tau$ peak is shifted to smaller values and becomes more broad. Such a shape change could have a significant impact on search strategies in this channel at the LHC.

We conclude by noting that a number of approximations have been used in order to make the NLO calculations tractable. Notably, we have not included the mass of the bottom quark in our computations, ignored off-shell effects for the top quark and neglected interference effects between radiation in the top quark production and decay stages. However, none of these is expected to amount to much more than a few percent correction. This should certainly not be a serious issue when considering single top

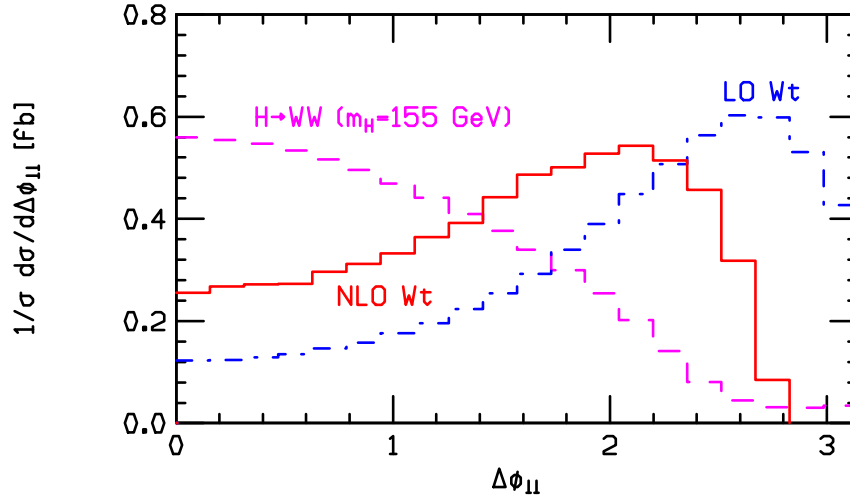


Fig. 3.2.28: The opening angle between the leptons in the $H \rightarrow W W$ and $W t$ processes, for the search for a Higgs of mass 155 GeV. Cross sections are normalized to unity, after suitable search cuts have been applied.

searches at the Tevatron, nor at the LHC when considering these channels as backgrounds. However such effects may become important when studying properties of the top quark in these channels at the LHC. In that case further study will be necessary and indeed the development of such improved tools is already underway [54].

Acknowledgements We thank K. Ellis for collaboration on some of the calculations presented here and acknowledge many helpful discussions with F. Maltoni and S. Willenbrock.

Parton-level comparison of MadEvent Monte Carlo events to NLO calculations

Contributed by: J. Lück, W. Wagner, C. Ciobanu

A good modeling of signal and background processes with Monte Carlo generators is essential for particle physics analyses. This is particularly true if one aims for the observation of a new process, like single-top production. Qualitatively a false discovery has to be avoided, quantitatively the significance of a signal has to be evaluated correctly.

In Run I, CDF used the PYTHIA program to generate single-top events [122, 123]. Several authors pointed out [124, 52] that the leading order contribution of single-top t -channel production as modeled in PYTHIA and HERWIG does not fully represent the measured final states.

This is a $2 \rightarrow 2$ process with a b quark in the initial state: $b + u \rightarrow d + t$ or $b + d \rightarrow u + t$. A b quark parton distribution function is used. The b quark stems originally from a gluon splitting into a $b\bar{b}$ pair. Since flavor is conserved in the strong interaction, a b quark has to be present in the event as well. PYTHIA creates the b through backward evolution following the DGLAP scheme. Using this method, only the soft region of the transverse momentum of the b is modeled well. The high- p_T tail is not estimated as accurately. In addition, the b spectrum comes out too far forward. In following we will call the b the 2nd b quark.

One can improve the modeling of single-top quark production by producing Monte Carlo events with matrix element generators and apply a shower Monte Carlo on the parton final states. To model the single-top t -channel kinematics it was proposed to generate two samples with the matrix element generator: A $2 \rightarrow 2$ sample, $b + q \rightarrow q^0 + t$, and a $2 \rightarrow 3$ sample with a gluon in the initial state, $g + q \rightarrow q^0 + t + b$. In the second process the 2nd b quark is produced directly in the hard process described by the matrix element. This sample describes the most important next-to-leading order contribution to t -channel production and is therefore suitable to describe the high- p_T tail of the 2nd b quark p_T distribution. However, the two samples have to be matched together to give one unified sample of Monte Carlo events. In their first Run II analyses CDF and DØ used a matching procedure based on the p_T spectrum of the 2nd b quark [125, 126]. CDF used the matrix element generator MadEvent [127, 128], DØ used the program CompHEP [129]. At CDF the p_T distributions of the 2nd b quark of LO and NLO sample were normalized to the ratio of the corresponding cross sections calculated by MADEVENT, $R = 2:56$. The intersection point of two curves was found to be $K_T = 18 \text{ GeV} = c$. Subsequently, events of the LO ($2 \rightarrow 2$) sample were accepted for the final sample if the p_T of the 2nd b quark was below K_T . Events of the NLO sample were selected if $p_T(2^{\text{nd}}b) > K_T$.

One important question which has to be addressed is how good the matching procedure is and how well the final Monte Carlo sample describes the single-top t -channel kinematics. To achieve this goal we compared the kinematic distributions of the primary partons obtained from the matched MADEVENT Monte Carlo sample with NLO differential cross sections that are made available by the ZTOP software [52]. We found that the shape of the kinematic distributions of the 2nd b quark, namely the p_T and the pseudorapidity distributions, are modeled quite well. However, we found a small rate difference for visible 2nd b quark jets with $p_T > 15 \text{ GeV}$ and $j_j < 2:8$, which are the jet cuts used in the CDF single-top analysis. Therefore, we adjusted the original matching procedure such that the rate of visible 2nd b quark jets in our matched MADEVENT sample is equal to the rate predicted by ZTOP [130]. Effectively, this results in a new intersection point $K_T = 9 \text{ GeV} = c$ for the matching procedure. As a result all visible 2nd b quarks of the matched sample are coming from the NLO ($2 \rightarrow 3$) sample. Figure 3.2.29 illustrates the matching procedure. We have evaluated the matched t -channel single-top Monte Carlo sample by comparing distributions at parton level to the NLO prediction from ZTOP. Figure 3.2.30 shows a few examples. We also compared kinematic distributions for the s -channel production, see figure 3.2.31. In general, we find very good agreement for the Monte Carlo modeling of the single-top kinematics. We quantify the remaining difference between the Monte Carlo and the NLO calculation by assigning weights to the Monte Carlo events. The weight is derived from a comparison of several kinematic distributions that are combined in a weighted average. We apply the single-top event selection to the Monte Carlo events and sum up the weights. As a result we find an estimate on the deviation of the acceptance in Monte Carlo compared to the NLO prediction. In the $W + 2$ jets bin we find a discrepancy of $1:8\% \pm 0:9\%$ (M C stat:.) for the t -channel, i.e. our study indicates that the Monte Carlo estimate of the acceptance is a little higher than the NLO prediction. In the s -channel we find excellent agreement, no evidence for a deviation, $0:3\% \pm 0:7\%$ (M C stat:.).

The general conclusion from our study is that the MADEVENT Monte Carlo events give an excellent representation of the single-top production process. Due to the matching procedure for the t -channel sample the NLO effects are sufficiently taken into account.

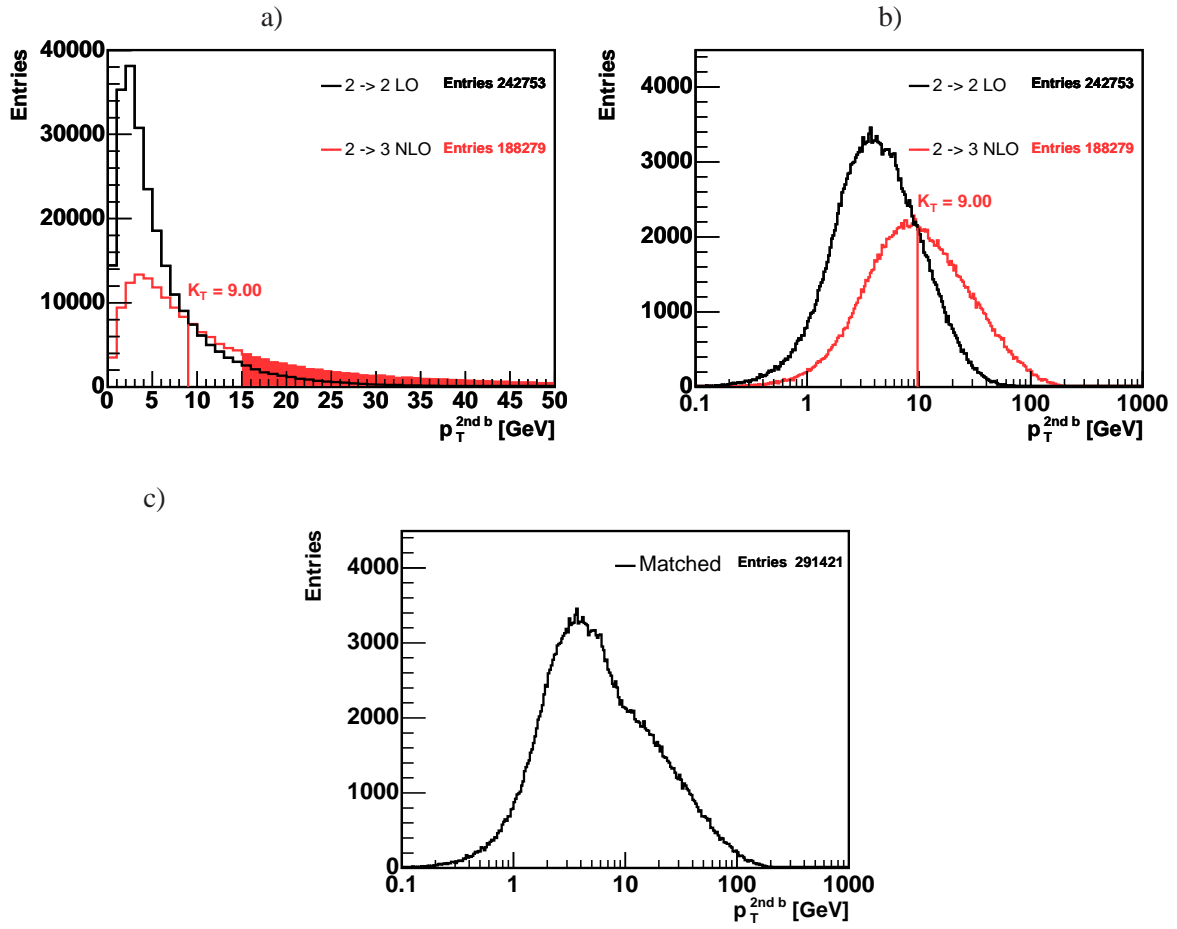


Fig. 3.2.29: Matching of the single-top t -channel samples in CDF. p_T distributions of the 2nd b quark: a) on a linear scale, b) on a logarithmic scale, for the 2 ! 2 and the 2 ! 3 process. The ratio of 2 ! 2 to 2 ! 3 events is adjusted such that the rate of 2nd b quarks with $p_T > 15$ GeV matches the NLO prediction. In c) the p_T distribution for the matched sample is shown.

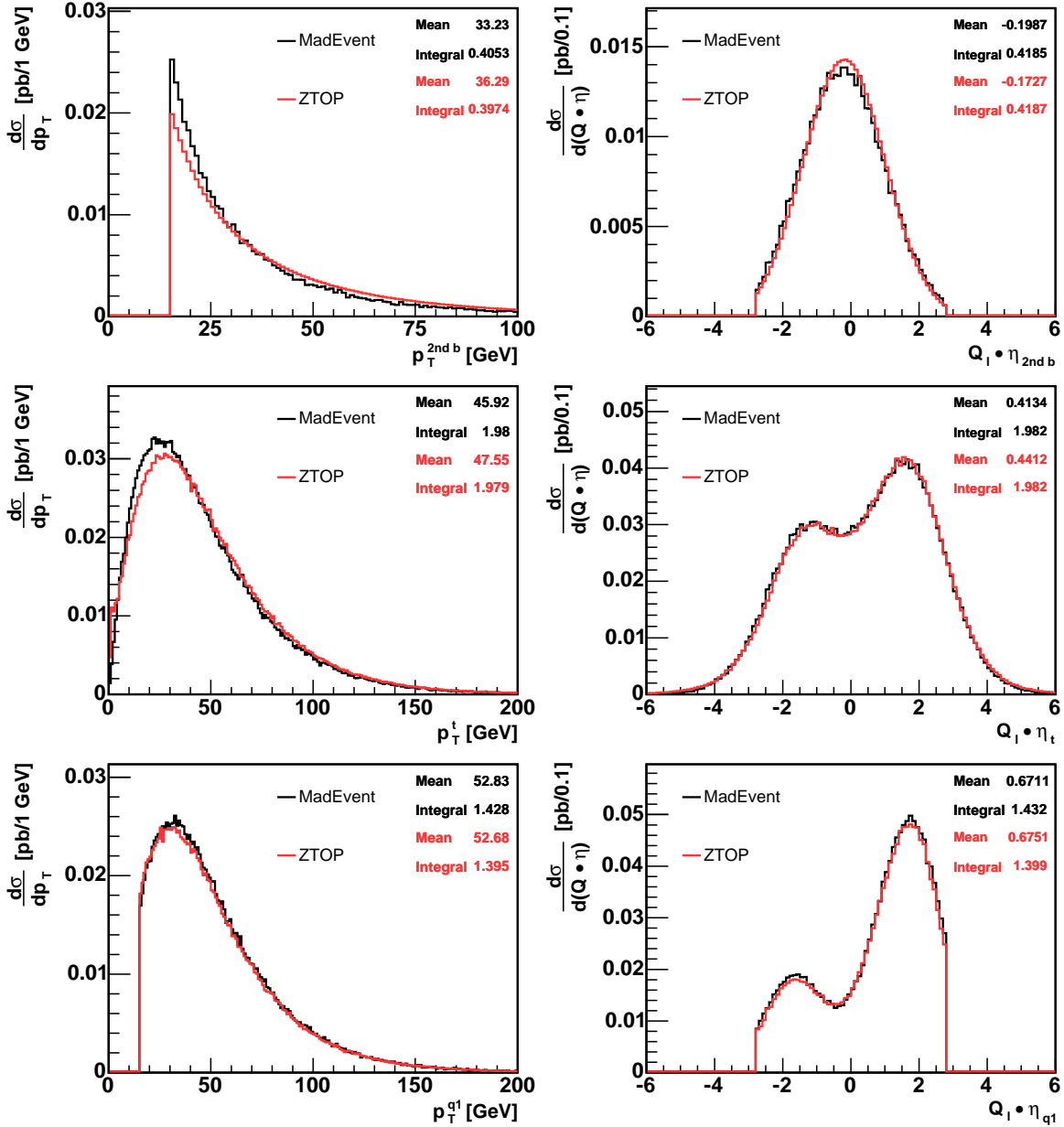


Fig. 3.2.30: Comparison of kinematic distributions at parton level for the matched t -channel single-top Monte Carlo sample with NLO calculations from ZTOP. The upper two plots show the p_T and pseudo-rapidity distribution for 2^{nd} b quarks. The middle row shows the distributions for the top quark. The lower two plots show the p_T and $Q_1 \cdot \eta$ distributions for the leading light quark jet.

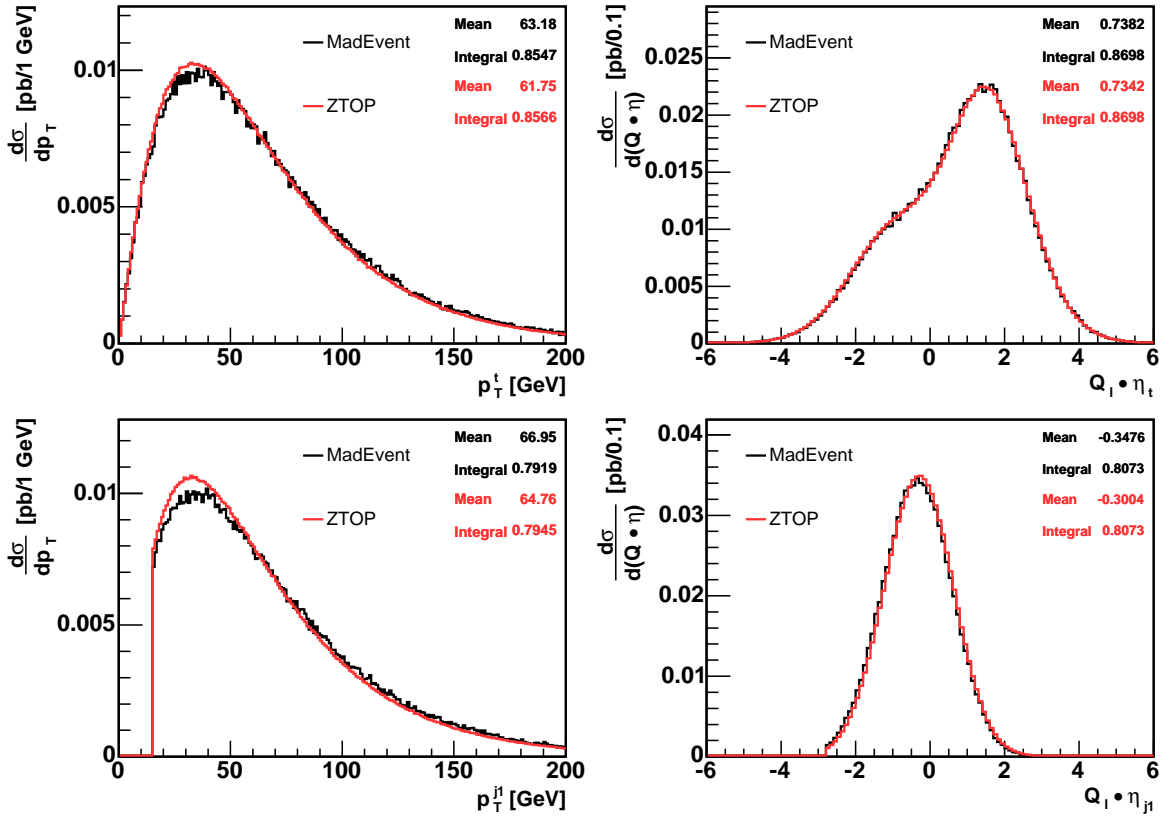


Fig. 3.2.31: Comparison of kinematic distributions at parton level for the matched s -channel single-top Monte Carlo sample with NLO calculations from ZTOP. The upper two plots show the p_T and pseudo-rapidity distribution of the top quark. The lower two plots show the same distributions for the leading jet.

Contributed by: E.E. Boos, V.E. Bunichev, L.V. Dudko, V.I. Savrin, A.V. Sherstnev

Introduction The CompHEP package [129] has been used to prepare a special event generator SingleTop to simulate the electroweak single top quark production with its subsequent decays at the Tevatron and LHC. Single top is expected to be discovered at the Tevatron Run II and will be a very interesting subject of detail studies at the LHC (see the review [30]).

The generator SingleTop includes all three single top processes and provides Monte-Carlo unweighted events at the NLO QCD level. In the paper [52] it has been argued that the NLO distributions for s -channel process are the same as the LO multiplied by a known k -factor. The LO cross sections for the s -channel process are shown in the table 3.2.13 and the NLO cross sections are taken from the papers [57, 49] and are shown in the table 3.2.14 We discuss shortly here only the main process with the largest rate, the t -channel production. The representative LO and NLO diagrams are shown in the Fig. 3.2.32 The top decay is not shown, however it is included at leading order with all spin correlations.

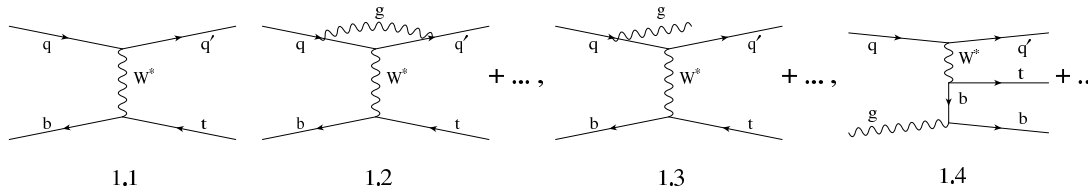


Fig. 3.2.32: LO and representative loop and tree NLO diagrams of the t -channel single top production

Table 3.2.13: The total LO cross section of s -channel single top quark production process (The LHC cross section of $pp \rightarrow t\bar{b}$ processes are equal 4.96 (3.09) pb; for the Tevatron the cross sections of $p\bar{p} \rightarrow t\bar{b}$ and $p\bar{p} \rightarrow \bar{t}b$ processes are the same and equal 0.3 pb (the numbers in brackets)).

Processes, pb			
$ud \rightarrow t\bar{b}$	$du \rightarrow t\bar{b}$	$dc \rightarrow t\bar{b}$	$cd \rightarrow t\bar{b}$
$us \rightarrow \bar{t}b$	$su \rightarrow \bar{t}b$	$sc \rightarrow \bar{t}b$	$cs \rightarrow \bar{t}b$
2.22 (0.291)	2.22 (0.006)	0.26(0.001)	0.26 (0.001)
$du \rightarrow \bar{t}b$	$ud \rightarrow \bar{t}b$	$cd \rightarrow \bar{t}b$	$sc \rightarrow \bar{t}b$
$su \rightarrow \bar{t}b$	$us \rightarrow \bar{t}b$	$dc \rightarrow \bar{t}b$	$cs \rightarrow \bar{t}b$
1.285 (0.291)	1.285 (0.006)	0.26(0.001)	0.26 (0.001)

Overview of the effective NLO approach. We compute by means of the CompHEP the LO order process $2 \rightarrow 2$ with the b -quark in the initial state and top spin correlated $1 \rightarrow 3$ subsequent decay, put it into PYTHIA [131] and switch on ISR/FSR. Then with CompHEP we compute the NLO tree level corrections – $2 \rightarrow 3$ processes with additional b - and light quarks or gluons in the final state including

Table 3.2.14: The total NLO cross section [49] ($M_t = 175$ GeV).

Collider	Process	t		\bar{t}		$t + \bar{t}$	
LHC	t -channel	152.6	3.1	90.0	1.9	242.6	3.6
	s -channel	6.55	0.14	4.1	0.1	10.6	0.17
Tevatron	t -channel	0.95	0.1	0.95	0.1	1.9	0.1
	s -channel	0.44	0.04	0.44	0.04	0.88	0.05

also the top decay with spin correlations. We split the phase space region in "soft" and "hard" parts on p_t of those additional b and light jets being from PYTHIA radiation in the "soft" and from the CompHEP matrix element calculation in the "hard" regions. The soft part is normalized in such a way that all parts being taken together give known from calculations the NLO cross section [57, 49] which are shown in the table 3.2.14 for the LHC and Tevatron. The splitting parameters are tuned based on the requirements that all the distributions become smooth after the normalization. The performed cross checks show an agreement with exact NLO calculations where the computed NLO distributions are correctly reproduced by our method. Therefore, generator "SingleTop" prepared in that way does not have a double counting problem, produces correctly the NLO rate and distributions, and includes all the spin correlations.

The first release of the generator [132] did not include the hard radiation of the light jets, while the latest version [133] currently used in the analysis by the Fermilab D0 and the LHC CMS collaborations includes all the mentioned properties.

Practical implementation of the method in generator SingleTop. The generator "SingleTop" (based on CompHEP program) realizes an effective NLO approach of event generation for the single top-quark processes by taking into account the main NLO corrections to kinematics. The model of simulation is based on the phase space slicing method.

The method begins with the t -channel cross section in the Born approximation, taking into account the full set of Feynman diagrams where the top quark appears with additional b and light quarks in the final state ($2 \rightarrow 3$). However, calculation of the process $2 \rightarrow 3$ at the tree level doesn't include large logarithmic QCD corrections (related to the process $g \rightarrow b\bar{b}$) that appears in the "soft" phase space region where the b quark has a small P_T . It is possible to calculate these corrections via standard renormalization procedure and include them into partonic distributions of the b -quarks in the proton. In this case the reaction $2 \rightarrow 2$ (with b -quark in the initial state) would be the LO approach of the t -channel process. In the same way another b -quark should appear also in the final state. It follows from the fact that b -quark can be produced in the proton only in $b\bar{b}$ pairs from the virtual gluon. One can simulate the final b -quark in the process $2 \rightarrow 2$ via ISR-mechanism. In this case b -quark could be produced by initial state radiation and will appear in the final state within a branch of parton shower, from the splitting function $g \rightarrow b\bar{b}$. One of these b -quarks (from gluon splitting) is the initial hard parton and the second one goes to the final state. The LO cross sections for the $2 \rightarrow 2$ processes are shown in the table 3.2.15. The LO cross sections of $2 \rightarrow 3$ processes are shown in the table 3.2.16, the cut $P_T(b) > 10$ GeV is applied.

Calculations of the process $2 \rightarrow 3$ at the tree level approach doesn't include large logarithmic corrections (related to the process $g \rightarrow b\bar{b}$), but the exact tree level calculations correctly simulate behavior

Table 3.2.15: The LO cross sections of t -channel $2 \rightarrow 2$ processes. (The total LHC cross sections of the process $pp \rightarrow t\bar{t}(t\bar{t})$ is 155.39 (89.85) pb; the Tevatron cross sections of $p\bar{p} \rightarrow t\bar{t}$ and $p\bar{p} \rightarrow t\bar{t} + b\bar{b}$ processes are the same and equal 0.966 pb (the numbers in brackets))

Processes, pb		
ub \rightarrow dt	ub \rightarrow st	dg \rightarrow ct
bu \rightarrow dt	bu \rightarrow st	gd \rightarrow ct
cb \rightarrow dt	cb \rightarrow st	sg \rightarrow ct
bc \rightarrow dt	bc \rightarrow st	gs \rightarrow ct
db \rightarrow ut		
bd \rightarrow ut		
sb \rightarrow ut		
bs \rightarrow ut		
129.26 (0.869)	15.01 (0.057)	11.12 (0.040)
ub \rightarrow dt	ub \rightarrow st	db \rightarrow ct
bu \rightarrow dt	bu \rightarrow st	bd \rightarrow ct
cb \rightarrow dt	cb \rightarrow st	sb \rightarrow ct
bc \rightarrow dt	bc \rightarrow st	bs \rightarrow ct
db \rightarrow ut		
bd \rightarrow ut		
sb \rightarrow ut		
bs \rightarrow ut		
66.99 (0.869)	10.05 (0.057)	12.81 (0.040)

of the b-quark in the "hard" phase space region with the large P_T . We will demonstrate, that combination of the processes $2 \rightarrow 2$ and $2 \rightarrow 3$ allows us to construct MC samples at "effective" NLO level approach. We can prepare correct events with "soft" b-quark via ISR simulation. But in this case we lose the significant contribution of the "hard" b-quark. We can probably come to an appropriate result if we would use different strategies to simulate the different kinematic regions of the phase space. Unfortunately, we can't naively combine the samples with $2 \rightarrow 2$ and $2 \rightarrow 3$ processes because in this case we will get double counting of some phase space regions. To avoid the problem of the double counting we propose to use different methods of MC simulation in the different phase space regions and combine them based on some kinematic parameters.

Figures 3.2.33-3.2.36 show the normalized distributions, that have been prepared for the Tevatron and LHC. On these plots we can see that the distributions for P_T and pseudorapidity of the top and light quarks looks similar (Figs. 3.2.33, 3.2.35), but the distributions of the additional b-quark (that comes from gluon-splitting) differ significantly (Figs. 3.2.34, 3.2.36). The distribution for pseudorapidity of additional ISR b, have a peaks at larger values than the distributions for processes $2 \rightarrow 3$ at tree level. The P_T spectra for the events that we prepare in PYTHIA with ISR simulation are "softer" than in tree level calculations. The main contribution from the large logarithmic appears in the "soft" region of P_T (b). Therefore, it is reasonable to use transverse momentum of additional b-quark as a kinematic parameter for slicing the phase space to hard and soft regions. To prepare events at NLO effective approach we apply the following procedure: first, we prepare the CompHEP events $2 \rightarrow 3$ (at tree level) with P_T (b)

Table 3.2.16: The LO cross sections of t-channel 2 ! 3 processes after the cut $P_T(b) > 10$ GeV (The total LHC cross sections of the process $pp \rightarrow t\bar{t}b(pp \rightarrow t\bar{t}b)$ is 82.3 (47.9) pb; the Tevatron cross sections of $pp \rightarrow t\bar{t}b$ and $pp \rightarrow t\bar{t}b$ processes are the same and equal 0.379 pb (the numbers in brackets); the cut is explained in the text).

Subprocesses		
ug ! dtb	ug ! stb	dg ! cb
gu ! dtb	gu ! stb	gd ! cb
cg ! dtb	cg ! stb	sg ! dt
gc ! dtb	gc ! stb	gs ! dt
dg ! ub		
gd ! ub		
sg ! ut		
gs ! ut		
68.8 (0.328) pb	7.6 (0.03) pb	5.9 (0.021) pb
ug ! dtb	ug ! tb	dg ! ctb
gu ! dtb	gu ! tb	gd ! ctb
cg ! dtb	cg ! tb	sg ! ctb
gc ! dtb	gc ! tb	gs ! ctb
dg ! utb		
gd ! utb		
sg ! utb		
gs ! utb		
36.2 (0.328) pb	4.9 (0.03) pb	6.8 (0.021) pb

larger than some critical value P_T^0 . Then we prepare events 2 ! 2 in the "soft" region of the phase space with $P_T(b) < P_T^0$. The cross section of 2 ! 2 events in the "soft" region we multiply by K-factor for taking into account loop corrections which do not change significantly the kinematic distributions. The value for K-factor we can calculate with the requirements of normalization of the events in the full phase space to the total NLO cross section, as demonstrated in the following equation:

$$\sigma_{NLO} = K \left(\sigma_{PYTHIA}(2 ! 2)_{P_T(b) < P_T^0} + \sigma_{COMPH EP}(2 ! 3)_{P_T(b) > P_T^0} \right)$$

The K-factor here is a function of slicing parameter P_T^0 , the total NLO cross section we know from exact NLO calculations [57, 49].

In case of LHC collider we have:

$$\sigma_{COMPH EP}(2 ! 3)_{P_T^b > 20\text{GeV}} = 108.7 \text{ pb};$$

$$\sigma_{COMPH EP}(2 ! 3)_{P_T^b > 10\text{GeV}} = 125.7 \text{ pb}$$

and $K=0.89$ for $P_T^0 = 20$ GeV, and $k=0.77$ for $P_T^0 = 10$ GeV.

In case of TEVATRON collider we have:

$$\sigma_{COMPH EP}(2 ! 3)_{P_T^b > 20\text{GeV}} = 0.46 \text{ pb}$$

$$\sigma_{COMPH EP}(2 ! 3)_{P_T^b > 10\text{GeV}} = 0.72 \text{ pb}:$$

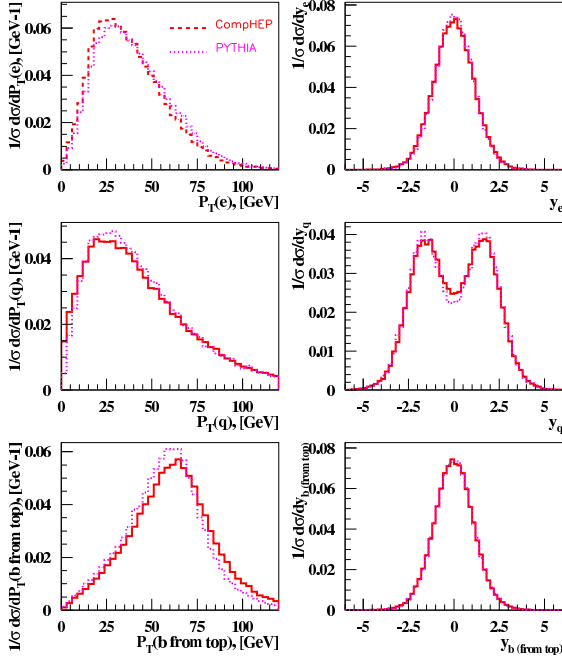


Fig. 3.2.33: The comparison of P_T and y distributions for the $pp \rightarrow t\bar{q} + b_{\text{ISR}}$ (PYTHIA) and $pp \rightarrow t\bar{q} + b_{\text{LO}}$ (CompHEP) simulations for the Tevatron. The distributions are normalized to unity and no cuts applied.

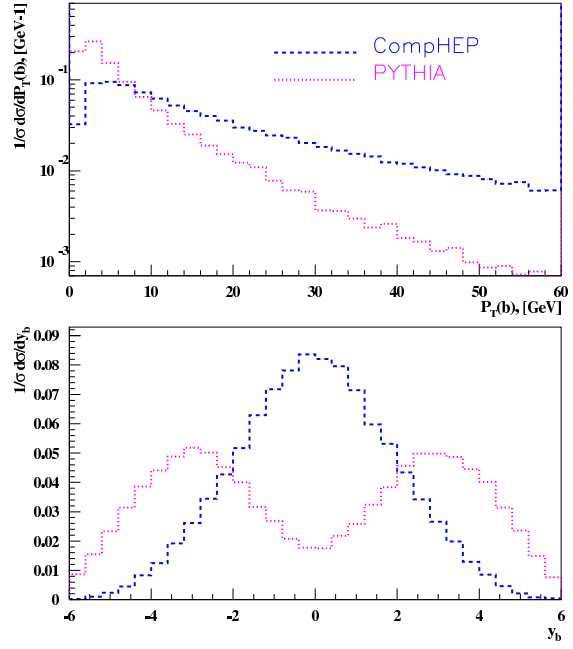


Fig. 3.2.34: The comparison of P_T and y distributions for the b_{ISR} and b_{LO} in the $pp \rightarrow t\bar{q} + b_{\text{ISR}}$ (PYTHIA) and $pp \rightarrow t\bar{q} + b_{\text{LO}}$ (CompHEP) simulations for the Tevatron. The distributions are normalized to unity and no cuts applied.

and $K=1.32$ for $P_T^0 = 20$ GeV, and $k=1.21$ for $P_T^0 = 10$ GeV.

The natural requirement for the correct slicing parameter P_T^0 is a smoothness of the final P_T distribution in the whole kinematic region for the additional b -quark. On the Fig. 3.2.37 and Fig. 3.2.39 shown the distributions for the $P_T^0 = 20$ GeV and we can see the bump at the matching point. After series of iterations we have found that P_T distribution becomes smooth enough with $P_T^0 = 10$ GeV. The result is shown in the Figure 3.2.38. The distributions for the LHC collider are shown in the figure 3.2.40 for the same value of $P_T^0 = 10$ GeV. The algorithm described above we call "effective NLO approach".

Comparison of the results. To check the correctness of our approach we compare our results with two independent NLO calculations. The programs ZTOP [52] and MCFM [53] provide the kinematic distributions at NLO level. The MCFM takes into account the NLO corrections in the decay of t -quark as well as in its production. The ZTOP includes NLO corrections only in the production of top quark. The ZTOP and MCFM programs provide the possibility to calculate NLO distributions, but do not simulate events which are important in the real analysis. We should note, that due to the model of showering for the final partons, generator "SingleTop" takes into account the most part of NLO corrections in the decay of t -quark as well as in the production. We compare the representative distributions from our effective NLO approach with exact NLO calculations. The results are shown in the Figures 3.2.41, 3.2.42. We can see how the events simulated in effective NLO approach correctly reproduce the exact NLO distributions

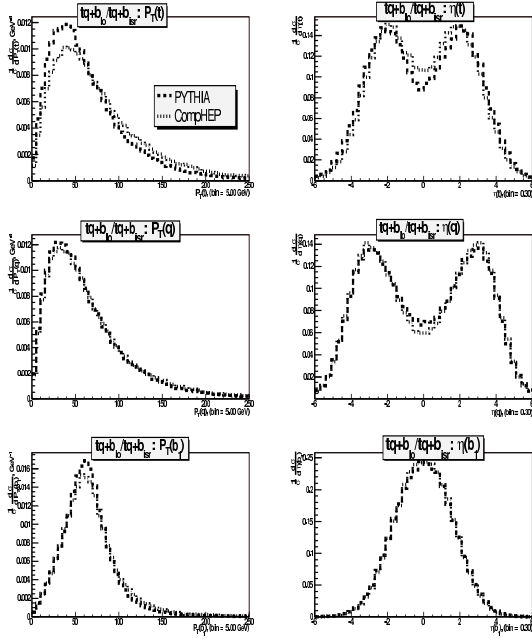


Fig. 3.2.35: The comparison of P_T and η distributions for the $pp \rightarrow tq + b_{\text{ISR}}$ (PYTHIA) and $pp \rightarrow tq + b_{\text{LO}}$ (CompHEP) simulations for the LHC. The distributions are normalized to unity and no cuts applied.

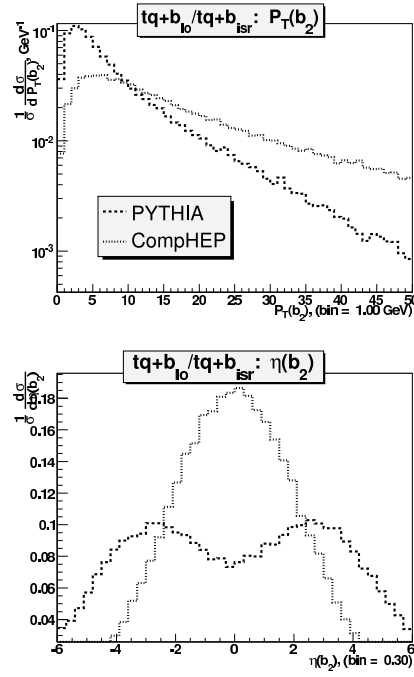


Fig. 3.2.36: The comparison of P_T and η distributions for the b_{ISR} and b_{LO} in the $pp \rightarrow tq + b_{\text{ISR}}$ (PYTHIA) and $pp \rightarrow tq + b_{\text{LO}}$ (CompHEP) simulations for the LHC. The distributions are normalized to unity and no cuts applied.

produced by ZTOP and MCFM programs. The good agreement in distributions demonstrates the correctness of the simple approach to model the most important part of NLO QCD corrections on the level of event simulations.

ACKNOWLEDGEMENTS The work is partly supported by RFBR 04-02-16476, RFBR 04-02-17448, Universities of Russia UR.02.02.503, and Russian Ministry of Education and Science NS.1685.2003.2 grants.

W +jets as a Background to Discovering Single Top Quarks

Contributed by: M.T. Bowen, S.D. Ellis, and M.J. Strassler

Standard Model production of W bosons and associated jets is currently obstructing the discovery of single-top-quark production at the Tevatron. This background is now known to be significantly larger than expected a few years ago. The systematic errors on prediction and measurement of this background, especially in the context of b tagging, have made a simple counting experiment virtually impossible, as the uncertainties are comparable to the single-top signal. It seems necessary to use the kinematic distributions (“shapes”) of the main backgrounds (W +jets, tt , QCD) in order to separate signal from background. However, predicting or measuring the shape of the W +jets background after b -tagging algorithms are applied, as required for single-top discovery, is itself subject to significant uncertainty. In this note, we point out a possible approach to reducing one aspect of this problem.

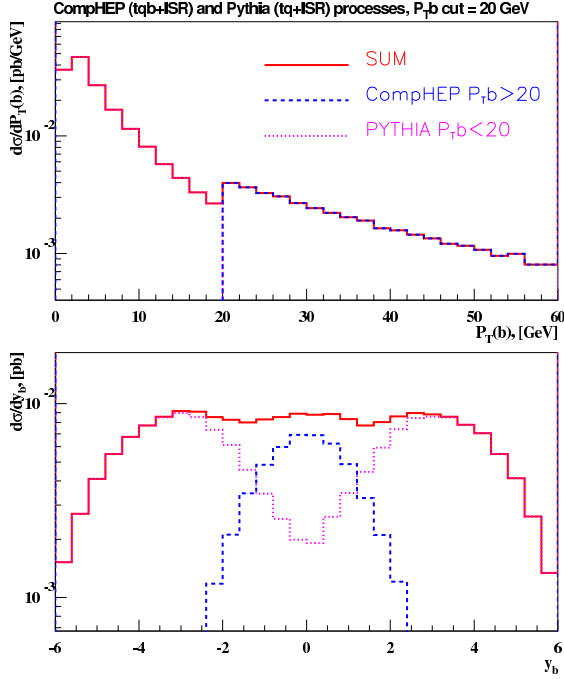


Fig. 3.2.37: The combined distributions for the "soft" $pp \rightarrow tq + b_{\text{ISR}}$ (PYTHIA) and "hard" $pp \rightarrow tq + b_{\text{O}}$ (CompHEP) regions for the Tevatron collider with $P_T^0(b) = 20$ GeV.

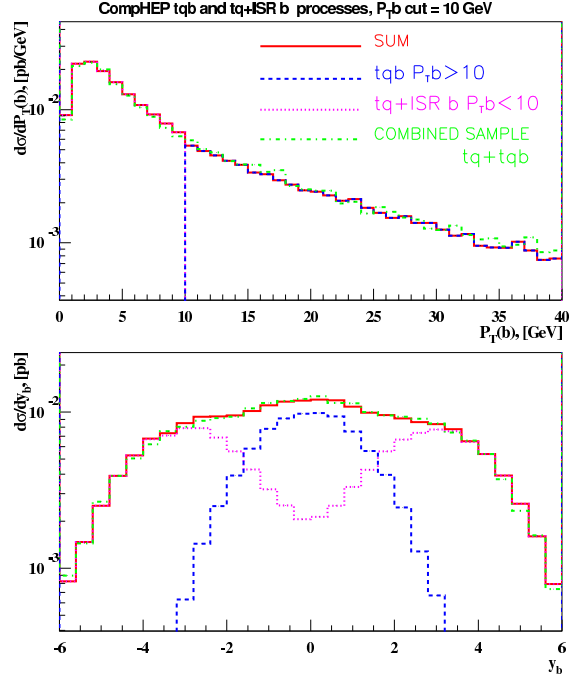


Fig. 3.2.38: The combined distributions for the "soft" $pp \rightarrow tq + b_{\text{ISR}}$ (PYTHIA) and "hard" $pp \rightarrow tq + b_{\text{O}}$ (CompHEP) regions for the Tevatron collider with $P_T^0(b) = 10$ GeV.

An analysis of the use of shape differences between signal and background was performed in Reference [65]. The use of asymmetries and correlations involving the lepton from the top decay and the jet associated with the t -channel production process were shown to dramatically mitigate problems from the $t\bar{t}$ background. The reduction of the W +jets background was shown to be significant, but still insufficient, unless systematic errors on the shape of W +jets can be brought down to roughly the 20 percent level. The challenges in doing so were discussed in section IV of [65]. The various contributions to the sample of W +jets *with a single* b -tag were compared, and it was shown that many different subprocesses, with many different initial and final states, are of comparable importance. Unfortunately, each of these subprocesses has a different shape. Unless their relative normalizations can be determined, it is impossible to know the shape of the total W +jets single-tag background with low uncertainty. Further, each of the many contributions has its own independent uncertainties, stemming from parton distribution functions (PDF's), loop corrections, and issues involving tagging and mistagging of heavy flavor, among others. It seems difficult to imagine that all of these subprocesses can separately be measured in data. Therefore, it is important to reduce the unknowns in this context using a combination of data, theory, and simulation.

Among the lessons of section IV of [65] was that roughly a third of the events entering the W +jets single-tag sample do so through the tagging of heavy flavor quarks emerging within the parton shower of a short-distance gluon. Consequently, a significant portion of the normalization uncertainty in certain subsamples is due to incomplete knowledge concerning the fragmentation of short-distance gluons to

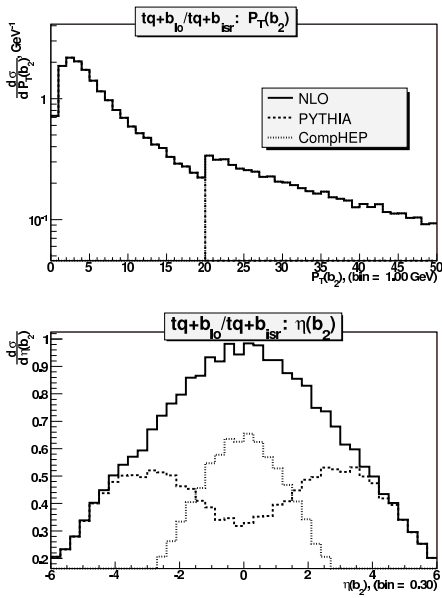


Fig. 3.2.39: The combined distributions for the "soft" $pp \rightarrow tq + b_{\text{ISR}}$ (PYTHIA) and "hard" $pp \rightarrow tq + b_{\text{LO}}$ (CompHEP) regions for the LHC collider with $P_T^0(b) = 20$ GeV.

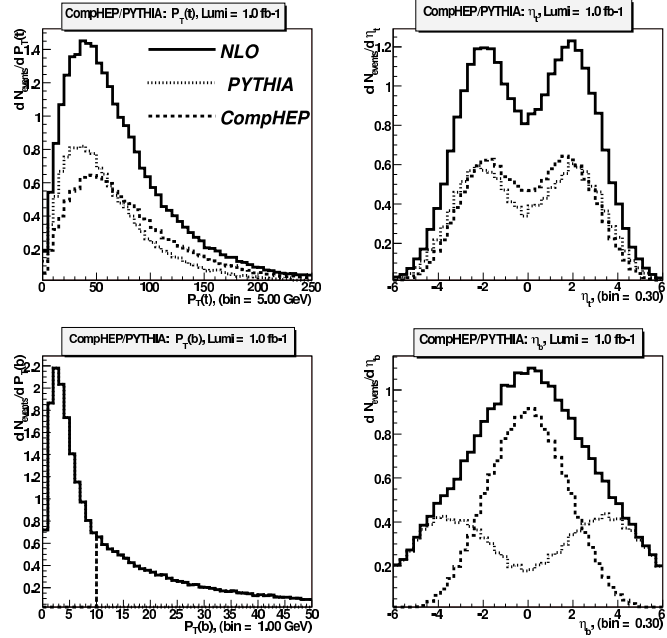


Fig. 3.2.40: The combined distributions for the "soft" $pp \rightarrow tq + b_{\text{ISR}}$ (PYTHIA) and "hard" $pp \rightarrow tq + b_{\text{LO}}$ (CompHEP) regions for the LHC collider with $P_T^0(b) = 10$ GeV.

heavy quark pairs, which leads to uncertainties in how often parton-level processes such as $ud \rightarrow W gg$ will receive a single b tag. (This problem extends well beyond single-top-quark production, of course; any similar process, such as $t\bar{t}h$ or Wh , will have background from gluon radiation and subsequent splitting to heavy quark pairs.) While Monte Carlo programs are relied upon to carry out this splitting in most studies, they have not been sufficiently verified up to the present time. Any neural net method for single-top-quark production trained on Monte Carlo simulations will suffer a substantial uncertainty from this source, unless the Monte Carlo can be tuned more convincingly to data.

Summary: Proposal to Study Gluon Splitting in $W + 1j$ Events To reduce the systematic error from gluon splitting to heavy flavor requires a combination of data and Monte Carlo. It has already been suggested [134] that events with a single W , Z or photon and a single hard jet are important tools for extracting heavy-flavor PDF's. We wish to emphasize further that one should view these events as tools for a study of gluon fragmentation to heavy flavor, and for reducing correlated uncertainties involving PDF's, fragmentation and heavy-flavor tagging. In particular, with integrated luminosities at the Tevatron exceeding 1 fb^{-1} , W events with a single hard jet represent an ample, relatively well-understood, gluon-rich and heavy-quark-poor resource. The study we present below suggests that the sample of W plus one high- p_T jet ($W + 1j$) provides an opportunity to study in some detail, via investigation of (sometimes multiple) secondary vertices and embedded muons, the fragmentation of gluons into heavy flavor, and the interplay of gluon splitting with tagging algorithms. Our results should be considered preliminary; much further study is required.

The only published intersection between theory and experiment for gluon-splitting to heavy quark

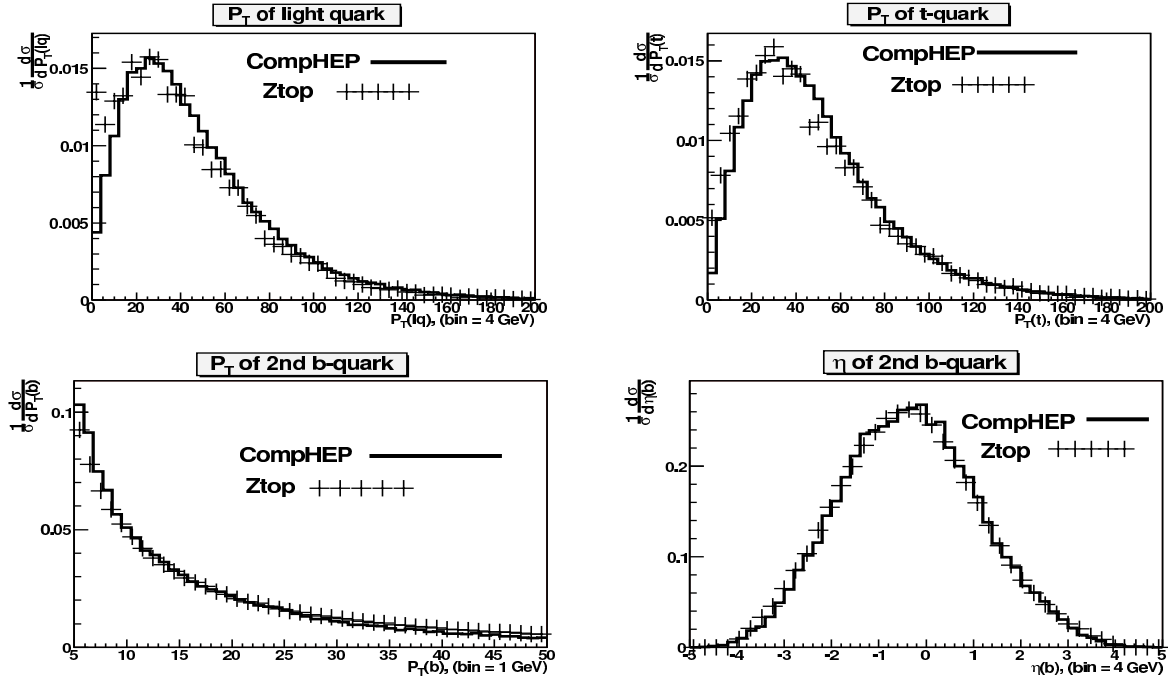


Fig. 3.2.41: The P_T and pseudorapidity distributions of final quarks in effective NLO approach (“SingleTop”) and exact NLO calculations (ZTOP) for the Tevatron collider.

pairs has been at e^+e^- colliders through the process $e^+e^- \rightarrow Z \rightarrow q\bar{q}g$, where the gluon radiated off of one of the quarks then fragments to a $c\bar{c}$ or $b\bar{b}$ pair. The kinematics of SLAC and LEP restricted the energy of this gluon to be in the 20–40 GeV range. Further, the production of the short-distance gluons in an e^+e^- collider takes place in a color environment different than that of a hadron-hadron collider. Thus the predictions of the gluon-fragmentation algorithms implemented in showering generators such as PYTHIA [135] and HERWIG [136] remain somewhat untested for Tevatron applications. It is therefore important to measure gluon splitting rates directly at the Tevatron, ideally in multiple settings.

Naively, the $W+1j$ sample provides such an opportunity, since at leading order (LO) there are no short-distance $W+b$ final states, except through negligibly small CKM mixing angles. Some fraction of the final states contain charm quarks, but almost all jets with multiple secondary vertices in this sample will come from a gluon fragmenting to either a $b\bar{b}$ or $c\bar{c}$ final state. The numbers below will show that even events with a single heavy-flavor tag will be substantially, or even dominantly, from the parton-shower of a gluon. Disentangling the various sources for heavy-flavor tags may be possible in this sample using the differences in impact parameter distributions for short-distance c and b quarks, as well the relative P_T of muons in the decays.

Let us be more specific: we define the $W+1j$ sample to be all events with one lepton, MET, one high- P_T , central jet, and no other high- P_T jets at any rapidity. This *exclusive* $W+1j$ cross-section can be calculated at NLO since it is the difference between the inclusive $W+1j$ and $W+2j$ cross-sections both at NLO, which have been evaluated [137]. We recommend using higher- P_T jets as they are, in general, under better theoretical control and are reconstructed with greater efficiency by detectors. Further, the rate at which gluons split to $Q\bar{Q}$ pairs increases significantly with energy, so the fraction of jets containing

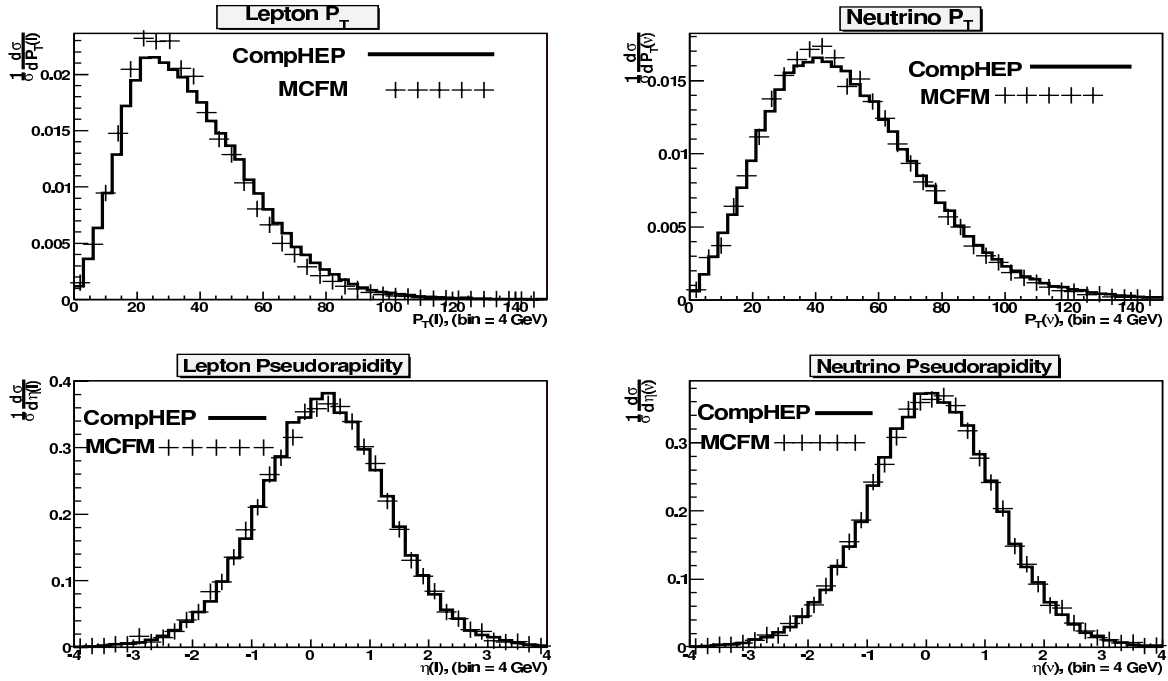


Fig. 3.2.42: The P_T and pseudorapidity distributions of final leptons from top-quark decay in effective NLO approach (“SingleTop”) and exact NLO calculations (MCFM) for the Tevatron collider.

$b\bar{b}$ and $c\bar{c}$ pairs becomes larger. What p_T cut best balances statistics and systematics will have to be determined by a future study.

Simulation of $t \rightarrow j$ Events The proposal above requires NLO studies for both $W + 1j$ and $W + 2j$ to normalize the $W + 1j$ exclusive event set. For now, we use the K-factor for $W + 1j$ inclusive production from [137] to normalize our event set. This overestimates the number of events the Tevatron experiments will have to work with, but probably by less than ten percent. Our crude simulation of the $W + 1j$ sample suggests there will be enough events at the Tevatron to measure the gluon splitting rate even with a small reduction in rate when the normalization is calculated more accurately.

To provide an estimate of the number of $t \rightarrow j$ events the Tevatron experiments will have to work with, we have generated an unweighted $t \rightarrow j$ event set using the LO event generator Madgraph [128] and CTEQ5L PDF’s [138]. Events are generated with the factorization and renormalization scales set to M_W , and a K -factor of 1.1 is taken from the $W + 1j$ inclusive NLO calculation in [137]. After accounting for the branching-ratio for $W \rightarrow e\bar{\nu}_e$, and the generic cuts given in Table 3.2.17, the numbers of events with 1 fb^{-1} of integrated luminosity are given in Table 3.2.18. The events are broken into various sub-channels, differing by the underlying source of the jet j . For simplicity, the cuts are applied to the the short-distance partons, not to the jets. Triggering efficiencies are not accounted for, but are expected to be at least 80% for all channels.

Table 3.2.18 shows the abundance of short-distance gluons in $t \rightarrow j$ events. The numbers of events in different channels suggests (though it does not prove) that by looking at $t \rightarrow j$ events with one and two secondary vertices, as well as events with one and two high- p_T embedded muons, the processes

Item	p_T	$j j$
$' g$	15 GeV	1:1
MET ()	15 GeV	-
j	40 GeV	1:1

Table 3.2.17: Detector cuts applied to partons in our study.

Channel	Events After Cuts
$' g$	24,000
$' q$	22,000
$' c$	2,200

Table 3.2.18: Numbers of events with 1 fb^{-1} for the subsets of $' j$ with the cuts from table 3.2.17. Here $'=(e, \mu)$, c is both c and \bar{c} , and q sums over all light quark and antiquark flavors. There is no $' b$ channel at LO, except through negligibly small CKM matrix elements such as V_{cb} .

$' g ! ' b$ and $' g ! ' c c$ can be disentangled both from each other and also from $' c$ and fake tags. Indeed, given that B meson decays frequently involve charm mesons, there is the possibility of some jets with four real secondary vertices.

Unfortunately, the contribution from short-distance light quark jets, and from gluons that shower only to light quarks, can lead to reconstructed secondary vertices, and constitutes a significant background to measuring gluon fragmentation to $c c$ and b . However we expect this effect can be constrained in several ways, including the absence of muons in such jets, and a different dependence on vertex position, charge multiplicity, etc.

The other competing short-distance process, with final state $' c$, needs to be determined in order to allow a measurement of gluon fragmentation, and is interesting in its own right. Though $' c$ events will give real secondary vertices and high- p_T muons, they provide at most one of each, and when both are present, the muon will intersect the vertex. Moreover, the charge of the embedded muon will be opposite to the charge of the isolated lepton, in contrast to events with gluon fragmentation, where the muon from the heavy flavor decay may have either charge. The theoretical rate for $' c$ production has a large systematic error from uncertainties in the s quark PDF, because initial-state strange quarks contribute over 80% of the rate at LO; the sample provides an opportunity to measure the s PDF and reduce such uncertainties [139, 134]. The NLO calculation (with the heavy quark mass included) has been completed [108]. To our knowledge, the corresponding experimental study has not yet been done.

Showering of $' g$ Events Using PYTHIA To get a sense for the number of $' g ! ' Q$ events the Tevatron experiments will have to work with, we allow the $' g$ events to undergo parton showering, using PYTHIA [135]. We take the factorization scale to be M_W , and we turn off initial-state radiation in order to focus solely on the evolution of the short-distance gluons; note gluons in initial state radiation are at low p_T and any heavy flavor quarks in their parton showers are rarely tagged. The specific numbers have large uncertainties, perhaps of order 30 percent, but they are only intended to be illustrative.

Channel	1 tag	2 tags
$' g \rightarrow b\bar{b}$	260	47
$' g \rightarrow c\bar{c}$	150	3
$' c$	280	-
$' q(g)$	300	-

Table 3.2.19: Numbers of $' j$ events with one or two tags. The last column is either for light quarks or gluons which do not fragment to heavy quark pairs. We have not tried to estimate the number of double tags for the second two processes.

For 1 fb^{-1} of data, and the generic cuts in Table 3.2.17, there are 24,000 $' g$ events. After showering, these short-distance gluons have fragmented to 620 $b\bar{b}$ pair and 1300 $c\bar{c}$ pairs. Because the b and c quarks from gluon fragmentation have smaller p_T than the original short-distance gluon, it is not obvious how many of these heavy quarks will lead to observable secondary vertices. Indeed a detector simulation would be necessary to estimate this rate. As a crude measure, we have estimated the number of tags per jet by modeling the tagging of each heavy quark parton inside a jet as *independent* of any other nearby heavy quark. While this completely ignores complications from $b \rightarrow c$ decays, and overlapping secondary vertices, it provides some measure of the number of events the Tevatron experiments may have to work with, and has the benefit of being straightforward as an estimate.

Each b parton from gluon fragmentation is tagged at a rate of $0.5 \tanh(p_T/36)$, where p_T is the b quark p_T . Charm quarks are tagged at a rate of $0.15 \tanh(p_T/42)$, and jets originating from light quarks and gluons without heavy quark pairs in them are mis-tagged at a rate of $0.01 \tanh(p_T/80)$.

We have not attempted to investigate the use of the muons from b and c decays, but we believe they should provide additional helpful information with complementary systematic uncertainties. Lepton-tagging of heavy quark jets has already been shown to work in top physics studies in Run II [140]. The event rate for $W + 1j$ production is also sufficiently high to overcome the relatively small branching ratios of $b \rightarrow X$ and $c \rightarrow X$.

We also wish to note that the excellent resolution of the Tevatron silicon trackers in the xy plane may allow measurement of the displacement in the xy plane between two different secondary vertices, as well as their distance from the primary vertex. Thus, an event with two heavy quarks could yield two impact parameters and either an angle or a distance between the two displaced vertices. Fitting to these distributions, using a Monte Carlo to simulate the heavy flavor decays, may well allow unknown parameters in the Monte Carlo description of gluon fragmentation to be pinned down more precisely.

Final Remarks The proposed study of secondary tags in $W + 1j$ events should also usefully supplement the ongoing $Z b$ studies at the Tevatron [141]. Currently, the b PDF is assumed to be zero at the “ b threshold” (4.5 GeV) and is generated by letting QCD evolution equations create it from the gluon PDF at Q_F greater than 4.5 GeV. The uncertainties in the b PDF are then almost completely tied to uncertainties in the gluon distribution. If one further relaxes the assumption of the b PDF being zero exactly at the b threshold, the uncertainties are even bigger. The b PDF can be studied in $Z + 1j$ events with secondary vertex tags [142, 141]. (The $Z + 1j$ study may also have sensitivity to the c PDF; though there are some experimental results from DIS production of charm that place some constraints [143, 144, 145, 146], the

uncertainties are still large.) A background to this study is $Z\gamma$, where the short-distance gluon then splits to heavy flavor. Cross-checking results between $Z+1j$ and $W+1j$ samples should help reduce systematic and statistical uncertainties in our understanding of these processes.

Angular correlations in single-top and $W+jj$

Contributed by: Z. Sullivan

Recent studies of single-top-quark production [147, 126] have emphasized the importance of reducing the $W+jj$ backgrounds. These backgrounds are strongly sensitive to achievable b -tagging efficiencies and jet-energy resolution. New theoretical examinations [148, 51] have shown that only modest improvements in $W+jj$ rejection can be made by improving cuts in pseudorapidity or b -jet assignment. Hence, additional information appears to be required.

It has been demonstrated that a spin correlation between the final-state lepton and non- b jet in single-top-quark production might lead to a useful angular discriminate against the $W+jj$ backgrounds at both the Tevatron [62] and the LHC [149]. These studies relied on leading order (LO) theoretical predictions. This Workshop has motivated a recent paper [64] (summarized here) that provides a next-to-leading order (NLO) confirmation of the LO angular correlations for both the single-top-quark signal and $W+jj$ backgrounds. In addition, sensitivity to top-quark rest-frame reconstruction is quantified, and additional angular correlations are shown to be effective discriminants.

In order to understand angular correlations, it is essential to understand the contribution from spin correlations versus kinematic correlations. Spin correlations in single-top-quark production and decay are a direct result of the electroweak nature of the processes. The matrix elements for both s -channel and t -channel single-top-quark production are proportional to

$$[\bar{p}_d \cdot (\not{p} - m_t \not{s}_t)] [p_e \cdot (\not{p} - m_t \not{s}_t)]; \quad (3.2.25)$$

where p_d and p_e are the four-momenta of the down-type quark and charged lepton in the event, p_t and m_t are the top-quark four-momentum and mass, and s_t is top-quark spin four-vector. In the top-quark rest frame $p_t = m_t(1;0;0;0)$, and $s_t = (0;\hat{s})$.

In Ref. [74], Mahlon and Parke showed that the direction of the down-type quark provides a convenient axis to project the top-quark spin, i.e., choose $\hat{s} = \hat{d}$ as in Fig. 3.2.43. With this choice, the matrix element reduces to $E_d E_e m_t^2 (1 + \cos \theta_{e^+d}^t)$. Since roughly 98% of the events at the Fermilab Tevatron are produced by pulling a d from the incoming antiproton, measuring $\cos \theta_{e^+p}^t$ provides the best possible measure of the spin correlation for s -channel production.

The only complication for s -channel production is reconstruction of the top-quark rest frame. Degeneracies in the measured neutrino momentum, and assignment of the b -jet to top-quark decay, degrade top-quark reconstruction. These kinematic effects soften the measurable angular correlations, as seen in the center plot of Fig. 3.2.44. However, the LO and NLO distributions agree exactly after top reconstruction up to an NLO K -factor. This has been confirmed in the fully correlated phase space, so Monte Carlo simulations can reliably predict these angles.

Angular correlations in t -channel single-top-quark production are more complicated. The d quark ends up in the highest- E_t non- b -tagged jet j_1 approximately $3/4$ of the time at the Tevatron. The other

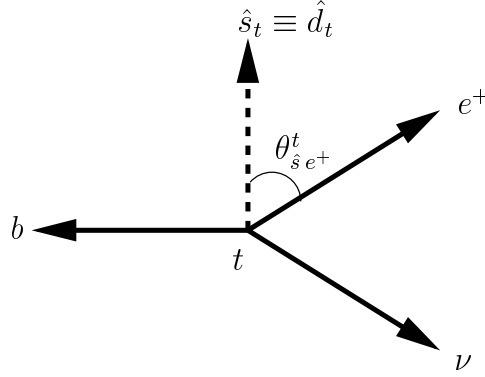


Fig. 3.2.43: Decay products of the top quark, and the angle $\theta_{\hat{s}_t e^+}^t$ between the charged lepton e^+ and the spin \hat{s}_t of the top quark in the top-quark rest frame. The spin is projected in the direction of the down-type quark d in the event.

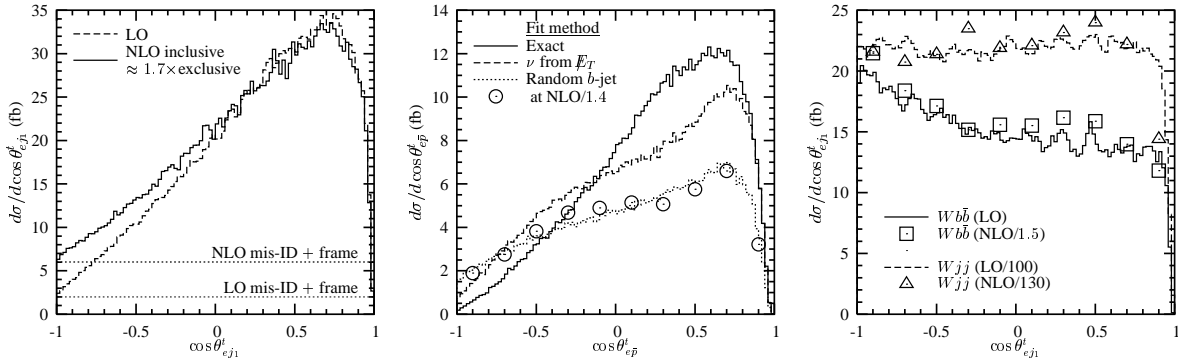


Fig. 3.2.44: Cosine of angle ($\cos \theta_{e^+ j_1}^t$) between the charged lepton and the highest- E_T light-quark jet in the top-quark rest frame for (left) t -channel single-top-quark production, and (right) $W jj$ production at the Tevatron. (Center) cosine of angle between the lepton and antiproton for s -channel single-top-quark production.

1=4 of the time a d -quark is in the initial state, and a perfect correlation exists with the incoming hadron (mostly the antiproton at the Tevatron). This adds a dilution factor, so that the matrix element is proportional to $(1 + \cos \theta_{d j_1}^t \cos \theta_{e^+ j_1}^t)$. The dilution factor $\cos \theta_{d j_1}^t = 1 - Q^2/(E_d^t E_{j_1}^t)$ is typically around 0.3, because the t -channel exchange of the W boson pushes j_1 forward toward the beam line. Hence, $\cos \theta_{e^+ j_1}^t$ is a good quantity to measure because of a combination of spin and kinematic correlations.

A complication in t -channel production is that additional initial-state radiation can occasionally be misconstrued as the hard forward jet in the event. Since this additional radiation is uncorrelated with the final-state lepton, it slightly flattens the distribution in Fig. 3.2.44. However, it has been shown [52] that LO Monte Carlos can be properly matched to NLO distributions. Using matched distributions, the softening of the correlation is seen to come solely from the misidentification of which jet contained the down-type quark. Spin-dependent matched distributions reliably predict the fully correlated angular correlations.

The analytic form of the correlations for s - and t -channel production at the LHC is the same as at the Tevatron. However, there is one striking difference in t -channel production. Because the LHC is a pp collider, t production comes almost entirely from a valence u quark in the initial state, while t

production comes mostly from valence a d quark in the initial state. This means that the spin correlation for τ production is almost 100% with the light jet j_1 , but for t production it is almost 100% with the beam axis.

An additional complication for τ production is determining which proton the d quark came from. The correlation suggests that a good choice for reconstruction is the proton remnant closest to the charged lepton, i.e., for $e^+ > 0$ use $P_p = \overline{P}^p(1;0;0; -1)=2$. Despite the fact that the best correlation is with the proton, the light jet tends to be very forward, and hence the dilution factor for using the Mahlon-Parke basis is close to 1. Early studies of fully-reconstructed events using the ATLAS detector simulation show that the single-top-quark and $W jj$ angular correlations are very similar to those at the Tevatron [150]. Further, it appears that the Mahlon-Parke basis works equally well for both τ and t production at the LHC.

The purpose of studying angular correlations is to find cuts to reduce the $W jj$ backgrounds. As seen in Fig. 3.2.44, the two general classes $W jj$ backgrounds are found to be well-represented by a LO calculation plus an NLO K -factor. This has been confirmed in the fully correlated angular distributions as well. In Fig. 3.2.45, the correlation between $\cos \theta_{e j_1}^t$ and $\cos \theta_{b j_1}^t$ demonstrates the power of using angular information. The flat distribution in $\cos \theta_{e j_1}^t$ for $W jj$ is seen to be an artifact of integrating over two broad peaks in the correlated phase space. A simple cut, such as $\cos \theta_{e j_1}^t > \cos \theta_{b j_1}^t$, can remove roughly 1=2 of the background with little signal loss in either single-top channel.

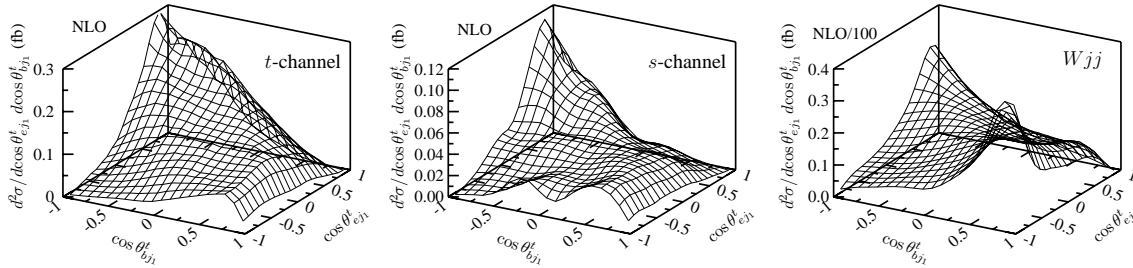


Fig. 3.2.45: Correlated angular distributions of the final-state particles in the top-quark rest frame of NLO (left) t -channel and (center) s -channel single-top-quark production, and (right) NLO $W jj$ production. This is a two-dimensional projection between $\cos \theta_{e j_1}^t$, where e is the charged lepton and j_1 is tagged as the highest- E_T light-quark jet, and $\cos \theta_{b j_1}^t$, where b is the b jet from the top-quark decay.

The signal in Fig. 3.2.45 peaks in one corner due to an additional angular correlation not used in previous analyses. In the real top-quark rest frame the b jet recoils against the W , and hence the charged lepton in the event. The strong spin correlation between the lepton and light jet j_1 leads to an almost degenerate phase space for single-top-quark production, with the b jet recoiling against the lepton- j_1 system. The angle between the b and j_1 is further enlarged, because the initial production mode is a two-body state with the top-quark recoiling against the light jet. The b picks up some of the top-quark's momentum, and the combination of kinematic boost and spin correlation pushes the jets far apart.

The large angle between the b and the charged lepton leads to the possibility of using $\cos \theta_{e j_1}^t$ as a way to choose which jet came from top decay. This is useful for s -channel production where it is not clear which b -jet to assign. The following procedure picks the correct assignment better than 80% of the time, and effectively removes the b -assignment uncertainty:

1. Construct two candidate top-quarks from the two highest- E_T jets j_i .
2. Call the b -jet from top decay the one with the smallest $\cos \theta_{e j_i}^t$ in its own candidate top-quark rest frame.

This is effectively equivalent to making the cut $\cos \theta_{eb}^t < \cos \theta_{e j_1}^t$ on the correlated angular distributions. The $W jj$ background is very close to flat in the plane of these two angles, and this cut will reduce the background by another factor of two. This sort of cut emphasizes the importance of having complete and accurate angular correlations, since it will cause the supposedly flat $W jj$ distribution $\cos \theta_{e j_1}^t$ in Fig. 3.2.44 to look exactly like the signal in that projection. Fortunately, the fully correlated distributions maintain the distinction.

Another useful distribution that arises from the large $\cos \theta_{b j_1}^t$ angle is the dijet mass. The dijet mass for the signal is pushed to large values, because the initial E_{Tj} tends to be large, and the jets are roughly back-to-back. This in contrast with the $W jj$ backgrounds, in which the momentum is roughly split between the W boson and the two jets, and leads to a softer dijet mass. Significant improvements in signal to background can be made by adding a minimum dijet mass cut of order 100 GeV.

Use of the fully correlated angular distributions will require detailed simulations of fully reconstructed events. Early indications from LHC are that the angular distributions are barely disturbed by detector effects [150]. This is not surprising from a quark-jet duality point of view, but it is less clear what the ultimate sensitivity to top-quark rest-frame reconstruction will be. Many new physics analyses will require complex cuts on phase space to separate signal from background. Single-top-quark production at the Tevatron presents an important opportunity to confirm that the NLO matched samples and full correlated angular distributions agree with real data.

The “Best Variables” Method and Implementation of Neural Networks in Physics Analysis

Contributed by: E.E. Boos, V.E. Bunichev, L.V. Dudko, A.A. Markina

The Basic Idea In High Energy physics a discrimination between a signal and corresponding backgrounds is especially important when the data statistics are limited or the signal to background ratio is small. In this case it is important to optimize all steps of the analysis. One of the main questions which arises in a physics analysis is which, and how many variables should be chosen in order to extract a signal from the backgrounds in an optimal way. The general problem is rather complicated and finding a solution depends on having a concrete process for making the choice, because usually it takes a lot of time to compare results from different sets of variables.

One observation which helps in making the best choice of the most sensitive variables is to study the structure of Feynman diagrams which contribute to the signal and background processes. Based on such analysis we can distinguish three classes of variables which are potentially most sensitive to the differences in signal and background processes.

The first class of variables is based on the analysis of singularities which usually appear in physics processes. Let us call those kinematic variables in which singularities occur as “singular variables”. What is important to stress here is that most of the rates for both the signal and the backgrounds come from the integration over the phase space region close to these singularities. One can compare the lists of

singular variables and the positions of the corresponding singularities in Feynman diagrams for the signal process and for the backgrounds. If some of the singular variables are different or the positions of the singularities are different for the same variable for the signal and for the backgrounds the corresponding distributions will differ most strongly. Therefore, if one uses all such singular variables in the analysis, then the largest part of the phase space where the signal and backgrounds differ most will be taken into account. One might think that it is not a simple task to list all the singular variables when the phase space is very complex, for instance, for reactions with many particles involved. However, in general, all singular variables can be of only two types, either s-channel:

$$M_{f_1, f_2}^2 = (p_{f_1} + p_{f_2})^2;$$

where p_{f_1} and p_{f_2} are the four momenta of the final particles f_1 and f_2 , or t-channel:

$$\hat{t}_{i, f} = (p_f - p_i)^2;$$

where p_f and p_i are the momenta of the final particle (or cluster) and the initial parton. For the $\hat{t}_{i, f}$ all the needed variables can be easily found in the massless case: $\hat{t}_{i, f} = \hat{s} e^{-Y} p_T^f e^{-j}$, where \hat{s} is the total invariant mass of the produced system, and Y is the rapidity of the total system (rapidity of the center mass of the colliding partons), p_T^f and Y_f are transverse momenta and pseudorapidity of the final particle f . The idea of using singular variables as the most discriminative ones is described in [80] and the corresponding method was demonstrated in practice in [151], [152], [153].

Singular variables correspond to the structure of the denominators of Feynman diagrams. Another type of interesting variables corresponds to the numerators of Feynman diagrams and reflects the spin effects and the corresponding difference in angular distributions of the final particles. In order to discriminate between a signal and the backgrounds, one should choose in addition to singular variables mentioned above those angular variables whose distributions are different for the signal and backgrounds. The set of these singular and angular variables will be the most efficient set for a Neural Network (NN) analysis.

The third type of useful variables which we call "Threshold" variables are related to the fact that various signal and background processes may have very different thresholds. Therefore the distributions over such kind of variables also could be very different keeping in mind that effective parton luminosities depend strongly on \hat{s} . The variable \hat{s} would be a very efficient variable of that kind. However, the problem is that in case of neutrinos in the final state one can not measure \hat{s} and should use the effective \hat{s} which is reconstructed by solving t, W-mass equations for the neutrino longitudinal momenta. That is why we propose to use not only the effective variable \hat{s} but different H_T variables as well.

To apply the method it is important to use a proper Monte-Carlo model of signal and background events which includes all needed spin correlations between production and decays. We illustrate the method by considering single top quark production at hadron colliders, the Tevatron and the LHC. The complete recipe how to model the single top production processes with NLO precision is described in the section 3.2. Comparing to a parton level analysis the detector smearing generically smooth out the distributions, and makes possible separation worse. However, kinematic properties of the processes basically remain the same after smearing, and no any new kinematic differences between a signal and backgrounds appear after smearing which could help in signal and background separation.

Demonstration of the Method Implementation of the above method in real analysis can be found in the papers describing Single Top quark search in D0 (Run I and Run II) [154], [155], [126], [156],[157] and CMS (to be published in CMS Physics Technical Design Report). In this section, we demonstrate how the above method works in case of the mostly simple single top quark production process, the s -channel production ($p p \rightarrow b + X$), and one of the main background processes ($p p \rightarrow W jj + X$) at the Tevatron. Typical Feynman diagrams for these signal and background processes are shown in the Fig. 3.2.46. As explained in the previous section, one should compare the singularities for the signal and background diagrams. The signal diagram Fig. 3.2.46 (1.1) has only one singularity, a pole at the mass of the top quark:

$$M_t^2 = (p_b + p_W)^2 \neq m_t^2;$$

(The pole for the W -boson decay is the same for the signal and for the background, and therefore the corresponding variable is not a sensitive variable here.) There are two singularities in the first background diagram Fig. 3.2.46 (2.1):

$$M_{g_1 g_2}^2 = (p_{g_1} + p_{g_2})^2 \neq 0;$$

$$\hat{t}_{u;(g_1 g_2)} = (p_{g_1} + p_{g_2} - p_u)^2 \neq 0;$$

corresponding to underlying soft and collinear singularities when additional partons become soft or coincident in direction.

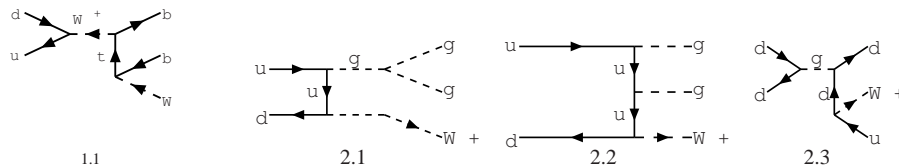


Fig. 3.2.46: Typical Feynman diagrams for the $W jj$ processes.

In diagram Fig. 3.2.46 (2.2) there are three singularities, but one ($\hat{t}_{u;(g_1 g_2)}$) is the same as in the first diagram:

$$\hat{t}_{u;g_1} = (p_{g_1} - p_u)^2 \neq 0;$$

$$\hat{t}_{u;g_2} = (p_{g_2} - p_u)^2 \neq 0;$$

$$\hat{t}_{u;(g_1 g_2)} = (p_{g_1} + p_{g_2} - p_u)^2 \neq 0;$$

We construct a complete set of singular variables using relations from the previous section and compare physics analysis using such a set of variables with analysis based on more simple often used set variables. For the comparison of different sets of variables we take the neural network (NN) technique as one of the most popular and efficient methods of signal and background separation. The efficiency criteria for different sets is the standard training parameter "Training Error function":

$$\chi^2 = \frac{1}{N_{\text{test}}} \sum_{i=1}^{N_{\text{test}}} (d_i - q_i)^2; \quad (3.2.26)$$

In the formula N_{test} is the number of test patterns, d_i is the desired NN output (1 for the signal and 0 for background), and o_i is the NN output. The lowest training χ^2 has led to best separation of signal and background by the constructed NN. Compare the χ^2 for different sets of input variables we can conclude which set of variables is more efficient.

The processes under consideration have been calculated using CompHEP [129] at the parton level, then decayed and processed with PYTHIA [131] in order to include initial-state and final-state radiation, and to fragment the final state partons into jets. Detector smearing of the jet energies has been included in our model by means of the SHW [158] program. For the NN training we use JETNET package [159].

The first set of variables consists of the complete set of singular variables for the $W + \text{jets}$ and s -channel signal processes:

$$\text{Set1} : M_{j1j2}; M_{\text{top}}; \hat{s}; Y_{\text{tot}}; P_{Tj1}; Y_{j1}; P_{Tj2}; Y_{j2}; P_{Tj12}; Y_{j12}$$

where Y_{tot} is the total rapidity of the center of mass of the initial partons reconstructed from the final state particles, using the reconstructed neutrino momentum via equation $M_W^2 = (p + p_{\text{lepton}})^2$. Next one is a simpler set:

$$\text{Set2} : P_{Tj1}; P_{Tj2}; H_{\text{all}}; H_{T\text{all}}$$

Here $H_{\text{all}} = \sum P_{E_f}$, and $H_{T\text{all}} = \sum P_{Tf}$, where the sums are over all final-state particles and jets.

The third set includes one singular variable (M_{top}) in the previous set:

$$\text{Set3} : P_{Tj1}; P_{Tj2}; H_{\text{all}}; H_{T\text{all}}; M_{\text{top}}$$

The results for the χ^2 are shown in Fig. 3.2.47 (Ncycle is the number of the Neural Net training cycles, it is proportional to the training time). The best network is defined as the one with lowest χ^2 , because the output from such a network is closer to the desired output. From this plot, one can see that the χ^2 for Set 1 of singular variables is lower then for the other two described above, and therefore the corresponding NN is better analysis tool.

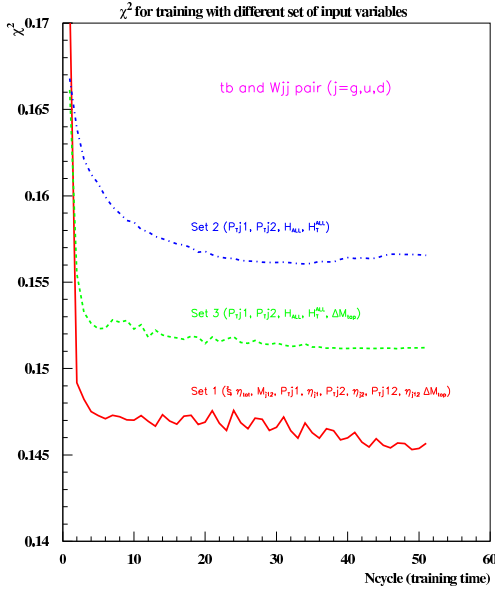


Fig. 3.2.47: Improvement of NN training for different sets of input variables.

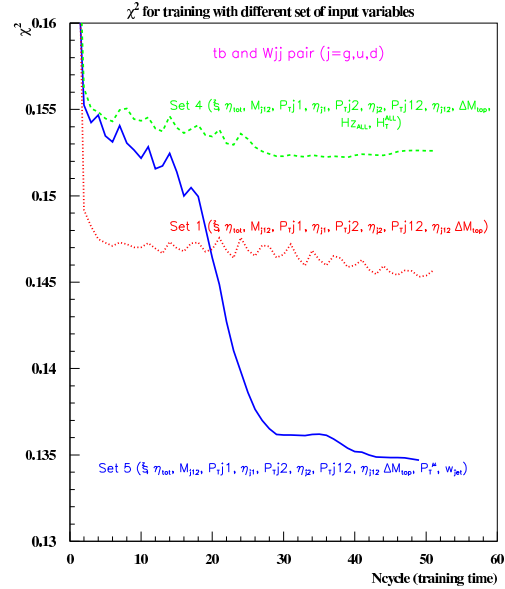


Fig. 3.2.48: Improvement of NN training for different sets of input variables.

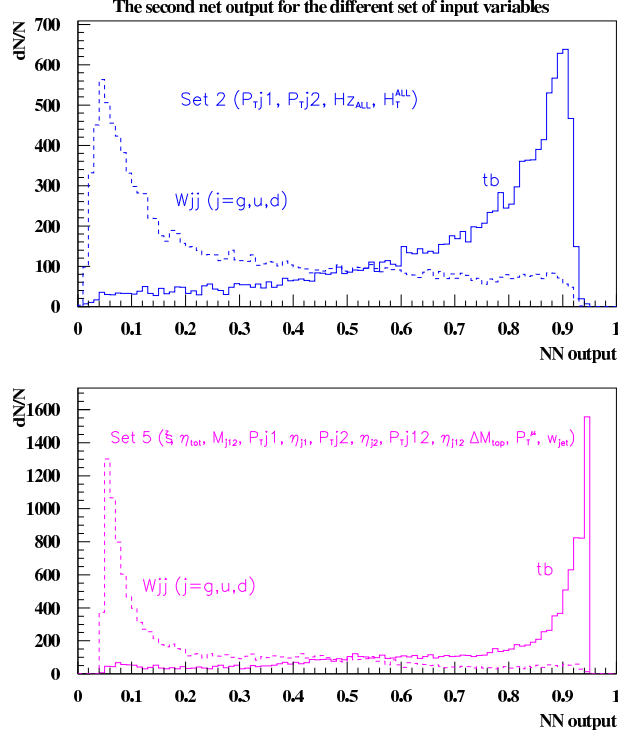


Fig. 3.2.49: Output of Neural Networks trained on the Set 2 and Set 5 of sensitive variables.

We tried to check the Set 1 for completeness by adding more kinematic variables, to see if there would be any improvement. We added the scalar sum of the final particles energy H_{all} , and the scalar sum of their transverse energy $H_{T\text{all}}$, and called this Set 4. We see that the χ^2 gets worse relative to Set 1 of the original network. This means that the additional kinematic variables do not add sufficient information to counter the increase in the number of degrees. But nevertheless, we can still search for other possible variables that contain information that will be useful for separating signal from background. In our case, where the signal is single-top quark production, we have a different probability for reconstructing a tagging muon in a jet from b decay than for misidentifying of a γ -tagged light jet as a b jet. In fact, the NN method can be regarded in some sense as a way of b -tagging. We introduce this information into the NN through the transverse momentum of the tagging muon, $p_T^{(\text{tag})}$, which is set to zero for untagged events. In addition, we include two more useful variables, the width (w_{jet}) of two jets with highest E_T . The final set of variables is Set 1 together with the three additional variables:

$$\text{Set5} : \text{Set1} + p_T^{\text{tag}} ; w_{\text{jet1}} ; w_{\text{jet2}}$$

The χ^2 for this final set is shown in Fig 3.2.48. The comparison of NN outputs for the Set 2 and Set 5 is shown in the Fig. 3.2.49. It is the lowest on the plot, therefore we can choose this set of variables for the analysis and get serious improvement in comparison with the simple Set 2.

It is possible to get further improvement, if we add the angular variables which we mentioned as the second class of sensitive variables. The necessary information on this type of variables can be found in the papers [75], [160], [64] (and references therein).

Implementation of Neural Network Technique in Physics Analysis Neural networks widely used in different fields of science and technology. The main advantages of this method are the following: with this method it is possible to analyze large number of sensitive variables; it takes into account non-linear correlations in the analysis space; it is universal and can be applied in the same way for different tasks. Based on the experience of single top search in D0 at the Run I and Run II analysis, we summarize shortly, how to apply NN technique for extracting a signal from the backgrounds. At the D0 Run I single top search analysis this method of NN implementation provided in 2 times better physics result than the classical analysis method.

We use the simple and most efficient in our case NN which we can teach (train) with a set of known examples – feedforward NN with supervised training. In this case, the first step in the analysis is to prepare the correct model of the signal and background events. This step was described in the section 3.2. At the next step, we need to prepare the set of variables which mostly reflect the difference in signal and background properties, this step is described in the previous sections (3.2). For the NN training we have to use only the variables which were simulated properly in the model and exclude the variables which distributions are different when we compare the complete model (signal and background) and real DATA (if it is available).

There are several background processes for the single top production. The kinematic properties for some of the backgrounds are significantly different. For example, QCD $W + \text{jets}$ production and $t\bar{t}$ production processes have different singularities, spin correlations and energy thresholds. In such a case it is more efficient to train different networks with different set of input variables for each background process. The same difference we can see for the signal processes. For the single top production we distinguish three signal processes (t -channel, s -channel and $t\bar{t}W$ production), each of them require a special approach and has unique properties which can help to extract it from the backgrounds. Therefore, the most effective separation of signal and background processes we can get by the set of NNs where each network is trained to recognize only one pair: one of the signal and one of the background processes. For the single top analysis we have three signal processes and five main background processes, in this case the most effective separation we can get by the set of fifteen NNs. It is not trivial to analyze fifteen outputs of NN and usually people can use some additional method to combine the network outputs and get the simple discriminator of the events. The reasonable method is to combine these NN outputs to additional NN (we call it Super NN) with five inputs (outputs of initial NN, each signal process consider separately) and one output. Such a network should be trained on the complete set of background processes which are mixed or weighted proportional by its contribution to the total background. As a result we will have three Super NN – each one for every signal process.

The further optimization of NN inputs is possible with the standard recommendations for the NN training. The first recommendation is to normalize input variables to the same region $[0;1]$ or $[-1;1]$. The second recommendation is to use logarithmic scale for the variables with a long tail in distribution.

The next step in the NN analysis is to find the most effective architecture of the NN and set of the training parameters. The criteria of χ^2 (equation 3.2.26) can help to find the optimal number of hidden nodes and set of training parameters. The optimal number of hidden nodes usually is within the region $[n; 2n + 1]$ where n is the number of input variables. One hidden layer is usually the proper choice for most of the tasks in HEP.

To avoid an overfitting problem one can use the standard solution and split the samples for the

training and testing parts, then train the NNs on the training events and check the χ^2 (equation 3.2.26) for the testing events. Additional check for the trained networks can be performed by the comparison of NN output distributions for the simulated events and real DATA. If the distributions are not the same we can conclude that the NNs were overfitted or we do not model properly some input variables. After these checks the NNs are ready to calculate the expected number of signal and background events from the model and count the events which are passed the NN filters from the DATA flow.

A detailed description of the Neural Network analysis of single top quark production at D0 can be found in the papers [151]-[157].

ACKNOWLEDGEMENTS The work is partly supported by RFBR 04-02-16476, RFBR 04-02-17448, Universities of Russia UR.02.02.503, and Russian Ministry of Education and Science NS.1685.2003.2 grants.

3.3 Tevatron Single Top Quark Searches

Physics goals

Contributed by: Schwienhorst

The main goal for the Tevatron experiments is to observe electroweak production of single top quarks for the first time. The focus of current searches is observing any single top quark production, including both the s -channel and t -channel modes. Once the production of single top quarks has been observed, the emphasis shifts to measurements of top quark properties and the $t\bar{t}W$ b coupling. The initial observation will serve as a measurement of the production cross section as well as the CKM matrix element V_{tb} , thus providing a test of CKM matrix unitarity. The initial samples of single top quark events can also be used to measure top quark properties such as top quark spin correlations. With further increasing datasets, emphasis will be on separating s -channel from t -channel production in order to probe details of the $t\bar{t}W$ b coupling.

The single top quark final state is also sensitive to models of new physics. Stringent limits on several different models can be set even before an actual observation of single top quark production.

Experimental signal signature

Contributed by: Garcia-Bellido

The two main production modes at the Tevatron are the t - and s -channel processes, shown in Fig.3.2.15 (a) and (b), respectively. The final state signature is thus characterized by a high energy isolated lepton and missing transverse energy from the decay of the W from the top quark into $l\nu$, and two or three jets. One of the jets originates from a b quark from the top quark decay and is usually central (low pseudorapidities) and energetic. In the s -channel, the other energetic jet is also from a b quark, and shares similar kinematics with the b from the top. Thus b quark identification, or b tagging, in the s -channel is equally likely between the b from the top quark decay and the b from the original interaction. In the t -channel there usually is, apart from the b jet from top quark decay, a moderately energetic light flavor jet and a high pseudorapidity low energy b quark jet from gluon splitting. This very forward or backward b jet is a unique feature of this signal, but it is rarely reconstructed and even more difficult to tag.

At the Tevatron the final state is CP invariant, thus equal numbers of top and anti-top quarks are produced.

Backgrounds

Contributed by: Garcia-Bellido

The main processes that can mimic the final state topology arising from single top quark production are: (i) W +jets events, where the W boson decays semileptonically and two or more associated jets are produced; (ii) $t\bar{t}$ events, where one or both top quarks decay leptonically; and (iii) QCD or multijet events.

The W +jets background is by far the most problematic to get rid of at the Tevatron. It consists of a leptonically decaying W boson and at least two associated quarks or gluons. W +jets events contain less energy in the event than the single top quark signals since they do not contain a heavy object like the top quark. But the cross section is very large in comparison to single top quarks, and the flavor composition of the associated jets is sufficiently complex, to make this background hard to model and even harder to get rid of as one applies b -tagging techniques, since they tend to shift distributions to be more signal-like and wash away any low energy features. This background has been estimated using simulated events, by ALPGEN for example, and is usually scaled to data to get the overall normalization right.

Top pair production has a cross section around twice as big as single top quark production. But the average energy in the event is larger, due to the presence of two top quarks, and events tend to be more spherical and have more jet multiplicity than single top quark events. The two top quarks produce two W bosons and two b -jets, the latter with very similar kinematics to the signal and therefore likely to be b -tagged as well. The same final state signature as in single top quark processes is obtained if only one of the W bosons decay leptonically and the other hadronically, or if both do, but only one lepton is reconstructed. This background can be properly simulated using ALPGEN or PYTHIA.

The QCD background typically enters as misreconstructed events, where a jet is wrongly identified as an electron, or a muon from a heavy flavor jet appears isolated in the detector. Multijet events may also contain heavy flavor jets or just light jets that are misidentified by the b -tagging algorithms. The transverse energy of QCD events is much less than signal events, and the mass of the system of the b -tagged jet, the lepton and the neutrino does not peak at m_{τ} , but the cross section is overwhelmingly large. This background is usually obtained directly from data, and after some initial basic criteria can be reduced in size to the same level as the signal.

Description of the $D\bar{O}$ search for single top quarks

Contributed by: Jain

This section describes the search for single top quarks in the s -channel and t -channel modes, using the $D\bar{O}$ detector [161] at the Tevatron. The data was recorded with a lepton+jets trigger, where the lepton is either an electron or a muon. The integrated luminosity was 226 pb^{-1} for the electron channel and 229 pb^{-1} for the muon channel. We perform a cut-based analysis using kinematic variables that discriminate between signal and background, and a multi-variate analysis using neural networks. We observe no significant deviation in data [126] from the Standard Model prediction, and hence, set upper limits at 95% CL, on the single top production cross section, in the s -channel and t -channel modes, of 10.6 pb and 11.3 pb , respectively, in the cut-based analysis, and 6.4 pb and 5.0 pb , respectively, in the neural network analysis.

Initial Event Selection and Yields We apply a loose initial selection in order to maximize the acceptance for the single-top quark signal while rejecting the W +jets and misreconstructed events. In the electron channel, we require exactly one isolated electron with the transverse momentum, $p_T > 15 \text{ GeV}$, and the detector pseudorapidity, $|j_{\text{det}}| < 1.1$. In the muon channel, events are selected by requiring exactly one isolated muon with $p_T > 15 \text{ GeV}$ and $|j_{\text{det}}| < 2.0$. For both channels, events are also required to have $E_T > 15 \text{ GeV}$, and between two to four jets, with the jet $p_T > 15 \text{ GeV}$ and $|j_{\text{det}}| < 3.4$. The

leading jet is required to be more central ($j_{\text{det}} < 2.5$), and have $p_T > 25$ GeV. Jets are defined using a cone algorithm with radius $R = 0.5$. In addition, misreconstructed events which are difficult to model, are rejected by requiring that the direction of \vec{E}_T is not aligned or anti-aligned in azimuth (ϕ) with the lepton or the jets. This selection has a negligible effect on the efficiency of signal events.

The fraction of signal-like events is further enhanced through the selection of b -quark jets that are identified by a secondary vertex tagging algorithm, that reconstructs displaced vertices from long-lived particles. In the τ -channel search, we additionally require that one of the jets is not b tagged, to account for the light flavor jet from the original interaction.

For both s -channel and τ -channel searches, we separate the data into independent analysis channels based on the final-state lepton flavor (electron or muon) and the b -tag multiplicity ($=1$ tag or $=2$ tags) to take advantage of the different final state topologies. In each channel, we find that the expected yield for the single top quark signal is small compared to the overwhelming backgrounds. We, therefore, use additional kinematic variables that allow us to discriminate between signal and background. The number of events for each signal, background, and data after the initial event selection are shown in Table 3.3.20 for the combined electron, muon, single-tagged, and double-tagged analysis sets.

Source	s -channel search	τ -channel search
$t\bar{b}$	5.5 1.2	4.7 1.0
$t\bar{q}b$	8.6 1.9	8.5 1.9
W +jets	169.1 19.2	163.9 17.8
$t\bar{t}$	78.3 17.6	75.9 17.0
Multijet	31.4 3.3	31.3 3.2
Total background	287.4 31.4	275.8 31.5
Observed events	283	271

Table 3.3.20: Estimates for signal and background yields, and the number of observed events in data after initial event selection for the combined electron, muon, single-tagged, and double-tagged analysis sets. The W +jets yields include the diboson backgrounds. The total background for the s -channel (τ -channel) search includes the $t\bar{q}b$ ($t\bar{b}$) yield. The quoted yield uncertainties include systematic uncertainties taking into account correlations between the different analysis channels and samples.

Discriminating Variables The variables that discriminate between the signal top quark signal and backgrounds were chosen based on an analysis of Feynman diagrams of these processes [162], and on a study of single top quark production at NLO [51, 58]. The variables fall into three categories: individual object kinematics, global event kinematics, and variables based on angular correlations. The list of variables is shown in Table 3.3.21. Figure 3.3.50 shows distributions of a few representative variables comparing the single top quark signal to the sum of backgrounds, and the data.

Cut-Based Analysis Here, we start from the list of discriminating variables, choose the best subsets, and find the optimal cuts [126] on each variable therein, by maximizing the signal to background ratio, and improving the expected cross section limits. (We define expected limits as the limit obtained if the observed counts were equal to the background prediction). The cuts scanned for the optimization

Variable	Description	Signal-Background Pairs			
		tb		t q b	
		W bb	tt	W bb	tt
Individual object kinematics					
$p_T(\text{jet1}_{\text{tagged}})$	Transverse momentum of the leading tagged jet	p	p	p	—
$p_T(\text{jet1}_{\text{untagged}})$	Transverse momentum of the leading untagged jet	—	—	p	p
$p_T(\text{jet2}_{\text{untagged}})$	Transverse momentum of the second untagged jet	—	—	—	p
$p_T(\text{jet1}_{\text{non-best}})$	Transverse momentum of the leading non-best jet	p	p	—	—
$p_T(\text{jet2}_{\text{non-best}})$	Transverse momentum of the second non-best jet	p	p	—	—
Global event kinematics					
$\frac{p}{s}$	Invariant mass of all final state objects	p	—	p	p
$p_T(\text{jet1}; \text{jet2})$	Transverse momentum of the two leading jets	p	—	p	—
$M_T(\text{jet1}; \text{jet2})$	Transverse mass of the two leading jets	p	—	—	—
$M(\text{alljets})$	Invariant mass of all jets	p	p	p	p
$H_T(\text{alljets})$	Sum of the transverse energies of all jets	—	—	p	—
$p_T(\text{alljets} - \text{jet1}_{\text{tagged}})$	Transverse momentum of all jets excluding the leading tagged jet	—	p	—	p
$M(\text{alljets} - \text{jet1}_{\text{tagged}})$	Invariant mass of all jets excluding the leading tagged jet	—	—	—	p
$H(\text{alljets} - \text{jet1}_{\text{tagged}})$	Sum of the energies of all jets excluding the leading tagged jet	—	p	—	p
$H_T(\text{alljets} - \text{jet1}_{\text{tagged}})$	Sum of the transverse energies of all jets excluding the leading tagged jet	—	—	—	p
$M(W; \text{jet1}_{\text{tagged}})$	Invariant mass of the reconstructed top quark using the leading tagged jet	p	p	p	p
$M(\text{alljets} - \text{jet}_{\text{best}})$	Invariant mass of all jets excluding the best jet	—	p	—	—
$H(\text{alljets} - \text{jet}_{\text{best}})$	Sum of the energies of all jets excluding the best jet	—	p	—	—
$H_T(\text{alljets} - \text{jet}_{\text{best}})$	Sum of the transverse energies of all jets excluding the best jet	—	p	—	—
$M(W; \text{jet}_{\text{best}})$	Invariant mass of the reconstructed top quark using the best jet	p	—	—	—
Angular variables					
$(\text{jet1}_{\text{untagged}})_{Q \cdot}$	Pseudorapidity of the leading untagged jet lepton charge	—	—	p	p
$R(\text{jet1}; \text{jet2})$	Angular separation between the leading two jets	p	—	p	—
$\cos(\cdot; \text{jet1}_{\text{untagged}})_{\text{top}_{\text{tagged}}}$	Top quark spin correlation in the optimal basis for the t-channel [106, 107, 74], reconstructing the top quark with the leading tagged jet	—	—	p	—
$\cos(\cdot; Q \cdot z)_{\text{top}_{\text{best}}}$	Top quark spin correlation in the optimal basis for the s-channel [106, 107, 74], reconstructing the top quark with the best jet	p	—	—	—
$\cos(\text{alljets}; \text{jet1}_{\text{tagged}})_{\text{alljets}}$	Cosine of the angle between the leading tagged jet and the alljets system in the alljets rest frame	—	—	p	p
$\cos(\text{alljets}; \text{jet}_{\text{non-best}})_{\text{alljets}}$	Cosine of the angle between the leading non-best jet and the alljets system in the alljets rest frame	—	p	—	—

Table 3.3.21: List of discriminating variables. A tick mark in the final four columns indicates in which signal-background pair of the Neural Net analysis the variable is used. A best-jet is defined as the jet in each event for which the invariant mass of the system of reconstructed W boson and jet is closest to 175 GeV. Jets that have not been identified by the b tagging algorithm are called “untagged” jets.

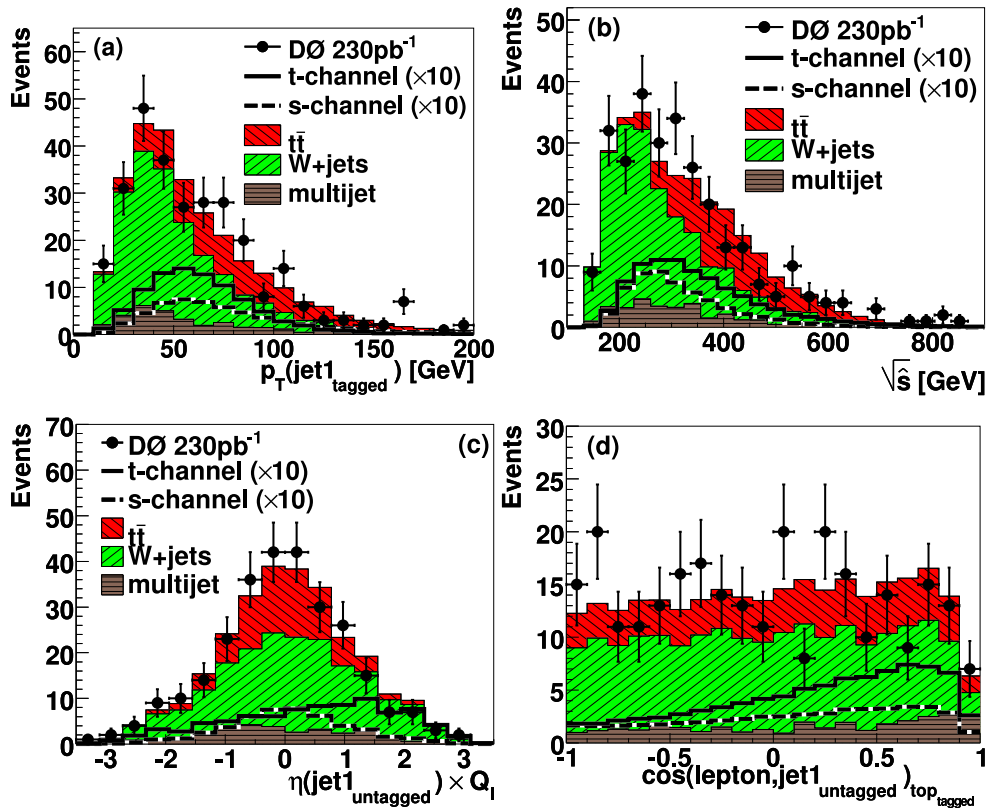


Fig. 3.3.50: Comparison of signal, background, and data for the combined electron, muon, single-tagged, and double-tagged analysis sets for representative discriminating variables. Shown are (a) the transverse momentum of the leading tagged jet, (b) the invariant mass of all final state objects, (c) the pseudorapidity of the leading untagged jet multiplied by the lepton charge, (d) the top quark spin correlation in the optimal basis for the t -channel. Signals are multiplied by ten.

are determined by the value of the respective variables in the signal Monte Carlo events, following the approach described in [163].

The event yields for each signal, background, and data, after the optimized cuts are shown in Table 3.3.22, for the combined electron, muon, single-tagged, and double-tagged analysis sets.

Neural Network Analysis Here, we combine the discriminating variables and perform a multi-variate analysis. We use the MLPFIT [164] neural network package. We choose to create networks for each search (s -channel and t -channel mode) by training on the single top quark signal against the two dominant backgrounds: W +jets and $t\bar{t}$. For W +jets, we train using a W $b\bar{b}$ Monte Carlo sample as this process best represents all W +jets processes. For $t\bar{t}$, we train on $t\bar{t}$ +jets which is dominant over the dilepton background.

Figure 3.3.51 shows the outputs of the neural networks for the data and the expected backgrounds, as well as the signals for the combined electron, muon, single-tagged, and double-tagged analysis sets. We see that the $t\bar{t}$ networks separate signal and $t\bar{t}$ backgrounds efficiently. The W $b\bar{b}$ networks are less efficient for the W +jets backgrounds because the event kinematics are similar between signal and

Source	s -channel search	t -channel search
$t\bar{b}$	4.5	3.2
$t\bar{q}b$	5.5	7.0
W +jets	102.9	72.6
$t\bar{t}$	27.6	55.9
Multijet	17.2	17.0
Total background	153.1	148.7
Observed events	152	148

Table 3.3.22: Signal and background yields, and the numbers of observed events in data, after selections in the cut-based analysis, for the combined electron, muon, single-tagged, and double-tagged analysis sets. The W +jets yields include the diboson backgrounds. The total background for the s -channel (t -channel) search includes the $t\bar{q}b$ ($t\bar{b}$) yield.

background.

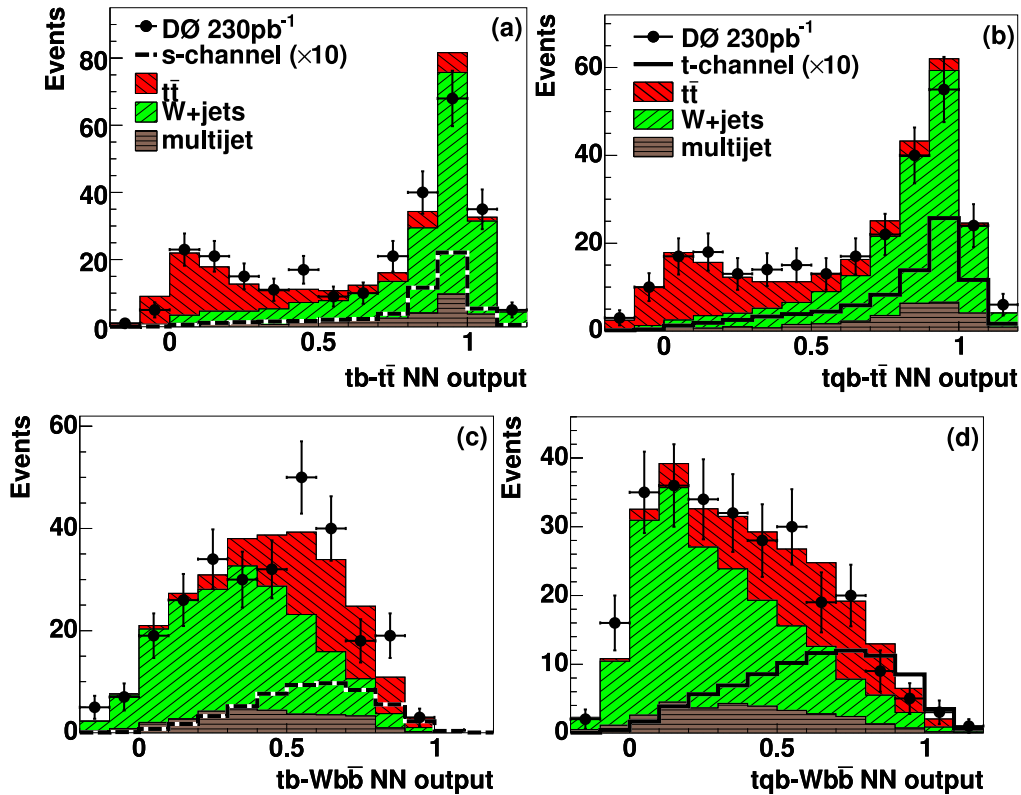


Fig. 3.3.51: Comparison of signal, background, and data for the neural network outputs, for the combined electron, muon, single-tagged, and double-tagged analysis sets. Shown are the outputs for (a) the $t\bar{b}$ - $t\bar{t}$ filter, (b) the $t\bar{q}b$ - $t\bar{t}$ filter, (c) the $t\bar{b}$ - W $b\bar{b}$ filter, and (d) the $t\bar{q}b$ - W $b\bar{b}$ filter. Signals are multiplied by ten.

Systematic uncertainties Systematic uncertainties are evaluated for the Monte Carlo signal and background samples, separately for the electron and muon channels and for each b -tag multiplicity. The most important sources of systematic uncertainty are listed in Table 3.3.23.

Source of systematic uncertainty	Uncertainty range (%)
Signal and background acceptance	
b -tag modeling	5 – 20
jet energy calibration	1 – 15
trigger modeling	2 – 7
jet fragmentation	5 – 7
jet identification	1 – 13
lepton identification	4
Background normalization	
theory cross sections	2 – 18
W +jets flavor composition	5 – 16
Luminosity	6.5

Table 3.3.23: Range of systematic uncertainty values for the various Monte Carlo signal and background samples in the different analysis channels.

Cross section limits We see from Table 3.3.22 and Figure 3.3.51 that the observed lepton+jets data agrees with the predicted Standard Model backgrounds within statistical uncertainty. We, therefore, set upper limits on the single top quark production cross section separately, in the s -channel and t -channel searches. The limits are derived using Bayesian statistics [165]. The likelihood function is proportional to the Poisson probability to obtain the number of observed counts. In the cut-based analysis, we use the total number of counts, and in the neural network analysis, we use the two-dimensional distributions of the $\tau\tau$ versus W bb network outputs, and construct a binned likelihood.

The prior probability for the signal cross section is assumed to be flat. The prior for the signal acceptance and background yields is a multivariate Gaussian, with a vector of means given by the estimates of the yields, and covariance matrix computed from the associated uncertainties to take into account all correlations. The effect on the shape of neural network outputs from uncertainties like b -tag modeling, jet energy calibration, jet identification, and trigger modeling, is also considered in the binned likelihood.

The expected and observed upper limits at 95% confidence level, after the initial event selection, and from the cut-based and neural network analyses, are shown in Table 3.3.24 for the combined electron, muon, single-tagged and double-tagged channels. We see that the limits improve upon applying cuts on the discriminating variables, but that tighter limits are obtained when the variables are combined using neural networks. The observed posterior probability densities as a function of the s -channel and t -channel cross section are shown in Fig. 3.3.52 for the cut-based and the neural network analyses.

We also plot contours of the observed posterior density at different level of confidence, in the two-dimensional plane of the t -channel versus the s -channel single top production cross sections, for the

neural network analysis, as shown in figure 3.3.53. In order to illustrate the sensitivity of this analysis to probe models of physics beyond the standard model, the expected SM cross section as well as several representative non-SM contributions are also shown. [81]

	Expected Limits		Observed Limits	
	s-channel	t-channel	s-channel	t-channel
Initial selection	14.5	16.5	13.0	13.6
Cut-based	9.8	12.4	10.6	11.3
Neural networks	4.5	5.8	6.4	5.0

Table 3.3.24: Expected and observed upper limits (in picobarns) at 95% confidence level, on the production cross sections of single top quarks in s-channel ($t\bar{b}$) and t-channel ($tq\bar{b}$) searches, for the combined electron, muon, single-tagged and double-tagged channels.

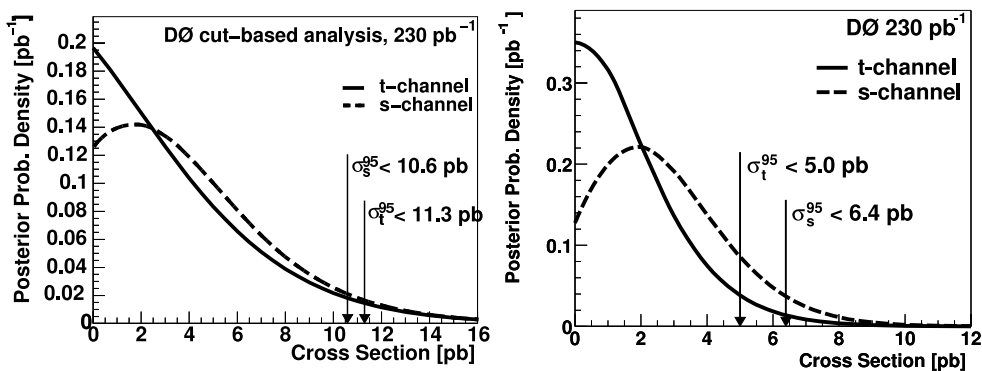


Fig. 3.3.52: The observed posterior probability density as a function of the single top quark cross section in the s-channel and the t-channel modes, using the combined electron, muon, single-tagged, and double-tagged analysis sets, for the cut-based (left) and neural network (right) analyses.

Conclusions To summarize, we find no evidence for single top quarks in 230 pb^{-1} of lepton+jets data collected by the DØ detector at $\sqrt{s} = 1.96 \text{ TeV}$. The upper limits on the single top production cross section in the s-channel and t-channel modes, at 95% CL, are 10.6 pb and 11.3 pb, respectively, using event counts in a cut-based analysis, and 6.4 pb and 5.0 pb, respectively, using binned likelihoods in a neural network analysis.

Description of the First CDF Run II Analysis

Contributed by: Ciobanu, Stelzer, Wagner

This section describes the first search for single top quark production in Run II of the Tevatron performed by CDF. Two analyses were carried out using an early data sample of 162 pb^{-1} of proton-antiproton collisions. The first analysis (“A1”) was a combined search for s and t channel single

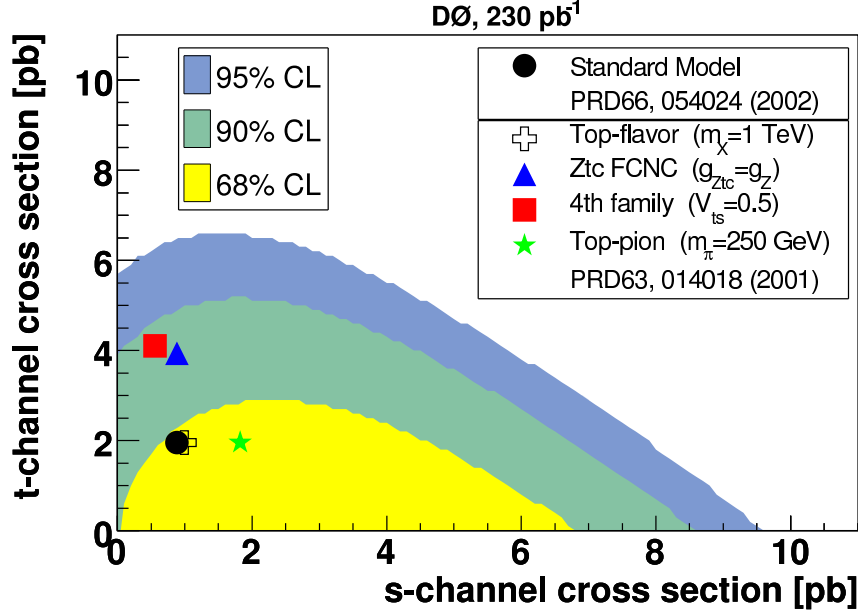


Fig. 3.3.53: Exclusion contours at 68%, 90%, and 95% confidence level on the observed posterior density distribution as a function of both the s -channel and t -channel cross sections in the neural networks analysis. Several representative non-standard model contributions from Ref. [81] are also shown.

top, while the second analysis (“A 2”) was a separate search for the t channel and the s channel individually. No significant evidence for a single top signal was found and an upper limit of 17.8 pb on the combined single top production cross section, at 95% confidence level was set. Upper limits of 10.1 pb and 13.6 pb were set on the production cross sections of t channel, and s channel single top, respectively [147].

The event selection for A 1 exploits the kinematic features of the signal final state, which contains a top quark, a bottom quark, and possibly additional light quark jets. To reduce multijet backgrounds, the W originating from the top quark is required to have decayed leptonically. We demand therefore a high-energy electron or muon ($E_T(e) > 20$ GeV, or $P_T(\mu) > 20$ GeV/c) and large missing energy from the undetected neutrino $E_T(\nu) > 20$ GeV. We reject dilepton events from $t\bar{t}$ and Z decays by requiring the dilepton mass to satisfy: $76 \text{ GeV}/c^2 < M_{\ell\ell} < 106 \text{ GeV}/c^2$. Exactly two jets with $E_T > 15$ GeV and $j_j < 2.8$ are required to be present in the event. A large fraction of the backgrounds is removed by demanding at least one of these two jets to be tagged as a b -quark jet by using displaced vertex information from the silicon vertex detector (SVX). The backgrounds surviving these selections can be classified as “non-top” and $t\bar{t}$. The non-top backgrounds are: Wbb , Wcc , Wc , mistags (light quarks misidentified as heavy flavor jets), non- W (events where a jet is erroneously identified as a lepton), and diboson WW , WZ , and ZZ .

Finally, we require the invariant mass of the reconstructed top quark to be within the range: $140 \text{ GeV}/c^2 < M_{t,b} < 210 \text{ GeV}/c^2$. We will refer to the above set of selection cuts as the “A 1 selection”.

The second analysis A 2 starts from the A 1 selection and forms two distinct subsets of events. The first subset is formed by retaining events with exactly one b -tagged jet, and also demanding that at least one of the two jets have $E_T > 30$ GeV. These requirements optimize the t -channel signal content of the

sample with respect to the backgrounds. The second subset is formed by selecting the double b -tagged events, i.e. the events where both jets are SVX b -tagged. This selection was found to be optimal for identifying s -channel signal events. The expected signal and background yields in 162 pb^{-1} of data are summarized in Table 3.3.25.

Process	Combined search A 1		Separate search A 2			
			Single-tag		Double-tag	
t-channel	2.8	0.5	2.7	0.4	0.02	0.01
s-channel	1.5	0.2	1.1	0.2	0.32	0.05
$t\bar{t}$	3.8	0.9	3.2	0.7	0.60	0.14
non-top	30.0	5.8	23.3	4.6	2.59	0.71
Total	38.1	5.9	30.3	4.7	3.53	0.72
Observed	42		33		6	

Table 3.3.25: Expected signal and background contributions and total number of events observed in 162 pb^{-1} after all selection cuts, described in the text, have been applied.

Methodology For the combined search A 1 the kinematic distribution of the total transverse energy in the event H_T is employed which looks similar for both signal channels while it looks different for the background processes. The CDF data and the Monte Carlo H_T distributions (using the contributions from Table 3.3.25) are shown in Fig. 3.3.54. We employ a maximum likelihood method to estimate the

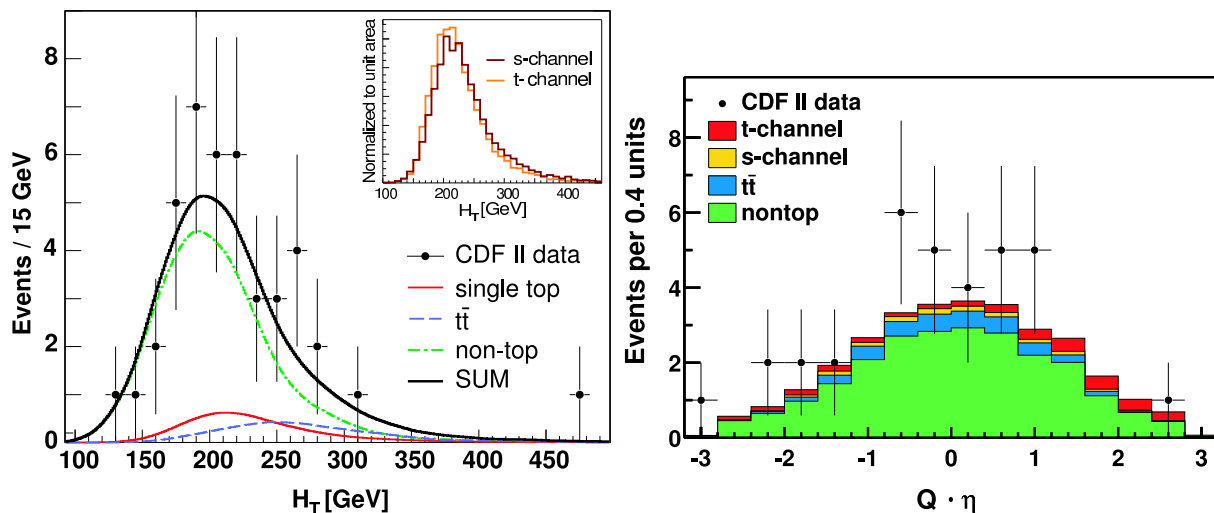


Fig. 3.3.54: The H_T and the $Q \cdot \eta$ distributions for CDF II data (points) compared with the Monte Carlo predictions. In both cases the distributions are normalized to the expected number of events from Table 3.3.25.

signal content in the data. The likelihood function is expressed as:

$$L(\sigma_{s+t}; \mu_1; \dots; \mu_9) = \frac{e^{-\sum_{i=1}^{N_{\text{bin}}} \mu_i} \prod_{i=1}^{N_{\text{bin}}} \mu_i^{d_i}}{\prod_{i=1}^{N_{\text{bin}}} d_i!} \prod_{j=1}^9 G(\mu_j); \quad (3.3.27)$$

where i indexes the H_T bins, and j indexes the nuisance parameters μ_j (two background rates and seven sources of systematic uncertainty) accounted for by using Gaussian functions $G(\mu_j)$. The number of data

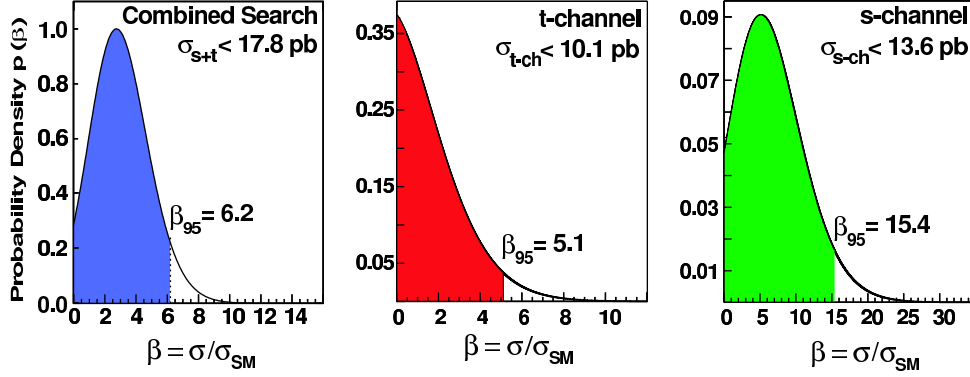


Fig. 3.3.55: The posterior probability density obtained by integrating the likelihood of Eq. (3.3.27) with respect to the nuisance parameters μ_j . In all three cases a flat prior is assumed to restrict signal cross-sections to physical (positive) values.

events in bin i are denoted d_i , while μ_i is the expected number of events in bin i and incorporates the full correlations between systematic effects modifying both the H_T shape and the signal rate. The μ_j parameters are integrated out numerically, and the resulting function (marginalized likelihood) is used to set the 95 % confidence level on the single top cross section.

For the individual search A 2, the t -channel analysis is performed in the single b -tag sample. In this subsample, we employ the kinematic distribution Q , i.e. the product of the lepton charge and the pseudorapidity of the non- b -tagged jet. The t -channel signal events are expected to exhibit an asymmetry toward the positive Q region. No such asymmetry is observed in the data (right plot of Fig. 3.54). The likelihood function used in the separate search closely resemble Eq. (3.3.27). To obtain sensitivity to the s -channel process a Poisson term for the number of double b -tagged events is added to the likelihood. The posterior probability density function for the combined search and the separate searches are shown in Fig. 3.3.55.

In summary, we find no significant evidence for electroweak single top quark production in 162 pb^{-1} of integrated luminosity recorded with CDF in Run II. We set upper limits of 10.1 pb at the 95% C.L. for the t -channel cross section, 13.6 pb for the s -channel and 17.8 pb for the combined search.

CDF single-top analysis with neural networks based on 695 pb^{-1}

Contributed by: Wagner

CDF has updated its single-top search using a dataset corresponding to 695 pb^{-1} . Two analyses are performed based on neural networks or likelihood functions, respectively. We described here briefly the neural network analysis, that has the better *a priori* sensitivity.

The event selection is very close to the one described in the previous section. The updated analysis uses in addition electrons measured in the forward calorimeter. The cut on the reconstructed invariant mass $M_{\tau b}$ is omitted, since this variables is fed into the neural network. The numbers of expected and observed events are listed in Table 3.3.26.

Process	N events	
τ -channel	16:7	1:7
s -channel	11:5	0:9
$t\bar{t}$	40:3	3:5
diboson, Z	17:2	0:8
$W + b\bar{b}$	170:7	49:2
$W + c\bar{c}$	64:5	17:3
$W + \tau$	69:4	15:3
$W + q\bar{q}$, mistags	164:3	29:6
non- W	119:5	40:4
Total	674:1	96:1
Observed	689	

Table 3.3.26: Expected number of signal and background events and total number of events observed in 695 pb^{-1} in the $W + 2$ jets dataset.

Using a neural network 14 kinematic or event shape variables are combined to a powerful discriminant. One of the variables is the output of a neural net b tagger. In Fig. 3.3.56 the distribution of this b tag variable is shown for the 689 data events in the $W + 2$ jets bin. The neural net b tagger gives an additional handle to reduce the large background components where no real b quarks are contained, mistags and charm-backgrounds. Both of them amount to about 50% in the $W + 2$ jets date sample even after the requirement that one jet is identified by the secondary vertex tagger of CDF.

Figure 3.3.57 shows the observed data compared to the fit result (a) and the expectation in the signal region (b) for the single-top neural network. For comparison the Monte Carlo template distributions normalized to unit area are also shown (c, d). The data are fitted with a binned likelihood function. The τ - and the s -channel are treated as one single-top signal assuming the ratio of the two processes to be the one predicted by the standard model. The most probable value of the likelihood function is $0.3^{+1.3}_{-0.8}$ (stat:) $+0.2_{-0.3}$ (syst:) pb. At present, this result yields no significant evidence for single-top production. The corresponding upper limit on the cross section is 3.4 pb at the 95% confidence level. The expected standard model value is $2.9 \pm 0.4 \text{ pb}$.

To separate τ - and s -channel production two additional networks are trained and a simultaneous fit to both discriminants is performed. The fit result is illustrated in Fig. 3.3.58 and summarized in Table 3.3.27. Again, there is no evidence for single-top production yet. However, the upper limits are already quite close to the predicted standard model values.

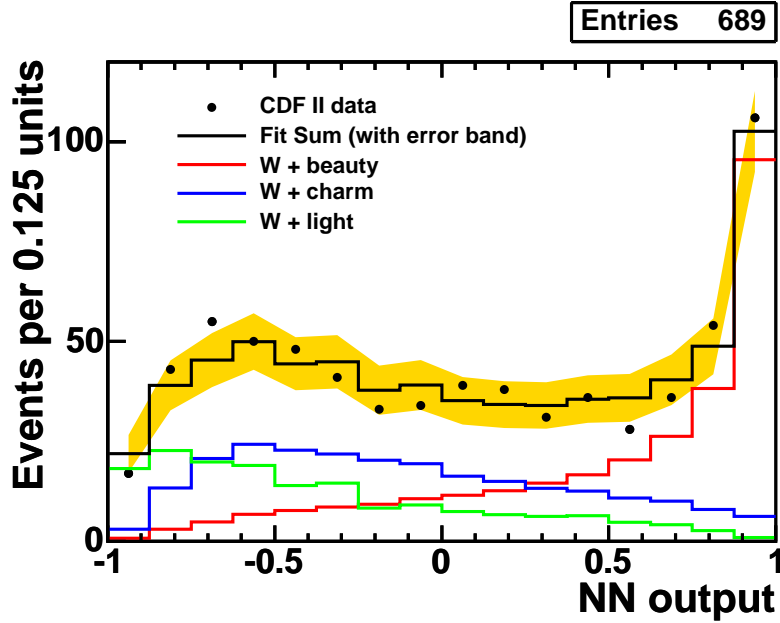


Fig. 3.3.56: Output distribution of the neural net b -tagger for 689 candidate events in the $W + 2$ jets bin. Overlaid are the fitted components of beauty-like, charm-like and mistag templates.

	t -channel	s -channel
Observed most probable value	$0.6^{+1.9}_{-0.6}$ (stat.) $+0.1_{-0.1}$ (syst.) pb	$0.3^{+2.2}_{-0.3}$ (stat.) $+0.5_{-0.3}$ (syst.) pb
Observed 95% C.L. upper limit	3.1 pb	3.2 pb
Expected 95% C.L. upper limit	4.2 pb	3.7 pb

Table 3.3.27: Fit results for the separate search for t - and s -channel single-top production. The expected limits are calculated from pseudo-experiments which included single-top quark events at the standard model rate.

Prospects for discovery

Contributed by: Jain, Wagner

Both DØ and CDF are currently working on increasing the acceptance and purity of the analysis as well as on several analysis methods which improve the search for single top quark production using different multivariate techniques. The sensitivity of the analysis for the combined $s + t$ mode, projected using CDF's 162 pb^{-1} dataset and employing neural networks, is shown in Fig. 3.3.59. Here, the significance is defined as $S = \frac{\mu}{\sigma} \sqrt{\frac{L}{L_0}}$, which can be interpreted as the statistical significance of the excess in the observed data above Standard Model predictions. A neural network was used to distinguish signal from background events. The cut on the network output was adjusted to optimize the value of $S = \frac{\mu}{\sigma} \sqrt{\frac{L}{L_0}}$ of the remaining events. No systematic uncertainties are included in this study. Based on statistical uncertainties only, CDF expects to see an excess corresponding to a 3 Gaussian fluctuation with a dataset of

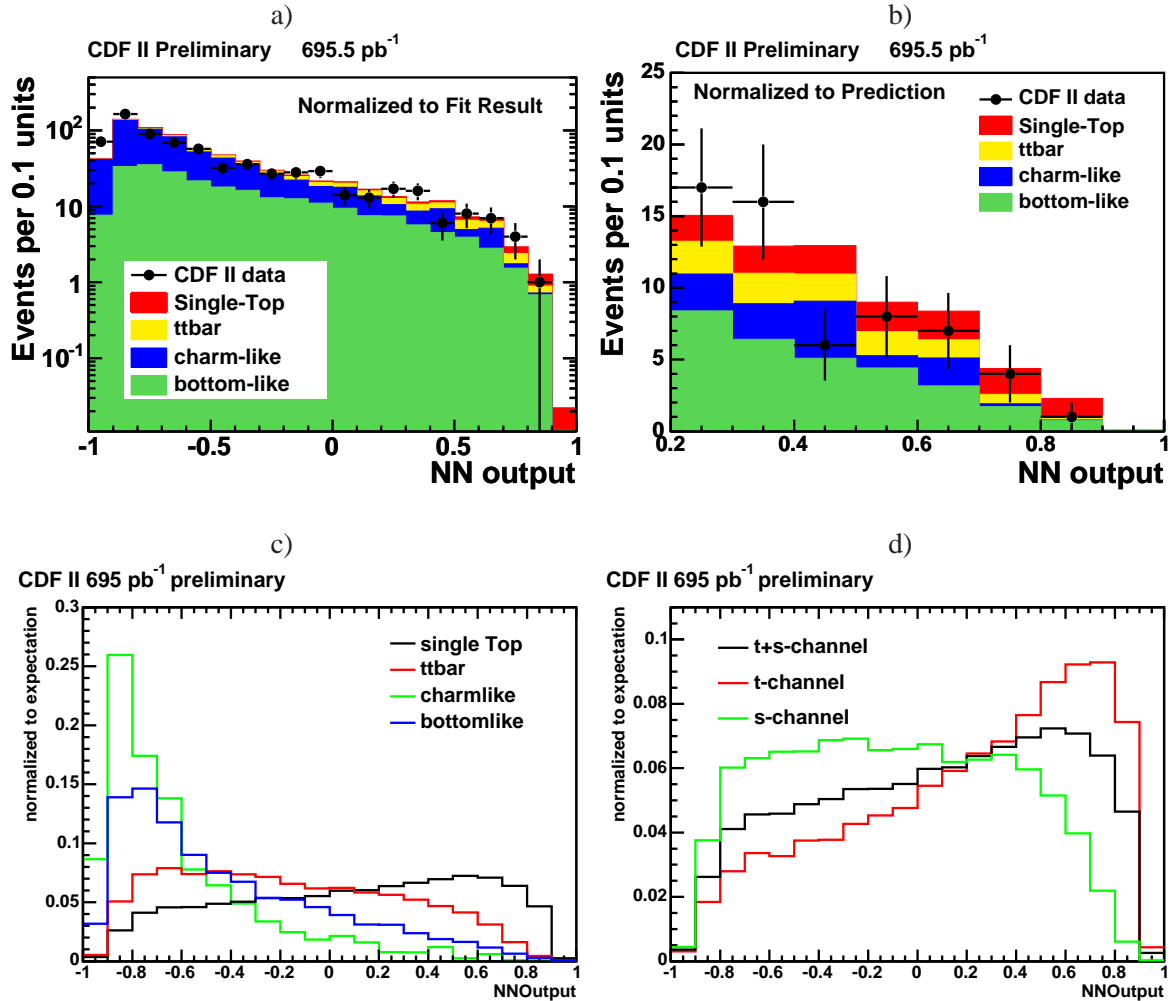


Fig. 3.3.57: Single-Top search with neural networks at CDF. The analysis is based on 695 pb^{-1} . a) data compared to the fit result, b) data compared to the standard model expectation in the signal region with neural network outputs larger than 0.4. c) and d): For comparison the Monte Carlo template distributions normalized to unit area are shown.

1.5 fb^{-1} .

The sensitivity of $D\emptyset$'s search for single top quarks at different integrated luminosities is shown in Fig. 3.3.60, for the s -channel and t -channel searches separately, by projecting twice the current $D\emptyset$ dataset of 230 pb^{-1} in order to simulate the effect of combining the data from the two experiments ($D\emptyset$ and CDF). Here, the significance is defined as the ratio of the peak of the Bayesian posterior probability density to the width of the distribution. This can be interpreted as the significance of a *measurement* of single top production cross section, where a measurement of the cross section can be defined by the peak of the probability distribution and its uncertainty by the corresponding width. All systematic effects are ignored as mentioned before. It can be seen that it is possible to observe the production of single top quarks in the t -channel mode with a 2.5 significance at 1 fb^{-1} , but that it is possible to observe them in the combined $s + t$ mode even earlier.

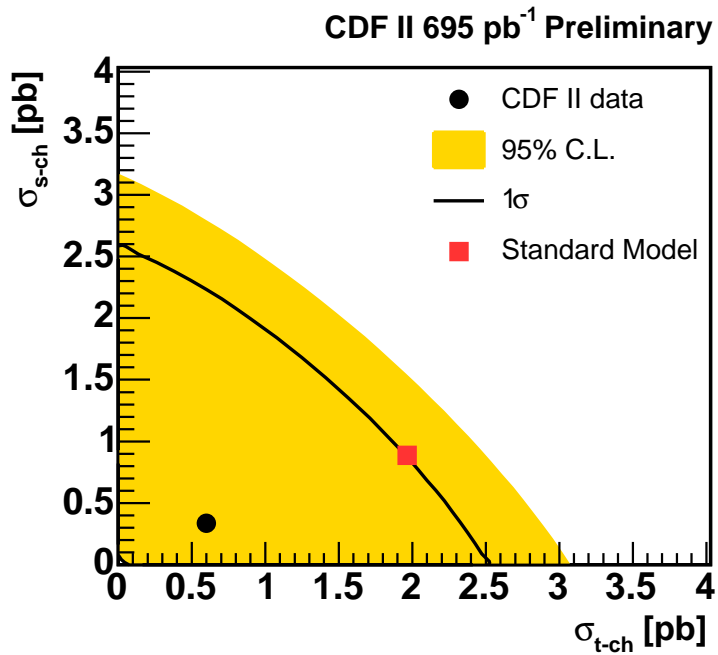


Fig. 3.3.58: Result of a simultaneous fit for the τ and s -channel production cross section to two-dimensional neural network discriminants.

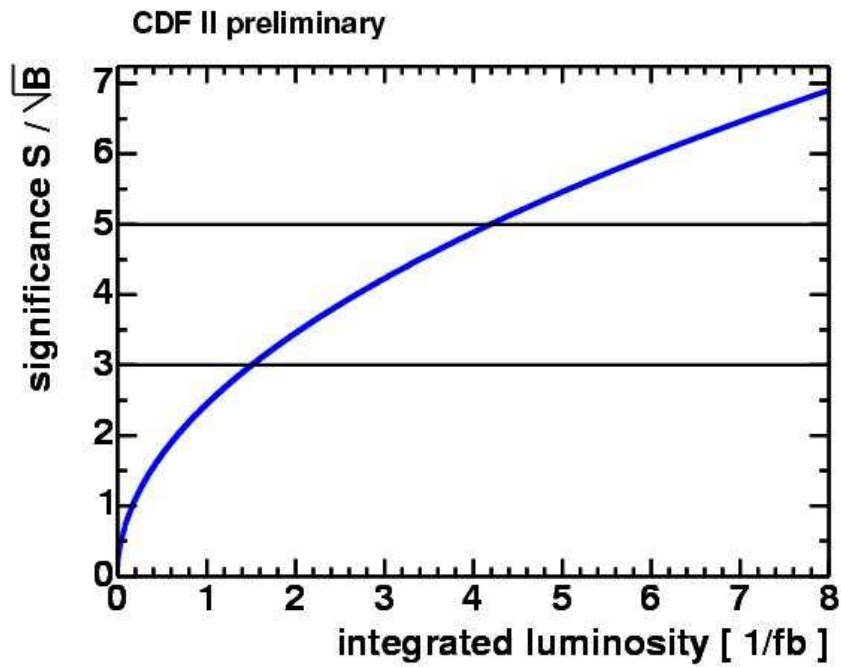


Fig. 3.3.59: The significance for Standard Model single top production in the combined $s + \tau$ mode, projected at different integrated luminosities, using CDF's initial 162 pb⁻¹ lepton+jets dataset. To discriminate signal and background a neural network is used. With about 1.5 fb⁻¹ of data we expect to have a 2 signal needed to claim evidence for single top production.

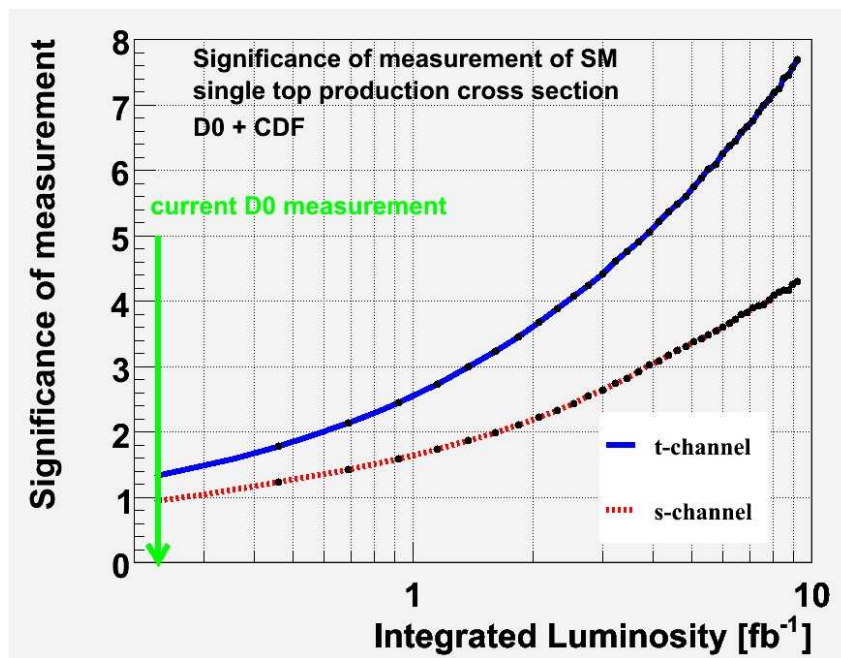


Fig. 3.3.60: The significance of a measurement of Standard Model single top quark production cross section, in the s -channel and t -channel modes, projected at different integrated luminosities, using DØ's initial 230 pb^{-1} lepton+jets dataset.

3.4 LHC Single Top Quark Searches

Introduction

At the LHC, the production of single top quarks accounts for a third of the top pairs production. With more than two millions single top events per experiment produced every year during a low luminosity run, a precise determination of all contributions to the total single top cross section seems achievable. These measurements will constitute the first direct measurement of σ_{tb} at the few percent level of precision, and also constitute a powerful probe for new physics, via the search for evidence of anomalous couplings to the top quark, or the measurements of additional bosonic contributions to the single top production.

The single top production mechanisms proceeds through three different sub-processes resulting in distinct final states, topologies and backgrounds. This Section establishes both ATLAS and CMS potentials for the cross section measurements of those three contributions. The event selections are presented extensively for both experiments and the performance are assessed in terms of statistical precision and systematic uncertainties. Both approaches address the experimental issues as the lepton identification, the jet reconstruction and the b-tagging performance as well as the strategies needed to evaluate Standard Model backgrounds from the data when possible.

Single top studies at ATLAS

Contributed by: Chevallier, Lleres, Lucotte,

Phenomenology of single top and SM backgrounds

Single top production

In the Standard Model framework, the single-top production is due to three different mechanisms: the W-boson gluon fusion mode, noted W_g , which includes the t-channel contribution; the associated production of a top quark and a W-boson, noted $W + t$; and the s-channel coming from the exchange of a charged boson W^\pm . We note however that these definitions are valid only at Leading Order (LO) level of corrections. The total NLO cross section for all three mechanisms amounts to about 300 pb at the LHC. Among those channels, the dominant contribution comes from the W_g processes, which account for about 240 pb. The $W + t$ contribution amounts for about 60 pb while the s-channel W mode is expected with a cross section of about 10 pb [52, 53, 60]. We note that in pp collision, the cross section for single-top processes are not charge symmetrically produced: the s-channel $t\bar{b}$ final state cross section is thus expected to be produced with a factor of 1.60 ± 0.01 higher than the $t\bar{t}$ final state. This ratio amounts to 1.67 ± 0.01 in the t-channel. This feature is of special interest since it generates a charge asymmetry in the leptonic final state that can be exploited in the analysis to reduce the contamination from the top quark pair production, which constitutes the main background to the single-top events selection.

In the Standard Model, the top quark decays almost exclusively into a W boson and a b quark. In the following, we use only the leptonic decay of the W's. The s-channel contribution from leptonic tau decays has been taken into account and is considered among signal events. For the associated production, we consider the two cases where the leptons originates either directly from the W produced in parallel to the top quark, or from the W-boson appearing in the top quark decay channel. Table 3.4.28 reports the

processes	BR (fb)
$W \rightarrow tb \rightarrow l^+ bb$	1,300
$W \rightarrow tb \rightarrow l \bar{b}$	800
$W \rightarrow tbq \rightarrow l^+ bbq$	32,040
$W \rightarrow tbq \rightarrow l \bar{b}q$	18,900
$W \rightarrow t \rightarrow qq^0 l b; l bqq^0 b$	9,320

Table 3.4.28: Cross sections convoluted by BR for single-top production. Those numbers are used in the LHC analyses. For further references, see previous Sections

cross sections corresponding to all three mechanisms depending on the charge of the final W-boson. Significant sources of uncertainties affect the theoretical predictions of the production cross sections: the $W \rightarrow tb$ channel is known with a precision of 7.5% at NLO, while the $W \rightarrow tq$ channel has an uncertainty of 3.5%. An uncertainty of 8% is quoted for the $W \rightarrow t$ channel. More details can be found in the previous sections.

At the time of the present analysis, only LO single-top generators were available for Monte Carlo studies. We use the TopRex [166] generator for the event production and selection efficiency determination, and normalize a posteriori the event yields to the NLO cross sections. It is obvious that this approach does not account for the possible biases in final state jet (or lepton) momentum distributions. The use of a NLO generator as MC@NLO [167] appears necessary to validate the selection as it becomes available.

Top pair production

At the LHC, the top pair production constitutes a dominant background to the single-top analyses. The total production cross section is $\sigma(t\bar{t}) = 835^{+52}_{-39}$ pb [30], about 3 times larger than the corresponding total single-top cross section, and more than 80 times that of the $W \rightarrow tb$ channel.

The main channel affecting the analysis is the "lepton+jets" channel, with a final state composed of two b jets, a high P_T lepton and missing energy; the di-lepton channel ($t\bar{t} \rightarrow l \bar{l} b \bar{b}$) where a high P_T lepton is lost in acceptance also constitute a major background. Finally, top pairs with one or both W decaying into a tau lepton where the τ decays into an electron or a muon, may also survive the selection ($t\bar{t} \rightarrow b \bar{b} \tau \tau$ or $(t \rightarrow b \tau)$). The cross sections used in the following analyses are reported in Table 3.4.29. Production cross sections are calculated up to NLO [167].

Even at NLO, the theoretical uncertainty is dominated by the choice of the renormalization scale: a scale variation of $\mu = 2$ to 2 results in an uncertainty of about 100 pb, representing an uncertainty of about 12%. As these events constitute our main background, it will therefore be necessary to use cross section directly from measurements on data to assess properly the contamination of our final sample.

Regarding the Monte Carlo studies carried on $t\bar{t}$ events, we use the (LO) TopRex generator and apply a scale factor on the production cross sections. Thus, the same remarks as for single-top mechanisms apply here. Further studies including the comparison of TopRex and the NLO generator generator

processes	BR (fb)
$tt \rightarrow l b jj (l = e;)$	242,420
$tt \rightarrow l \bar{l} b (l = e;)$	38,096
$tt \rightarrow l^+ b$	9,520
$tt \rightarrow b jj$	121,210

Table 3.4.29: Cross sections convoluted with the Branching Ratio for top pair production used in our analysis

MC@NLO [167] have already started [168].

W+jet production

$W QQ$ events where Q stands for b or c quarks involve the presence of long-lifetime particle jets that are also present in our signal sample. The corresponding cross section has been computed at LO and is about the same order of magnitude that for the signal. However, NLO calculations [169] are available. They have been performed by imposing some realistic constraints to the partons present in the final state. Numbers together with the requirements applied on the final partons are reported in Table 3.4.30 for the various final states.

processes	Cross sections			Specific requirements
	N_{LO} (fb)	L_O (fb)		
$W^+ jj \rightarrow e^+ jj$	669,000	10	773	$p_T^j \geq 15; p_T^l \geq 20$
$W^- jj \rightarrow e^- jj$	491,000	10	558	$p_T^j \geq 15; p_T^l \geq 20$
$Z jj \rightarrow e^- e^+ jj$	105,000	5	116	$p_T^j \geq 15; p_T^l \geq 20$
$W^+ bb \rightarrow e^+ bb$	3,060	60	1300	$p_T^j \geq 15; p_T^l \geq 20$
$W^- bb \rightarrow e^- bb$	2,110	50	900	$p_T^j \geq 15; p_T^l \geq 20$
$Z bb \rightarrow e^- e^+ bb$	2,280	30	1800	$p_T^j \geq 15; p_T^l \geq 20$

Table 3.4.30: Cross sections for W+jets and Z+jets events [169]

As no event generator including NLO calculations is presently available, we use the (LO) TopRex generator for the event production and normalize the corresponding cross sections to the NLO values. This method imposes us to reproduce the criteria applied in the phenomenological approach [169], in order to normalize properly our selection efficiencies.

W+light jets events constitute a major source of background because of a cross section several orders of magnitude above the signal. In our case, this processes can mimic the signal if two light jets are wrongly tagged as a b-jet. Some calculations provide the NLO cross section [169] for specific final states including $W+j$, $W+jj$ and $W+jjj$ events, with a leptonic decay for the W : in these calculations, requirements that reproduces typical LHC acceptance and energy thresholds are imposed on leptons and

jets composing the final states. To estimate the NLO cross sections for our selection, we use the same method as for the $W \rightarrow Q \bar{Q}$ events, reproducing (when possible) the effects of the applied cuts at the parton level. All available generators are presently LO generators and the numbers used for this analysis are quoted in 3.4.30. Background production makes use of the HERWIG [170] generator for $W + \text{jets}$. It appears necessary to use of more appropriate generators (ALPGEN, AcerMC, MC@NLO) will be needed for future checks.

Di-boson production

Similarly, diboson events with light constitute backgrounds to our signal because of the presence a high- P_T lepton as well as b-jets in the final states. The $W Z \rightarrow l \bar{l} b \bar{b}$ production cross sections have been computed at the NLO level for specific final states including a high- P_T lepton (electron or muon) and is found to be $\sigma_{BR} = 426 \text{ fb}$. The $Z Z \rightarrow l \bar{l} b \bar{b}$ has a cross section of 340 fb . The WW production where a light jet is mistagged as a b-jet has also to be considered. The corresponding cross section is $18,500 \text{ fb}$. Samples have been generated using the PYTHIA generator.

Discriminant variables in single-top event analyses

The three single-top processes result in quite distinct final states and topologies, leading to the definition of specific analyses in each case. The discrimination between them makes use of difference in jet multiplicity, number of b-tagged jets required, as well as angular distributions between lepton and/or jets present in the final states. Besides, important difference subsist in the level of backgrounds that are faced in the various analyses, leading to the development of tools dedicated to the rejection of specific backgrounds.

We present in this section the basic set of relevant variables that are used to differentiate single-top events from main SM backgrounds. The selection of single-top events is based upon the presence of an isolated high- P_T lepton and a high missing transverse energy to reject non- W events. Events are required to contain at least two high- P_T jets, among which exactly one or two have to be identified as coming from the hadronization of a b quark. This set of requirements allows to reduce significantly QCD, and more generally, the jet production contamination. Global and topological variables may also be used to discriminate further top pair and W +jets events from our signal. We use in our case the total transverse energy of the events as well as the reconstructed top mass.

Lepton selection

In the ATLAS detector, the electron acceptance is defined in the pseudo-rapidity range $|\eta| < 2.5$. Beyond that range, the absence of tracking information makes the lepton identification more complex. The electron transverse energy is determined with a precision of :

$$\frac{\Delta E_T}{E_T} = 12\% = \frac{P}{E} = \frac{P}{E} = \frac{P}{E} = 24.5\% = \frac{E_T}{E} = 0.7\%$$

Fig. 3.4.61 displays a comparison of the lepton P_T distribution for single-top events and all various backgrounds. Leptons present in the QCD $pp \rightarrow b \bar{b}$ samples originate mainly from the semi-leptonic decays

of b hadrons and are thus much softer than those coming from a W boson decay. Leptons originating from decays in $t\bar{t} \rightarrow b\bar{b} + \text{jets}$ and $t\bar{t} \rightarrow b\bar{b} + \text{jets}$ events also have much lower E_T spectra. All those backgrounds are therefore very sensitive to the lepton P_T threshold used in the analysis. On the upper range of the distribution, W-boson produced leptons tend to be harder in top events than in W+jets events.

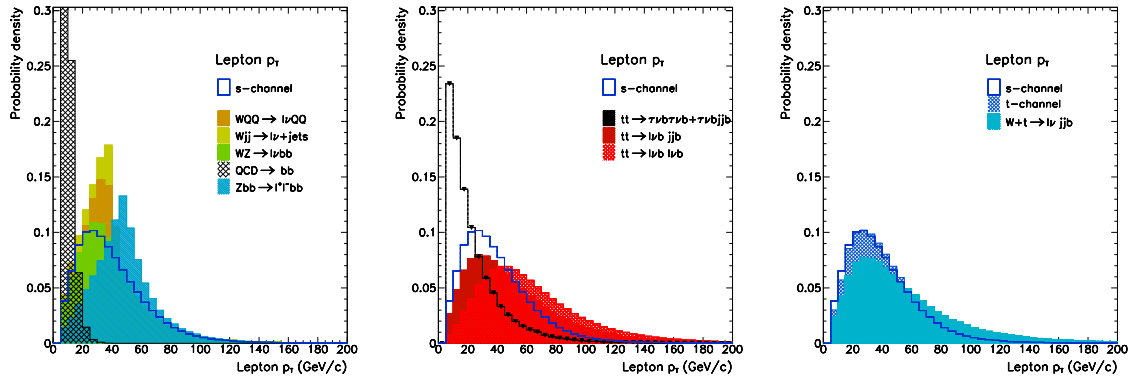


Fig. 3.4.61: Lepton transverse momentum probability density for signal and backgrounds.

The average P_T is about $40 \text{ GeV}/c$ for the s-channel, $50 \text{ GeV}/c$ for $t\bar{t}$ events and has to be compared with the mean value of $30 \text{ GeV}/c$ for WZ and $W + Q Q$ productions. A threshold of $25 \text{ GeV}/c$ is set to select a high- P_T lepton. This value corresponds to the lepton trigger threshold that is used to detect such events, and allows to reduce significantly non-W as well as tau decays' s top pair events contamination.

The lepton is required to be isolated. The lepton isolation is defined as the distance to the closest jet by $R = \frac{p_T}{\sqrt{p_T^2 + p_z^2}}$. Note that jets are defined by the use of a cone algorithm whose performance are described in Ref. [171]. The isolation of a high- P_T lepton with respect to the closest jet depends upon the topology of events. In a high jet multiplicity environment like $t\bar{t}$ and single top events, the $R(\text{lepton}; \text{jet})$ value tend to be lower than in a simple W+jets event. A cut at $R(\text{lepton}; \text{jet}) > 0.4$ is set for the selection.

To remove events with two leptons like $Z \rightarrow l^+ l^-$ and dileptonic top pairs, a veto is performed in any pairs of leptons with opposite signs and above $10 \text{ GeV}/c$. Note that this lepton veto may introduce some systematic effects due to the mis-identification of the lepton sign as well as a lower lepton identification efficiency at a lower P_T threshold. These effects have to be addressed in a full event reconstruction stage. Note that the sign of the selected lepton provides the nature of the single-top event: a positron or positive muon will sign a $t\bar{b}$ final state, while an electron or muon will sign a $t b$ decay.

Missing energy E_T

The missing energy physically originates from the presence of a neutrino in the W-boson decays. Missing transverse energy is shown in Fig. 3.4.62 for signal and backgrounds.

Significant differences can be seen in the distributions which carry a significant discriminating power:

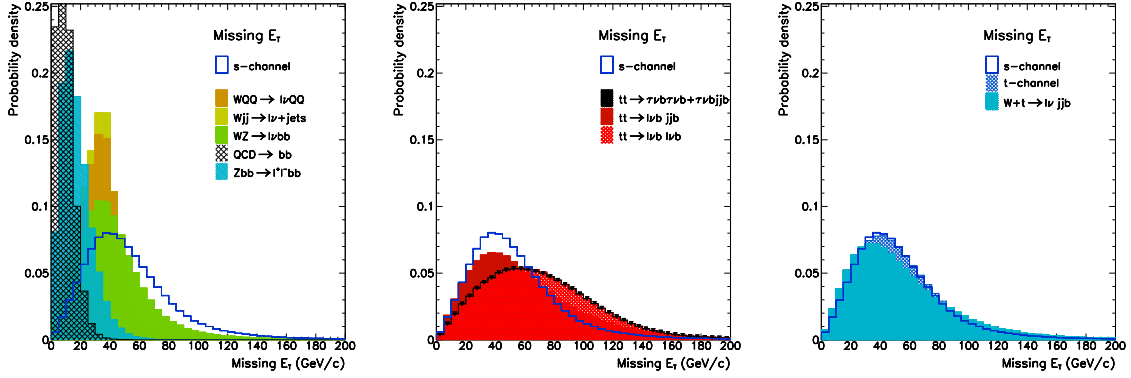


Fig. 3.4.62: Transverse missing energy for signal and backgrounds.

average values are around $30 \text{ GeV} = c$ for W +jets production and about $55 \text{ GeV} = c$ for single-top productions; those values are raised above or higher than $60 \text{ GeV} = c$ for "lepton+jet" and "dilepton" top pair events.

A threshold at $25 \text{ GeV} = c$ is thus applied so as to select a leptonic W decays. The use of the full spectrum may however help the discrimination against backgrounds with softer E_T like WZ , WQQ , and W +jets events, as well as against events with harder E_T spectrum like top pairs. A likelihood approach could thus benefit the selection.

This variable is extremely sensitive to the performance of the hadronic and electromagnetic energy measurement of the detector. Angular and energy resolution, the identification capabilities of noisy calorimeter cells, the modelling of the underlying events and the pile-up effects thus appear as key factors in the missing energy measurement. Again, full reconstruction studies are required to assess the magnitude of those effects.

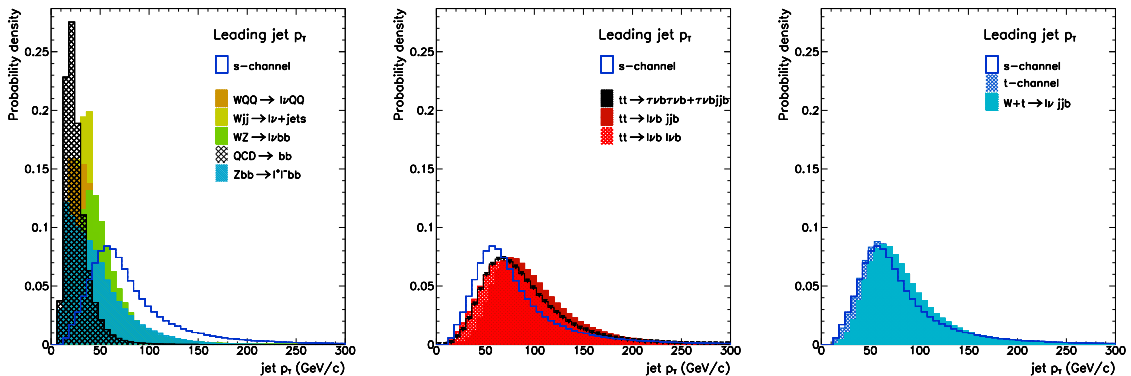


Fig. 3.4.63: Transverse momentum for the leading jet for signal and backgrounds.

Light jets

A jet is identified as a group of clusters falling within a fixed cone algorithm defined with a radius of $R = \sqrt{\frac{\Delta\eta^2 + \Delta\phi^2}{2}} = 0.4$. In ATLFAST [171], jets are defined in the pseudo-rapidity range $|\eta| \leq 5.0$ with a p_T above $15 \text{ GeV} = c$. The jet energy resolution is given by:

$$\frac{\Delta E}{E} = 50\% = \frac{p}{E = G \text{ eV}} \quad 3\% \text{ for } j_{\text{jet}} \leq 3$$

$$\frac{\Delta E}{E} = 100\% = \frac{p}{E = G \text{ eV}} \quad 7\% \text{ for } j_{\text{jet}} \geq 3:$$

Distributions for the two highest p_T jets also are shown in Fig. 3.4.63. Those Figures show that tt events have harder p_T spectra than the other processes, with average values of about $100 \text{ GeV} = c$ and $70 \text{ GeV} = c$ respectively for the leading and 2nd highest jet energy. Those values are respectively 80 and $50 \text{ GeV} = c$ for all three single-top processes. For WQQ and $W + \text{jets}$ events, the average energies are found at much lower values, around $35\text{-}40 \text{ GeV} = c$ for the leading jet and $20\text{-}30 \text{ GeV} = c$ for the second highest jet energy.

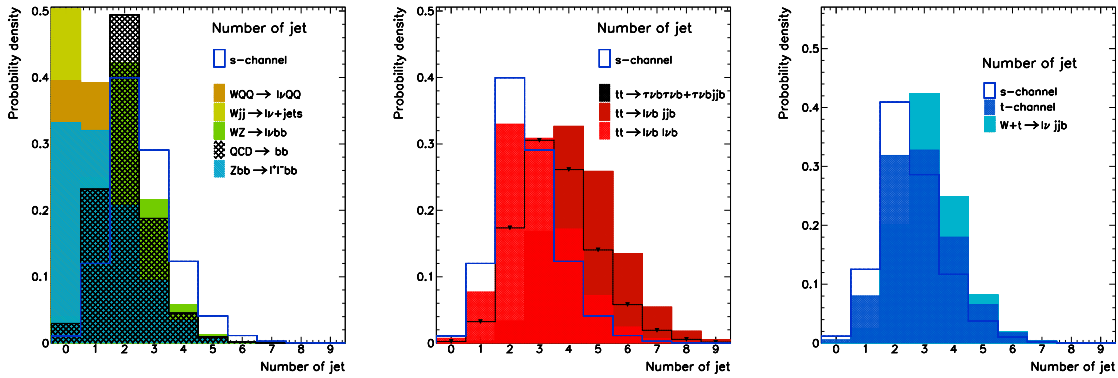


Fig. 3.4.64: Number of jets for signal and backgrounds.

The preselection requires at least two jets above a threshold of $25 \text{ GeV} = c$ in order to reduce the QCD, $W + \text{jets}$ as well as WZ/WW contamination. Again, the use of the full spectrum may be revealed useful as an input to a likelihood function. Jet multiplicity plays a crucial role in discriminating the single-top s -channel from all backgrounds as shown in Fig. 3.4.64, where all jets above $15 \text{ GeV} = c$ are represented. About 40% single-top s -channel events have exactly two jets and 70% have two or three jets. Jet multiplicity is smaller for both $W + \text{jets}$ and WQQ events with only about 30% events reconstructed with more than one jet. On the contrary, more than four jets are expected in the "lepton+jets" and "tau+jets" tt events in about 70% cases. Significant differences can also be seen among the three single-top production mechanisms. In the associated $W + t$ sample, about 45% events have exactly three jets, as expected from the hadronic decay of the W -boson associated to the Top quark. In this sample, about 40% events have more than three jets. In the W -gluon fusion events, the top decay gives a (b-)jet and a leptonic W as well as a b- and a non-b hadrons that can form eventually two extra jets.

It thus appears that the analysis must be performed in bins of jet multiplicity. At the preselection stage, selected events are required to have exactly two or three jets above $15 \text{ GeV} = c$ with, among them, at least two above $25 \text{ GeV} = c$. This requirement is crucial to reduce the $t\bar{t}$ contamination level.

Two issues must be addressed at this stage. The use of NLO generators for both signal and backgrounds may affect significantly those results: it seems mandatory to use them as they become available so as to quantify the effects on selection efficiencies. The second issue concerns the gluon Initial State Radiation (ISR) and Final State Radiation (FSR) modelling and its impact on the selected jet multiplicity: ISR affect crucially the number of jets that can be selected in the events while FSR have an impact on the jet energy due to the gluon emission in or outside the jet initiated by the parton. The selection efficiency thus depends closely upon the ISR and FSR modelling. These effects are addressed in Section 3.4 devoted to the estimates of the systematic uncertainties affecting the analysis. These two remarks emphasize the role of the jet definition: the choice of a cone algorithm with a larger radius ($R = 0.7$ for eg.) or the use of a k_T -algorithm to form the jet will affect the result of such analysis.

b-tagged jets

A jet can be identified as a b-jet only in the pseudo-rapidity range $|\eta_j| < 2.5$ corresponding to the tracking acceptance. In ATLFAST [171], the parametrization makes use of a combined tagging efficiency of 60% for b initiated jets above $35 \text{ GeV} = c$ in P_T . The corresponding mistag rate is 1% for u,d,s quark jets (factor 100 rejection) and 10% of tagging efficiency for c-quark jets.

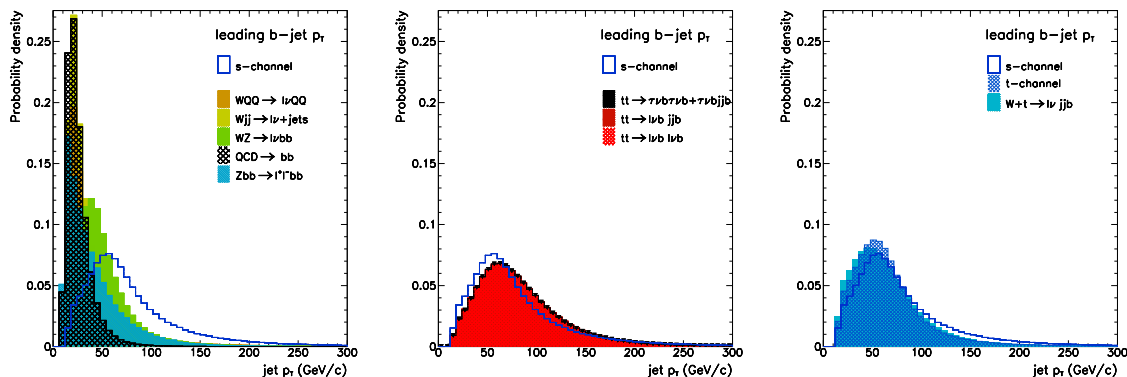


Fig. 3.4.65: Leading b-jet transverse momentum for signal and backgrounds.

Figs. 3.4.65 and 3.4.66 display the P_T distributions for the two leading b-tagged jets in signal and background events. The average is about $80 \text{ GeV} = c$ (resp. $40 \text{ GeV} = c$) for the leading jet (resp. 2nd leading b-jet). Jets present in QCD $p\bar{p} \rightarrow b\bar{b}$ events have a significantly softer spectrum than all others sources of backgrounds with an average value well below $30 \text{ GeV} = c$ (resp $29 \text{ GeV} = c$). However, the cross section being several orders of magnitude, it is important to set the threshold above as high as possible to prevent from a high contamination. It has been checked that out of 5×10^6 events, 17 events have 1 b-tagged jet (while none pass the 2-btag requirement) for a $30 \text{ GeV} = c$ threshold. This number falls to 11

at $40 \text{ GeV} = c$ and 7 at $50 \text{ GeV} = c$. This gives confidence that a $35 \text{ GeV} = c$ threshold is relevant for our selection. WQQ events also contain softer b-tagged jets (the same holds for c-jets in W +jets sample) than single-top events, as well as b-jets originated from Z decays, with an average P_T of $60 \text{ GeV} = c$ (resp. below $30 \text{ GeV} = c$). A high threshold in the highest b-jet P_T can therefore help reject significantly the QCD and W +jets background. A looser cut may be applied to the 2nd b-jet to further eliminate remaining WQQ events.

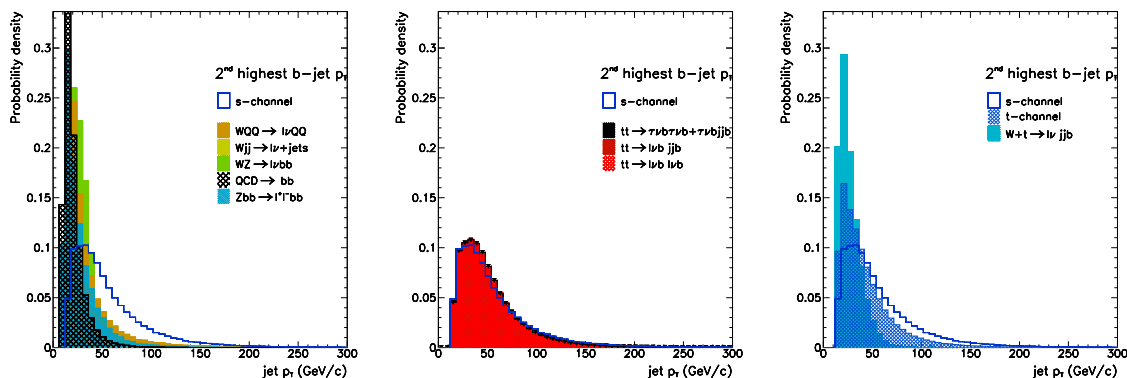


Fig. 3.4.66: 2nd highest b-jet transverse momentum for signal and backgrounds.

The expected number of b-tagged jet in the acceptance is shown in Fig. 3.4.67 for signal and all backgrounds. About 90% WQQ events have only one b-tagged jet, the other being either out of acceptance or below the P_T threshold. No QCD events out of 5,000,000 pass the requirement on two b-tagged jets. The situation is dramatically different in tt and W events which both contain more than 13% events with two b-tagged jets. Requiring more than one b-tagged jet is therefore mandatory to improve the rejection of QCD and W +jets backgrounds. Regarding the two other single-top mechanisms, the number of b-tagged jets is not as high as for the s -channel events. If one indeed expects two b-hadrons in the Wg channel, the second b-jet is missed in a significant fraction of time because the b parton is produced along the beam pipe, mostly outside the tracking acceptance and with a low P_T , as can be seen in Fig. 3.4.66. The probability to see a second b-tagged jet in this sample is less than 15%. For $W+t$ events, no second b is expected, which results in more than 97% events with only one b-tag, the remaining 2nd b-tagged jet coming mostly from charm decay.

The b-jet multiplicity strongly depends upon the b-tagging capabilities of the detector. A high efficiency and a low mistag rate will affect the discrimination against non-top background, making an impact in the analysis sensitivity. Section 3.4 will address the effects of deviations from the nominal expected performance on the systematic uncertainties affecting the selection efficiencies.

Total transverse energy H_T

The total transverse energy of the event is shown to have a significant discriminant power against both top pair and $W+t$ jets production. While the tt events tend to contain harder jets, the latter are

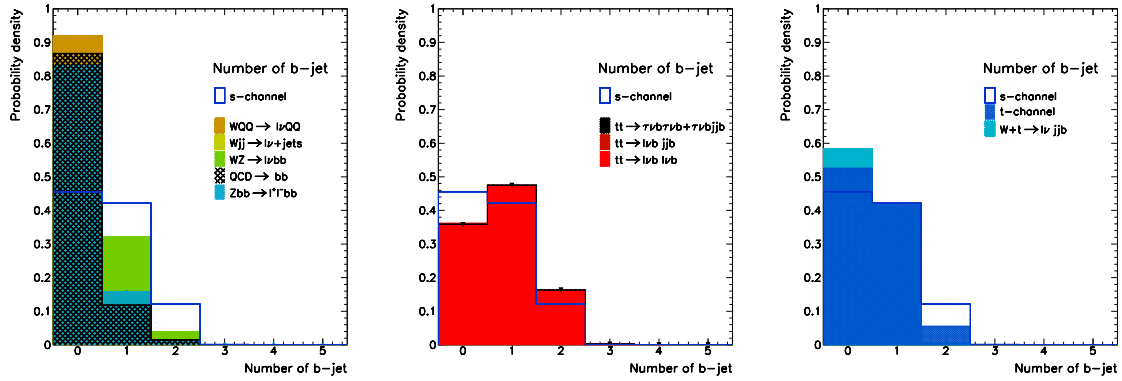


Fig. 3.4.67: Number of b-tagged jets for signal and backgrounds.

characterized by the presence of softer jets in the final state compared to those for the signal. One usually uses the scalar sum of transverse energy computed over jets as well as leptons and missing energy. Obviously this variable is correlated to the number of jets and therefore careful treatment must be applied. In our selection H_T is defined as:

$$H_T = \sum_{\text{jet}} E_T^{\text{jet}} + E_T^l + m E_T :$$

Probability density for this quantity is represented in Fig. 3.4.68 for signal and the various backgrounds. The H_T distribution peaks at around $180 \text{ GeV} = c$ for $W Q Q$ events while the average value for the W channel is about $230 \text{ GeV} = c$. For $t\bar{t}$ events in the various channels the distributions peak around $300 \text{ GeV} = c$. A window in H_T seems therefore to bring a significant rejection power against both $W Q Q$ and $t\bar{t}$ backgrounds.

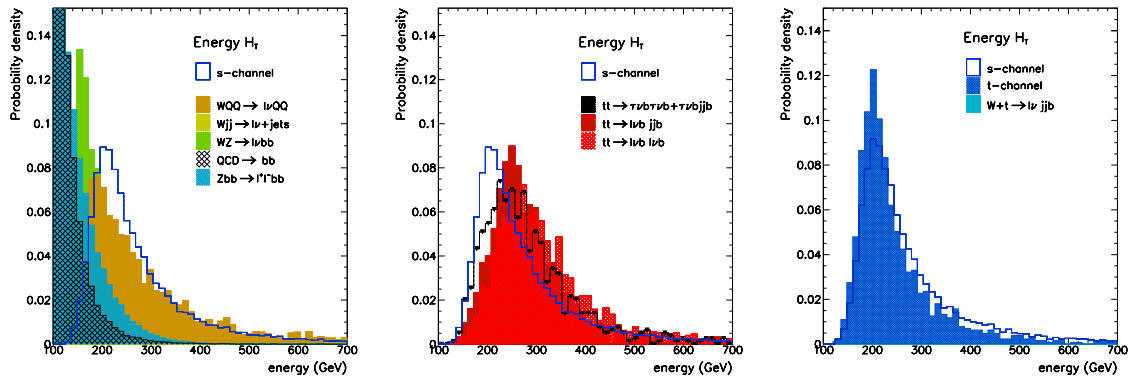


Fig. 3.4.68: Distribution of the energy H_T for signal and backgrounds.

Reconstructed Top mass m_t

With the LHC statistics, one can consider reconstructing a top mass from its decay products in order to reduce further the non-top background contamination of the selected sample. In our case where the W-boson decays leptonically, one faces an ambiguity arising from the determination of the neutrino longitudinal momentum: while the neutrino transverse energy can be inferred from the transverse missing E_T , the longitudinal momentum is unknown. It is however possible to obtain the p_z by using the W-mass as a constraint. The longitudinal momentum can thus be written as:

$$p_z(\pm) = \frac{b \pm \sqrt{b^2 - 4ac}}{2a}$$

where :

$$a = E^2(l) - p_T^2(l) ; b = 2 \frac{m_W^2}{2} + p_T^{\sim}(l) p_T^{\sim}(\tilde{l}) - p_z(l)$$

and

$$c = E^2(l) p_T^2(\tilde{l}) - \frac{m_W^2}{2} + p_T^{\sim}(l) p_T^{\sim}(\tilde{l})$$

Usually the twofold ambiguity is lifted by choosing the solution that gives the lowest p_z . In our case though we choose not to apply this criterium but apply a criterium at a later stage of the selection. One has to notice that this method may have no solution: this corresponds to events where the transverse reconstructed W mass is larger than the W boson mass due to resolution effects. In this case we keep the real part of the solution, following the DØ prescription.

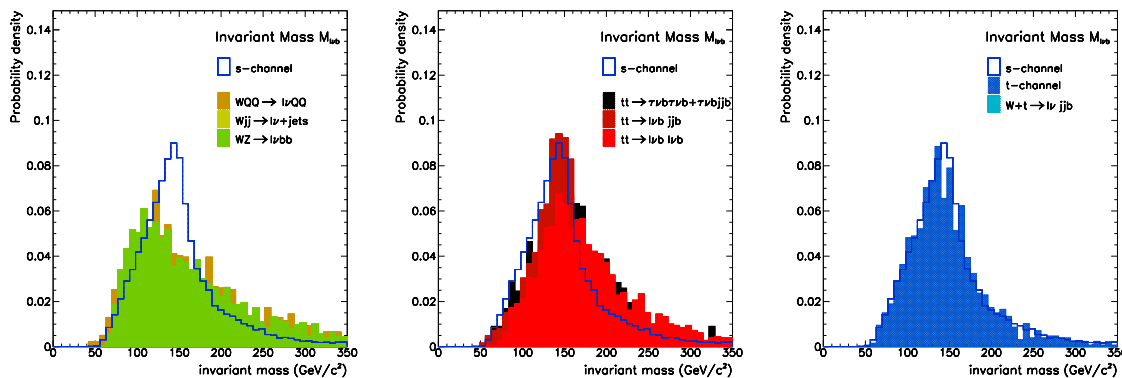


Fig. 3.4.69: Distribution of the reconstructed top mass for signal and backgrounds.

Once the solutions to p_z are found there are four possible combinations to reconstruct the top quark momentum and mass: two depending on the neutrino solution and two due to the presence of the b-tagged jets. We choose to keep the solution leading to the highest P_T top [172]. Figs. 3.4.69 show the probability densities associated to the reconstructed top mass for signal and the various backgrounds,

s-channel cross section measurement

The measurement of the s-channel may appear as the most delicate of the three main single-top

processes, because of its relatively low cross section compared to the two others. It is however one of the most interesting because the production of $t\bar{b}$ final state events is directly sensitive to contributions from extra W bosons or charged Higgs bosons as predicted in two Higgs doublet model (2HDM) of type II [173]. The present analysis is extensively detailed in Ref. [174].

Preselection

In ATLAS, the s -channel analysis is based upon the following criteria: selected event must have at least one high- P_T lepton in the central region with a P_T above $25 \text{ GeV} = c$ and a total transverse missing energy above $25 \text{ GeV} = c$. The event must pass a secondary lepton veto cut, applied to any lepton above $10 \text{ GeV} = c$ with a sign opposite to that of the selected high P_T lepton. The sign of the high P_T lepton is used to determine the "flavour" of the final top and b-quark pair: a positive (negative) charge lepton signs a $t\bar{b}$ ($\bar{t}b$) final state.

processes	$t\bar{b}$ final state		$\bar{t}b$ final state	
s-channel	1;200	7	840	4
t-channel	1;860	35	1;120	20
W+t channel		8		5
$t\bar{t}$ background				
$t\bar{t} ! e b j\bar{b}$	2;220	75	2;220	75
$t\bar{t} ! e b e b$	2;790	40	2;790	40
$t\bar{t} ! b; b$	360	28	360	28
$t\bar{t} ! b; j\bar{b}$	60	10	60	10
Z/W+jets background				
WQQ	2;250	50	1;410	30
W jj! e ;jj	1;710	170	1;260	120
W Z ! e b\bar{b}	90	10	60	5
Zbb ! e ⁺ e b\bar{b}	7	3	7	3

Table 3.4.31: Number of pre-selected events in the "2b0j" sample expected for an integrated luminosity of 30 fb^{-1} . Uncertainties come from Monte Carlo statistics only

The event must have exactly two or three jets above $15 \text{ GeV} = c$. Among those, two must be above $25 \text{ GeV} = c$. Finally, the events are then required to have, among those two or three selected jets, two b tagged jets with a P_T above a threshold of $30 \text{ GeV} = c$. Selected events are thus classified as "2b0j" (2 b-tagged jets and no extra light jet above $15 \text{ GeV} = c$) or as "2b1j" events (2 b-tagged jets plus one extra light jet and no 4th jet above $15 \text{ GeV} = c$). Note that the requirement of two b-tagged jets is crucial to reduce the contamination of W+jets events that have a cross section several orders of magnitude that of the signal. To a lesser extent, this is also true for $t\bar{t}$ events since among the 2-jet and 3-jet events, only a few of them have 2 b-tagged jets. Table 3.4.31 reports the number of expected events with 30 fb^{-1} .

About 1,200 (840) \bar{W} events are pre-selected in the $t\bar{b}$ ($t\bar{b}$) final states. The dominant background comes from the top pair production in the dilepton and "lepton+jets" channels, followed by the WQQ contamination. The remaining W+jets contamination is due to the high cross section for such events, and is expected, at this stage, to be slightly above the signal expectation. The resulting S/B ratio is about 11% (9%) in the $t\bar{b}$ ($t\bar{b}$) final state. It is obvious that the combination of both final states is required to improve the sensitivity.

For 2-jet samples, the signal efficiency is slightly above 3.0%. No QCD events are selected out of 5×10^6 . Top pair events are selected with an efficiency below 0.1% in the "lepton+jets" channel while tau+jets events are almost negligible. On the contrary "dilepton" (including "ditau") top pair events are selected with a higher efficiency ranging from 0.25 to 0.5%. Overall, this results in an almost equal contamination originating from "lepton+jets" and "dilepton" channels, due to the difference in branching ratios. As expected, the $\bar{W} Q Q$ contamination is greatly reduced by a 2-b tag requirement with a 0.2% selection efficiency. At the same time, only 1.2% WW and WZ diboson events are selected. $\bar{W} + \text{jets}$ events are removed because of the presence of non-b softer jets, with a final yield depending upon the mistag rate, for which we take to be equals to 1% in the present analysis. Regarding the three-jet samples, the signal efficiency is about 1.9%. While the double tag requirement keeps the $\bar{W} + \text{jets}$ contamination relatively low, the signal is swamped in the $t\bar{t}$ background with a much lower S/B below 1%.

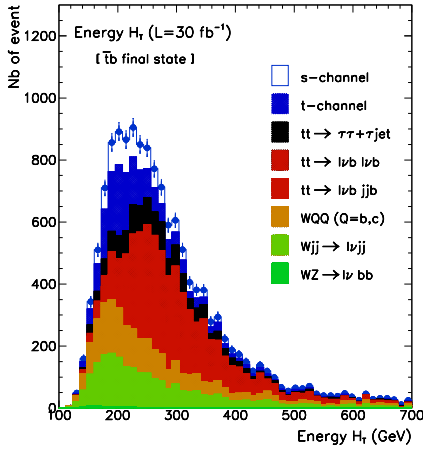


Fig. 3.4.70: Event yield for the H_T distribution for 30 fb^{-1} .

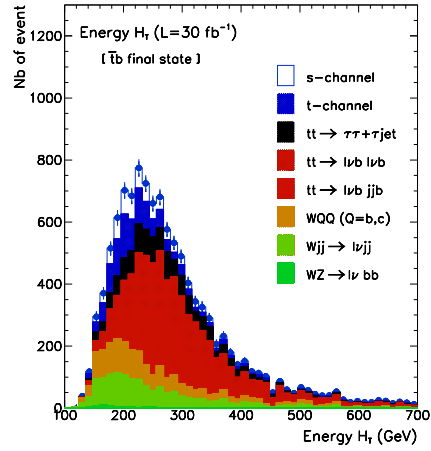


Fig. 3.4.71: Event yield for the $M_{l b}$ distribution for 30 fb^{-1} .

Results have been interpreted as a function of the integrated luminosity. In 2-jet events, a 5×10^{-5} discovery requires about 5 fb^{-1} . The use of the 3-jet samples does not bring any significant improvement since at least 60 fb^{-1} are needed to reach the same yields. The statistical sensitivity to the cross section measurements has also been evaluated from the ratio $\frac{P}{S+B} = \frac{S}{S+B}$ which provides the sensitivity of the signal to signal and background statistical fluctuations. A statistical sensitivity of 7% can be achieved by combining both $t\bar{b}$ and $t\bar{b}$ final state analyses with an integrated luminosity of 30 fb^{-1} . To reduce further the systematic uncertainties associated to the background estimates, we can choose to apply further require-

ments on topological variables. Figure 3.4.70 displays the distribution of the total transverse energy of the events while Fig. 3.4.71 shows the reconstructed (leptonic) top mass after the preselection.

HT window optimization

After the pre-selection stage, the remaining sample is characterized by a low ratio signal over background of about 10% with dominant backgrounds originating from the top pair and $W Q Q$ production. In order to purify the sample, we apply further requirements based on the total transverse energy H_T measured in the event and on the top mass reconstructed from the b jet and the leptonic decays of the W boson.

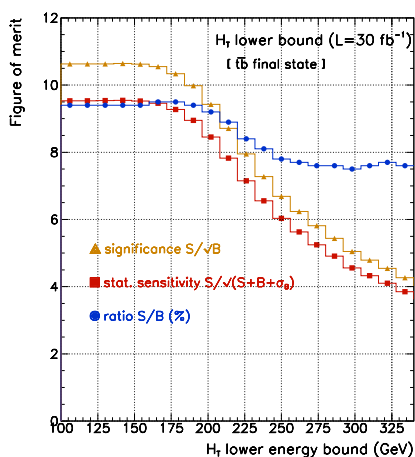


Fig. 3.4.72: Optimization for the H_T lower bound: are shown the ratio S/B , statistical significance and the sensitivity as function of the threshold

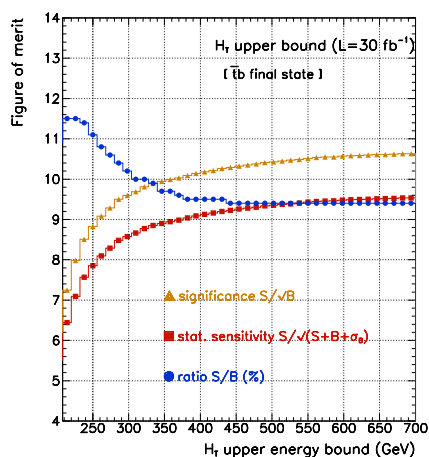


Fig. 3.4.73: Optimization for the H_T upper bound: are shown the ratio S/B , statistical significance and the sensitivity as function of the threshold

In order to optimize the upper and lower bounds applied on H_T , one can use three estimators: the ratio S/B , which reflects the sample purity as function the threshold values; the statistical significance $S = \frac{p}{B}$; and the sensitivity defined as $S = \frac{p}{S + B + \sigma_B}$, which includes the systematic uncertainty in background estimate, set at $\sigma_B = 12\% B$. Figs.3.4.72 and Fig. 3.4.73 show the sensitivity as function of the H_T energy cut for both the lower and upper bounds.

The optimal choice for the window results from a compromise between a minimal loss in statistical sensitivity and a maximal improvement in the purity: the lower threshold is set at 170 GeV while the upper bound is set at 300 GeV. The signal efficiency is decreased by about 40% for the signal. The corresponding loss is about 50% for $t\bar{t}$ events and above 70% for $W Q Q$ and $W + jets$ events, resulting in a slight S/B ratio increase.

Top mass window optimization

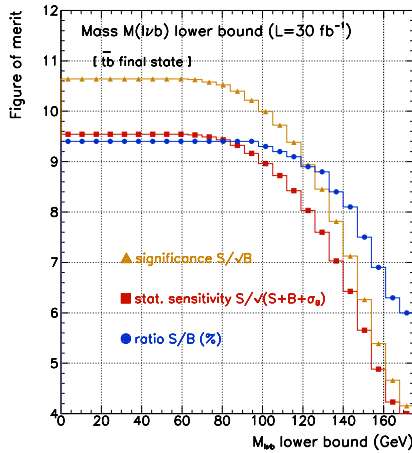


Fig. 3.4.74: Optimization for $M(lb)$ window lower boundary, using the ratio S/B , the significance and the sensitivity as function of the threshold

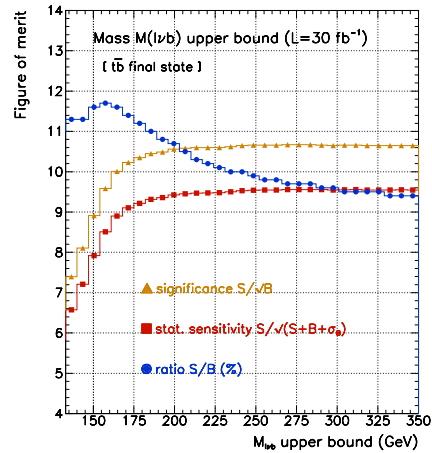


Fig. 3.4.75: Optimization for $M(lb)$ window upper boundary, using the ratio S/B , the significance and the sensitivity as function of the threshold

The optimization of the lowest and upper bounds has been performed in the same way as for the H_T quantity. Fig. 3.4.74 and Fig. 3.4.75 show the sensitivity as function of the $M(lb)$ cut respectively for the lower and the upper bounds. The choice of a reconstructed mass in the $[120;200] \text{ GeV} = c^2$ range increases the ratio S/B by 40% to about 14% at the loss of half the acceptance in signal efficiency. We also estimate the top purity in our sample by using the MC truth information and comparing the true top momentum p_T^{true} and $\phi_{\text{top}}^{\text{true}}$ with the corresponding reconstructed values p_T^{rec} and $\phi_{\text{top}}^{\text{rec}}$. For a match defined by the two requirements $|p_T^{\text{rec}} - p_T^{\text{true}}| < 20 \text{ GeV} = c$ and $|\phi_{\text{top}}^{\text{rec}} - \phi_{\text{top}}^{\text{true}}| < 0.4$ an overall purity above 60% is measured using the highest top P_T criterium. Further studies on this topics are still on going in order to optimize the performance.

Topological selection: statistical precision

Table 3.4.32 reports the number of selected events after the H_T and the top mass criteria have been applied. The signal efficiency is reduced by 2/3 after both criteria have been applied. At the same time, non-top backgrounds are reduced by 80%. In the top pair background, the contamination from "dilepton" events is decreased by 90% while the "lepton+jet" is decreased by 70%. Note that no significant $W + \tau$ events survive the topological selection.

The total number of events expected for an integrated luminosity of 30 fb^{-1} . For the $t\bar{t}$ final state, about 385 signal events survive with 2,760 background events, resulting in an improved S/B ratio of $S/B = 13.9\%$. For the $t\bar{b}$ final state, 275 signal events are remaining for a total background of 2,242, resulting in a S/B ratio of 12.3%. In both cases, the main background is due to the "lepton+jets" top pair production (about 30% of the total), followed by the Wg single-top (27%). Heavy flavour WQQ events now constitute less than 20% of the remaining background, which is about the same order than $W + \text{jets}$ events. Other top pair backgrounds (including tau decays) and WZ production appear at

processes	tb final state		tb final state	
s-channel	385	2	275	1
t-channel	666	30	410	20
W+t channel	–	–	–	–
tt background				
tt ! e b jjb	750	35	750	35
tt ! e b e b	395	20	395	20
tt ! b; b	105	7	105	7
tt ! b; jjb	20	2	20	2
W+jets background				
WQQ	460	20	290	15
W Z ! e ;bb	18	1	12	1
W jj ! e ;jj	350	20	260	15

Table 3.4.32: Number of selected events in the "2b0j" sample expected for an integrated luminosity of 30 fb^{-1} for both final states. Uncertainties come from Monte Carlo statistics only

a negligible level.

The statistical sensitivity to the cross section measurement has been re-evaluated after the topological selection. It is obvious that the application of any further selection criterium resulting in a decrease of the number of expected signal events may result in a poor statistical sensitivity.

Systematic uncertainties

Common experimental systematic uncertainties originate from three main sources: the jet energy scale, the b-tagging efficiency and mistag rate, and the modelling of ISR and FSR effects. These sources affect the signal as well as the background the background selection efficiencies.

Jet energy scale

Uncertainty in the jet energy scale affects all jet P_T distributions, hence resulting in a bias in the jet selection efficiency. This also has a significant impact on the jet veto performance that is used in our analysis as well as in the determination of the missing energy, H_T and the reconstructed top mass that are used in the topological selection. In order to quantify such effect, the energy of each jet has been shifted up and down in the Monte Carlo by a value corresponding to the jet P_T uncertainty, and half of the difference in the selection efficiency was taken as a systematic uncertainty. A variation of 3.5% is measured in the signal efficiency ϵ_W , resulting in a relative error of 1.8% due to the uncertainty of the jet energy scale. For the background processes, this effect is shown to have a poor impact on to the top pair production. On the other hand, the rejection of W+jets events, which contain softer jets,

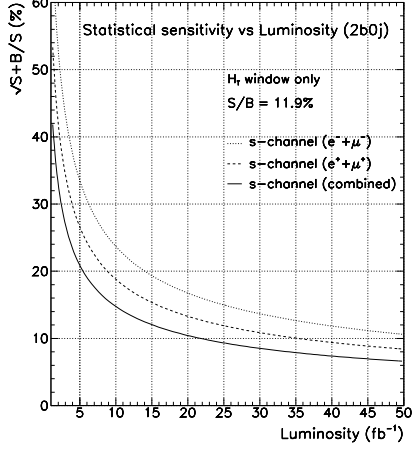


Fig. 3.4.76: Statistical sensitivity as a function of the integrated luminosity as only the H_T requirement is applied.

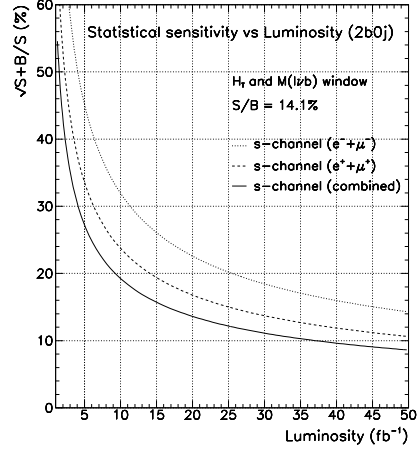


Fig. 3.4.77: Statistical sensitivity as a function of the integrated luminosity after the topological selection.

depends significantly from the knowledge of the jet energy scale. A total background variation of 6.8% is measured, thus resulting in a systematic uncertainty of 3.4%.

b-tagging efficiency

Another source of systematics comes from the imperfect knowledge of the b-tagging efficiency and mistag rates. As can be inferred from the selection described in Section 3 b-tagging performance is crucial for background rejection. A variation of b-tagging efficiency thus directly results in a variation of the relative contribution of each sample.

For signal events a 2.6% change in the selection efficiency is seen for a 1% variation of the b-tagging efficiency. This change is similar for most backgrounds, with a variation of 2.7% for the summed backgrounds. This results in a relatively stable S/B ratio over the full range of variation of ϵ_b .

This observation results in a reduced dependence of the cross-section measurement to the exact determination of the b-tagging efficiency. In our case, a 5% variation in the b-tagging efficiency will result in a 13.5% change in the number of selected signal and background events. It is obvious that, the S/B ratio being stable, this number does not reflect the uncertainty in the cross-section. We however conservatively quote half of this number as our systematics associated to the cross-section measurement, ie: 7.0% (including the MC statistics).

The uncertainty on the mistag rate impacts mainly the rejection of W+jets events : in our case a 5% mistag rate results in a 10% variation of the W+jets events. This translates to an uncertainty of 3.5% in the total background estimate. The total uncertainty quoted is thus 8.0%. This number however makes of the b-tagging and mistag rate knowledge one of our main source of errors, which is expected from a double-tag based analysis.

ISR/FSR modelling

Another source of uncertainty is the modelling of the event and the effects of initial and final gluon radiations. ISR dramatically directly affects the jet multiplicity of the event, while uncertainty in the FSR modelling affects the determination of the jet energy scale, which may result in a change of the selection efficiency. For b-jets the effects are particularly significant in the WQQ selection, as seen in Fig. 3.4.78. We quantified this effect by switching ON and OFF the ISR and the FSR separately, and by taking 10% of the observed shift in selection efficiency as a systematic. This value constitutes a (very) conservative approach and corresponds to the expected precision of the strong coupling constant α_s determination at the LHC [175].

For the signal events selection, a relative variation of 4.9% is seen for the ISR alone while an effect of 6.0% is observed for the FSR. We thus quote an error of 7.9% as the sum of both effects.

Backgrounds are differently affected by the ISR/FSR modelling. Top pair backgrounds are increased as the ISR are switched OFF because of the increased population of 2-jet events. On the other hand, as the FSR is switched OFF, most of those processes are reduced compared to signal variations. FSR particularly affects the WQQ events selection, since switching Off the FSR tend to increase the jet energy and thus the jet selection efficiency. A factor 20% is found to affect the WQQ selection. The total effect on the sum of all backgrounds is estimated as the quadratic sum of both ISR and FSR effects. An uncertainty of 7.3% for the total background. This number is clearly an overestimate of this effect.

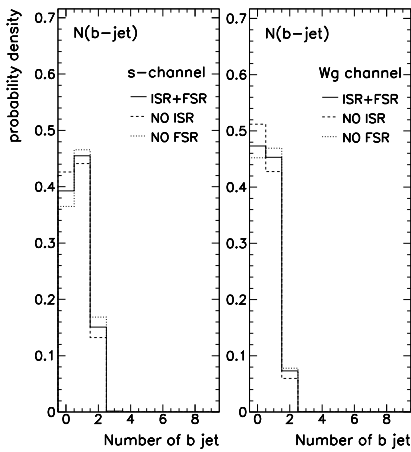


Fig. 3.4.78: Impact of ISR and FSR on b-jet multiplicity for s- and Wg single-top channels

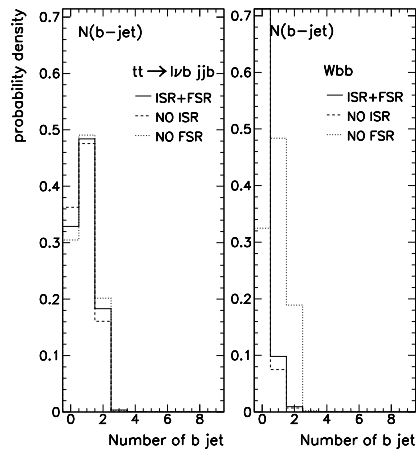


Fig. 3.4.79: Impact of ISR and FSR on b-jet multiplicity for top pair and WQQ productions

Background estimates

All of the background estimates rely upon Monte Carlo that are used to compute the selection efficiencies. Those generators employ LO matrix element for the hard parton scattering followed by parton showering to simulate radiation and fragmentation. We use in our cases PYTHIA v6.2, TopRex v4.1 and HERWIG v6.4 for the event generation, and normalized the event yields to the NLO cross-section. However, even at NLO the theoretical sources of uncertainty are significant. As a consequence, direct measurements from data itself will be required.

The sources of theoretical uncertainties come from the choice of the renormalization and factorization scales, the choice of the parton distribution functions and the uncertainty in the input parameters such as the top mass and the b-fragmentation function. The single-top cross-section is expected to decrease with the top mass value: a 4 GeV uncertainty results in an 9% uncertainty in the s-channel cross-section and 5% in the t-channel. The knowledge of the PDF (b- and gluon-PDF for t-channel) contributes significantly to the errors. Regarding the top pair production, the cross-section including the NLO+NLL corrections is quoted with an uncertainty of 12%. This number results of a contribution from the scale uncertainty (about 6%) and from the PDF where the level is at 10% (MRST vs CTEQ5M) for $m_t = 175 \text{ GeV}$. The difference between the two sets is about 3% but is highly sensitive to the input value used for $\alpha_s(M_Z)$.

Regarding the Wbb ($e b\bar{b} + X$) production, recent computations with MCFM lead to an uncertainty of 20% in the NLO cross-sections, this result being obtained with the use of a LHC-like selection applied on the final lepton and jets. Regarding W +jet backgrounds, a conservative approach has been chosen and an uncertainty of 20% is quoted as well. Summing all background contributions (in the fraction of selected events) result in a total theoretical error of 11%. Note that the input top mass also has an impact in the selection efficiencies determination, the jet P_T distributions depending upon the mass of the decaying particle. For a higher top mass value, jet P_T distributions are shifted towards higher values, leading to a better pre-selection efficiency for all top events production: an effect of about 2% is seen in the selection efficiency of W and $W + t$ channels as one goes from 175 to 180 $\text{GeV} = c^2$. This is considered as negligible in regards to the other sources of error.

Summary: s-channel cross section measurement in ATLAS

The precision on the cross section has been assessed for an integrated luminosity of 30 fb^{-1} at different stages of the analysis. After the simple preselection stage, results show a good statistical sensitivity but higher level of systematic uncertainties:

$$\text{---} = 7\%_{\text{stat}} \quad 13\%_{\text{exp}} \quad 11\%_{\text{bckgd theo}} \quad 5\%_{\text{lum i}}$$

Using both the H_T and reconstructed top mass results in a significantly reduced level of systematics at the price of a loss in statistical sensitivity:

$$\text{---} = 12\%_{\text{stat}} \quad 12\%_{\text{exp}} \quad 11\%_{\text{bckgd theo}} \quad 5\%_{\text{lum i}}$$

In all cases, systematic errors are expected to dominate the cross section determination. Experimental effects are dominated by the ISR/FSR modelling effects because of the importance of the jet multiplicity requirement in the selection. The other significant effect comes from the knowledge of the b-tag and

mistag rates, since the double-tag also constitutes a central point in the selection. It is obvious that the error associated to the ISR/FSR modeling is an overestimation, and that this uncertainty will be constrained by comparison of Drell-Yann data and the event generators. B-tagging should also benefit from the use of a huge b-enriched control sample. Finally, theoretical uncertainties are the same order of magnitude of the statistical errors. They should be reducible if we are able to estimate the background contamination directly from the data. Besides, the uncertainty in the parton structure functions should also be reduced by constraints from the W leptonic asymmetry measurements.

t-channel cross section measurement

The measurement of the t-channel cross section benefits from a significantly higher statistics compared to the s-channel analysis. The final topology is also significantly different of that of the s-channel, and leads to a specific selection. The present analysis can be found in Ref. [174].

Event selection

We select t-channel events in the channel where the W boson decays leptonically. This leads to requirements on the presence of a high P_T lepton and a high missing transverse energy. To remove events with two leptons like $Z \rightarrow \ell^+ \ell^-$ and dileptonic top pairs, a veto is performed in any pairs of leptons with opposite signs and above $10 \text{ GeV} = c$, just as in the s-channel analysis.

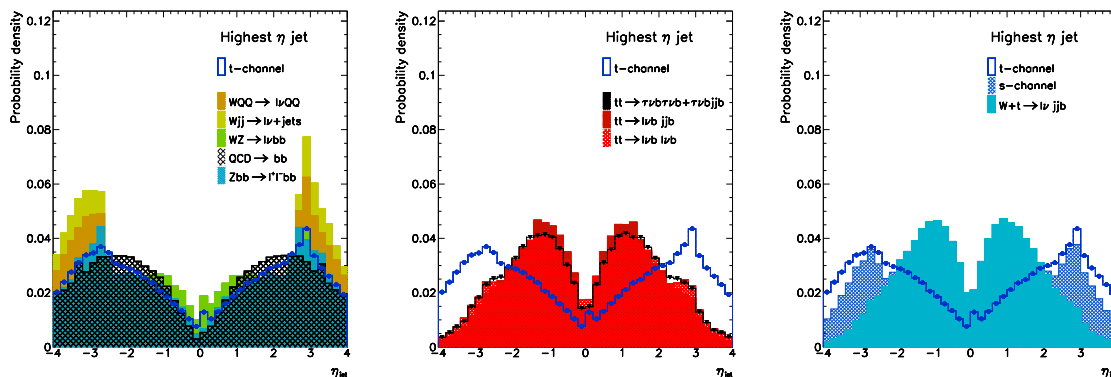


Fig. 3.4.80: Pseudo-rapidity of the highest jet in two jet events for signal and backgrounds.

The situation is different from the latter analysis in the domain of reconstructed jets. More than 60% of t-channel events have two or three jets. Among those jets, one points towards the forward region, beyond the pseudo-rapidity range $|\eta_{jet}| > 2.5$. This is a distinct feature which is used to discriminate from the other top quark production sources, as shown in Fig. 3.4.80. This forward jet must also pass a high P_T threshold in order to reduce the contamination from W +jets, WQQ and QCD , WZ and QCD events. Figure 3.4.81 displays the momentum of the selected forward jet in 2 jet final state events.

Among the two or three jets, at least one jet must be b tagged in the central pseudo-rapidity region. The other b jet present in the final state is usually emitted towards the very forward region, outside the tracker acceptance and thus out of reach of the b-tagging algorithm in most cases.

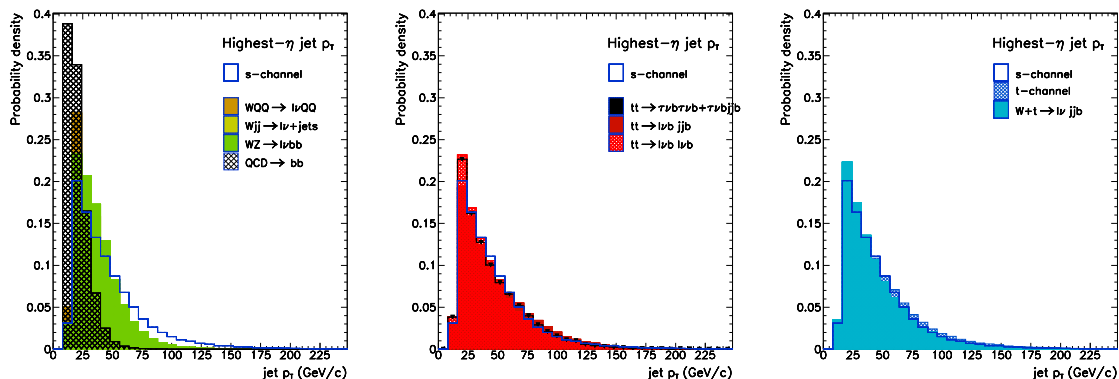


Fig. 3.4.81: Transverse momentum for the forward jet in two jet events and for signal and backgrounds.

Efficiencies and background rejection

A preliminary analysis has been developed in ATLAS. The selection requires the presence of an isolated high P_T lepton above $25 \text{ GeV} = c$, missing transverse energy above $25 \text{ GeV} = c$ and makes use of a secondary lepton veto. At least one jet must be b tagged with a transverse momentum above $50 \text{ GeV} = c$. The event must contain a forward jet above the pseudo-rapidity $j_{jet} \eta > 2.5$ with a transverse momentum above $50 \text{ GeV} = c$. Selected events are then splitted into two 2 jet and 3 jet final states. Like in the s-channel analysis, the selection is splitted into the two final states $t\bar{b}$ and $\bar{t}b$ in order to reduce the contamination from the charge symmetric top pair production. Table 3.4.33 reports the event yields expected in the two final states for an integrated luminosity of 10 fb^{-1} .

In two-jet final state, signal events are selected with an efficiency of about 1%, leading to a total of 3,000 events in 10 fb^{-1} . The dominant background comes from the WQQ production despite the central high P_T b jet requirement. The efficiency for those events is well below the per mill level. Remaining backgrounds consists in top pair events in both the “dilepton” and “lepton+jets” channels, although the low multiplicity cut removes most of them. Finally, the contamination from the other (s- and Wt-) single-top channels represents less than 5% of the selected events. At the end, the ratio S/B is above 3 for an integrated luminosity of 10 fb^{-1} . Figure 3.4.82 displays the event yields for the H_T distribution and an integrated luminosity of 10 fb^{-1} .

In three jet final states, the situation is less favorable because of a higher contamination from high multiplicity events like top pair production. Two situations are considered depending on the number of b tagged jet contained in the event.

For events with exactly one b tagged jet and two light jets, the signal efficiency is slightly above 1%. The dominant background comes from the top pair production in both the “lepton+jets” and the “dilep-

processes	2 jet final state (tbq)		3 jet final state (tbq)		
t-channel	3;130	40	3;410	40	54 2
s-channel	80	1	40	1	negl.
W+t channel	50	2	120	4	negl.
tt background					
tt ! e b jjb	205	10	1;890	35	17 1
tt ! e b e b	215	10	560	15	11 1
tt ! b; b	15	1.5	30	2	negl.
tt ! b; jjb	10	2.5	60	6	negl.
Z/W+jets background					
WQQ	230	15	60	5	7 2
W jj ! e ;jj	120	8	30	3	negl.

Table 3.4.33: Number of selected events in the "1b1j", "2b1j" and "1b2j" samples expected for an integrated luminosity of 10 fb^{-1} for tbq final state. Uncertainties come from Monte Carlo statistics only

ton" channels. The contamination from those events amounts to about 40% of the selected sample. As expected, the single-top Wt channel now also constitutes a significant background, representing 2% of the total. The third jet requirement removes most of the W+jet and WQQ backgrounds. The ratio S/B is about 1.2. Figure 3.4.82 displays the corresponding event yields for the H_T distribution and an integrated luminosity of 10 fb^{-1} .

For events composed with 2 b tagged jets and one light (forward) jet, the signal efficiency is decreased to 0.17%. This is due to the fact that the second b jet present in such events is expected to point towards the very forward region, thus being out of the tracker acceptance. About 50 events are expected in 10 fb^{-1} . In this case, dominant backgrounds are the top pair events. The ratio S/B is about 1.5, making this channel the least significant in terms of statistical precision.

In this preliminary analysis, no use is made of the H_T nor the reconstructed leptonic top mass. We may consider using those variables to purify the selected sample. This may be the case if a better control of the systematic uncertainty associated to the background estimates is required.

Summary: t-channel cross section measurement in ATLAS

With a cross-section corresponding to about a third of that for the top pair production, the t-channel processes will be the first single-top production accessible with the early data at the LHC. Contrary to the situation at the TeVatron, the main background comes from the top pair production, well above the W+jets and WQQ events. The statistical precision is about 4% for an integrated luminosity of 1 fb^{-1} and well below 1% with 30 fb^{-1} .

This measurement will however be limited by the systematic errors. The dominant uncertainties comes from the jet energy scale and the ISR/FSR modeling, which affect directly the selection efficien-

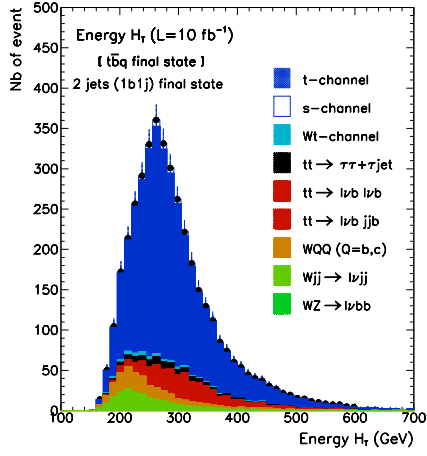


Fig. 3.4.82: Event yields for the H_T distribution for a $t\bar{t}q$ 2-jet final state events for 10 fb^{-1} .

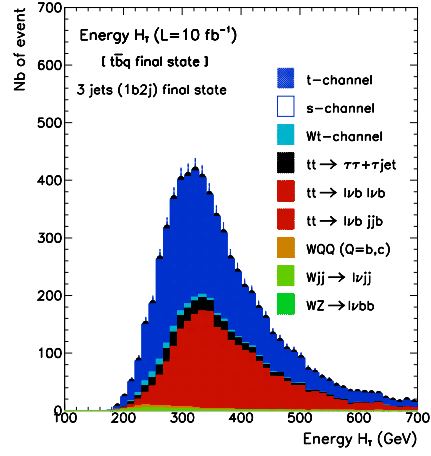


Fig. 3.4.83: Event yields for the H_T distribution for a $t\bar{t}q$ 3-jet final state events for 10 fb^{-1} .

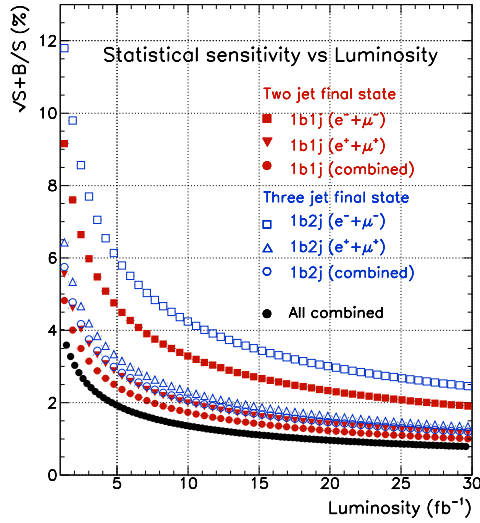


Fig. 3.4.84: Statistical precision as a function of the luminosity for the t -channel analysis in two- and three-jet events and for $t\bar{t}q$ and $t\bar{t}b$ final states. The result of the combination of all channels is also shown.

cies for both signal and backgrounds. The b-tagging systematic error is expected to be reduced compared to the s-channel analysis where two b-tags were required. The uncertainty associated to the background estimate is again a major source of error and, as in the s-channel case, will require the use of data itself. With a simple selection, the precision on the cross-section is expected to be:

$$\delta = 1.0\%_{\text{stat}} \quad 11.0\%_{\text{exp}} \quad 6\%_{\text{bckgd theo}} \quad 5\%_{\text{lim i for L}} = 30 \text{ fb}^{-1}$$

which shows how sensitive the selection is to the experimental and background estimates effects. Same remarks as for the s-channel measurement apply.

Wt associate production cross section measurement

The $W + t$ -channel is the second largest source of single top production. Due to the presence of a second W in the final state, Wt events are topologically similar to $t\bar{t}$ background events and are therefore difficult to separate.

Event selection

As for the s and t-channels, we select $W + t$ events by requiring a single high P_T lepton and a high missing transverse energy. Such a selection criterion implies that one W boson decays leptonically and that the second W boson must decay into two jets. Therefore, the selected events have exactly three jets with one of them tagged as a b-jet. This allows to reject part of $t\bar{t}$ background. In addition, by requiring a 2-jet invariant mass within a window around the W mass, it is possible to eliminate most events that do not contain a second W , i.e. all backgrounds other than $t\bar{t}$. Indeed, as shown in Fig. 3.4.85, a sharp peak in the 2-jet invariant mass distribution is observed for the $W + t$ and $t\bar{t}$ events.

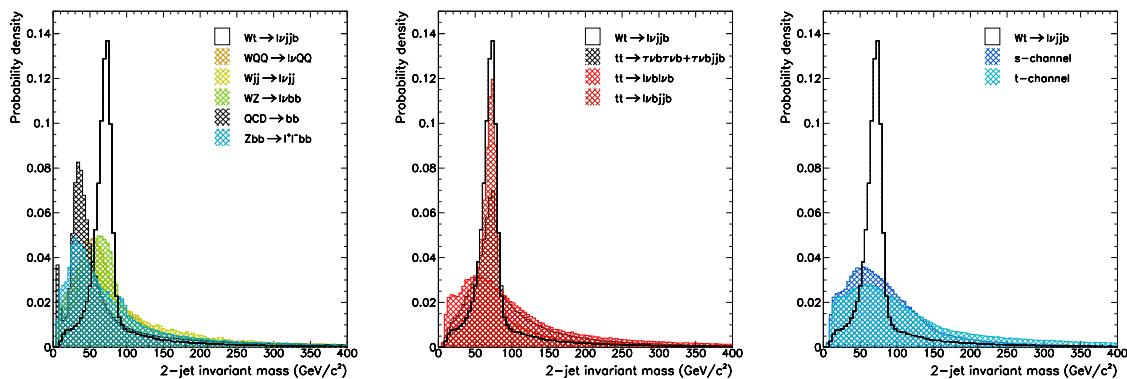


Fig. 3.4.85: 2-jet invariant mass for signal and backgrounds.

Efficiencies and background rejection

The selection for the preliminary analysis presented here requires the presence of an isolated high P_T lepton above $25 \text{ GeV}/c$ and a missing transverse energy above $25 \text{ GeV}/c$. In addition, a secondary lepton veto cut is applied to any lepton above $10 \text{ GeV}/c$ with a sign opposite to that of the selected high P_T lepton. The event must contain, among three jets of P_T above $25 \text{ GeV}/c$, one b-tagged jet with a transverse momentum greater than $50 \text{ GeV}/c$. An additional constraint on the 2-jet invariant mass ($55\text{-}85 \text{ GeV}/c^2$) is required.

The efficiencies are reported in Table 3.4.34. The numbers of events expected for an integrated luminosity of 30 fb^{-1} and the expected individual signal-to-background ratios are also tabulated in Table 3.4.34. The calculated values include only the electron/positron contribution of the leptonic components.

The $W + t$ events are selected with an efficiency of about 4.6%. Top pair events are selected with a global efficiency of around 1.7% (3.3% for the “lepton+jets” channel, which is the main $t\bar{t}$ background). As expected, the other sources of background are greatly reduced by the selection criteria; we obtain efficiencies less than 0.05% for W/Z+jets channels and 0.2%-0.3% for the two other single top production channels.

The predicted global signal-to-background ratio for the $W + t$ -channel is 0.1 and the main background contribution comes from the top pair production in the “lepton+jets” channel.

Process	Efficiency	Nb of events	Individual S/B ratio
W+t-channel	4.58 0.02	12;852 46	
s-channel	0.20 0.01	62 1	206
t-channel	0.34 0.01	2;572 42	5
$t\bar{t}$ background			
$t\bar{t} ! e b j\bar{b}$	3.33 0.01	121;834 331	0.1
$t\bar{t} ! e b e b$	0.27 0.01	794 18	16
$t\bar{t} ! b b$	0.07 0.01	206 9	62
$t\bar{t} ! b j\bar{b}$	0.22 0.01	7;985 121	1.6
W/Z+jets background			
$W b\bar{b} ! e b\bar{b}$	0.006 0.001	negl.	-
$W j\bar{j} ! e j\bar{j}$	negl.	negl.	-
$W Z ! e b\bar{b}$	0.044 0.003	negl.	-
$Z b\bar{b} ! e^+ e^- b\bar{b}$	0.014 0.002	negl.	-

Table 3.4.34: Efficiency, number of events expected for an integrated luminosity of 30 fb^{-1} and individual signal-to-background ratio for single top processes and background channels. Uncertainties come from Monte Carlo statistics only.

The signal-to-background ratio can be slightly improved (by a factor of 10%) by applying further cuts

on the total transverse momentum and on the centrality variable defined as:

$$\text{centrality} = \frac{\text{jet } p_T^{\text{jet}}}{\text{jet } p_T^{\text{jet}}}$$

As we can clearly see in Fig. 3.4.86, centrality values are much larger for the $W + \tau$ events than for most of background events.

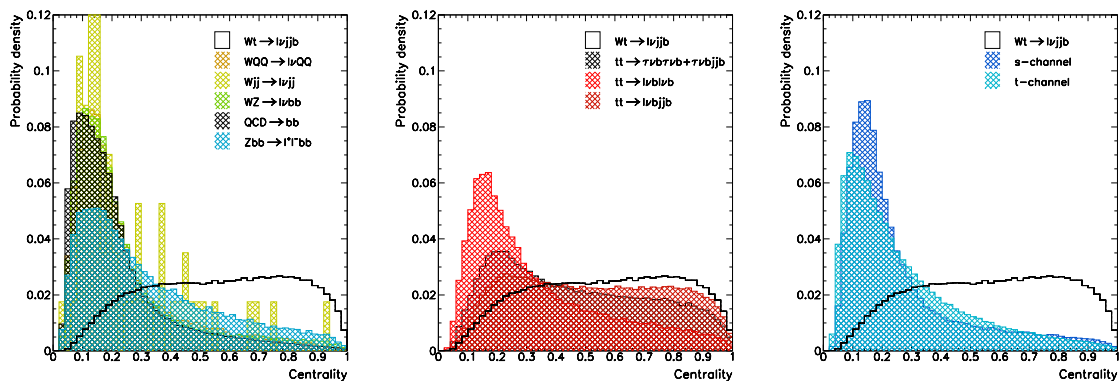


Fig. 3.4.86: Event centrality for signal and backgrounds.

Figs. 3.4.87 and 3.4.88 display the event yields for the total transverse momentum and centrality for an integrated luminosity of 30 fb^{-1} , respectively.

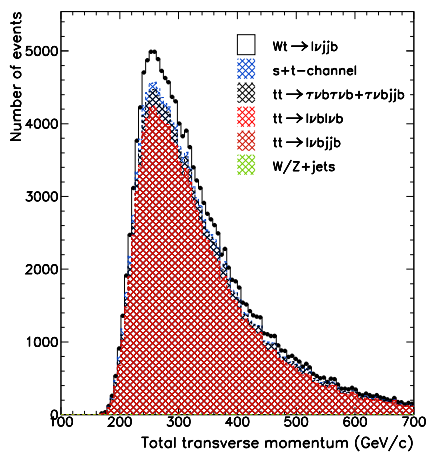


Fig. 3.4.87: Event yields for the total transverse momentum distribution for 30 fb^{-1} .

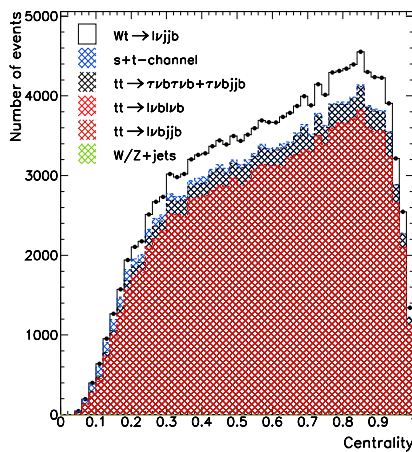


Fig. 3.4.88: Event yields for the centrality distribution for 30 fb^{-1} .

The performance in terms of statistical sensitivity has been determined for the three jet final state events and is shown as a function of the integrated luminosity in Fig. 3.4.89. A 10% sensitivity can be achieved with 1 fb^{-1} by combining both electron and muon channels.

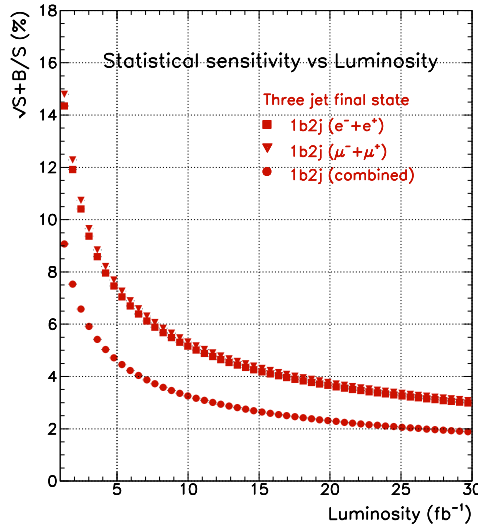


Fig. 3.4.89: Statistical precision as a function of the luminosity for the Wt -channel analysis in three- jet events.

Summary: Wt channel cross-section measurements

The $W + t$ channel analysis benefits from the relative high cross-section of about 70 pb. However, due to high similarities with top pair events, the selection is hampered by a high level of background contamination. This characteristics makes the Wt cross-section very difficult to measure with the early data at the LHC. The chosen strategy is based on the splitting of the event selection into two jet and three jet final states. In both cases, the main background comes from the top pair production with a S/B ratio well below 10%, making the prior precise determination of the top pair production cross-section mandatory. Combining both electron and muon channels as well as all two and three jet final states leads to a statistical precision slightly below 6% for an integrated luminosity of 1 fb^{-1} . This translates into a precision of about 2-3% at the end of the low luminosity run.

Single top studies at CMS

Contributed by: Giammanco, Slabospitsky

This Section summarizes the CMS analyses published in the Physics TDR Vol.II and in Ref. [176] and [177]. All results presented here assume 10 fb^{-1} of integrated luminosity, including the detector uncertainties that will be available at that time (as estimated in Ref. [178]).

Signal and background event simulation

Two generators, SingleTop [179] (based on the CompHEP package [129]) and TopRex [166] were used to generate events for all three single-top production processes. The background processes, namely, $W b\bar{b}$, $W b\bar{b} + j$, and $W + 2j$ were generated with CompHEP, TopReX, MadGraph [128], and Alpgen[180] programs as indicated in the Table 3.4.35. The hard process events containing all needed

information were passed to PYTHIA 6.227 [181] for showering, hadronization and decays of unstable particles. The $t\bar{t}$ and $W + \text{jets}$ background events were generated with the same PYTHIA version. All simulations were done with $M_t = 175 \text{ GeV} = c^2$ and $M_b = 4.7 \text{ GeV} = c^2$, proper considerations of the spin correlations, and the finite W -boson and t -quark widths. The list of the signal and background process cross sections as well as generators used are given in the Table 3.4.35. Both the full simulation chain (OSCAR and ORCA) and a fast simulation (FAMOS) were used.

Process	BR, pb	generator
t-ch. ($W \rightarrow e \nu$)	18 (NLO)	SingleTop (NLO)
t-ch. ($W \rightarrow \mu \nu$)	81.7 (NLO)	TopReX (NLO)
s-ch. ($W \rightarrow \mu \nu$)	3.3 (NLO)	TopReX (NLO)
$t\bar{t}W$ ($2W \rightarrow e \nu$)	6.7 (NLO)	TopReX (NLO)
$t\bar{t}W$ ($1W \rightarrow e \nu$)	33.3 (NLO)	TopReX (NLO)
$t\bar{t}$ (inclusive)	833 (NLO)	PYTHIA (LO)
$W \rightarrow b\bar{b}$ ($W \rightarrow e \nu$)	100 (LO)	TopReX (NLO)
$W \rightarrow b\bar{b} + \text{jets}$ ($W \rightarrow e \nu$)	32.4 (LO)	MadGraph (NLO)
$W + 2j$ ($W \rightarrow e \nu$)	987 (LO)	CompHEP (NLO)
$W + 2j$ ($W \rightarrow \mu \nu$)	2500 (LO)	ALPGEN (LO)
$Z \rightarrow e^+ e^- + b\bar{b}$	116 (LO)	CompHEP (NLO)

Table 3.4.35: Cross section values (including branching ratio and kinematic cuts) and generators for the signal and background processes (here $e = e; \mu$). Different generator-level cuts are applied.

Reconstruction algorithms and triggers

A detailed description of the reconstruction algorithms and triggers used in the single top studies can be found in Ref. [178]. A short description is included below. Muons are reconstructed by using the standard algorithm combining tracker and muon chamber information; isolation criteria are based on tracker and calorimeter information. The electrons are reconstructed by combining tracker and ECAL information. The jets are reconstructed from the hadronic calorimeter signals by the Iterative Cone algorithm with the cone size of 0.5; for the calibration both the Monte Carlo (in the t -channel analysis) and the $W + \text{jets}$ (in the $t\bar{t}W$ - and s -channel) methods are used. For b -tagging a probability algorithm based on the impact parameter of the tracks is used.

The **transverse missing energy** is reconstructed as follows:

$$\tilde{E}_T = \sum_X \tilde{P}_T^X + \sum_X E_T^{\text{tower } X} + \sum_X (E_{T, \text{jet}}^{\text{calib}}) (E_{T, \text{jet}}^{\text{raw}}) \quad (3.4.28)$$

where E_T^{tower} is the sum of transverse energy of towers, $E_{T, \text{jet}}^{\text{calib}}$ ($E_{T, \text{jet}}^{\text{raw}}$) is the transverse energy of calibrated (uncalibrated) jets. For the final states with one isolated lepton the neutrino (\tilde{E}_T) longitudinal component, $P_{z; \nu}$, is extracted from the quadratic equation:

$$M_W^2 = 2 E_{\tilde{E}_T} P_{z; \nu}^2 + (\tilde{E}_T)^2 - \tilde{P}_T^2; \quad \tilde{E}_T = P_{z; \nu} + P_{z; \nu} \quad (3.4.29)$$

This equation has two solutions:

$$P_{z; j}^{(1,2)} = \frac{A P_{z; j} - \sqrt{A^2 P_{z; j}^2 - P_{T; j}^2}}{P_{T; j}^2}; \text{ where } A = \frac{M_W^2}{2} + P_{T; j} \sqrt{E_{T; j}^2 - P_{T; j}^2} \quad (3.4.30)$$

Among the two solutions of Eq. (3.4.29) the minimal value of $P_{z; j}$ is used for W -boson momentum reconstruction.

About 30% of the events have negative values due to the finite detector resolution and to the presence of extra missing energy. In this case for t-channel analysis the parameter M_W in Eq. (3.4.30) is increased until it becomes zero. Using this value of M_W , $P_{z; j}$ is calculated from Eq. (3.4.30). For the $t\bar{t}$ and s-channels analyses, only the real part of $P_{z; j}$ is used for further analysis.

The **transverse mass of the W -boson** is defined as

$$M_T^W = \sqrt{2(P_{T; j} \sqrt{E_{T; j}^2 - P_{T; j}^2} - \vec{P}_{T; j} \cdot \vec{E}_{T; j})} \quad (3.4.31)$$

The **sum of the transverse momentum vectors** of all reconstructed objects

$$\vec{P}_{T; j} + \vec{E}_{T; j} + \sum_i \vec{E}_{T; j, jet; i} \quad (3.4.32)$$

is found to be very effective for signal/background separation.

The **“jet charge”** (Q_j) is defined as the sum of the charges of the tracks inside the jet cone, weighted over the projections of the track momenta along the jet axis.

The **lepton isolation** criterion used is to sum the p_T of all the tracks in a cone of $R < 0.2$ around the lepton track, and to reject the event if this sum is greater than 5% of the lepton p_T .

The present study is based on leptonic decay channels ($e e$ or $\mu \mu$) of the W -boson. The signal is triggered by the trigger on leptons. The HLT p_T thresholds from the CMS DAQ-TDR are assumed: 19 GeV (≥ 29 GeV) for the single muon (electron); with $j_j \geq 2.1$ and $j_e \geq 2.4$.

t-channel cross section measurement

The analysis presented in Ref. [176] makes use of muonic decays of the top. The final state in t-channel includes one isolated muon, missing energy (neutrino), one or two jets from b-quarks, and one “forward” hadronic jet. A specific feature of single top events is production of a light jet in the forward/backward direction (see Figs. 3.4.90) providing an additional possibility for background suppression. The additional b-quark is produced with small transverse momentum, so this analysis requires only two jets, one of them b-tagged.

The selection requires:

only one isolated muon with $p_T > 19$ GeV and $j_j < 2.1$ (HLT selection);

$E_{miss} > 40$ GeV;

at least two hadronic uncalibrated jets, with $p_T > 20$ GeV;

at least one of the selected jets should pass the b-tag;

the second (light) jet should be in the forward region ($|j_L| > 2.5$);

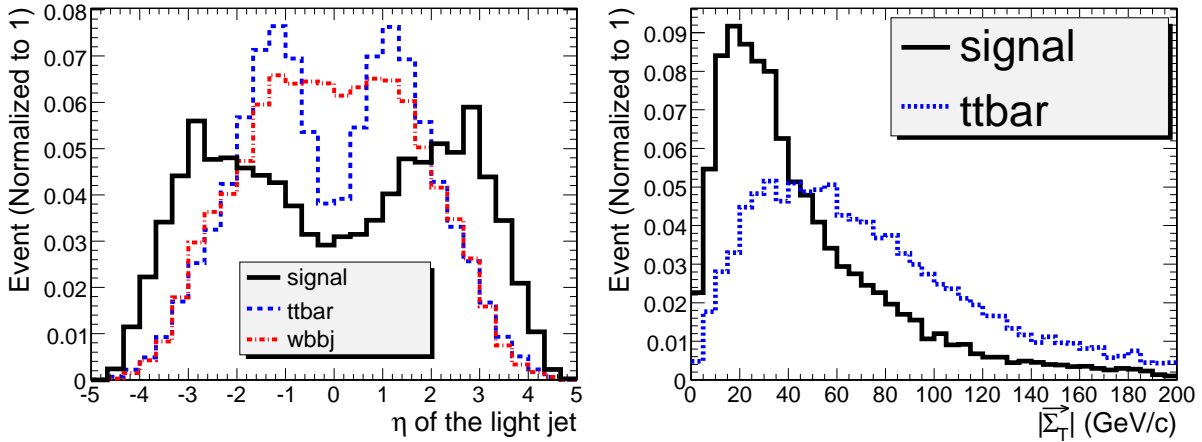


Fig. 3.4.90: The distributions of pseudorapidity (η) of the light jet (left), and of $\tilde{\gamma}_T$ (j) (right).

after calibration these two jets must have $p_T^{\text{calib}} > 35 \text{ GeV}$ and no other hadronic jets with $p_T^{\text{calib}} > 35 \text{ GeV}$ is allowed (jet veto).

The GARCON program [182] is used for further optimization of the cuts. The signal-over-background ratio times significance is chosen as an optimization criterion, obtaining:

b-jet: $p_T > 35.0 \text{ GeV}$, $j_j < 2.5$ and b-tag discriminator > 2.4 ;

light forward: $p_T > 40.0 \text{ GeV}$ and $j_j > 2.5$;

$\tilde{\gamma}_T$ cut window: $(0.0, 43.5) \text{ GeV}$; $50 < M_T^W < 120 \text{ GeV}$

reconstructed top mass window: $110 \text{ GeV} < M_{\text{rec}}(bW) < 210 \text{ GeV}$.

	signal	tt	w bbj	w j	w jj
N(events) at 10 fb^{-1}	$1.8 \cdot 10^5$	$8.33 \cdot 10^6$	$3.24 \cdot 10^5$	$9.7 \cdot 10^7$	$9.9 \cdot 10^5$
isolated muon	0.73	0.14	0.52	0.16	0.81
$p_{T_B} > p_{T_j} > E_T$	0.036	$6.4 \cdot 10^3$	$3.4 \cdot 10^3$	$9 \cdot 10^6$	$3 \cdot 10^3$
veto on 3 rd jet	0.021	$5.8 \cdot 10^4$	$1.6 \cdot 10^3$	$4 \cdot 10^6$	$1.1 \cdot 10^3$
$0.0 < \tilde{\gamma}_T < 43.5 \text{ GeV}$	0.018	$4.1 \cdot 10^4$	$1.2 \cdot 10^3$	$4 \cdot 10^6$	$6.8 \cdot 10^4$
$50 < M_T^W < 120$	0.015	$2.2 \cdot 10^4$	$9.6 \cdot 10^4$	$1 \cdot 10^6$	$5.4 \cdot 10^4$
$110 < M_{\text{rec}}(bW) < 210$	0.013	$1.4 \cdot 10^4$	$5.8 \cdot 10^4$	0	$4.1 \cdot 10^4$
Number of events	2389	1188	195	0	402

in GeV

Table 3.4.36: Number of events (t-channel) and cumulative efficiencies for each cut used in the analysis of t-channel single top production. The symbol “ $p_{T_B} > p_{T_j} > E_T$ ” means: $p_{T_B} > 35 \text{ GeV}$, $p_{T_j} > 40 \text{ GeV}$, $j_j > 2.5$, $E_T > 40 \text{ GeV}$.

The efficiencies of these cuts and the resulting number of events are given in the Table 3.4.36. The resulting signal-to-background ratio and the significance are: $N_S/N_B = 1.34$ and $S_{\text{stat}} = \frac{p}{N_S + N_B} = 37.0$. The final distribution of the reconstructed top mass is shown in Fig. 3.4.91.

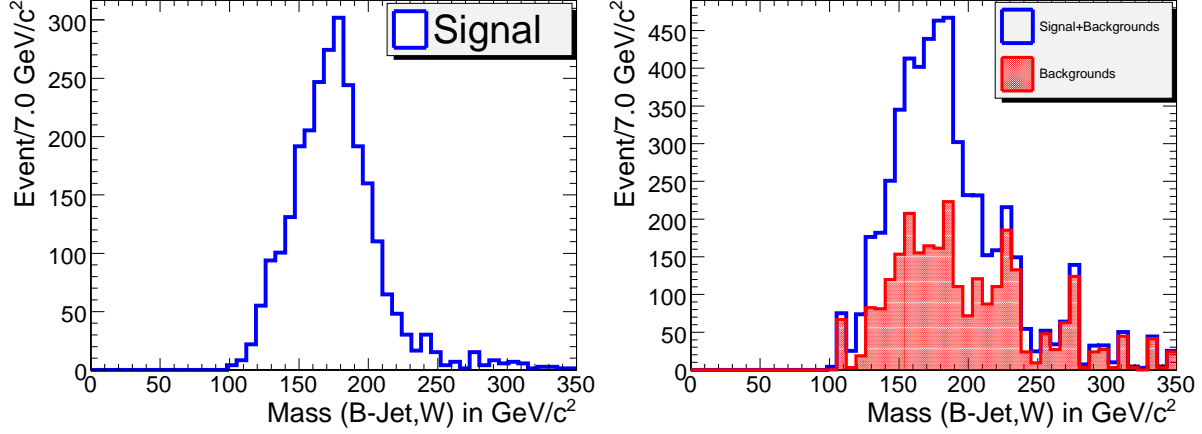


Fig. 3.4.91: The distribution on the reconstructed top mass, for signal only (left) and with background included (right).

sample	selected	N_{th}	JES	$N_{b\ tag}$	N_{syst}	N_{stat}
t-channel	2389	96	71	96	153	49
$t\bar{t}$	1188	59	73	48	105	34
$W\ b\bar{b}j$	195	33	6	8	35	14
$W\ jj$	402	20	0	16	26	20

Table 3.4.37: Number of selected events (t-channel) at 10 fb^{-1} with uncertainties due to different sources. N_{syst} represents the theoretical, JES and b-tagging uncertainties. N_{stat} is expected statistical uncertainty.

The systematic uncertainties (see Section 3.4) evaluated for 10 fb^{-1} are given in Table 3.4.37. In summary, the statistical error is 2.7%, the total systematic error excluding the 5% luminosity uncertainty is 8%, resulting in a total error of 10%.

W t associated production cross section measurement

The $pp \rightarrow t\bar{t}W$ process contains two W-bosons and a b-quark in the final state. The final states considered in Ref. [177] are $l^+l^-\cancel{E}_T b$ and $l^-\cancel{E}_T bjj$ for the di-leptonic and semi-leptonic modes, respectively. The dominant background arises from $t\bar{t}$ production. Other backgrounds are t- and s-channel single top production, $W\ b\bar{b}j$, $W + jets$, $W\ W + jets$, and to a lesser extent QCD multi-jet background.

Jet quality requirements and extra jet reduction

The most significant difference between $t\bar{t}W$ events and $t\bar{t}$ events is the number of jets in the final state. However, most of the time there are also additional jets due to the underlying event, pile-up or calorimeter noise. These “extra jets” were identified and excluded from the counting by consideration

of five jet quality variables (see [177]). It was found that the most discriminating variables are E_T^{max} (the maximum tower E_T in a cone of 0.5) and N_{track} (the number of associated tracks). A Fisher discriminant [183] (F) is constructed from the jet quality variables to separate real jets from extra jets. Each jet is classified value F into one of three categories: good ($F < 0.5$), loose ($0.5 < F < 1.0$) and bad ($F > 1.0$) jets. This method yields 84.3% efficiency on true jets and rejects 86.9% of extra jets. Only “good” jets and “loose” jets are used in preselection and event reconstruction. The jet multiplicity after the extra jet reduction in semi-leptonic channels reveals that the number of good jets peaks at the 2 and 3 jet bins for signal events, and at the 3 and 4 jet bins for $t\bar{t}$ backgrounds.

Event selection and reconstruction

The kinematic cuts used for this study are presented in Table 3.4.38 and Table 3.4.39. For the semi-leptonic channel, two non- b -like jets with $m_{jj} < 115 \text{ GeV} = c^2$ are used for reconstruction of the W -boson (that decays hadronically). In events with a 4th jet that survives jet veto cuts, it is required that the invariant mass of the 4th jet with any of the selected non- b -like jets must be outside a window of $M_W \pm 20 \text{ GeV} = c^2$. For the leptonic decays of the W -boson it is required that $M_T^W < 120 \text{ GeV} = c^2$.

Leptons	Jets
$j(e)j < 2:4, j(\mu)j < 2:1$ $p_T(e; \mu) > 20 \text{ GeV} = c$ no other lepton with $p_T > 5 \text{ GeV} = c$	leading jet: $j < 2:4, p_T > 60 \text{ GeV} = c, \text{disc} > 0$ at most one extra jet No other jets with $p_T > 20 \text{ GeV} = c$
Missing $E_T: E_T > 20 \text{ GeV}$	

Table 3.4.38: Kinematic cuts used in the di-leptonic channel. The final electron and muon should have the opposite charges.

Leptons
$p_T(e) > 30 \text{ GeV} = c, p_T(\mu) > 20 \text{ GeV} = c, j(e)j < 2:4, j(\mu)j < 2:1$ no other lepton $p_T > 10 \text{ GeV} = c$
Jets (after removing all bad quality jets)
b -like jet: good quality, $\text{disc} > 2, j < 2:5, p_T > 35 \text{ GeV} = c$ non- b -like jet: good quality, $j < 3:0, \text{disc} < 0$ if $j < 2:5, p_T > 35 \text{ GeV} = c$ Jet counting: one b -like jet and 2 non- b -like jets Jet veto: no other “good” or “loose” jets with $p_T > 20 \text{ GeV} = c$ and $j < 3$
Missing $E_T: E_T > 40 \text{ GeV}$

Table 3.4.39: Kinematic cuts used in the semi-leptonic channel. The presence of a good fourth jet would veto the whole event.

To find the correct pairing of b -jet and reconstructed W -boson (coming from top decay) the following variables were used: the p_T of (b, W) systems; the separation of the b -jet with each of the W in $(\eta; \phi)$ space; the “charges” of jets (see Section 3.4) and W -bosons (see Ref. [177] for details). A Fisher discriminant based on these variables is used for discriminating leptonic top events from hadronic

top events. A cut of 0.56 is optimal in separating these 2 types of events, and 72% of the events are correctly paired.

To further enhance the signal to background ratio the following “global” cuts are applied:

Efficiency of the reconstructed $t\bar{t}$ system: $\epsilon_{\text{eff}}(t\bar{t}) > 60 \text{ GeV} = c$.

Scalar sum of transverse energies H_T : $H_T < 850 \text{ GeV}$.

Reconstructed top quark mass: $110 \text{ GeV} < m(t) < 230 \text{ GeV} = c$.

Efficiency of the reconstructed top quark: $20 \text{ GeV} = c < p_T(t) < 200 \text{ GeV} = c$.

Efficiencies and expected yields

The efficiencies estimated with Monte Carlo samples are converted to the effective cross sections by multiplying the production cross sections of each process. The effective cross sections, as well as the expected yields with 10 fb^{-1} of data for all signal and background samples, are shown in Table 3.4.40 and 3.4.41. The signal to background ratio is found to be 0.37 for di-leptonic channel and 0.18 for semi-leptonic channel.

	$t\bar{t}$ dil.	$t\bar{t}$ dil.	$t\bar{t}$ oth.	WW dil.	WW oth.	t ch. lept.
Production	6.667	92.222	737.778	11.111	88.889	81.667
HLT	4.865	74.090	346.151	7.674	27.259	41.409
2 leptons	1.944	25.150	21.012	2.574	0.226	2.309
Lepton p_T	0.675	7.919	0.703	0.543	0.012	0.098
1 extra jet	0.459	6.574	0.664	0.416	0.010	0.067
Jet p_T , 1 b-jet	0.307	5.234	0.556	0.339	0.004	0.033
$E_T > 20$	0.184	3.864	0.379	0.017	0.000	0.018
2 jet	0.170	3.640	0.349	0.017	0.000	0.016
2 jet	0.150	2.734	0.221	0.015	0.000	0.012
Final select.	0.057	0.145	0.000	0.006	0.000	0.000
Expected events	567	1450	55	61	10	20

Table 3.4.40: Summary of cross section times branching ratio times efficiencies at each stage of the analysis for the di-leptonic channel. All values are in picobarns. The last row is the expected number of events for 10 fb^{-1} . Multi-jet background has been estimated separately. When only a limit on the number of events is stated, this is due to MC statistics.

The ratio method

The *ratio method* is developed to reduce systematic uncertainties related to the dominant $t\bar{t}$ background. We define a $t\bar{t}$ -rich control region and use ratio of efficiencies to estimate the yield of $t\bar{t}$ in the signal region. The kinematics of $t\bar{t}$ and $t\bar{t}$ are similar so $t\bar{t}$ is present in the control region, therefore the ratio of efficiencies for $t\bar{t}$ is also used. The signal and background yield is determined by the

	tW	tt	t ch.	s ch.	Wbb	W2j	W3j	W4j	Multi-jet
Total cross section	60	833	245	10	300	7500	2166	522	9.73 10 ⁹
HLT	18.9	263.9	39.5	1.52	34.0	1006	300	73	1.86 10 ⁵
Presel. & isolation	9.05	179.4	12.0	0.54	2.15	52	35	12	1325
jet & lepton p _T , jet veto	1.28	18.5	1.31	0.046	0.061	0.60	4.9	1.0	4.23
b-tagging	0.669	6.13	0.476	0.013	0.016	0.10	0.99	0.26	0.85
kinematic cuts	0.223	0.999	0.047	0.002	0.003	0.017	0.101	0.008	0.105
Signal box cuts	0.170	0.771	0.035	0.001	0.001	0.013	0.054	0.008	0.051
Events in 10 fb ⁻¹	1699	7709	351	14	10	130	539	80	508

Table 3.4.41: Summary of cross section times branching ratio times efficiencies at each stage of the analysis for the semi-leptonic channel. All values are in picobarns. The last row is the expected number of events for 10 fb⁻¹.

following equation:

$$S = \frac{R_{tt}(N_s - N_s^o) - (N_c - N_c^o)}{R_{tt} - R_{tW}} ; \quad (3.4.33)$$

$$B = \frac{(N_c - N_c^o) - R_{tW}(N_s - N_s^o)}{R_{tt} - R_{tW} + N_s^o} ; \quad (3.4.34)$$

Here R_x is the ratio of efficiencies $R_x = \epsilon_x(\text{control region})/\epsilon_x(\text{signal region})$ for $x = tt; tW$; N_s (N_c) is total number of events in the signal (control) region; N_s^o (N_c^o) is the estimated number of non- tt background events in the signal (control) region.

For the ratio method to work it is important to find a control region with similar kinematics except with one more jet. It is expected that systematic uncertainties from PDF, JES and b tagging cancel to a large extent, while the luminosity uncertainty drops out for the tt background. The lepton selection and jet quality requirements in the control region is identical to the signal region. The differences are outlined below.

Di-leptonic. A second jet is required with $p_T = 20 - 80$ GeV, $j_j < 2.4$ and b-tagged (disc > 0). No other jets with $p_T > 20$ GeV are allowed. The background region is found to be filled by 97.9% di-leptonic tt , 0.4% other tt decays, 1.6% di-leptonic tW , and 0.1% for leptonic t channel single top while WW +jets yield is negligible.

Semi-leptonic. It requires 2 jets with $p_T > 30$ GeV, 2 more jets with $p_T > 20$ GeV, and no bad jets with $p_T > 20$ GeV. It is required that one of the 2 high- p_T jets is b-tagged (disc > 2), and that both low- p_T jets be not tagged (disc < 0). The $b - W$ pairing is done in the same way, with a 72% correct pairing. It is found that the tt purity in the control region is 93.9%. The non- tt events are mainly composed of W +jets (2.8%), tW (2.0%) and t-channel single top (1.2%). The ratio of efficiencies are found to be $R_{tW} = 0.319$ and $R_{tt} = 3.31$.

The tt cross section does not show up in the ratio method. The effect is 0.8% for t-channel single top and 3.1% for W +jets. It is found to be negligible for other backgrounds. The systematic uncertainties for both channels are shown in table 3.4.42.

Particular care was dedicated to the estimation of the effect of pileup. A difference of 30% between normal pileup and no pileup is used as an estimate of the systematic uncertainty.

Dileptonic mode The analysis is found to be rather sensitive to the pileup, as the relative shift of the

“measured” cross section is $+20.4\%$ for no pileup, and -16.2% for double pileup, while is the difference between the check sample and the reference sample 4.6% (which has purely statistical origin). The value of 6.1% is used as the systematic uncertainty.

Semi-leptonic mode The extracted cross section varies by $+35\%$ for no pileup and -63% for double pile-up so a systematic uncertainty of 10.3% is obtained. This is clearly an overestimation of the effect.

Source	Uncertainty	= (di-lept.)	= (semi-lept.)
Statistical uncertainty	—	8.8%	7.5%
Integrated luminosity	5%	5.4%	7.8%
$t\bar{t}$ cross-section	9%	<i>negligible</i>	<i>negligible</i>
t-channel cross-section	5%	<i>negligible</i>	0.8%
W+jets cross-section	10%	<i>not applicable</i>	3.1%
WW+jets cross-section	10%	1%	<i>not applicable</i>
Jet energy scale	5%-2.5%	19.7 %	9.4%
b tagging efficiency	4% - 5%	8.7 %	3.6%
PDF	1	+4%/-6.0%	1.6%
Pileup	30%	6.1 %	10.3%
MC statistics	—	9.9%	15.2%
Total uncertainty		23.9%(syst.) 9.9%(MC)	16.8%(syst.) 15.2%(MC)

Table 3.4.42: Summary of uncertainties of cross section measurement.

The results from the ratio method were used in the significance calculation. In addition, the uncertainty on the background expectation, evaluated for di-leptonic ($\sigma_B = 9.5\%$) and semi-leptonic ($\sigma_B = +3.6\% = 4.4\%$), was taken into account. The resulting significance is 4.2 for the di-leptonic channel and 5.1 for the semi-leptonic channel. Combining the two channels gives a total significance of 6.4.

s-channel cross section measurement

The present analysis of the s-channel single top production is based on leptonic channels, i.e. the top is identified and reconstructed by its semileptonic decays into $l\bar{b}$ final states, with $l = e; \mu$. For this study, a fast simulation of the CMS detector with FAMOS was used, see [176, 177] for details.

The signal events are triggered by the single lepton triggers. Since this production mode suffers from low statistics, one could envisage the introduction of a combined trigger $e + \text{jet}$, with threshold $19 < E_T < 25$ GeV for the electron (in order to make the electronic sample more coherent with the muonic sample) and $45 < E_T < 55$ GeV for the jet. This value has been chosen to be the same as the threshold for the $e + \text{jet}$ in the already existing $e + \text{jet}$ trigger.

Preselection

The preselection criteria are as follows:

The event has to fire at least one of the previously described triggers (including the proposed $e + j$). The event must contain one isolated lepton (μ or e) with $p_T > 19 \text{ GeV}$ and $j_{j=2:4} > 2.1$ for muons (electrons) and no other lepton above 10 GeV .

Exactly two uncalibrated jets must have $p_T > 30 \text{ GeV}$ and $j_{j=2:5} > 2.5$ and no other jet has to be present with $p_T > 20 \text{ GeV}$.

Both jets should have a positive b-tagging discriminator value.

The event should have $E_T > 30 \text{ GeV}$.

The transverse mass of the W -boson M_T^W should be less than 100 GeV .

Details on the effect of the preselection cuts are given in Table 3.4.43. As before, the multi-jet QCD contribution is neglected.

Cut	s-ch.	t-ch.	tt	W bb	W t(lW ! l)
“HLT”	37.5 0.2%	42.5 0.1%	30.1 0.1%	29.4 0.1%	46.5 0.1%
Isolation	33.7 0.2%	39.0 0.1%	21.7 0.1%	28.2 0.1%	42.3 0.1%
E_T cut	27.3 0.2%	31.9 0.1%	17.4 0.1%	22.6 0.1%	34.4 0.1%
M_T^W cut	23.2 0.2%	26.3 0.1%	13.6 0.1%	18.4 0.1%	29.2 0.1%
$N_{j=2}$	11.9 0.1%	11.5 0.1%	11.9 0.1%	0.88 0.03%	18.5 0.1%
$N_{j=2:4}$	8.9 0.1%	8.2 0.1%	1.84 0.04%	0.76 0.03%	7.09 0.05%
b-tag	3.07 0.07%	0.72 0.02%	0.28 0.02%	0.14 0.01%	0.34 0.01%
N_{ev}	1010 10	5880 70	23300 200	1400 35	1150 40

Table 3.4.43: Efficiencies of the preselection cuts, with respect to the initial number of events. For all process (except of tt) the final W decays into charged lepton ($l = e, \mu$) and neutrino. “HLT” includes the $1e$, 1μ and $e + j$ triggers. N_{ev} is the number of events surviving these cuts (the uncertainties are only those due to the limited Monte Carlo statistics).

Genetic Algorithm analysis

The following observables have been chosen in order to further discriminate between signal and background after preselection: (i) the jet b-tagging discriminants; (ii) the calibrated jet transverse momenta; (iii) the mass of the reconstructed top; (iv) $j_{(t;b)}$ (v) the scalar sum of the transverse momenta of all the reconstructed objects. The reconstructed top quark is formed by the reconstructed W and one of the two b-jets, chosen according to the value of the “jet charge” (Q_j , see Section 3.4). Since in top decays the W and the original b quark have opposite sign of the charge, the jet with Q_j “most opposite” to the W is used for top reconstruction, leading to a probability of 67% to identify the correct pairing.

The cuts on these variables are optimized by means of the GARCON program [182]. The surviving events after these cuts are shown in cascade in Table 3.4.44. With this selection, after an integrated luminosity of 10 fb^{-1} one gets $N_S/N_B = 0.13$.

Systematic uncertainties

In addition to contributions described before, the following sources of systematic uncertainty are considered:

Cut	s-channel	t-channel	$\tau\tau$	$W\ b\bar{b}$
$b\text{-tag}(j_1) > 0.4, b\text{-tag}(j_2) > 0.1$	85%	75%	78%	85%
$p_T(j_1) > 50\text{ GeV}, p_T(j_2) > 50\text{ GeV}$	68%	53%	70%	37%
$120 < M(l_1 b) < 220\text{ GeV}$	52%	34%	46%	26%
$25 < p_T(l_1 b) < 160\text{ GeV}$	48%	32%	43%	26%
$\tau < 20\text{ GeV}$	35%	15%	10.6%	12.5%
$H_T < 340\text{ GeV}$	27%	10.7%	5.4%	11.1%
number of surviving events	273	630	1260	155

Table 3.4.44: Final cuts and their efficiencies, with respect to the preselected samples, for the signal and the main backgrounds. For s- and t-channel and $W\ b\bar{b}$ samples the final W -boson decays into lepton ($e; \mu$) and neutrino. $\tau\tau$ samples includes all W -boson decay modes.

Top mass. The variation of m_τ within $\pm 2\text{ GeV}$ around top mass $m_t = 175\text{ GeV}$ leads to the relative systematic error on the selection efficiency $\delta_{\text{sys}}^{m_t} = 0.5\%$ for the s-channel single top.

Parton Distribution Functions. To extract the dependence on the PDF uncertainty, two different PDF sets were used: CTEQ6.1 and CTEQ6.1M [184]. The result is $\delta_{\text{sys}}^{\text{PDF}} = 0.7\%$.

Initial/Final State Radiation modeling. The model parameters were varied in the ranges $Q_{CD} = 0.25 - 0.1\text{ GeV}$ and $Q_{m\text{ax}}^2$ from 0.25 to 4 \hat{s} . The extreme values of the efficiencies are taken as systematic error: $\delta_{\text{sys}}^{\text{rad}} = 0.5\%$.

The estimation of these errors of theoretical origin has at present been done only for the signal selection. But we expect them to be significant also for the background, in particular ISR/FSR modeling should be very important for the $\tau\tau$ rejection.

sample	selected		JES	b-tag	M_{top}	PDF	ISR/FSR
S: s-channel	273	—	3	11	1.5	2	1.5
B: t-channel	630	25	8	25	—	—	—
B: $\tau\tau$	1260	63	75	50	—	—	—
B: $W\ b\bar{b}$	155	8	7	6	—	—	—

Table 3.4.45: Number of selected events after 10 fb^{-1} and systematic uncertainties.

Background normalization (ratio method)

The $\tau\tau$ events in Table 3.4.45 are, in 41% of the cases, $\tau\tau \rightarrow l^+ b\bar{b}$ events with a lepton missed, and in the remain cases $\tau\tau \rightarrow l^+ b\bar{q}q$ events with two jets missed ($\tau\tau \rightarrow q\bar{q}q\bar{q}$ events give a negligible contribution). These two categories of events are very differently affected by the Jet Energy Scale variation. In general, any variation going in the direction of more jets gives a better rejection of the $\tau\tau \rightarrow l^+ b\bar{q}q$ component with respect to the signal, while the $\tau\tau \rightarrow l^+ b\bar{b}$ events, having two quarks, are affected almost in the same way as the signal.

$\tau\tau! \ell^+ \ell^- + X$ enriched control sample

In this case three jets are required instead of two and only the muon channel is used. The selection efficiency for $\tau\tau! \ell^+ \ell^-$ events is found to be 1:08%. The ratio R_{c1} between the efficiencies in the main sample and in this control sample is $R_{c1} = 0:0149$, whose variations under JES and b-tagging efficiency systematic shifts are $R_{c1} = 0:0015(\text{JES}) \quad 0:0003(\text{b-tag})$.

$\tau\tau! \ell^+ \ell^+ + X$ enriched control sample

This sample is obtained requiring two leptons with different flavours with the opposite sign. The selection efficiency for $\tau\tau! 2\ell$ events is found to be 0:822%. The ratio R_{c2} between the efficiencies in the main sample and in this control sample is $R_{c2} = 0:0681$, whose variations under JES and b-tagging efficiency systematic shifts are $R_{c2} = 0:0010(\text{JES}) \quad 0:0004(\text{b-tag})$.

Results

The number of selected signal (N_S) and background (N_B) events and their estimated uncertainties are listed in Table 3.4.45. The cross section is extracted as

$$= \frac{N_{\text{tot}} - b^0 - R_{c1}(N_{c1} - b_{c1}^0) - R_{c2}(N_{c2} - b_{c2}^0)}{L}; \quad (3.4.35)$$

where b^0 is the sum of the non-top backgrounds in the main sample, N_{c1} and N_{c2} are the total events selected in the two control regions, and b_{c1}^0 and b_{c2}^0 are their contamination by non-top backgrounds, single top and other $\tau\tau$ decays. The statistical error is evaluated to be 18%. The total systematic uncertainty is 31%, where the largest contribution arises from the effect of the JES uncertainty on the $\tau\tau$ single-lepton background. The use of ‘‘Energy Flow’’ techniques, including the charged tracks information, is expected to significantly reduce this uncertainty. The total error, including also the 5% luminosity uncertainty and the statistical error, is 36%.

The contribution from multi-jet backgrounds

A special treatment has been devoted to QCD events with jets, due to the huge cross section. The currently available samples have very small statistics and typically no events remain after the application of pre-selection cuts. Therefore, in order to estimate the impact of the QCD-background the cuts are applied separately, assuming they are uncorrelated.

For t-channel study these cuts are: (a) one isolated muon ($p_T > 19 \text{ GeV} = c$); (b) $E_T > 40 \text{ GeV}$ and only two jets; one B-jet and one light forward jet. It was found a satisfactory suppression of the multi-jet events as compared to other background process ($N_{\text{QCD}} = N_{\text{bckg}} = 6924 = (8:9 \cdot 10^4) = 0:078$ (see [176]) and the QCD-background was not considered in the analysis of the t- and s-channel single top production.

More detailed investigation of this problem was done for $t\bar{W}$ -channel [177]. The selection cuts are arranged into cut groups whose efficiencies are estimated with the Monte Carlo samples. The product of efficiencies is an indicator of the total efficiency.

Three cut groups are used in the di-leptonic channel: lepton, E_T , jet. The same procedure is applied on signal sample to find the ratio of total efficiency to the product of efficiencies. The ratio is

used to correct the product of efficiencies found in multi-jet sample and the result is 5.6 events. Four cut groups are used in the semi-leptonic channel: jets, leptons, kinematics and finally signal region and b tagging. The b tagging requirement is taken out from jets group to have reasonable statistics for the efficiency measurement. By comparing the product of efficiencies with total efficiency of applying cut groups in series, the cut groups are found to be anti-correlated which would result in an over-estimate of the yield. The result of 508 events is kept to be conservative [177].

Systematic uncertainties

The following sources of systematic uncertainty are common for all three channels: (i) the **theoretical errors** to the total rates of the signal is $\sim 4\%$, rising to 10% for $t\bar{W}$. The uncertainties in the background events are assumed to be: 5% for $t\bar{t}$ [30], 17% for $Wbbj$, 7% for $W + jets$, 5% for Wjj [169], and 5% for Wbb (ii) the **jet energy scale (JES) uncertainty**: using a calibration method based on $t\bar{t}$ events, the JES uncertainty after 10 fb^{-1} integrated luminosity is expected to be $\sim 5\%$ ($\sim 2.5\%$) for jets with $p_T > 20 \text{ GeV}$ ($p_T > 50 \text{ GeV}$). In the region between 20 and 50 GeV a linear dependence is assumed. (iii) **b-tagging identification uncertainty**: of $\sim 4\%$ on the overall selection efficiencies is expected on the b-tagging efficiencies. (iv) the **luminosity uncertainty**, expected to be $\sim 5\%$.

Conclusions

The selection strategies developed in CMS for all the three single top production modes, and their effectiveness, are shown taking into account the expected statistics after 10 fb^{-1} . All analyses will be systematics dominated. For the s-channel and $t\bar{W}$ -associated cases, control samples have been proposed in order to constrain the dominant $t\bar{t}$ background.

The resulting signal-to-background ratio and the significance for the t-channel are: $N_S/N_B = 1:34$ and $S_{\text{stat}} = N_S \sqrt{\frac{P}{N_S + N_B}} = 37:0$, with a statistical error of 2.7%, and a systematic error excluding the 5% luminosity uncertainty of 8%, resulting in a total error of 10%.

For $t\bar{W}$ -channel we expect to reach the significance of 4.2 (5.1) for the di-lepton (semi-leptonic) channel, increasing to 6.4 after combining the two channels. The total uncertainty is $\sim 23.9\%$ (syst.) $\sim 9.9\%$ (MC) for di-lepton and $\sim 16.8\%$ (syst.) $\sim 15.2\%$ (MC) for semi-leptonic channels. The total systematic uncertainty for the s-channel is 31%.

The analyses presented are still ongoing, and major updates are foreseen soon. The experience gained during the effort for the Physics TDR Vol.II tells us that a good control of jets is crucial in single top physics, due to the need for a jet counting at relatively low energy, where the CMS calorimetry alone is probably not adequate for precision measurements. ‘‘Energy Flow’’ algorithms, not yet available in CMS, are expected to sizably improve the precision, by complementing the calorimetry with the informations from the very precise CMS Tracker; muon chambers and electromagnetic calorimeter may also give a significant improvement, through muon and electron/photon identification and correction inside jets.

Along this direction of improvement a first step is already being pursued, with the use of tracks

and vertexes: an observable

$$= \frac{\sum_i p_T^i}{E_T(\text{jet})}; \quad (3.4.36)$$

is defined for each jet, where the sum runs over all the tracks inside the jet cone, fulfilling the following requirements:

have at least 5 hits in the Tracker;

$p > 2 \text{ GeV}$;

compatibility of the track with the primary vertex: $|z_{\text{track}} - z_{\text{tx}}| < 0.4 \text{ cm}$.

A lower cut on this observable (e.g. > 0.2) gives a good rejection of noise even at very low $E_T(\text{jet})$, and thanks to the last requirement (tracks compatible with the primary vertex) the dependence on pile-up is greatly reduced. Very preliminary results show that with the help of this new “jet cleaning” criterion, b -rejection is greatly improved in all single top analyses.

3.5 From the Tevatron to the LHC

R. Schwienhorst

Department of Physics & Astronomy, Michigan State University, East Lansing, MI 48824, USA

A. Lucotte

Laboratoire de Physique Subatomique & Cosmologie (LPSC), 53, avenue des Martyrs 38026 GRENOBLE CEDEX

In the transition from the Tevatron to the LHC, several aspects of single top quark physics change. At the Tevatron, the main goal is to observe the electroweak mode of top quark production for the first time. That will be followed by initial measurements. Hence, the emphasis is on extracting the signal from the backgrounds, using optimized methods. By contrast, by the time the LHC analyses are starting, single top quark production should already have been discovered, and the focus shifts to precision measurements, and to using single top events as tools to probe the EW sector and to look for new physics.

Table 3.5.46 shows how the production cross sections change from the Tevatron to the LHC for the different single top quark production modes. The s -channel cross section increases roughly by a

accelerator	s -channel (pb)	t -channel (pb)	$W t$ (pb)
Tevatron (t)	0.44	0.99	0.1
LHC (t)	6.6	156	34
LHC (\bar{t})	4.1	91	34

Table 3.5.46: Cross sections (in pb) at NLO for single top quark production at the Tevatron and the LHC [52, 60].

factor of ten from the Tevatron to the LHC. Since the backgrounds increase by a similar amount, it will be challenging at both colliders to observe s -channel production separately. It should nevertheless be possible to measure the s -channel cross section separately and thus compare the s -channel to the t -channel. Such a comparison is very sensitive to physics beyond the SM, as Fig. 3.3.53 shows.

Compared to the s -channel, the increase in production cross section is much more dramatic for the t -channel. Here, the larger center-of-mass energy means that we are accessing a part of phase space where the gluon and b -quark parton distribution functions are much larger, resulting in an increase of the production cross section by two orders of magnitude. Even at the Tevatron, the large cross section makes this channel the main target for the initial observation of single top. At the LHC, the cross section is so large that it should be possible to collect large samples of single top quark events which can be used to study the top quark electroweak coupling in detail.

Similar to the t -channel, the production cross section for associated production also increases by more than two orders of magnitude. While the cross section at the Tevatron is too small for this process to be observed, it is sufficiently large at the LHC to not only observe this mode of single top quark production but also to study the $t\bar{W} b$ coupling in detail.

At the Tevatron, comparing the s -channel and t -channel production cross sections will be a test of the SM prediction and a good probe for Physics beyond the SM. At the LHC, it will be possible to compare all three production modes with each other, thus providing an even more sensitive probe, in particular to modifications of the $t\bar{W} b$ coupling [81].

Summary of commonalities between TeV and LHC

The most important commonality between the Tevatron and the LHC is of course the physics process and the final state signature, in particular for s -channel and t -channel single top quark production. Many of the lessons learned from theoretical studies of single top quark production at one collider translate to the other collider as well. This is in particular true for the comparisons of single top quark production at LO and NLO [49, 52, 50, 51, 58, 53, 60] and dedicated studies of correlations in the single top final state [148, 64]. Similarly, the improvements in producing simulated single top events for a detector simulation benefit both the Tevatron and LHC analyses.

Experimentally, this results in similar basic event selection cuts, though the Tevatron cuts are kept somewhat looser in order to maximize the signal acceptance. At the LHC, single top events are produced more copiously, thus allowing for somewhat tighter cuts to extract the signal.

The backgrounds to this final state signature are also similar, although they come in different proportions. At the Tevatron, the most important background is from W +jets production, with a smaller contribution from $t\bar{t}$ production. At the LHC, the situation is reversed, and the $t\bar{t}$ background dominates over the W +jets background. Nevertheless, since both backgrounds need to be modeled well at both colliders.

Due to the complexity of the final state, the focus on detector performance and understanding is also similar between Tevatron and LHC. Selecting signal events with high efficiency requires excellent reconstruction efficiency for electrons, muons, jets, missing transverse energy, and b -quark tagging. For the t -channel signal, it is especially important to reconstruct jets in the forward region with high efficiency. Separating the signal from the large backgrounds requires understanding and good energy resolution for electrons, muons, jets, and missing transverse energy. The main difference between the signal and the large background from W +jets production is the presence of a top quark in the final state, and reconstructing the top quark mass accurately aids greatly in rejecting the W +jets background.

Summary of differences between TeV and LHC

The main difference between Tevatron and LHC single top searches is the expected number of signal events. Both the signal cross sections and the expected total integrated luminosity are smaller at the Tevatron than at the LHC. Thus the single top searches at the Tevatron are statistics limited, and even the complete projected Run II dataset will only yield a small set of tens of single top quark events. By contrast, the LHC should be able to yield many hundreds of single top quark events. This has several consequences.

Tevatron analyses are employing multi-variate analysis techniques to extract the single top quark signal. These techniques significantly improve the sensitivity to SM single top quark production, which is important for the initial discovery. They are not as useful for later measurements of top quark and tW b coupling measurements because they bias kinematic distributions and limit the sensitivity to possible new physics.

The LHC samples will have much higher event statistics, especially in the t -channel, making it easier to extract the single top signal in a cut-based analysis.

In order to extract the signal with high significance, it will be very important to model the backgrounds accurately at the Tevatron. There will be a sizable fraction of background events in the

signal region, and understanding the size and shape of the backgrounds limits the sensitivity of the search.

At the LHC, it should be easier to extract a relatively clean sample of single top events. It will also be easier to find orthogonal samples and sidebands which can be used to estimate the background accurately.

At the Tevatron, the statistical uncertainty will be large compared to the systematic uncertainty. Thus, cross section measurements are aimed at maximizing the signal acceptance and place less importance on minimizing systematic uncertainties.

The statistical uncertainty will be small at the LHC, making it important to understand systematic effects. In particular the uncertainty on the different background contributions will be a limiting factor, together with the jet energy scale uncertainty and initial- and final-state radiation.

Conclusions

Selecting single top quark events with high efficiency, especially t -channel events with their unique final state signature, requires jet identification in the forward detector region. In order to take advantage of the angular correlations in single top quark events, requiring leptons in the pseudorapidity region $|\eta| > 1$ is also important (see Sec. 3.2). These are both areas where the Tevatron experience can be applied directly to the LHC. Moreover, at the LHC, reconstructing jets in the forward region is not only important for t -channel single top but also for searches for Higgs boson production through vector boson fusion. This is one example where both Tevatron and LHC single top analysis experience translates directly to other searches.

Since the backgrounds to single top quark production are similar at the Tevatron and the LHC, experiences about background modeling at the Tevatron will be relevant at the LHC.

Most likely, SM single top quark production will have already been discovered at the Tevatron before the LHC analyses begin. Information from the Tevatron about the measured experimental cross section and basic kinematic properties can thus be used to optimize the LHC searches, especially if there is a hint of new physics from the Tevatron.

Similarly, the accurate top quark mass measurements from the Tevatron also help in improving the signal model for the LHC. The top quark mass will be measured accurately in top quark pair events. This information can be used in the single top searches, both in the modeling of the single top signal, and in reducing systematic uncertainties in the measurement of the CKM matrix element V_{tb} . Reducing the top quark mass uncertainty by 1 GeV will reduce the uncertainty on the t -channel cross section at the Tevatron (LHC) by 1.6% (0.75%) [52]. Other measurements which can be done at the Tevatron that will improve the systematic uncertainty at the LHC are of parton distribution functions, in particular for heavy quarks.

The Tevatron single top analyses employ advanced analysis methods. While such methods are likely not going to be required to extract the single top quark signal at the LHC, they will be used extensively in other LHC searches, for example for the SM Higgs boson or searches for new physics beyond the SM. Several of these searches for new physics involve top quarks, for example searches for a charged Higgs boson that arises in supersymmetric models. Here the Tevatron experience in modeling of backgrounds and correlations in complex final states will be very relevant. And the Tevatron and LHC

experiences together in selecting and reconstructing SM top quark events will be useful in searches for any new physics involving the top quark.

4 Precise predictions for W boson observables

4.1 Introduction

Contributed by: D. Wackerath

Electroweak gauge boson production processes are one of the best, most precise probes of the Standard Model (SM). The electroweak physics program involving single W and Z boson production at hadron colliders has many facets:

The comparison of direct measurements of the W boson mass (M_W) and width (Γ_W) in W pair production at LEP2 and single W production at the Tevatron, with indirect measurements from a global fit to electroweak precision data measured at LEP1/SLD, represents a powerful test of the SM. Any disagreement could be interpreted as a signal of physics beyond the SM. At present, direct and indirect measurements of M_W and Γ_W agree within their respective errors [185]: M_W (LEP2/Tevatron) = 80.392 ± 0.029 GeV⁴ versus M_W (LEP1/SLD) = 80.363 ± 0.032 GeV and Γ_W (LEP2/Tevatron) = 2.147 ± 0.060 GeV versus Γ_W (LEP1/SLD) = 2.091 ± 0.003 GeV. Continued improvements in theory and experiment will further scrutinize the SM.

The precise measurements of M_W and the top quark mass (m_t) provide an indirect measurement of the SM Higgs boson mass, M_H , and a window to physics beyond the SM, as discussed in Section 2.1 and illustrated in Fig. 2.1.1. Future more precise measurements of M_W together with m_t will considerably improve the present indirect bound on M_H : At the LHC, for instance, with anticipated experimental precisions of $\Delta M_W = 15$ MeV and $\Delta m_t = 1$ GeV, M_H can be predicted with an uncertainty of about $\Delta M_H / M_H = 18\%$ [186].

The measurement of the mass and width of the Z boson and the total W and Z production cross sections can be used for detector calibration and as luminosity monitors [187], respectively.

The W charge asymmetry and Z rapidity distributions severely constrain quark Parton Distribution Functions (PDFs).

New, heavy gauge bosons may leave their footprints in forward-backward asymmetries, A_{FB} , and the distribution of the invariant mass of the lepton pair, $M(\ell\ell)$, produced in Z boson production at high $M(\ell\ell)$. In Figure 4.1 [188] the effects of a Z^0 on $A_{FB}(M(\ell\ell))$ at the LHC are shown, assuming a number of different models of extended gauge boson sectors, and compared with simulated data assuming a specific model. As can be seen, measurements of A_{FB} at the LHC will be able to distinguish between different new physics scenarios provided, of course, the SM prediction is well under control.

In order to fully exploit the potential of the Tevatron and LHC for electroweak (EW) precision physics, the predictions have to be of the highest standards as well. The omission of EW radiative corrections in the comparison of predictions with data could result in fake signals of non-standard physics. For instance, in Ref. [189] it has been shown that the effects of weak non-resonant corrections on the tail of the transverse mass distribution of the lepton pair, $M_T(\ell\ell)$, produced in $pp \rightarrow W \rightarrow \ell\ell$ at the Tevatron, from which Γ_W can be extracted, are of the same order of magnitude as effects due to non-SM values of the W width. Another example is WZ production at the LHC, which is a sensitive probe of the non-abelian structure of the SM EW sector. As demonstrated in Ref. [190], for instance, effects

⁴The most recent measurement by CDF finds $M_W = 80.413 \pm 0.048$ GeV (see <http://fcdfwww.fnal.gov/physics/ewk/2007/wmass/>).

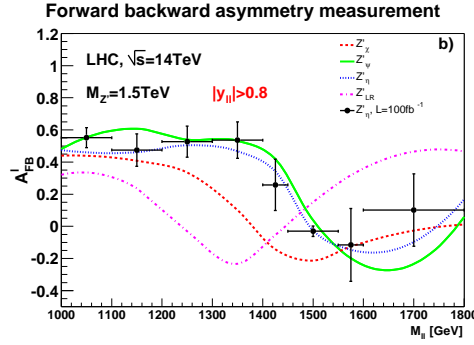


Fig. 4.1.92: The forward-backward asymmetry, $A_{FB}(M_Z)$, of single Z^0 production in $pp \rightarrow Z^0 \rightarrow l^+ l^-$ at the LHC for a number of models with heavy, non-standard gauge bosons. Taken from Ref. [188].

Theory includes:	Effects on observable:	Experimental precision:
final-state QED (approximation) [191]	shift in M_W : -65 20 MeV for $W \rightarrow e$ -168 20 MeV for $W \rightarrow \mu$	Tevatron RUN I: $M_W^{\text{exp}} = 59$ MeV $M_W^{\text{exp}} = 87$ MeV
full EW $\mathcal{O}(\alpha)$ corrections to resonant W production (pole approximation) [192, 193]	shift in M_W : 10 MeV	Tevatron RUN II: $M_W^{\text{exp}} = 27$ MeV
full EW $\mathcal{O}(\alpha)$ corrections	affects distributions at high Q^2 and direct W measurement shift in M_W : 7 MeV [189]	Tevatron RUN II: $M_W^{\text{exp}} = 25 - 30$ MeV
multiple final-state photon radiation	shift in M_W : 2(10) MeV in the $e(\mu)$ case [194]	LHC: $M_W^{\text{exp}} = 15$ MeV

Table 4.1.47: Impact of EW radiative corrections on W boson observables, in particular M_W and Γ_W extracted from the $M_T(l)$ distribution, confronted with present and anticipated experimental accuracies [186, 195, 196, 197, 198].

of non-standard weak gauge boson self-couplings can be similar in size and shape to the effects of EW corrections, and, thus, not including the latter could be mistaken as signals of new physics. Consequently, in recent years a lot of theoretical effort has gone into improving the predictions for W and Z production processes in order to match (or better exceed) the anticipated experimental accuracy. This not only requires the calculation of higher-order corrections but also their implementation in Monte Carlo (MC) integration programs for realistic studies of their effects on observables. A list of publicly available MC programs that include higher-order QED/EW corrections is given in Table 4.2.48 and a more detailed description of available calculations and different approaches can be found in Section 4.3.

The importance of fully understanding and controlling EW radiative corrections to precision W and Z boson observables at hadron colliders is illustrated in Table 4.1.47 on the example of a precise W mass and width measurement. It demonstrates how theoretical progress is driven by improvements in the experimental precision. For predictions to be under good theoretical control it requires a good understanding of the residual theoretical uncertainties. Therefore, the EW theory working group of

this workshop addressed the following questions: What is the residual theoretical uncertainty of the best, presently available predictions for W boson production at hadron colliders? Do we need more theoretical improvements to be able to fully exploit the EW physics potential of the Tevatron and the LHC? Our goal is to provide an estimate of the remaining theoretical uncertainties for a number of W boson observables relevant for:

- W mass and width measurements,
- luminosity monitoring,
- new physics searches at high invariant masses, and
- extraction of quark PDFs.

As a first step, in the spirit of the LEPI/II CERN yellow books, we perform a tuned numerical comparison of the following publicly available codes that provide precise predictions for W observables including electroweak $\mathcal{O}(\alpha_s)$ corrections: HORACE, SANC, and WGRAD2. First results of a tuned comparison of W and Z production cross sections and kinematic distributions can be found in Ref. [199]. As an indicator of the intrinsic theoretical uncertainty of predictions obtained with these codes due to missing higher-order corrections, we study the impact of different choices for the EW input parameter scheme and of leading higher-order (irreducible) QCD and EW corrections connected to the α_s parameter. We also discuss the effects of multiple photon radiation using HORACE. A detailed comparison of available calculations for Z boson production is work in progress.

In the following, we first review the status of predictions for W and Z boson observables at hadron colliders and summarize the dominant effects of electroweak corrections. We then present the results of a tuned numerical comparison of the MC programs HORACE, SANC, and WGRAD2, and discuss the effects of multiple photon radiation. After a discussion of the impact of small- x effects, non-perturbative dynamics, the Sudakov form factor S_{NP} , PDF uncertainties, and heavy quark effects on the transverse momentum distribution of the vector boson (c_{F}), we conclude with an estimate of the theoretical uncertainties and a recommendation of required theoretical improvements.

4.2 Theoretical status

Contributed by: D. Wackerath

Fully differential cross sections for single W and Z boson production at hadron colliders are known at next-to-next-to-leading order (NNLO) QCD [200, 201, 202, 203] (and references therein). Predictions for the W transverse momentum distribution, $c_{\text{F}}(W)$, an important ingredient in the current W mass measurement at the Tevatron, include an all-order resummation of leading logarithms arising from soft gluon radiation [204, 205]. The complete EW $\mathcal{O}(\alpha_s)$ corrections to $pp;pp \rightarrow W \rightarrow l$ and $pp;pp \rightarrow Z; \rightarrow ll$ have been calculated in Ref. [206, 189, 207, 208] and [209], respectively. Predictions including multiple final-state photon radiation have been presented in Ref. [194, 210, 211]. Most of these higher-order calculations have been implemented in MC programs and a list of some of the publicly available codes providing precise prediction for W and Z boson observable at hadron colliders can be found in Table 4.2.48. W and Z boson observables are strongly affected by EW corrections. Their main characteristics can be summarized as follows:

- Photon radiation off the final-state charged lepton can considerably distort kinematic distributions and usually makes up the bulk of the effects of EW corrections. For instance, W and Z boson

HORACE:	Multiple final-state photon radiation in \bar{W} and Z production as solution of QED DGLAP evolution for lepton structure functions [194, 211], matched with exact EW $\mathcal{O}(\alpha_s)$ corrections to \bar{W} production [208]. http://www.pv.infn.it/hepcomplex/horace.html
PHOTOS:	QED corrections in “any” particle decay, multiple-photon radiation, NLO precision for Z decays, full exact phase-space treatment. http://cern.ch/wasm/goodies.html
RESBOS:	QCD corrections to \bar{W} and Z production, soft gluon resummation, and final-state QED $\mathcal{O}(\alpha_s)$ corrections [204, 212]. http://www.pa.msu.edu/balazs/ResBos
SANC:	EW $\mathcal{O}(\alpha_s)$ corrections to \bar{W} and Z production: automatically generates Fortran code for one-loop corrections at parton level [207, 213]. http://sanc.jinr.ru and http://pcphsanc.cern.ch
WGRAD2:	QED $\mathcal{O}(\alpha_s)$ and weak one-loop corrections to \bar{W} production [189]. http://ubpheno.physics.buffalo.edu/dow/wgrad.html
WINHAC:	Multiple final-state photon radiation in \bar{W} production via YFS exponentiation of soft photons [210]. http://placzek.home.cern.ch/placzek/winhac
ZGRAD2:	QED $\mathcal{O}(\alpha_s)$ and weak one-loop corrections to Z production with proper treatment of higher-order terms around the Z resonance [209]. http://ubhex.physics.buffalo.edu/baur/zgrad2.tar.gz

Table 4.2.48: Publicly available MC programs that provide precise predictions including QED and/or electroweak corrections for \bar{W} and/or Z boson production at hadron colliders. A more detailed description is provided below.

masses extracted respectively from the transverse mass and invariant mass distributions of the final-state lepton pair are shifted by $\mathcal{O}(100)$ MeV due to final-state photon radiation. This is due to the occurrence of mass singular logarithms of the form $\log(Q^2 = m_l^2)$ that arise when the photon is emitted collinear to the charged lepton. In sufficiently inclusive observables these mass singularities completely cancel (KLN theorem). But in realistic experimental environments, depending on the experimental setup, large logarithms can survive. The more inclusive treatment of the photon emitted in $\bar{W}^+ \rightarrow e^+ e^-$ decays results in a significant reduction of the final-state QED effects when lepton identification cuts are applied whereas in the muon case large logarithms survive. Because of their numerical importance at one-loop, the higher-order effects of multiple final-state photon radiation have to be under good theoretical control as well [194, 210, 211].

The impact of initial-state photon radiation is negligible after proper removal of the initial-state mass singularities by universal collinear counterterms to the quark PDFs. This mass factorization introduces a dependence on the QED factorization scheme: in complete analogy to QCD both the QED DIS and $\overline{\text{MS}}$ scheme have been introduced in the literature [214, 193]. Recently, quark PDFs became available that also incorporate QED radiative corrections [215], which is important for a consistent treatment of initial-state photon radiation at hadron colliders.

At high energies, i.e. in tails of kinematic distributions, for instance $M_{ll} = M_Z$ and $M_{T(l)} = M_W$, Sudakov-like contributions of the form $\log^2(Q^2 = M_V^2)$ ($M_V = M_{W,Z}$ and Q is a typical energy of the scattering process) can significantly enhance the EW one-loop corrections. These corrections originate from remnants of UV singularities after renormalization and soft and collinear initial-state and final-state radiation of virtual and real weak gauge bosons. In contrast to QED and QCD the Bloch-Nordsieck theorem is violated [216], i.e. even in fully inclusive observables these large logarithms are present due to an incomplete cancellation between contributions from real and virtual weak gauge boson radiation. Moreover, the \bar{W} and Z boson masses serve as physical cut-off parameters and real \bar{W} and Z boson radiation processes are usually not included, since they result in different initial and/or final states. The EW logarithmic corrections of the form $\log^N(\frac{Q^2}{M_V^2})$; $N = 2L$ ($L = 1; 2 \dots$ for 1-loop, 2-loop, \dots) to 4-fermion processes are known up to 2-loop \mathcal{N}^3 order and are available in form of compact analytic formulae (see, e.g., Refs. [217, 218, 219] and references therein).

First studies of effects of combined EW and QCD corrections [212], higher-order EW Sudakov-like logarithms (see, e.g., Ref. [220]) and multiple final-state photon radiation [194, 210, 211] suggest that for the anticipated precision at the LHC these effects need to be included in the data analysis. Moreover, the model for non-perturbative QCD contributions [221], small x effects [222] and the impact of heavy-quark masses [223] need to be well understood for a detailed description of the $\sigma_T(W)$ distribution (see Section 4.6 for more details). Several groups are presently working on the combination of EW and QCD radiative corrections in one MC program, the interface of higher-order EW calculations, i.e. multiple photon radiation from final-state leptons and EW Sudakov logarithms, with fixed $\mathcal{O}(\alpha_s)$ calculations, and the calculation of mixed QED/QCD two-loop corrections of $\mathcal{O}(\alpha_s)$, which are not yet available. The ultimate goal is to provide one unified MC program that includes all relevant QED, EW and QCD radiative corrections to \bar{W} and Z boson production that matches the anticipated experimental capabilities of the Tevatron and LHC for EW precision physics.

4.3 Description of higher-order calculations and MC programs

HORACE

Contributed by: C. M. Carloni Calame, G. Montagna, O. Nicrosini, and A. Vicini

HORACE [224, 225, 208] is a Monte Carlo generator for precision simulations of charged-current and neutral-current Drell-Yan processes $pp \rightarrow W \rightarrow l_1 l_2$ and $pp \rightarrow Z \rightarrow l_1 l_2$ ($l = e, \mu$) at hadron colliders.

In its original version [224, 225] HORACE is based on a pure QED parton shower approach to account for final-state-like QED corrections, both at $\mathcal{O}(\alpha_s)$ and at higher orders, in leading logarithmic approximation. For the calculation of multiple photon corrections, the QED parton shower algorithm developed in Refs. [226, 227] is used.

The predictions of HORACE for multi-photon effects have been compared with those of the independent generator WINHAC in Ref. [228], finding good agreement. As shown in Refs. [224, 225], higher-order QED contributions are necessary for a number of precision studies at hadron colliders, particularly in view of high-precision measurements of the W boson mass at the Tevatron Run II and at the LHC.

Recently HORACE has been improved and, in its present version, includes: (i) the exact $\mathcal{O}(\alpha_s)$ electroweak corrections to the charged-current process $pp \rightarrow W \rightarrow l_1 l_2$, and (ii) higher-order QED contributions in the parton shower approach (initial- and final-state corrections). In order to avoid double counting of leading logarithmic contributions, already included in the parton shower, a matching procedure between fixed order and resummed calculation has been developed. The theoretical and computational details about the matching are too lengthy to be described here and can be found in Ref. [208].

Because it is well known that quark mass singularities, originating from initial-state photon radiation, can be factorized out of the partonic cross section and reabsorbed into a redefinition of the PDFs, in analogy to gluon emission in QCD, a subtraction to all orders of initial-state collinear singularities arising from photon radiation has been developed and implemented in HORACE. After subtraction of quark mass singularities, the QED initial-state radiation turns out to be small with respect to the effects of final-state radiation.

At the time of writing, exact $\mathcal{O}(\alpha_s)$ electroweak corrections to Z production are not accounted for in HORACE, but their inclusion in association with parton shower effects is foreseen in a future release.

Acknowledgments

The work of C.M. Carloni Calame is partially supported by a Royal Society Short Visit grant.

PHOTOS

Contributed by: P. Golonka and Z. Was

PHOTOS [229, 230, 231] is a universal Monte Carlo event generator simulating QED final-state radiative corrections in decays of particles and resonances. Having a form of an independent module, it cooperates with other event generators in the simulation chains of many experimental collaborations, including the ones for the LHC (for details, see references in available PHOTOS literature). Over 15 years of its history the core of the photon-emission algorithm has not changed significantly; however,

areas of its applicability, numerical stability, and precision have been improved in the span of last few years. Recent needs of experimental collaborations to use PHOTOS for high-precision estimates in certain channels motivated us to review the performance of the PHOTOS algorithm in certain areas of interest. Let us review here, in chronological order, the most important papers that cover the versions of PHOTOS code and related improvements in physical content,

The best documented 2.0 version of PHOTOS [230], allowed generating configurations with up to two photons in every elementary decay process⁵. It was supposed to be used as a “crude” tool, certainly not for high-precision studies. In particular, the effects of interference were treated with rough approximation or were not included at all.

In 2003, the version 2.07 of PHOTOS was released as a part of the TAUOLA-PHOTOS-F package [232]. In terms of precision, it contained a process-dependent correction weight for \bar{W} decays, see Ref. [233].

In 2004 and 2005, the universal, process-independent (approximated) interference weight, better control of numerical stability (allowing to use PHOTOS for decays of particles at the LHC energy scales), and multiple-photon, “exponentiated” emission were introduced. At the same time, systematic comparison tests of PHOTOS as a high-precision tool in certain decay channels began. Initially, such tests were conducted for Z, W and \bar{W} decays [231]. These achievements, including the method for tests, based on MC-TESTER [234], are documented in [235].

In 2006, we firstly focused our studies on the performance of PHOTOS at NLO precision and leptonic Z decays. PHOTOS has been extended to include the NLO effects. As a result, predictions of PHOTOS simulations match perfectly those produced by generators based on the full matrix-element calculation (differences are not recognizable in samples of 100 mln generated events) [236]. Similar upgrade of PHOTOS to complete NLO for \bar{W} decays might also have been straightforward; nevertheless, it would probably not be needed.

The NLO effects of scalar QED [237] were also installed for B-meson decays into pairs of scalars. This may be of interest not only for the Belle and BaBar communities, but for LHCb as well. This proves the flexibility of PHOTOS design as well: even though the scalar QED is not the ultimate theory of photon emission from pions, the separation of the matrix-element and phase-space points to a possible implementation of shape factors (to be obtained from experimental data). Note also that PHOTOS generation covers the complete phase-space for multi-photon configurations.

From the technical side, the mainstream version of PHOTOS is maintained as a single, compact block of FORTRAN77/95 code, which communicates with other generators by means of HEPEVT event record. However, a version in C++ [238] exists since 1999, yet its popularity is limited due to ongoing discussions of the standards for C++ event record. Recent developments are straightforward to include in the C++ version, if interest is expressed.

⁵PHOTOS scans the whole tree of the event record and its action is applied for every branching which can be interpreted as an individual decay (of a final but also intermediate step in the decay cascade).

SANC

Contributed by: A. Arbuzov, D. Bardin, S. Bondarenko, P. Christova, L. Kalinovskaya, and R. Sadykov

In the evaluation of the electroweak (EW) radiative corrections (RC) to the Drell-Yan-like processes we exploit the automatized system SANC [213]⁶. The system provides complete one-loop results for the EW corrections at the partonic level both for the neutral and charged-current processes. The SANC system automatically generates FORTRAN codes for corrected differential distributions. We subdivide the EW RC into the virtual ones, the ones due to soft photon emission, and the ones due to hard photon emission. An auxiliary parameter δ separates the soft and hard photonic contributions. For the real photon emission integration over the phase space can be performed either (semi-)analytically or by means of a Monte Carlo integrator.

To get the cross section at the hadronic level we convolute the partonic cross section with quark density functions. To avoid double counting of the quark mass singularities we subtract them (using a QED DIS-like subtraction scheme) from the density functions. Linearization of the subtraction procedure is done as described in Ref. [207].

In order to have the possibility to impose cuts, we use the Monte Carlo integration routine based on the Vegas algorithm [239]. In this case we perform a 4(6)-fold numerical integration to get the hard photon contribution to the partonic (hadronic) cross section. One-loop virtual EW corrections are calculated using the \overline{R} gauge and the on-mass-shell renormalization scheme. They are used as form factors standing before different structures of the matrix element. The latter is automatically generated with help of the helicity amplitude method. To get the total EW correction we sum up the contributions of the soft and hard photon emission and the ones of the virtual loops. The cancellation of the dependence on the auxiliary parameter δ in the sum is achieved numerically.

For the case of charged-current Drell-Yan process an extended description of our approach can be found in Ref. [207]. Some results of a tuned comparison with other programs were presented in Ref. [199].

Acknowledgments

The work of the SANC team is partially supported by INTAS grant N^o 03-51-4007 and by RFBR grant 04-02-17192 (AA).

WGRAD2/ZGRAD2

Contributed by: U. Baur and D. Wackerroth

WGRAD2 [193, 189] and ZGRAD2 [209] are parton-level Monte Carlo programs that include the complete $\mathcal{O}(\alpha_s)$ electroweak radiative corrections to $p\bar{p} \rightarrow W^+W^-X$ (WGRAD2) and $p\bar{p} \rightarrow Z\gamma X$ ($\gamma = e, \mu$) (ZGRAD2). For the numerical evaluation, the Monte Carlo phase space slicing method for next-to-leading-order (NLO) calculations described in Ref. [240, 241] is used. Final-state charged lepton mass effects are included in the following approximation. The lepton mass regularizes the collinear singularity associated with final state photon radiation. The associated mass

⁶SANC is available at <http://sanc.jinr.ru> and <http://pcphsanc.cern.ch>

singular logarithms of the form $\ln(\hat{s}=m^2)$, where \hat{s} is the squared parton center of mass energy and m_l is the charged lepton mass, are included in the calculation, but the very small terms of $\mathcal{O}(m^2/\hat{s})$ are neglected.

As a result of the absorption of the universal initial-state mass singularities by redefined (*renormalized*) PDFs [193, 214], the cross sections become dependent on the QED factorization scale μ_{QED} . In order to treat the $\mathcal{O}(\alpha_s)$ initial-state photonic corrections to W and Z production in hadronic collisions in a consistent way, the MRST2004QED set of parton distribution functions [215] should be used, which currently is the only set of PDFs which includes QED corrections. Absorbing the collinear singularity into the PDFs introduces a QED factorization scheme dependence. The squared matrix elements for different QED factorization schemes differ by the finite $\mathcal{O}(\alpha_s)$ terms which are absorbed into the PDFs in addition to the singular terms. WGRAD2 and ZGRAD2 can be used both in the QED $\overline{\text{MS}}$ and DIS schemes, which are defined analogously to the usual $\overline{\text{MS}}$ [242] and DIS [243] schemes used in QCD calculations.

WGRAD2 and ZGRAD2 can be used both with an s -dependent width, or a constant width, as well as different input parameter schemes. Radiative corrections beyond $\mathcal{O}(\alpha_s)$ are partially implemented in both programs.

Acknowledgments

This research was supported by the National Science Foundation under grant No. PHY-0244875 and No. PHY-0456681.

WINHAC

Contributed by: S. Jadach and W. Placzek

WINHAC [210] is a Monte Carlo event generator for Drell–Yan processes in proton–proton, proton–antiproton and nucleus–nucleus collisions. It features multiphoton radiation in W -boson decays within the Yennie–Frautschi–Suura (YFS) exclusive exponentiation scheme and the $\mathcal{O}(\alpha_s)$ electroweak radiative corrections for W decays. The latter have been provided to us by the SANC group. Implementation of the total $\mathcal{O}(\alpha_s)$ electroweak radiative corrections to the full charged-current Drell–Yan process is under way in the collaboration with the SANC group.

The current version of WINHAC includes a direct interface to PYTHIA for the QCD and/or QED initial-state radiation (ISR) parton shower, proton-remnants treatment and hadronization. One of the consequences of these effects is non-zero transverse momentum of the W -bosons. In addition to unpolarized W -boson production, the program provides options for generation of transversely and longitudinally polarized W -boson in the Born approximation. In the recent version we have also added an option for generation of the Born-level neutral-current (through $Z = \gamma$) Drell–Yan process. For the PDFs, WINHAC is interfaced with the PDFLIB package as well as with its recent successor LHAPDF. In the latter case WINHAC gives the possibility to compute auxiliary weights corresponding to PDF errors provided with some PDF parametrizations; all these weights are calculated in a single MC run. In the case of nucleus–nucleus collisions, an option for switching on/off nuclear shadowing effects for PDFs is provided. Nuclear beams are defined through the input parameters by setting atomic numbers A , charge numbers Z and energies of two colliding nuclei. This collider option was applied to studies presented

in Ref. [244]. We also provide a special parton-level version of the program, called WINDEC, for generation of multiphoton radiation in \bar{W} decays that can be interfaced with an arbitrary MC generator of the \bar{W} -production process.

For QED radiative corrections WINHAC has been compared with the Monte Carlo generator HORACE, both for the parton level processes and for proton–proton collisions at the LHC. Good agreement of the two programs for several observables has been found [228]. The comparisons with PHOTOS also show good agreement of the two generators for the QED final-state radiation (FSR) [231].

A similar event generator for the Z-boson production, called ZINHAC, is under development now. We also work on constrained MC algorithms for the QCD ISR parton shower that could be applied to Drell–Yan processes, see, e.g., Ref. [245].

CALCULATION PRESENTED IN REF. [206]

Contributed by: S. Dittmaier and M. Krämer

Ref. [206] contains a detailed description of the calculation of the $\mathcal{O}(\alpha_s^2)$ corrections to W production at hadron colliders and a discussion of results for the Tevatron and the LHC. In particular, the full $\mathcal{O}(\alpha_s^2)$ calculation is compared with a pole approximation for the W resonance. The case of Z-boson production is not considered. For the analysis performed in Ref. [199], the calculation of Ref. [206] has been extended (i) to include final-state radiation beyond $\mathcal{O}(\alpha_s)$ via structure functions and (ii) by implementing the $\mathcal{O}(\alpha_s)$ -corrected PDF set MRST2004QED. The photon-induced processes $q\bar{q} \rightarrow q\bar{q}\gamma$ and $q\bar{q} \rightarrow q\bar{q}\gamma\gamma$ have been calculated as described in Ref. [246]. The evaluation of the $q\bar{q}\gamma$ channel has been technically improved by employing a generalization of the dipole subtraction approach [247] to non-collinear-safe observables, as partially described in Ref. [248].

4.4 Results of a tuned comparison of HORACE, SANC and WGRAD2

Contributed by: A. Arbuzov, D. Bardin, U. Baur, S. Bondarenko, C. M. Carloni Calame, P. Christova, L. Kalinovskaya, G. Montagna, O. Nicrosini, R. Sadykov, A. Vicini, and D. Wackerroth

Setup for the tuned comparison

For the numerical evaluation of the cross sections at the Tevatron ($\sqrt{s} = 1.96$ TeV) and the LHC ($\sqrt{s} = 14$ TeV) we chose the following set of Standard Model input parameters:

$$\begin{aligned}
 G &= 1.16637 \cdot 10^{-5} \text{ G eV}^{-2}; & \alpha_s &= 1.13703599911; & \alpha_s(M_Z^2) &= 0.1176 \\
 M_Z &= 91.1876 \text{ G eV}; & M_Z &= 2.4924 \text{ G eV} \\
 M_W &= 80.37399 \text{ G eV}; & M_W &= 2.0836 \text{ G eV} \\
 M_H &= 115 \text{ G eV}; \\
 m_e &= 0.51099892 \text{ keV}; & m_c &= 0.105658369 \text{ G eV}; & m_b &= 1.77699 \text{ G eV} \\
 m_u &= 0.06983 \text{ G eV}; & m_c &= 1.2 \text{ G eV}; & m_t &= 174 \text{ G eV} \\
 m_d &= 0.06984 \text{ G eV}; & m_s &= 0.15 \text{ G eV}; & m_b &= 4.6 \text{ G eV} \\
 |V_{ud}| &= 0.975; & |V_{us}| &= 0.222 \\
 |V_{cd}| &= 0.222; & |V_{cs}| &= 0.975 \\
 |V_{cb}| &= |V_{ts}| = |V_{ub}| = |V_{td}| = |V_{tb}| = 0
 \end{aligned} \tag{4.4.37}$$

The W and Higgs boson masses, M_W and M_H , are related via loop corrections. To determine M_W we use a parametrization which, for $100 \text{ G eV} < M_H < 1 \text{ TeV}$, deviates by at most 0.2 MeV from the theoretical value including the full two-loop contributions [249] (using Eqs. (6,7,9)). Additional parametrizations can also be found in [250, 251].

We work in the constant width scheme and fix the weak mixing angle by $c_w = M_W/M_Z$, $s_w^2 = 1 - c_w^2$. The Z and W -boson decay widths given above are calculated including QCD and electroweak corrections, and are used in both the LO and NLO evaluations of the cross sections. The fermion masses only enter through loop contributions to the vector boson self energies and as regulators of the collinear singularities which arise in the calculation of the QED contribution. The light quark masses are chosen in such a way, that the value for the hadronic five-flavor contribution to the photon vacuum polarization, $\chi_{\text{had}}^{(5)}(M_Z^2) = 0.027572$ [252], is recovered, which is derived from low-energy e^+e^- data with the help of dispersion relations. The finestructure constant, $\alpha(0)$, is used throughout in both the LO and NLO calculations of the W production cross sections.

In the course of the calculation of W observables the Kobayashi-Maskawa-mixing has been neglected, but the final result for each parton level process has been multiplied with the square of the corresponding physical matrix element V_{ij} . From a numerical point of view, this procedure does not significantly differ from a consideration of the Kobayashi-Maskawa-matrix in the renormalisation procedure as it has been pointed out in [253].

To compute the hadronic cross section we use the MRST2004QED set of parton distribution functions [215], and take the renormalization scale, μ_r , and the QED and QCD factorization scales, μ_{QED} and μ_{QCD} , to be $\mu_r^2 = \mu_{\text{QED}}^2 = \mu_{\text{QCD}}^2 = M_W^2$. In the MRST2004QED structure functions, the factorization of the photonic initial state quark mass singularities is done in the QED DIS scheme which we

Tevatron and LHC	
electrons	muons
combine e and γ momentum four vectors, if $R(e; \gamma) < 0.1$	reject events with $E_\gamma > 2 \text{ GeV}$ for $R(\gamma; \mu) < 0.1$
reject events with $E_\gamma > 0.1 E_e$ for $0.1 < R(e; \gamma) < 0.4$	reject events with $E_\gamma > 0.1 E_\mu$ for $0.1 < R(\gamma; \mu) < 0.4$

Table 4.4.49: Summary of lepton identification requirements.

therefore use in all calculations reported here. It is defined analogously to the usual DIS [243] schemes used in QCD calculations, i.e. by requiring the same expression for the leading and next-to-leading order structure function F_2 in deep inelastic scattering, which is given by the sum of the quark distributions. Since F_2 data are an important ingredient in extracting PDFs, the effect of the $\mathcal{O}(\alpha_s)$ QED corrections on the PDFs should be reduced in the QED DIS scheme.

The detector acceptance is simulated by imposing the following transverse momentum (p_T) and pseudo-rapidity (η) cuts:

$$p_T(\ell) > 20 \text{ GeV}; \quad |\eta(\ell)| < 2.5; \quad \ell = e, \mu; \quad (4.4.38)$$

$$\cancel{p}_T > 20 \text{ GeV}; \quad (4.4.39)$$

where \cancel{p}_T is the missing transverse momentum originating from the neutrino. These cuts approximately model the acceptance of the CDF II and DØ detectors at the Tevatron, and the ATLAS and CMS detectors at the LHC. Uncertainties in the energy measurements of the charged leptons in the detector are simulated in the calculation by Gaussian smearing of the particle four-momentum vector with standard deviation which depends on the particle type and the detector. The numerical results presented here were calculated using σ values based on the DØ(upgrade) and ATLAS specifications.

The granularity of the detectors and the size of the electromagnetic showers in the calorimeter make it difficult to discriminate between electrons and photons with a small opening angle. In such cases we recombine the four-momentum vectors of the electron and photon to an effective electron four-momentum vector. To simplify the comparison we use the same recombination procedure at the Tevatron and the LHC. We require that the electron and photon momentum four-vectors are combined into an effective electron momentum four-vector if their separation in the pseudorapidity – azimuthal angle plane,

$$R(e; \gamma) = \frac{p_T(e; \gamma)}{\sqrt{(p_T(e; \gamma))^2 + (p_T(\gamma; e))^2}}; \quad (4.4.40)$$

is $R(e; \gamma) < 0.1$. For $0.1 < R(e; \gamma) < 0.4$ events are rejected if $E_\gamma > 0.1 E_e$. Here E_γ (E_e) is the energy of the photon (electron) in the laboratory frame.

Muons are identified by hits in the muon chambers and the requirement that the associated track is consistent with a minimum ionizing particle. This limits the photon energy for small muon – photon opening angles. For muons at the Tevatron and the LHC, we require that the energy of the photon is $E_\gamma < 2 \text{ GeV}$ for $R(\gamma; \mu) < 0.1$, and $E_\gamma < 0.1 E_\mu$ for $0.1 < R(\gamma; \mu) < 0.4$. We summarize the lepton identification requirements in Table 4.4.49. For each observable we will provide “bare” results, i.e. without smearing and recombination (only lepton separation cuts are applied) and “calo” results,

i.e. including smearing and recombination. We will show results for kinematic distributions and total cross sections, at LO and NLO, and the corresponding relative corrections, $(\%) = \frac{d_{\text{NLO}} - d_{\text{LO}}}{d_{\text{LO}}}$, at both the Tevatron and the LHC. If not stated otherwise, we consider the following charged current processes: $pp(p\bar{p}) \rightarrow W^+ \rightarrow l^+ \bar{\nu}_l$ with $l = e; \mu$.

W boson observables

σ_W : total inclusive cross section of W boson production.

The results for σ_W at LO and EW NLO and the corresponding relative corrections are provided in Table 4.4.50.

$\frac{d}{dM_T(l)}$: transverse mass distribution of the lepton-lepton-neutrino pair.

The transverse mass is defined as

$$M_T(l) = \sqrt{2p_T(l) p_T(\bar{\nu}) (1 - \cos \theta)}; \quad (4.4.41)$$

where $p_T(\bar{\nu})$ is the transverse momentum of the neutrino, and θ is the angle between the charged lepton and the neutrino in the transverse plane. The neutrino transverse momentum is identified with the missing transverse momentum, \cancel{p}_T , in the event.

The relative corrections for different M_T ranges are shown in Figs. 4.4.93, 4.4.95 for bare cuts and in Figs. 4.4.94, 4.4.96 for calo cuts.

$\frac{d}{dp_T^l}$: transverse lepton momentum distribution.

The relative corrections are shown in Fig. 4.4.97 for bare cuts and in Fig. 4.4.98 for calo cuts.

$A(y)$: W charge asymmetry for leptons.

The charge asymmetry of leptons in W decays [193] is defined as

$$A(y) = \frac{d^+ - dy_1 - d^- - dy_1}{d^+ - dy_1 + d^- - dy_1}; \quad (4.4.42)$$

where y_1 is the lepton rapidity and

$$d^\pm = d(pp; p\bar{p} \rightarrow l X); \quad (4.4.43)$$

In Fig. 4.4.99 (with bare cuts) and Fig. 4.4.100 (with calo cuts) we show the difference $A(y)$ between the NLO EW and LO predictions for the charge asymmetries at the Tevatron and the LHC.

We find numerical agreement within the statistical uncertainties of the Monte Carlo integration. In Figs. 4.4.94, 4.4.96 (upper right figures), we observe a discrepancy between SANC and WGRAD/HORACE predictions for the $M_T(e\bar{\nu}_e)$ distributions at the LHC (with calo cuts). This difference is presently under study. We do not expect that it will persist and, thus, do not consider it in the estimate of the residual theoretical uncertainties in Section 4.7. The good numerical agreement is also illustrated in detail in Fig. 4.4.101, where we show the relative differences $\delta = (\text{HORACE-X})/\text{HORACE}$, $X = \text{SANC, WGRAD}$, for the $M_T(l^+ \bar{\nu}_l)$ and p_T^+ distributions at the LHC and the Tevatron (with calo cuts).

Tevatron, $pp \rightarrow W^+ \rightarrow e^+ e^-$						
	bare cuts			calo cuts		
	LO [pb]	NLO [pb]	[%]	LO [pb]	NLO [pb]	[%]
HORACE	773.509(5)	791.14(2)	2.279(3)	733.012(5)	762.21(3)	3.983(4)
SANC	773.510(2)	791.04(8)	2.27(1)	733.024(2)	762.03(9)	3.96(1)
WGRAD2	773.516(5)	791.01(5)	2.268(7)	733.004(6)	762.00(5)	3.956(6)
Tevatron, $pp \rightarrow W^+ \rightarrow \mu^+ \mu^-$						
	bare cuts			calo cuts		
	LO [pb]	NLO [pb]	[%]	LO [pb]	NLO [pb]	[%]
HORACE	773.509(5)	804.18(2)	3.965(3)	732.913(6)	738.16(3)	0.716(4)
SANC	773.510(2)	804.07(6)	3.951(7)	732.908(2)	738.01(5)	0.696(7)
WGRAD2	773.516(5)	804.11(1)	3.955(2)	732.917(6)	738.00(1)	0.693(2)
LHC, $pp \rightarrow W^+ \rightarrow e^+ e^-$						
	bare cuts			calo cuts		
	LO [pb]	NLO [pb]	[%]	LO [pb]	NLO [pb]	[%]
HORACE	5039.11(4)	5140.6(1)	2.014(2)	4924.17(4)	5115.5(2)	3.886(4)
SANC	5039.21(1)	5139.5(5)	1.99(1)	4925.31(1)	5113.5(4)	3.821(9)
WGRAD2	5039.16(7)	5139.6(6)	1.99(1)	4924.15(5)	5114.1(6)	3.86(1)
LHC, $pp \rightarrow W^+ \rightarrow \mu^+ \mu^-$						
	bare cuts			calo cuts		
	LO [pb]	NLO [pb]	[%]	LO [pb]	NLO [pb]	[%]
HORACE	5039.11(4)	5230.5(2)	3.798(4)	4925.16(5)	4944.5(2)	0.393(4)
SANC	5039.21(1)	5229.4(3)	3.775(7)	4925.31(1)	4942.5(5)	0.349(9)
WGRAD2	5039.16(7)	5229.9(1)	3.786(3)	4925.30(7)	4943.0(1)	0.360(3)

Table 4.4.50: Tuned comparison of LO and EW NLO predictions for σ_W from HORACE, SANC, and WGRAD2. The statistical error of the Monte Carlo integration is given in parentheses.

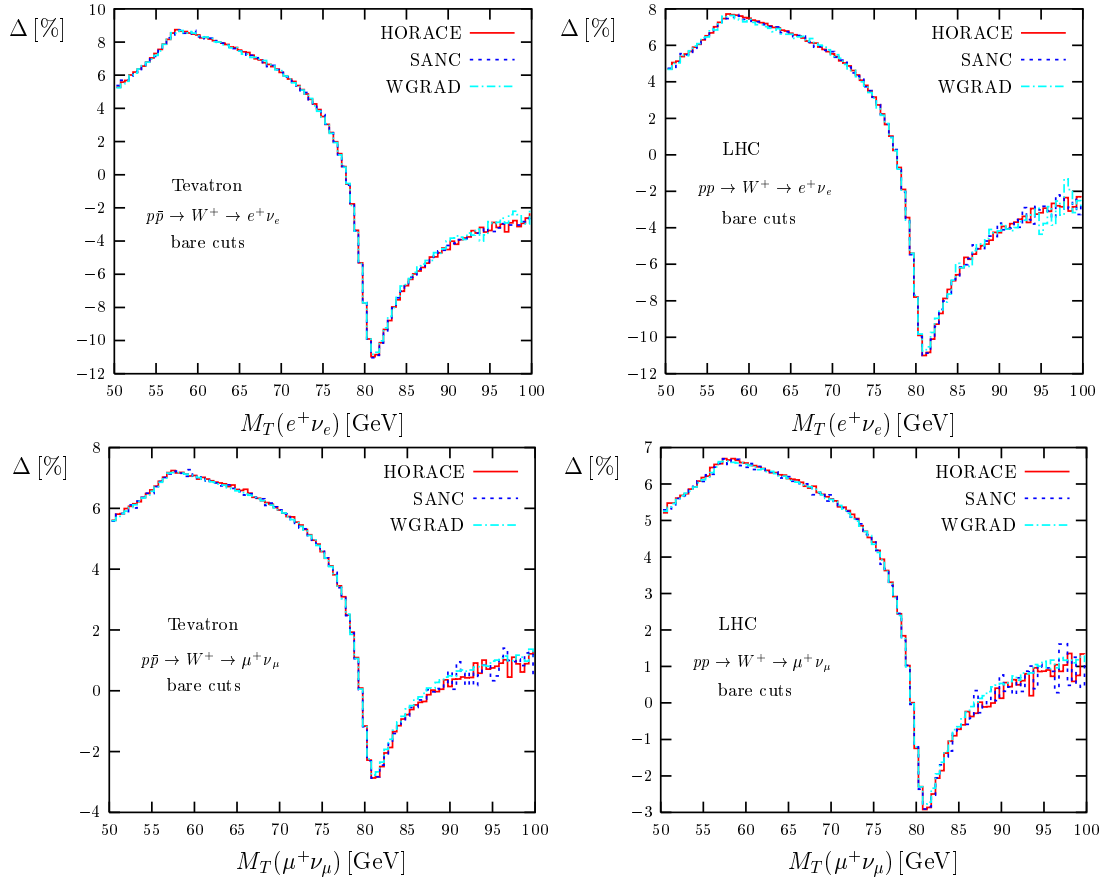


Fig. 4.4.93: The relative correction due to electroweak $\mathcal{O}(\alpha_s)$ corrections to the $M_T(1)$ distribution for single W^+ production with bare cuts at the Tevatron and the LHC.

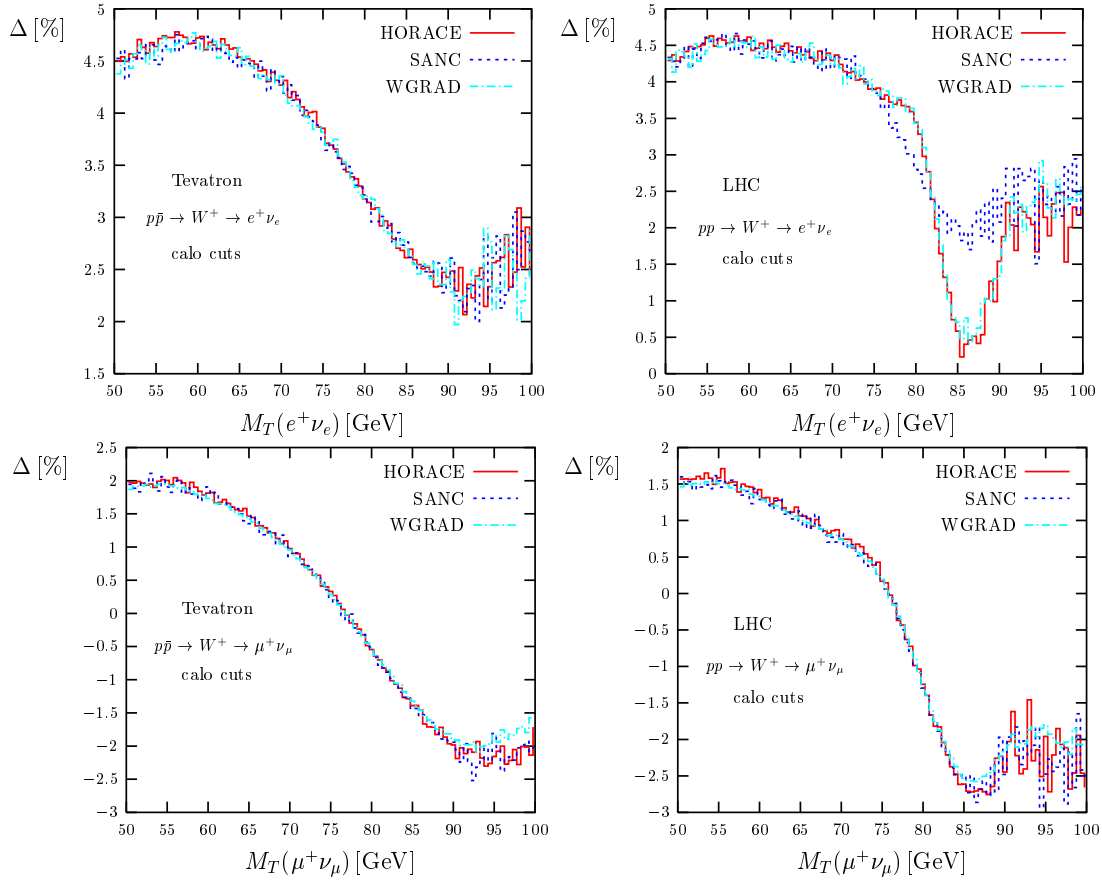


Fig. 4.4.94: The relative correction due to electroweak $\mathcal{O}(\alpha_s)$ corrections to the $M_T(1)$ distribution for single W^+ production with calo cuts at the Tevatron and the LHC.

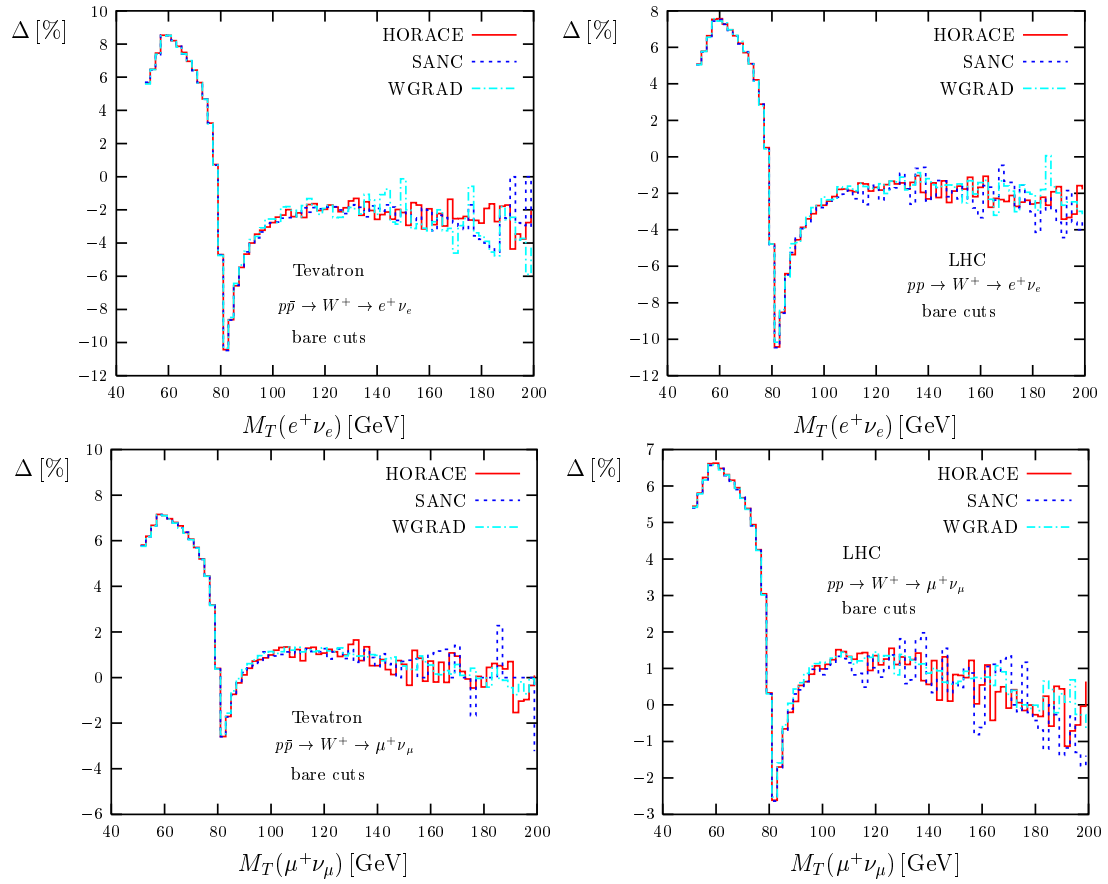


Fig. 4.4.95: The relative correction due to electroweak $\mathcal{O}(\alpha_s)$ corrections to the $M_T(l\nu)$ distribution for single W^+ production with bare cuts at the Tevatron and the LHC.

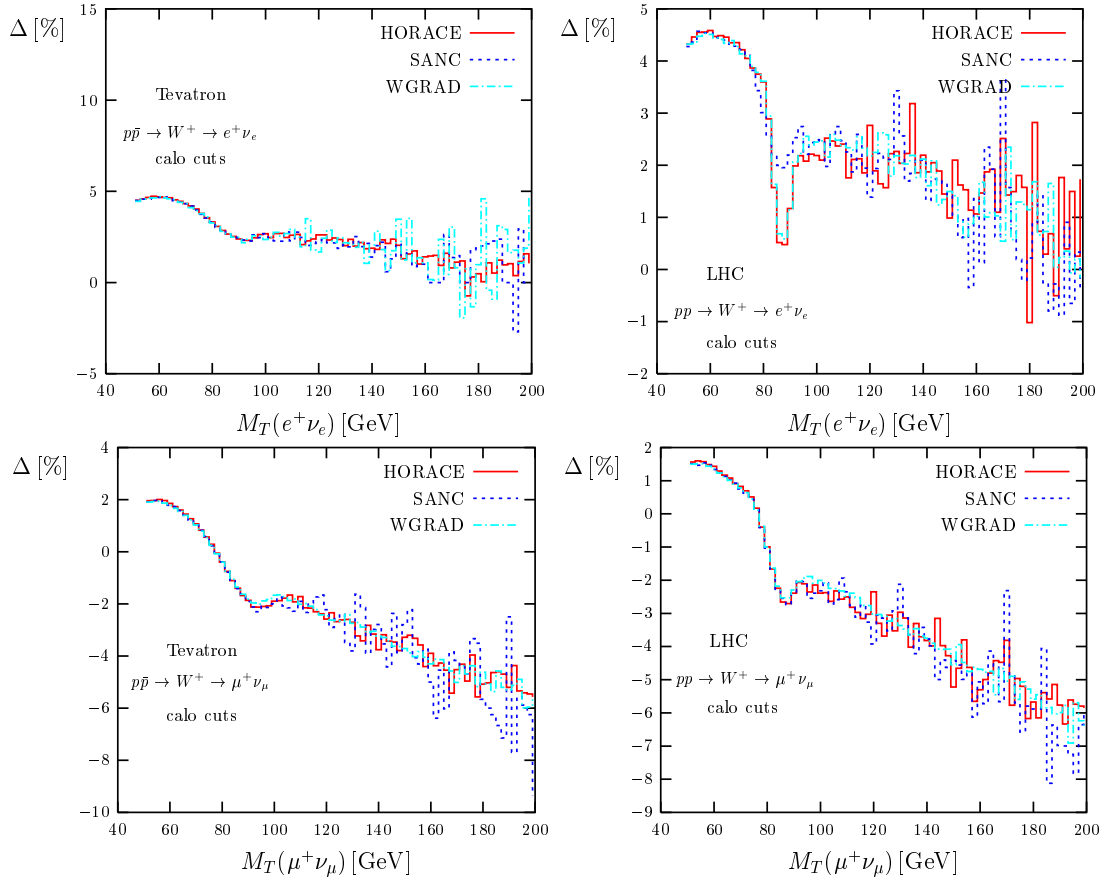


Fig. 4.4.96: The relative correction due to electroweak $\mathcal{O}(\alpha_s)$ corrections to the $M_T(1)$ distribution for single W^+ production with calo cuts at the Tevatron and the LHC.

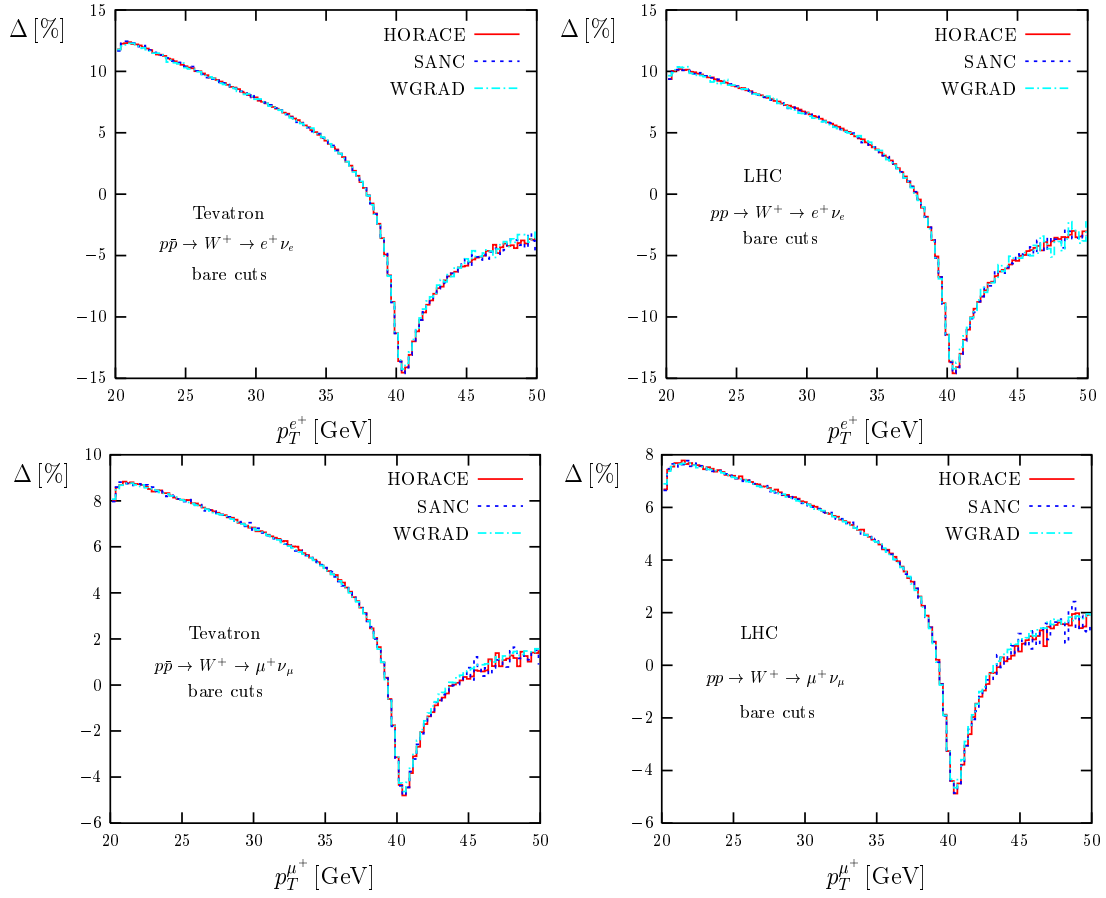


Fig. 4.4.97: The relative correction due to electroweak $\mathcal{O}(\alpha_s)$ corrections to the p_T distribution for single W^+ production with bare cuts at the Tevatron and the LHC.

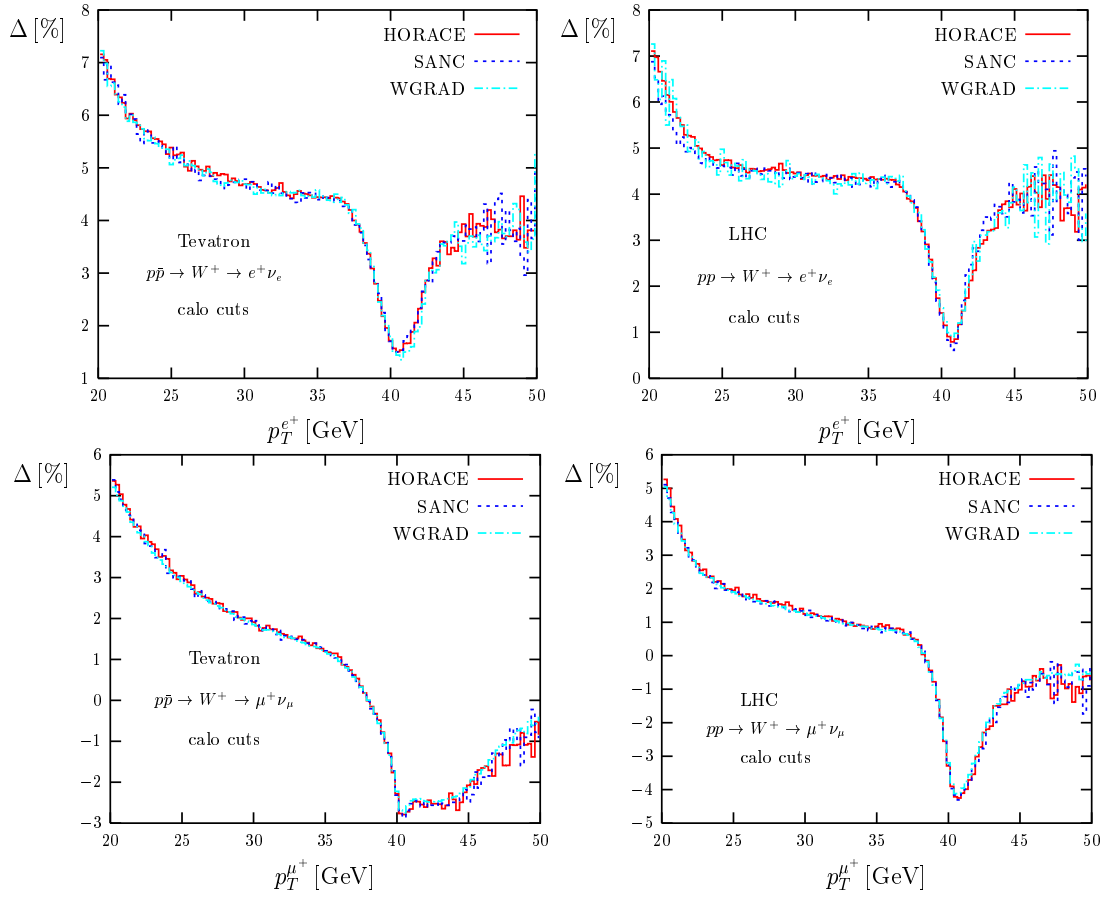


Fig. 4.4.98: The relative correction due to electroweak $\mathcal{O}(\alpha_s)$ corrections to the p_T distribution for single W^+ production with calo cuts at the Tevatron and the LHC.

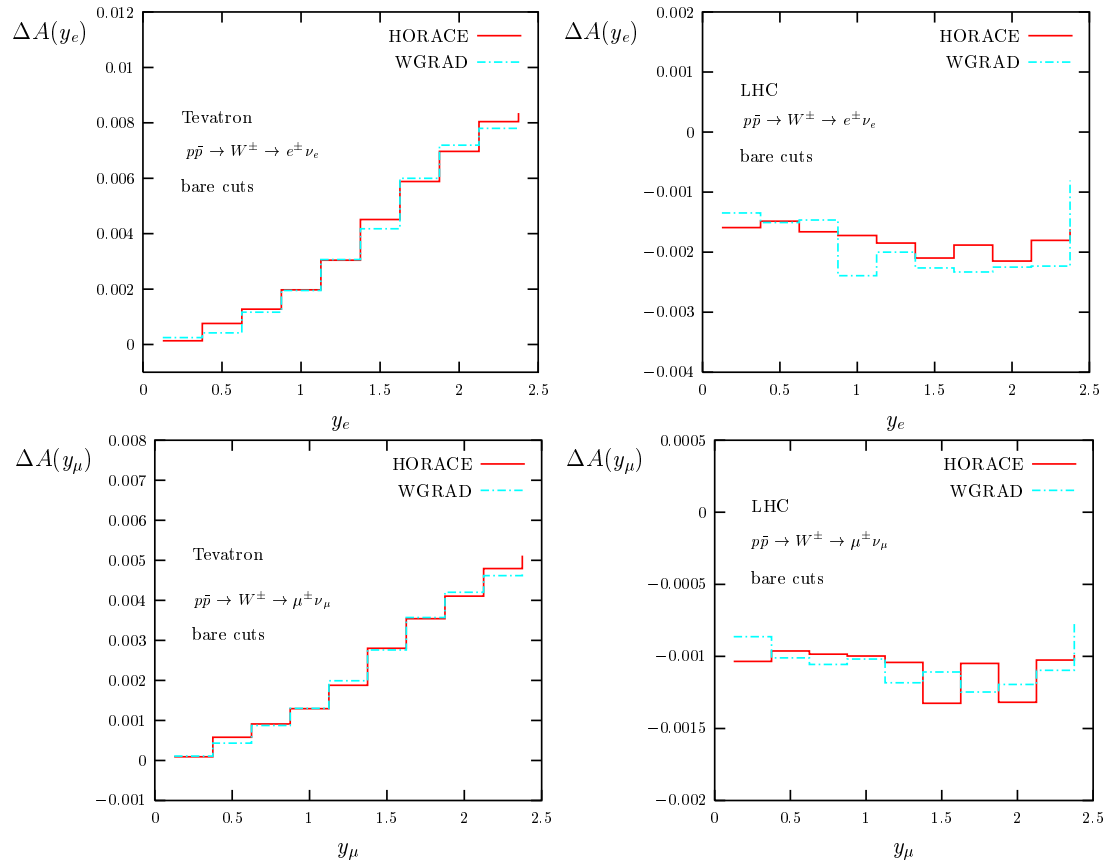


Fig. 4.4.99: The difference between the NLO and LO predictions for $A(y_1)$ due to electroweak $\mathcal{O}(\alpha_s)$ corrections for single W production with bare cuts at the Tevatron and the LHC.

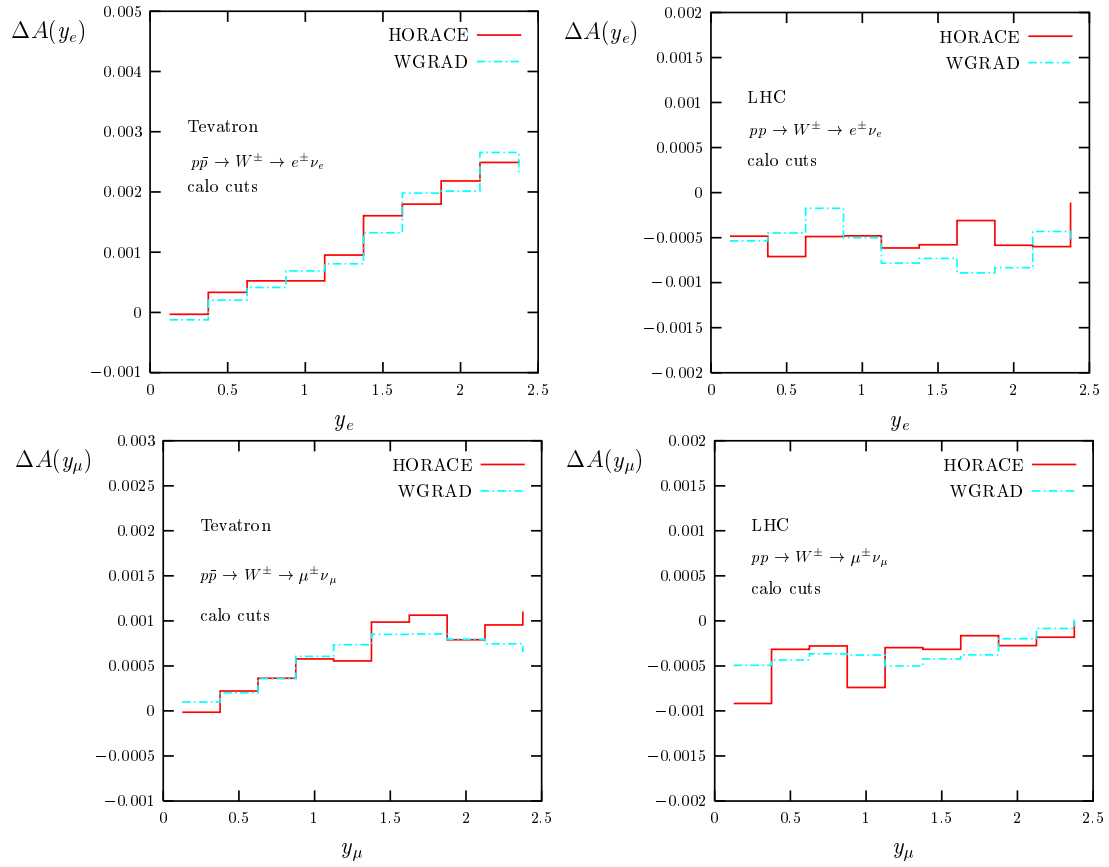


Fig. 4.4.100: The difference between the NLO and LO predictions for $A(y_1)$ due to electroweak $\mathcal{O}(\alpha_s)$ corrections for single W production with calo cuts at the Tevatron and the LHC.

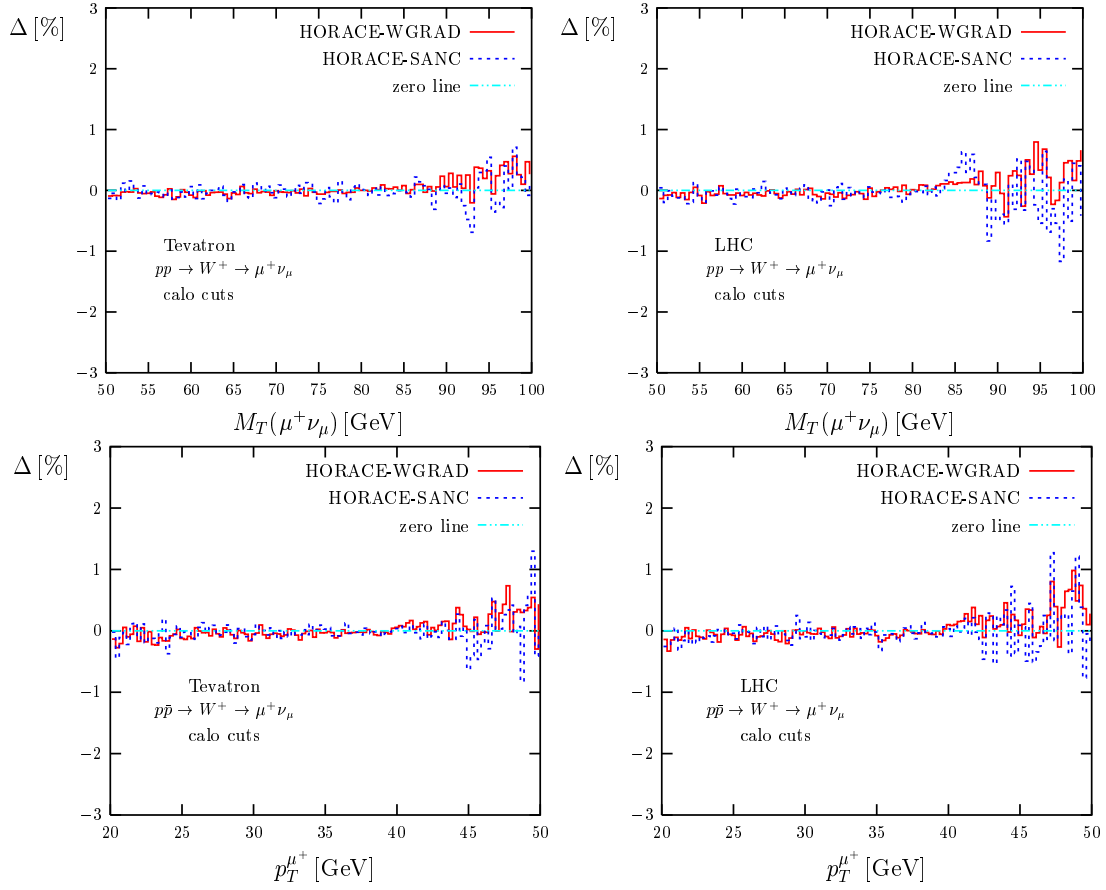


Fig. 4.4.101: Relative difference between HORACE and SANC NLO predictions as well as HORACE and WGRAD NLO predictions for the $M_T(\mu^+)$ and p_T^+ distributions for single W^+ production with calo cuts at the Tevatron and the LHC.

	Tevatron		LHC	
	$W^+ \rightarrow e^+ e^-$	$W^+ \rightarrow \mu^+ \mu^-$	$W^+ \rightarrow e^+ e^-$	$W^+ \rightarrow \mu^+ \mu^-$
	bare cuts			
NLO [pb]	791.14(2)	804.18(2)	5140.6(1)	5230.5(2)
NLO+ mPR [pb]	791.50(5)	804.39(4)	5143.4(3)	5232.2(3)
	calo cuts			
NLO [pb]	762.21(3)	738.16(3)	5115.5(2)	4944.5(2)
NLO+ mPR [pb]	762.01(6)	739.86(5)	5114.5(4)	4956.5(3)

Table 4.5.51: Comparison of EW NLO predictions without and with multiple final-state photon radiation (mPR) for W to $pp;pp \rightarrow W^+ \rightarrow e^+ e^-; \mu^+ \mu^-$ with bare and calo cuts at the Tevatron and LHC using HORACE.

4.5 Effects of multiple photon radiation

Contributed by: C. M. Carloni Calame, G. Montagna, O. Nicosini, A. Vicini, and D. Wackerroth

As discussed in Section 4.2, photon radiation off the charged lepton(s) in the final state (FSR) can considerably affect the predictions for W and Z boson observables. Therefore, the effects of multiple photon radiation (mPR), which is dominated by final-state radiation, need to be under good theoretical control when extracting for instance the W mass and width from W observables at the Tevatron and LHC. The MC programs HORACE, PHOTOS and WINHAC provide predictions for W production processes that include multiple FSR as described in Section 4.3. In the following discussion of the numerical impact of mPR on the total W production cross section (σ_W) and the $M_T(l)$ and p_T^\perp distributions the results have been obtained with HORACE.

In Table 4.5.51, NLO EW predictions for W are compared with predictions that include in addition mFSR. While mPR does not considerably affect the total cross section, the $M_T(l)$ and p_T^\perp distributions can be significantly distorted by mPR, as shown in Figs 4.5.102,4.5.104. When only bare cuts are applied, mPR enhances the NLO EW corrections to the $M_T(l)(p_T^\perp)$ distribution in the peak region by up to about 2%(2.5%) in the electron case and about 0.5% in the muon case. When lepton identification cuts are applied, the effects of mPR are strongly reduced in the electron case but largely survive in the muon case, as shown in Figs 4.5.103,4.5.105. In Ref. [224], the corresponding, additional shift in M_W due to mPR when extracted from the $M_T(l)$ distribution was determined to be 10 MeV in the muon case and negligible in the electron case, when assuming realistic lepton identification criteria (similar to the calo cuts used in this report).

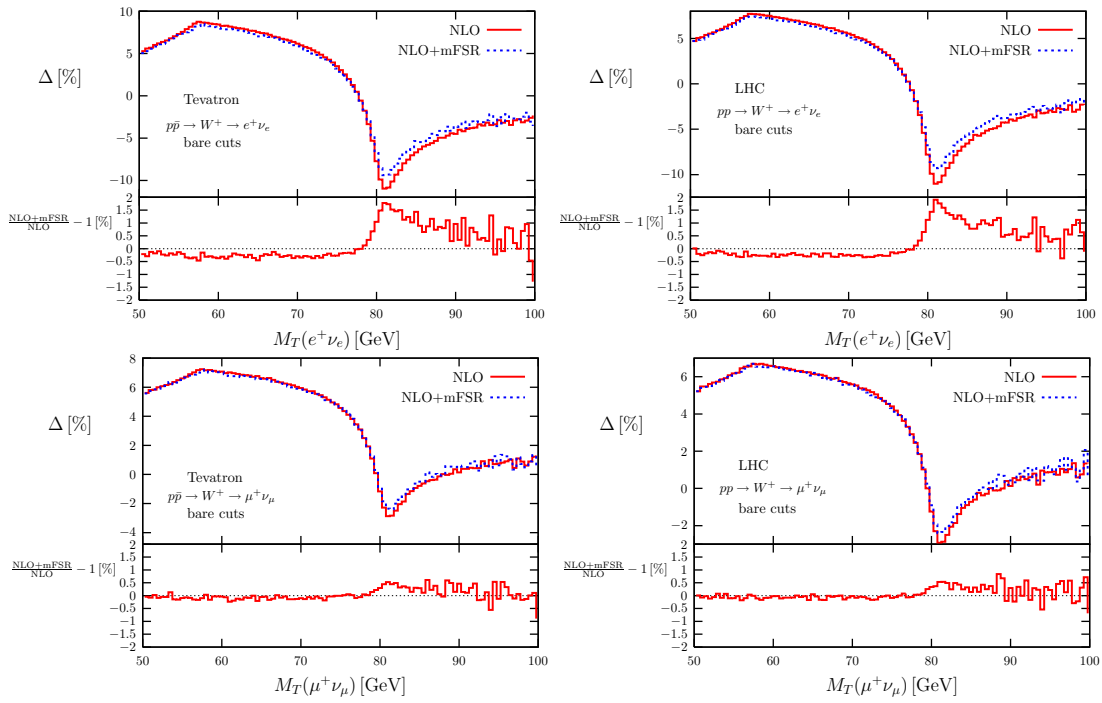


Fig. 4.5.102: The relative correction due to electroweak $\mathcal{O}(\alpha_s)$ corrections ('NLO') and when in addition including multiple final-state photon radiation ('NLO+mFSR') to the $M_T(1)$ distribution for single W^+ production with bare cuts at the Tevatron and the LHC. Also shown in the inset below is the relative difference between $M_T(1)$ distributions with and without mFSR. The results have been obtained with HORACE.

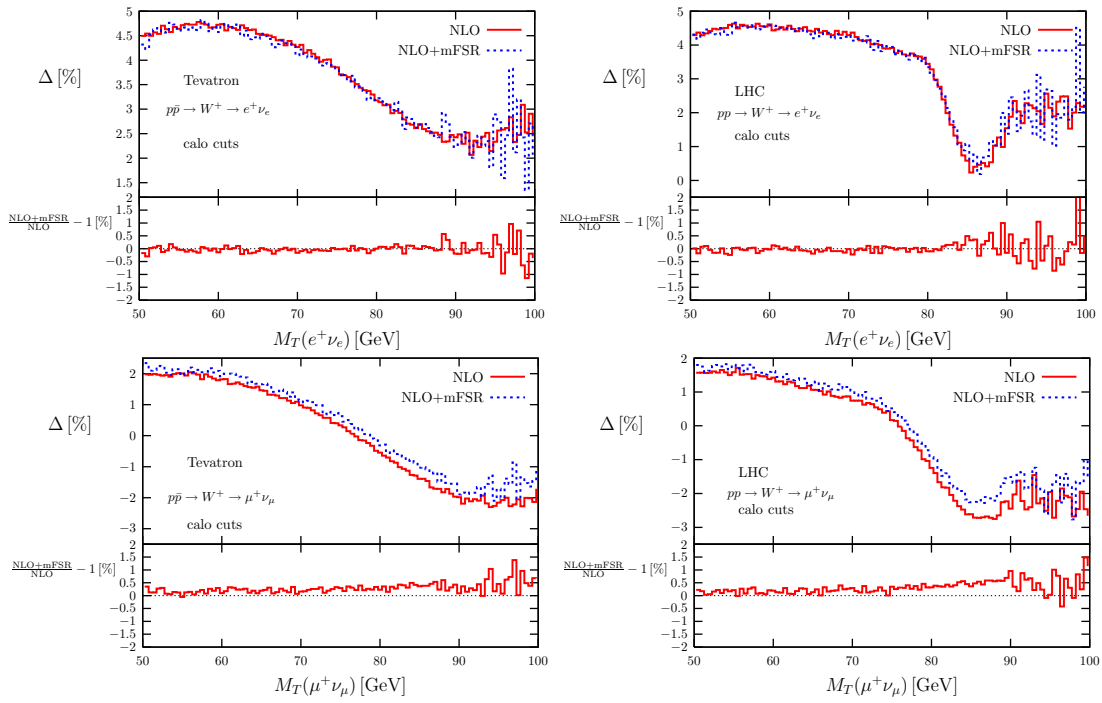


Fig. 4.5.103: The relative correction due to electroweak $\mathcal{O}(\alpha_s)$ corrections ('NLO') and when in addition including multiple final-state photon radiation ('NLO+mPR') to the $M_T(\ell)$ distribution for single W^+ production with calo cuts at the Tevatron and the LHC. Also shown in the inset below is the relative difference between $M_T(\ell)$ distributions with and without mPR. The results have been obtained with HORACE.

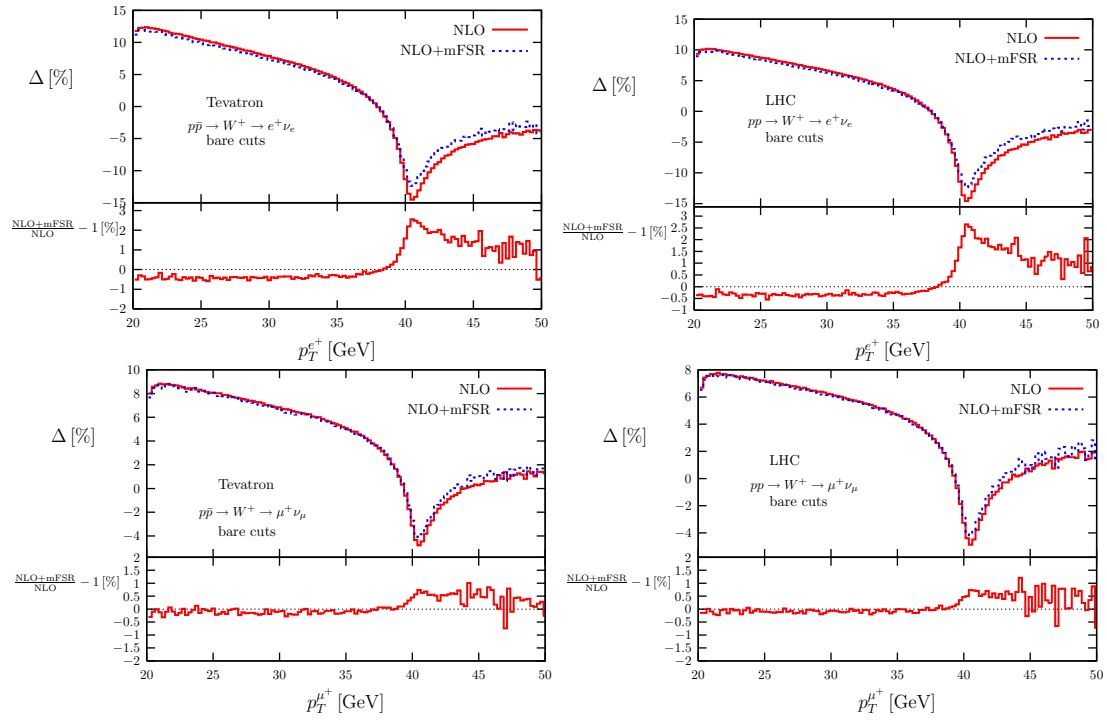


Fig. 4.5.104: The relative correction due to electroweak (NLO) and when in addition including multiple final-state photon radiation (NLO+mFSR) to the p_T^1 distribution for single W^+ production with bare cuts at the Tevatron and the LHC. Also shown in the inset below is the relative difference between p_T^1 distributions with and without mFSR. The results have been obtained with HORACE.

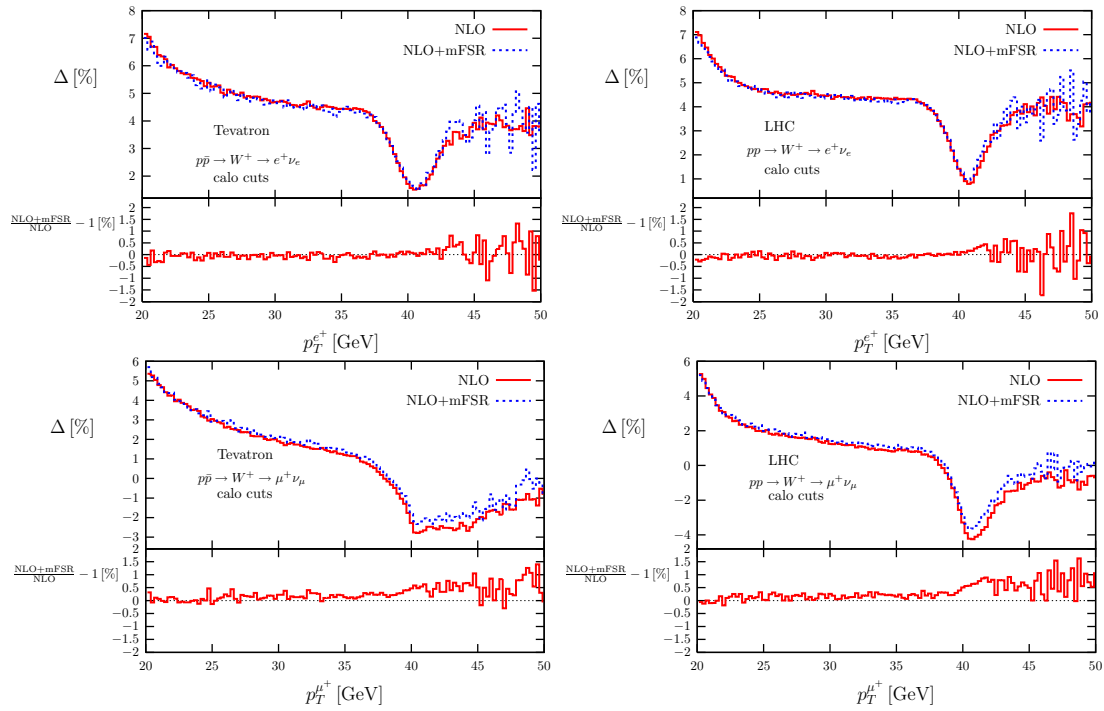


Fig. 4.5.105: The relative correction Δ due to electroweak $\mathcal{O}(\alpha_s)$ corrections ('NLO') and when in addition including multiple final-state photon radiation ('NLO+mPR') to the p_T^1 distribution for single W^+ production with calo cuts at the Tevatron and the LHC. Also shown in the inset below is the relative difference between p_T^1 distributions with and without mPR. The results have been obtained with HORACE.

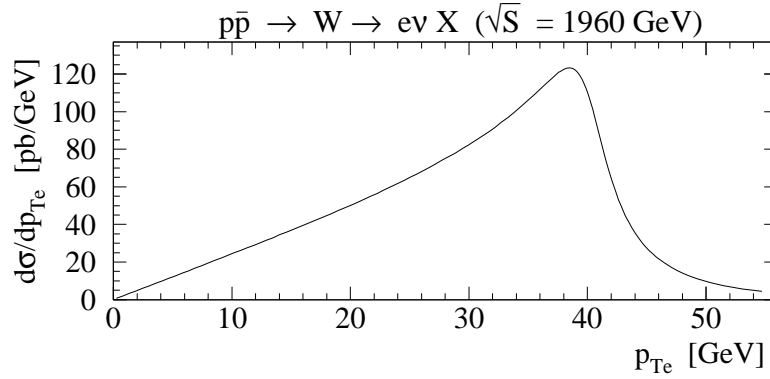


Fig. 4.6.106: Transverse momentum distribution $d\sigma/dp_{T_e}$ of the electrons from the decay of W bosons in the Tevatron Run-2 in the resummation calculation.

4.6 High-precision transverse momentum distributions in W boson production

Contributed by: S. Berge, P. M. Nadolsky, and F. I. Olness

In this section we discuss theoretical predictions for distributions in the transverse momentum q_T of the W boson, the transverse momenta p_{T_e} and p_{T_ν} of the decay charged lepton and neutrino, and the transverse mass of the decay lepton pair $m_{T_e} = \sqrt{2(p_{T_e} p_{T_\nu} + p_{T_e} p_{T_\nu})}$. Since these distributions are used to extract the W boson mass M_W , the associated theoretical uncertainties must be kept under control.

If the boson's transverse momentum q_T is much smaller than the boson's virtuality Q , the calculation of the transverse momentum distribution must include an all-order sum of large logarithms $\ln^n(q_T/Q)$. The formalism for summation of $\ln^n(q_T/Q)$ logarithms in Drell-Yan-like processes is well established at moderate scattering energies ($Q \ll \sqrt{S}$), when no other large logarithms are present [254]. When formulated in space of the impact parameter b (conjugate to q_T via a two-dimensional Fourier transform), it is proven to all orders by a factorization theorem [255, 256, 257].

Resummation in the b -space formalism [204, 258, 259] (currently implemented at NNLL/NLO accuracy) is employed in recent measurements of W and Z observables at the Tevatron. As precision of the experimental analysis continues to improve, new effects must be included in the resummation framework to keep up with modern demands. The shape of q_T spectrum may be appreciably altered by only partly known NNLO corrections, as well as by variations in parameters of the PDF's and nonperturbative resummed function. At the LHC, W and Z bosons will be produced by the scattering of partons with small momentum fractions ($x \ll 0.005$) and potentially affected by radiative contributions associated with $\ln(1/x)$ logarithms [222]. A large fraction of the bosons will be produced in heavy-quark scattering. Heavy-quark masses m_Q act as additional hard momentum scales and suppress multiple parton radiation at $q_T \sim m_Q$ in charm and bottom scattering, leading to harder q_T distributions than in the dominant process of quark-antiquark scattering [223]. In this report, we review recent progress in understanding of these factors and quantify their impact on the measured value of the W boson mass. Further details pertinent to our discussion can be found in Refs. [258, 222, 223, 221].

We concentrate on the p_{T_e} distribution of the final-state charged lepton, since it is more sensitive to the q_T of W boson than the m_{T_e} distribution and less affected by experimental uncertainties than p_T

distribution. To visualize percent-level changes in $d = d_{p_{T,e}}$ caused by various effects, we show several plots of the fractional difference $d^{mod} = d_{p_{T,e}} = d^{ref} = d_{p_{T,e}} - 1$ of the cross sections obtained under “reference” (ref) and “modified” (*mod*) theoretical assumptions. Our attention primarily focuses on the cross section near the kinematical (Jacobian) peak at $p_{T,e} = M_W = 2 = 40$ GeV (cf. Fig. 4.6.106), where $d = d_{p_{T,e}}$ is most sensitive to M_W : We compare modifications in $d = d_{p_{T,e}}$ caused by changes in theoretical assumptions with modifications caused by explicit variations of M_W .

4.6.1 Theory overview

In the b -space resummation framework (also called Collins-Soper-Sterman, or CSS formalism [254]), the differential cross section for production of a boson V at small to moderate q_T takes the form

$$\frac{d}{dQ^2 dy d\alpha_T^2} = \int \frac{d^2b}{(2\pi)^2} e^{iq_T \cdot b} \tilde{W}(b; Q; x_A; x_B) + Y(q_T; Q; x_A; x_B); \quad (4.6.44)$$

where y is the rapidity of the vector boson, and $x_{A,B} = Q e^{\pm y} \frac{p_{\perp}}{S}$ are the Born-level partonic momentum fractions. The all-order sum of $\int \frac{d^2b}{(2\pi)^2} \ln^m(\alpha_T^2 = Q^2)$ arising at $q_T \neq 0$ is contained in a Fourier-Bessel transform integral of a b -space form factor $\tilde{W}(b; Q; x_A; x_B)$. It is this integral that has the most impact on the W mass measurement. The regular NLO contribution $Y(q_T; Q; x_A; x_B)$ is substantial only at large q_T and won't receive much of our attention.

The form factor $\tilde{W}_{ab}(b; Q; x_A; x_B)$ factorizes at all b as

$$\tilde{W}(b; Q; x_A; x_B) = \frac{1}{S} \sum_{j,k=u,d,s,c,b} X_{jk}^{(0)} e^{S(b; Q)} P_j(x_A; b) P_k(x_B; b); \quad (4.6.45)$$

The Sudakov function $S(b; Q)$ and b -dependent parton distributions $P_j(x; b)$ for finding a quark (anti-quark) of flavor j in the proton are universal in Drell-Yan-like processes and semi-inclusive deep-inelastic scattering (SIDIS) [255]. The coefficient $X_{jk}^{(0)}$ includes process-specific constant factors from the Born cross section $\sigma_{qj} \propto |V|^2$. All terms in Eq. (4.6.45) can be computed in perturbative QCD when the momentum scale $1/b$ is much larger than 1 GeV, i.e., in the dominant region of b at both colliders.

The contribution of the nonperturbative region at $b \gtrsim 1 \text{ GeV}^{-1}$ is also tangible and must be properly modeled to describe the region $q_T \lesssim 20$ GeV. It is constrained through the global analysis of $p_{T,e}$ -dependent Drell-Yan and Z boson data [258, 221]. For this purpose, we separate the perturbative (small- b) and nonperturbative (large- b) terms in $\tilde{W}(b; Q; x_A; x_B)$ by rewriting Eq. (4.6.45) as

$$\tilde{W}(b; Q; x_A; x_B) = \tilde{W}_{LP}(b; Q; x_A; x_B) e^{F_{NP}(b; Q)}; \quad (4.6.46)$$

where the leading-power (logarithmic in b) term \tilde{W}_{LP} is given by a model-dependent continuation of the perturbative contribution to the region $b \gtrsim 1 \text{ GeV}^{-1}$, and the nonperturbative exponent $e^{F_{NP}(b; Q)}$ absorbs power-suppressed terms proportional to even powers of b [260]. In global fits, the preferred $F_{NP}(b; Q)$ has approximately quadratic dependence on b (i.e., $F_{NP}(b; Q) \propto b^2$). It may be therefore interpreted as a source of the Gaussian smearing of the b -space form factor (and transverse momentum distributions) introduced by nonperturbative dynamics.

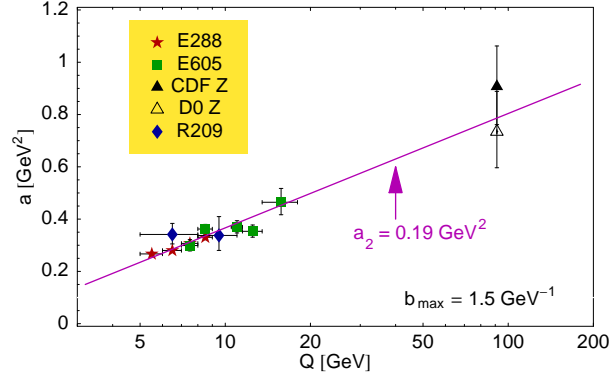


Fig. 4.6.107: The “Gaussian smearing” parameter $a(Q)$ preferred by the low-mass Drell-Yan and Tevatron Run-1 Z boson p_T data in the model of Ref. [221]. The derivative of $a(Q)$ with respect to $\ln Q$ observed in the fit (the slope a_2 of the solid line) agrees with its independent estimate made in the renormalon analysis [261].

4.6.2 Universality of nonperturbative resummed contributions

The best-fit form of $F_{NP}(b;Q)$ is correlated with the assumed large- b behavior of \tilde{w}_{LP} ; which differs between the available models [254, 261, 262, 263, 264]. We have recently proposed [221] a simple revision of the “ b ansatz” for $\tilde{w}_{LP}(b;Q; x_A; x_B)$ [254, 258, 259], which leads to several improvements over previous studies. The new model extends the range where $\tilde{w}_{LP}(b;Q; x_A; x_B)$ is approximated by a known finite-order perturbative prediction to larger values of b and, by doing so, improves agreement with all analyzed p_T data from low-mass Drell-Yan pair and Tevatron Z boson production. The best-fit parametrization of $F_{NP}(b;Q) = b^2 a(Q)$ is found to be in a good agreement with a semi-quantitative estimate in renormalon analysis and lattice QCD [261] and has reduced dependence on the collision energy \sqrt{s} . The “Gaussian smearing” parameter

$$a(Q) = a_1 + a_2 \ln \frac{Q}{3.2 \text{ GeV}} + a_3 \ln(100 x_A x_B)$$

grows practically linearly with $\ln Q$ (i.e., $a_{1,2} \approx a_3$). The value of the dominant coefficient a_2 from the fit agrees well with the renormalon analysis estimate, where it arises from soft gluon subgraphs and does not depend on \sqrt{s} or flavor of initial-state quarks and hadrons. As a result of the above improvements, the revised b model leads to more confident predictions for the nonperturbative contribution at collider energies by exposing its soft-gluon origin and universality.

Uncertainties in theoretical predictions caused by variations in $F_{NP}(b;Q)$ can be estimated with the help of the Hessian matrix method, developed recently to quantify errors in the global PDF analysis (see, e.g., Ref. [17], and references therein). In this approach, the central value of the observable X is computed for the best-fit set $a_{\text{best}} = \{a_1; a_2; a_3\}$ of the nonperturbative function parameters. In addition, X is computed for six “extreme” parameter sets $a_{(i)}$ ($i = 1; 2; 3$) corresponding to the maximal positive and negative displacements of a along three eigenvectors of the Hessian matrix within the parameter region satisfying $\chi^2_{\text{best fit}} \pm 1$. The “extreme” parameter sets are listed in Table 4.6.52. The 1σ error in X is estimated by

$$X = \frac{1}{2} \sum_{i=1}^3 \frac{\Delta X^2}{X(a_{(i)}^+) X(a_{(i)}^-)} :$$

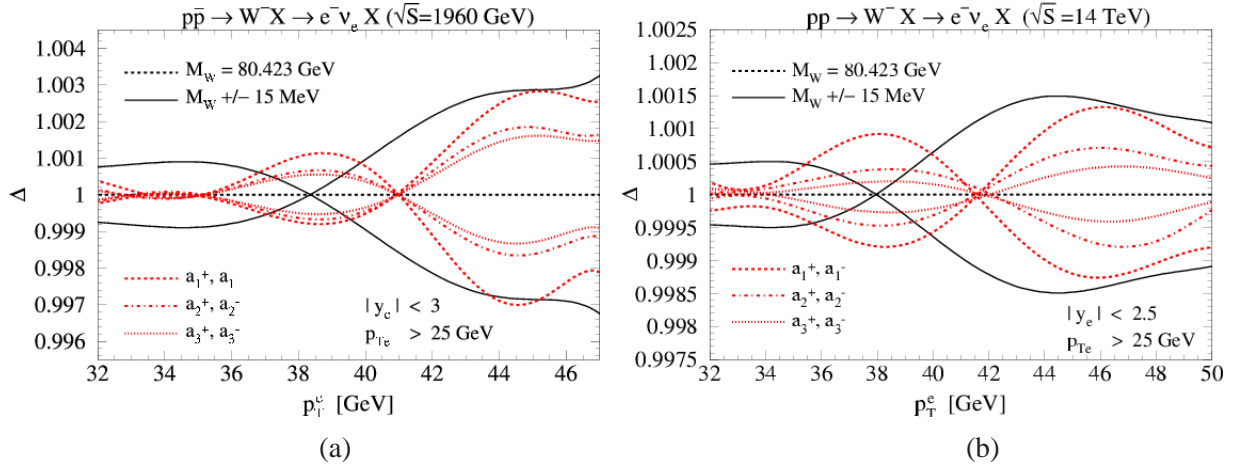


Fig. 4.6.108: Fractional changes in $d\sigma/dp_{T_e}$ in W boson production at the Tevatron and LHC caused by variations of M_W by ± 15 MeV for the central parametrization of $F_{NP}(b;Q)$ (solid black lines), and by six ± 1 variations of $F_{NP}(b;Q)$ in the Hessian method for the central value of $M_W = 80.423$ GeV (dashed and dotted red lines).

Parametrization:	$C_3 = b_0$			$C_3 = 2b_0$		
Set/parameter	a_1	a_2	a_3	a_1	a_2	a_3
$a_{(1)}^+$	0.208	0.198	-0.034	0.262	0.181	-0.059
$a_{(1)}$	0.192	0.168	-0.017	0.233	0.135	-0.039
$a_{(2)}^+$	0.21	0.169	-0.024	0.240	0.182	-0.055
$a_{(2)}$	0.192	0.199	-0.029	0.254	0.134	-0.044
$a_{(3)}^+$	0.208	0.195	-0.024	0.232	0.153	-0.057
$a_{(3)}$	0.193	0.174	-0.029	0.262	0.162	-0.042

Table 4.6.52: Parameters of the six “extreme” sets $a_{(i)}$ ($i=1;2;3$) for the nonperturbative functions $F_{NP}(b;Q)$ published in Ref. [221].

Variations in d_{pT_e} for the extreme parametrizations of $F_{\text{NP}}(b;Q)$ at the Tevatron and LHC are shown in Fig. 4.6.108(a) and Fig. 4.6.108(b). We plot the ratio $(d_{\text{pT}_e}^{a(i)} / d_{\text{pT}_e}^{\text{ref}}) = (d_{\text{pT}_e}^{a(i)} / d_{\text{pT}_e}^{\text{ref}})$, where $(d_{\text{pT}_e}^{\text{ref}})$ is the “reference” cross section evaluated with the central values of $f_{a_{1,2,3}}g$ and a W boson mass of $M_W = 80.423 \text{ GeV}$. $(d_{\text{pT}_e}^{a(i)})$ are the cross sections for the extreme parameter sets $a_{(i)}$ ($i = 1;2;3$) and the central M_W , shown by dashed and dotted lines. The magnitude of these deviations is comparable to the effect of a variation of M_W by 15 MeV (solid black lines), although their pT_e dependence is not exactly the same as the shift in d_{pT_e} caused by the variation of M_W . Figure 4.6.108 indicates that the remaining uncertainties in $F_{\text{NP}}(b;Q)$ may introduce an error of up to $10\text{-}20 \text{ MeV}$ (estimated as in Fig. 4.6.108) in the M_W measurement in the pT_e channel.

4.6.3 New features at small x

The global pT fits [258, 221] analyze the pT -dependent data from low-mass Drell-Yan pair and Z boson production at $x_{A,B} \lesssim 10^{-2}$. At $x \lesssim 10^{-2}$, where no such data currently exist, W and Z boson production may be subject to additional transverse momentum broadening, as suggested by fits of resummed q_{T} distributions to data from semi-inclusive deep inelastic scattering at $x = 10^{-4} \text{--} 10^{-2}$ [265, 266]. This broadening may substantially exceed the range of uncertainties in d_{pT_e} quoted in the previous subsection.

Using crossing relations, we estimate its magnitude in W and Z boson production based on the SIDIS results [222]. The BLNY parametrization of $F_{\text{NP}}(b;Q)$ [258] is modified to include an additional term $(\gamma(x) + \gamma(x_B))b^2$; where the function $\gamma(x)$ parametrizes the cumulative effect of unaccounted higher-order contributions to the b -dependent PDF’s $P_j(x;b)$ at nearly nonperturbative impact parameters ($b \sim 1 \text{ GeV}^{-1}$). Since $P_j(x;b)$ are included in the resummed form factors both in Drell-Yan-like processes and SIDIS, the function $\gamma(x)$ can be constrained using the SIDIS data from HERA. This function satisfies $\gamma(x) \sim 1/x$ for $x \ll x_0$, and $\gamma(x) \sim 0$ for $x \gg x_0$, where the free parameter x_0 is chosen in the range $10^{-3} \text{--} 10^{-2}$. Since $\gamma(x)$ vanishes at large x , this model agrees with the existing Drell-Yan pT data. At $x < 10^{-2}$, the growth of $\gamma(x)$ leads to harder q_{T} distributions without affecting the inclusive production rate.

At the Tevatron, the small- x broadening may be seen only at large rapidities, such as forward Z boson production displayed in Fig. 4.6.109. It marginally affects the M_W measurement, dominated by events with small boson rapidities. The most pronounced effects may be visible in the pT_e distribution (cf. Fig. 4.6.110), where variations due to the broadening are comparable to the effect of a variation of M_W by 20 MeV ($> 50 \text{ MeV}$) at $|y_e| < 1$ ($|y_e| > 1$).

At the LHC, the small- x broadening may be observed at all rapidities. Our model can estimate its magnitude for boson rapidities less than about 2.5, roughly corresponding to the x region covered by the SIDIS data. In Z boson production (Fig. 4.6.111(a)), the distribution with $\gamma(x) \notin 0$ is clearly shifted toward higher q_{T} . The q_{T} shift is even larger in the production of W bosons, cf. Fig. 4.6.111(b), as a result of the smaller boson mass ($M_W < M_Z$) and less restrictive leptonic cuts. Furthermore, the shift is slightly larger in W^+ boson production than in W^- boson production because of the flatter rapidity distribution for W^+ bosons. The shown q_{T} broadening propagates into the leptonic transverse mass and lepton transverse momentum distributions. Both the m_{T_e} and p_{T}^e methods for the measurement of M_W

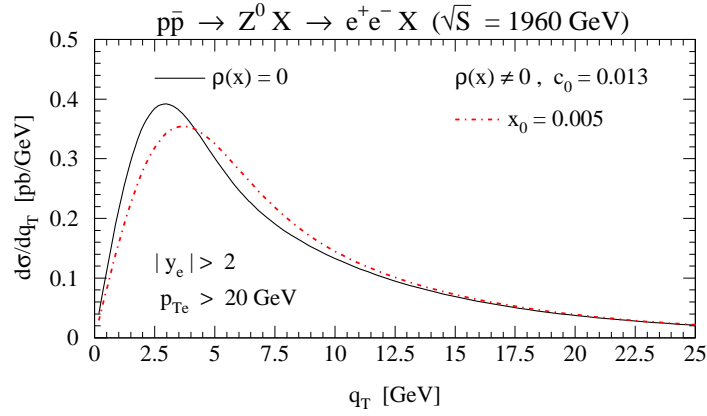


Fig. 4.6.109: Transverse momentum distributions of Z bosons in the Tevatron Run-2 for events with both decay electrons registered in the forward ($y_{e^+} > 2$; $y_{e^-} > 2$) or backward ($y_{e^+} < -2$; $y_{e^-} < -2$) detector regions. The solid (black) curve is the standard CSS cross section, calculated using the BLNY nonperturbative function [258]. The dashed (red) curve includes the additional term responsible for the q_T broadening in the small- x region.

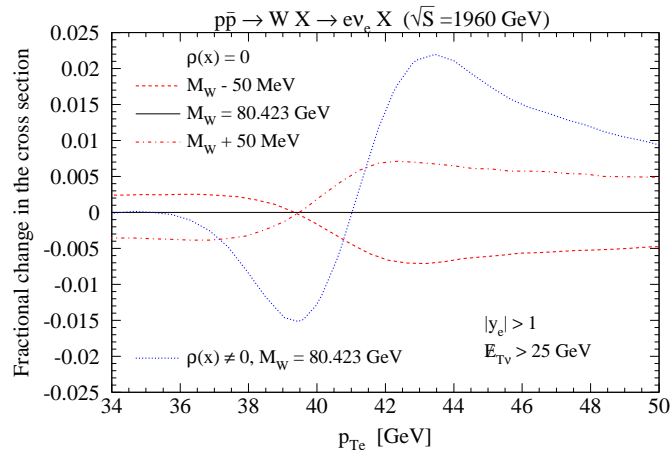


Fig. 4.6.110: The fractional change in the $d = dp_{T_e}$ distribution in forward W boson production at the Tevatron ($|y_e| > 1$, $E_{T_e} > 25$ GeV) due to the small- x broadening (blue dotted line) [222]. The dashed and dot-dashed lines correspond to $M_W = 50$ MeV in the case when the broadening is absent.

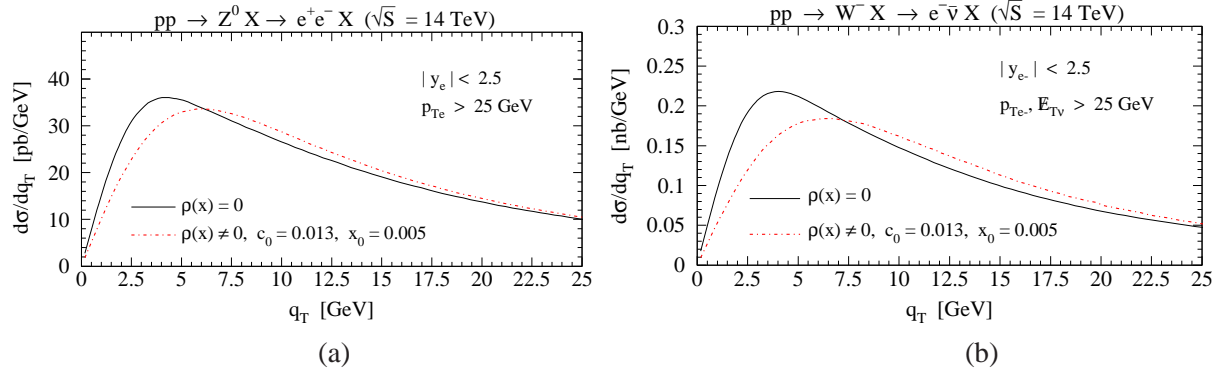


Fig. 4.6.111: (a) Transverse momentum distributions of Z bosons at the Large Hadron Collider with (dashed) and without (solid) the small- x effects. The events are selected by requiring $|y_e| < 2.5$ and $p_{T_e} > 25$ GeV for both decay electrons. (b) Same for W^- bosons. The decay leptons are required to satisfy $|y_e| < 2.5$, $p_{T_e} > 25$ GeV, $E_{TV} > 25$ GeV.

are affected in this case, in contrast to the Tevatron, where the m_{T_e} method is almost not susceptible to the broadening.

4.6.4 Heavy quark effects

About 20% ; 30% , and 15% of W^+ ; W^- ; and Z^0 bosons at the LHC will be produced in scattering processes involving at least one charm or bottom initial-state quark or antiquark. The tangible rate of heavy-flavor contributions at the LHC contrasts that at the Tevatron, where only 8% (3%) of W^- (Z^0) bosons are produced in c or b quark scattering. Since the heavy-quark masses suppress multiple parton radiation at small transverse momenta, they must be implemented in the resummation calculation in order to correctly predict q_T distributions at the LHC energy. The improved treatment of heavy-quark masses changes the q_T distribution at the LHC by an amount comparable to other systematic uncertainties affecting the W^- boson mass measurement [223].

For this purpose, we formulate the CSS resummation formalism in a general-mass variable flavor number (S-ACOT) factorization scheme [267, 268], which preserves correct $m_{c,b}$ dependence at low momentum scales and resums heavy-quark collinear contributions at large momentum scales. The feasibility of the CSS resummation in the S-ACOT scheme has been first demonstrated in Ref. [269]. In W^- boson production in the heavy-scattering channels, the S-ACOT scheme predicts harder q_T distributions than the zero-mass variable flavor number (ZM-VFN) scheme used in previous studies. The improved treatment of $m_{c,b}$ in the S-ACOT scheme modifies p_{T_e} distributions for W^- bosons at the LHC by an amount comparable to the effect of $M_W = 10$ MeV (see Fig.4.6.112). The $m_{c,b}$ dependence is somewhat less pronounced in W^+ and especially Z^0 production, as a result of smaller heavy-flavor contents in these processes. It is negligible at the Tevatron.

4.6.5 PDF uncertainties

PDF uncertainties in the M_W measurement were estimated in the Tevatron Run-1 by repeating the analysis for select sets of parton densities, which did not cover the full span of allowed variations in the PDF parameters. A more systematical estimate can be realized by applying the new techniques for the PDF error analysis. The choice of the PDF set affects q_T distributions directly, by changing the PDF's in the

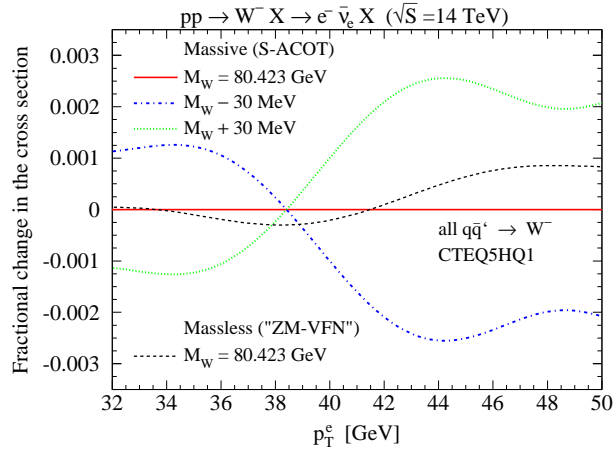


Fig. 4.6.112: The fractional change in the $d = d p_T^e$ distribution for W boson production at the LHC due to the improved treatment of heavy-quark mass terms in the CSS resummation [223]. The solid red line ($M_W = 80.423$ GeV), dotted green line ($M_W = +30$ MeV) and dot-dashed blue line ($M_W = -30$ MeV) are reference distributions that include the full $m_{c,b}$ dependence in the general-mass variable-flavor number (S-ACOT) scheme. The dashed black line is the distribution in the zero-mass variable-flavor number (ZM-VFN) scheme, which neglects $m_{c,b}$ dependence in perturbative contributions.

factorized QCD cross section, but also indirectly, by modifying the nonperturbative function $F_{NP}(b;Q)$ in the resummed form factor. For a chosen form of $F_{NP}(b;Q)$, the PDF errors can be evaluated within the Hessian matrix method, by repeating the computation of σ_T distributions for an ensemble of sample PDF sets.

Variations in the resummed σ_T spectrum for W^+ production at the LHC are shown in Fig. 4.6.113 for 41 CTEQ6.5 PDF sets [270] and KN1 nonperturbative function [221]. Depending on the choice of the PDF set, $d = d\sigma_T$ at small σ_T changes by up to 4% from its value for the central PDF set (CTEQ65M), except for very small σ_T . The variations in the PDF's modify *both* the normalization and shape of $d = d\sigma_T$. Although the changes in the shape are relatively weak at $\sigma_T < 15$ GeV, they may affect the measurement of M_W in the $p_{T,e}$ method. These results do not reflect possible correlations between the PDF's and $F_{NP}(b;Q)$ in the global fit to p_T data, introduced by the dependence of $F_{NP}(b;Q)$ on the normalizations of the low- Q Drell-Yan cross sections. The correlation between free parameters in the PDF's and $F_{NP}(b;Q)$ will be explored in the future by performing a simultaneous global analysis of the inclusive cross sections and p_T -dependent data.

4.6.6 σ_T spectrum and final-state QED corrections

As discussed in Sections 4.2, 4.5, electroweak corrections to Drell-Yan W and Z boson production are dominated by the QED radiation from the final-state charged lepton, which results in some loss of the charged lepton's momentum to the surrounding cloud of soft and collinear photons. The final-state QED (FQED) radiation changes the extracted value of M_W by shifting the Jacobian peak in the $p_{T,e}$ distribution in the negative direction. In contrast, the initial-state radiation and interference terms mostly change the overall normalization of the Jacobian peak and have a smaller effect on the determination of M_W . The combined effect of the $\mathcal{O}(\alpha_s)$ FQED correction and the resummed QCD correction was estimated for the Run-2 observables by using a new computer program RESBOS-A (RESBOS with FQED effects) [212].

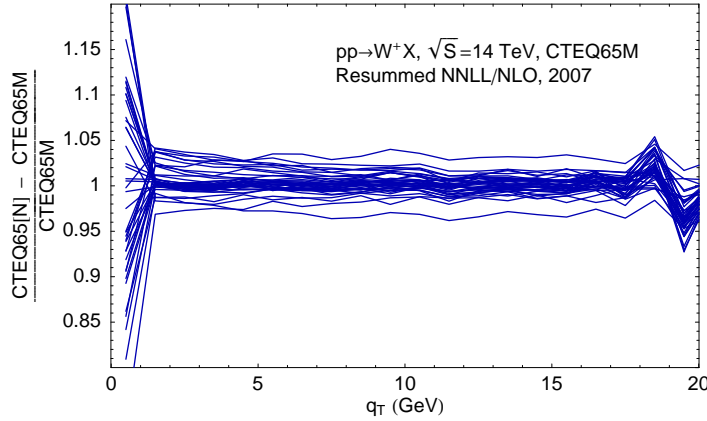


Fig. 4.6.113: Variations in the W^+ transverse momentum distribution, $d = d/dq_T$, at the LHC for 40 CTEQ6.5 PDF sets [270] with respect to the CTEQ6.5M PDF set.

The FQED and resummed QCD corrections to the Born-level shape of the Jacobian peak in the m_{T_e} distribution were found to be approximately (but not completely) independent. The reason is that the m_{T_e} distribution is almost invariant with respect to the transverse momentum of W bosons, so that the QCD correction reduces, to the first approximation, to rescaling of the Born-level m_{T_e} distribution by a constant factor. The relationship between FQED and QCD corrections is more involved in the leptonic p_T distributions, which depend linearly on q_T of W bosons. In the p_T^e channel, the combined effect does not factorize into separate FQED and QCD corrections to the Born-level cross section.

4.6.7 Conclusion

We have reviewed recent advances in the understanding of resummed q_T distributions for electroweak bosons. The q_T resummation formalism is realized at the NNLL/NLO level of accuracy and includes such new ingredients as the dominant NLO electroweak contributions, correct dependence on heavy-quark mass terms, and an improved model for the nonperturbative recoil at $x \ll 10^{-2}$. Other important aspects of q_T resummation, such as the behavior of higher-order radiative contributions at $x < 10^{-2}$ and correlations between the PDF's and nonperturbative resummed function must be assessed to ensure that the systematic uncertainties in the M_W measurements are under full control. The dynamics of these factors can be tested by measuring fully differential distributions of lepton pairs in a wide range of Q and y in the Tevatron Run-2.

Acknowledgments

This work was partially supported by the U.S. Department of Energy under grant DE-FG03-95ER40908, contract DE-AC02-06CH11357, and the Lightner-Sams Foundation.

4.7 Estimate of theoretical uncertainties due to missing higher-order corrections

Contributed by: A. Arbuzov, D. Bardin, U. Baur, S. Bondarenko, C. M. Carloni Calame, P. Christova, L. Kalinovskaya, G. Montagna, O. Nicrosini, R. Sadykov, A. Vicini, and D. Wackerroth

In order to estimate the residual theoretical uncertainties due to missing higher-order corrections

of predictions obtained by electroweak precision tools such as HORACE, SANC, and WGRAD2, we study in the following the effects of different choices for the EW input parameter scheme and of leading higher-order (irreducible) QCD and EW corrections connected to the α_s parameter. For definiteness we use WGRAD2. Similar results can be easily obtained with HORACE and SANC as well. In Table 4.7.53 and Fig. 4.7.114 we compare the predictions of the tuned comparison using the setup described in Section 4.4 (labeled as 'NLO at $\mathcal{O}(\alpha_s^3)$ ') with predictions that are obtained as follows:

'NLO at $\mathcal{O}(\alpha_s^3)$ incl. h.o.':

The EW input parameter scheme of the tuned comparison is used as described in Section 4.4. But we replace the Z mass renormalization constant $M_Z^2 = \text{Re}^{-Z}(M_Z^2)$ by

$$M_Z^2 = \text{Re}^{-Z}(M_Z^2) \frac{(\hat{\Sigma}^Z(M_Z^2))^2}{M_Z^2 + \hat{\Sigma}^Z(M_Z^2)} ; \quad M_W^2 = \text{Re}^{-W}(M_W^2) \quad (4.7.47)$$

where $\hat{\Sigma}^V(\hat{M}^V)$ denote the transverse parts of unrenormalized(renormalized) vector boson self energies, and include higher-order (irreducible) corrections connected to the α_s parameter, \mathcal{H}^O , by performing the replacement

$$\frac{M_Z^2}{M_Z^2} \rightarrow \frac{M_W^2}{M_W^2} ! \frac{M_Z^2}{M_Z^2} \rightarrow \frac{M_W^2}{M_W^2} \quad \mathcal{H}^O \quad (4.7.48)$$

as described in detail in Ref. [209] (Appendix A).

'NLO at $\mathcal{O}(\alpha_s^2)$ incl. h.o.':

In addition to the modifications described above, we change the EW input parameter scheme (\mathcal{G}^0 scheme \rightarrow \mathcal{G} scheme) by replacing

$$(0) ! \frac{p_{2G} M_W^2}{2G} \rightarrow 1 \frac{M_W^2}{M_Z^2} ;$$

so that

$$d(\mathcal{G}^2) = [d_{\text{NLO}}(\alpha_s^3) - 2 \text{rd}_{\text{LO}}(\alpha_s^2)] \frac{p_{2G} M_W^2}{(0)} \rightarrow 1 \frac{M_W^2}{M_Z^2} \quad \#_2 ;$$

where r parametrizes the radiative corrections to muon decay (see also Ref. [199]).

As illustrated in Table 4.7.53 and Fig. 4.7.114 for the LHC the relative differences between the different predictions, $\delta = d_{\text{NLO}}(\alpha_s^3) - (d_{\text{h.o.}} - 1)$ and $A(Y_1) = A(Y_1)_{\text{NLO}}(\alpha_s^3) - A(Y_1)_{\text{h.o.}}$, are at most about 1.5% for M_W , and the $M_T(1)$, P_T^1 distributions, and up to about $4 \cdot 10^5$ for the charge asymmetry of leptons in W decay. We find the same relative differences at the Tevatron. Since switching to the \mathcal{G} scheme changes the shape of the $M_T(1)$ distribution, a more detail study of how these effects translate into a shift in M_W is warranted. Moreover, other sources of residual theoretical uncertainties, for instance missing higher-order EW Sudakov logarithms and the QED scale dependence, need to be under control as well.

4.8 Experimental Uncertainties

Contributed by: C. Hays and D. Wackerath

	Tevatron, σ_W [pb]	LHC, σ_W [pb]
	$pp \rightarrow W^+ \rightarrow \mu^+ \nu_\mu$	$pp \rightarrow W^+ \rightarrow \mu^+ \nu_\mu$
NLO at $\mathcal{O}(\alpha^3)$	738.00(1)	4943.0(1)
NLO at $\mathcal{O}(\alpha^3)$ incl. h.o.	745.80(1)	4995.5(1)
NLO at $\mathcal{O}(\alpha^3)$ incl. h.o.	747.62(1)	5006.5(1)

Table 4.7.53: Comparison of predictions for σ_W to $pp \rightarrow W^+ \rightarrow \mu^+ \nu_\mu$ with calo cuts at the Tevatron and the LHC. The higher-order predictions include corrections beyond $\mathcal{O}(\alpha^3)$ other than mPR, in addition to the complete set of electroweak $\mathcal{O}(\alpha^2)$ corrections (see text for more details). For this comparison, we use WGRAD2 results for definiteness.

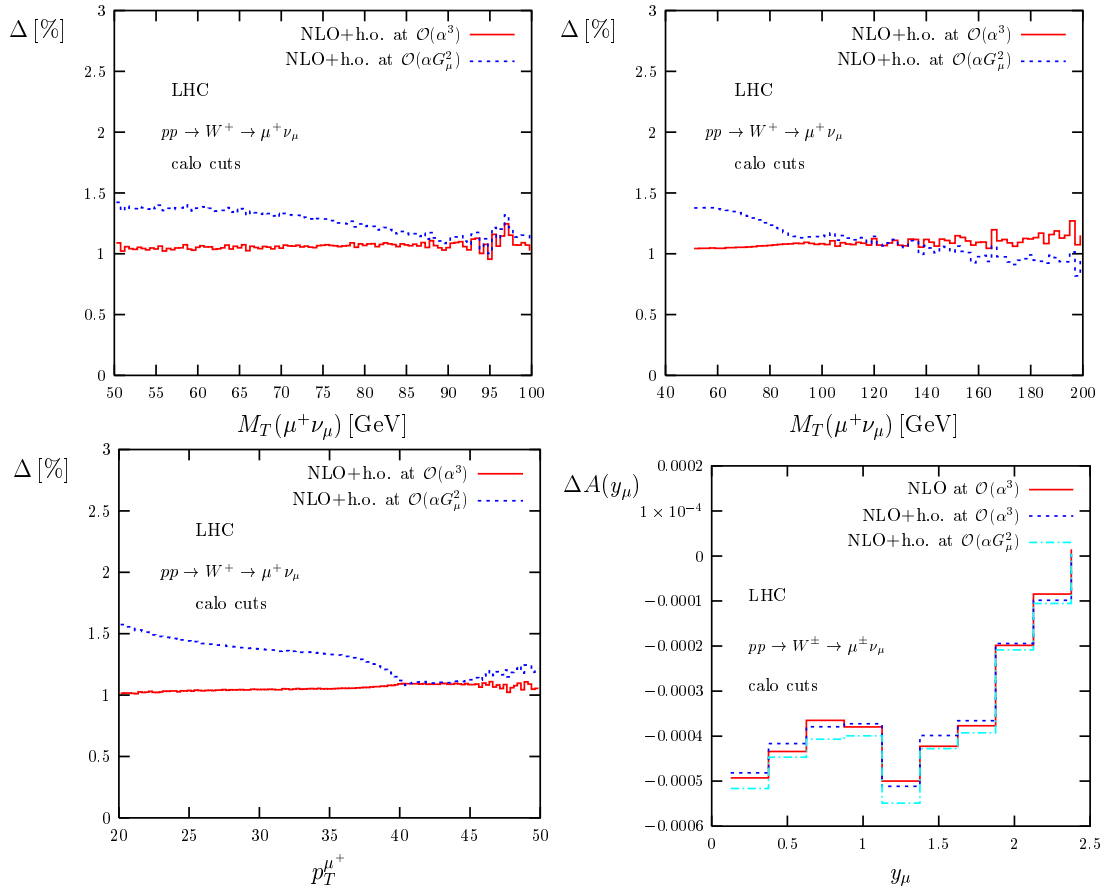


Fig. 4.7.114: Relative differences between NLO and higher-order predictions for the $M_T(\mu^+\nu_\mu)$, $p_T^{\mu^+}$ and $A(y_\mu)$ distributions for single W^+ production with calo cuts at the LHC. The higher-order predictions include corrections beyond $\mathcal{O}(\alpha^3)$ other than mPR, in addition to the complete set of electroweak $\mathcal{O}(\alpha^2)$ corrections (see text for more details). For this comparison, we use WGRAD2 results for definiteness.

The W boson observables studied in this report – the total W boson production cross section (σ_W), the $M_T(l)$ and p_T^l distributions, and the W boson charge asymmetry for leptons (A_{Y_1}) – have been measured by the CDF and DØ collaborations⁷. The W boson mass is dominantly extracted from the $M_T(l)$ distribution, as described in Section 5. Possible improvements in the W boson mass measurement at the LHC by using the transverse momentum distribution of the charged lepton have been studied in Ref. [271]. In the following we briefly summarize present and anticipated experimental uncertainties in the measurements of σ_W , A_{Y_W} , A_{Y_1} and M_W and discuss their implications on further improvements of theoretical predictions.

4.8.1 Total W and Z boson production cross section

As pointed out earlier, given the large W and Z boson production rates at the LHC, the total W and Z boson production cross sections are expected to be used for detector calibration and as luminosity monitors [187]. The 72 pb^{-1} CDF combined e and μ result for the total W boson production cross section is [272]:

$$\sigma(W) = \text{Br}(W \rightarrow l) = 2775 \pm 10(\text{stat}) \pm 53(\text{sys}) \text{ pb} ;$$

which corresponds to a relative precision of 2%. The 96 pb^{-1} DØ result is [273]

$$\sigma(W) = \text{Br}(W \rightarrow l) = 2989 \pm 15(\text{stat}) \pm 81(\text{sys}) \text{ pb} ;$$

The 72 pb^{-1} CDF combined e and μ result for the total Z production cross section is [272]:

$$\sigma(Z) = \text{Br}(Z \rightarrow ll) = 254.9 \pm 3.3(\text{stat}) \pm 4.6(\text{sys}) \text{ pb} ;$$

The DØ 148 pb^{-1} result is [274]:

$$\sigma(Z) = \text{Br}(Z \rightarrow ll) = 329.2 \pm 3.4(\text{stat}) \pm 7.8(\text{sys}) \text{ pb} ;$$

These results exclude the Tevatron luminosity uncertainty of about 6%, of which 4% is correlated between experiments. The W and Z boson measurements have a few systematic uncertainty components that are different, so combining them should give the most accurate luminosity measurement. The measurements of σ_W and σ_Z at the LHC are expected to reach a relative precision of 3.3% ($W \rightarrow ll$) and 2.3% ($Z \rightarrow ll$) for $L = 1 \text{ fb}^{-1}$ and to be limited again by the luminosity uncertainty of about 5% [271]. As long as the luminosity uncertainty cannot be drastically improved, a theoretical uncertainty of 1.5% due to missing higher order EW corrections (see Section 4.7) is not worrisome. However, the impact of these uncertainties on precise electroweak measurements at the LHC based on W/Z ratios should be studied in more detail.

4.8.2 W boson and lepton charge asymmetry

The W boson charge asymmetry (A_{Y_W}) is a sensitive probe of valence quark PDFs. Recent theoretical advances include the calculation of the fully differential cross section at NNLO QCD to W/Z boson production [203], which will help to further constrain quark PDFs. In Fig. 4.8.115 we show the

⁷A collection of the most recent EW results can be found at the CDF and DØ physics results websites, www-cdf.fnal.gov/physics/ewk and www-d0.fnal.gov/Run2Physics/WWW/results/ew.htm

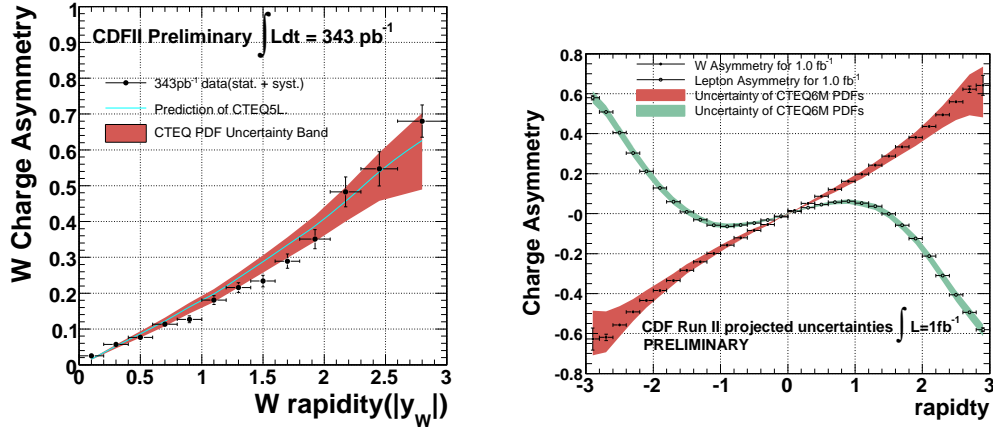


Fig. 4.8.115: The measured (with $L = 343 \text{ pb}^{-1}$) [275, 276] and projected ($L = 1 \text{ fb}^{-1}$) [275, 276] CDF W charge asymmetry $A(y_W)$ and lepton asymmetry in $pp \rightarrow W \rightarrow l \bar{\nu}_l$.

W boson charge asymmetry as measured by CDF with $L = 343 \text{ pb}^{-1}$ [275, 276] and a projection to 1 fb^{-1} [275, 276]. In Table 4.8.54 we provide the combined statistical and systematic uncertainties for three representative rapidities, $y_W; y_1 = 1; 1.8; 2.6$, of the present $D\phi$ measurement of the muon asymmetry with 230 pb^{-1} [277] and the projected CDF measurement of the W boson and lepton asymmetry with 1 fb^{-1} [275, 276]. In Ref. [278] the PDF uncertainty in a measurement of $A(y_W)$ at the LHC has been estimated to be 4%. As shown in Table 4.8.54, the impact of different choices of EW input schemes on $A(y_1)$ is negligible. We expect to observe similar effects in $A(y_W)$ which, however, needs to be studied in more detail.

4.8.3 W boson mass

The most precise single W boson mass measurement is presently provided by CDF [279] (see also Section 5), yielding a combined CDF and $D\phi$ measurement of [280]

$$M_W = 80.429 \pm 0.039 \text{ GeV} :$$

A Tevatron precision of about 20 MeV is anticipated with 2 fb^{-1} . The extraction of the W boson mass from the $M_T(l)$ distribution is sensitive to effects that distort the shape of the distribution around the Jacobian peak. In Fig. 4.7.114 we observed a distortion of the $M_T(l)$ and p_T^l distributions when comparing the strictly NLO results of $\mathcal{O}(\alpha_s^3)$ with the result obtained at $\mathcal{O}(\alpha_s^2)$. Therefore, a more detailed study is warranted to determine the shift in M_W due to these effects when using the $M_T(l)$ distribution and ratios of W and Z boson distributions. In the latter case, they may largely cancel, but this has to be determined by a careful study.

4.9 Conclusion

In this report we gave an overview of the state-of-the-art of precision calculations for single W production at the Tevatron and the LHC. We performed a tuned comparison of the Monte Carlo programs HORACE,

Observable	σ_W	charge asymmetry $A_{Y_W}; A_{Y_1} = 1; 1.8; 2.6$	M_W
<i>experimental precision: (Section 4.8)</i>			
Tevatron (now)	2%	A (Y_1): 0.0078; 0.0484; - (DØ)	39 MeV
Tevatron ($1 \text{ } 2 \text{ fb}^{-1}$)	-	A (Y_W): 0.0043; 0.0073; 0.030 (CDF) A (Y_1): 0.0056, 0.0078, 0.076 (CDF)	20 MeV
LHC	3.3%	-	15 MeV
<i>impact of h.o. corrections and theoretical uncertainties:</i>			
Observable	σ_W	A (Y_1)	M_W (e)
mPR ($1 =$) (Section 4.5)	. 0.2%	-	10(2) MeV
EW input scheme/missing h.o. (Sect. 4.7)	1.5%	. 4 10^5	tbd
σ_T broad. (Section 4.6.3)	-	-	20-50 MeV
heavy q mass (Section 4.6.4)	-	-	. 10 MeV
nonperturb. (Section 4.6.2)	-	-	. 17 MeV

Table 4.8.54: Present and anticipated experimental uncertainties of W boson observables are compared to effects of higher-order corrections, i.e. beyond $\mathcal{O}(\alpha_s)$, as well as theoretical uncertainties studied in this report. Details are provided in the respective sections. Experimental uncertainties on σ_W do not include the 6% luminosity uncertainty.

SANC and WGRAD2, taking into account realistic lepton identification requirements. As a result of this comparison we found good numerical agreement of the predictions for the total W production cross section, the $M_T(l)$, P_T^l distributions and the lepton charge asymmetry. The effects of higher-order QED corrections have been studied as well using HORACE. To estimate the residual theoretical uncertainty due to missing higher-order corrections and different choices of the EW input parameter scheme we compared the strictly NLO results with predictions that in addition include leading QCD and EW two-loop corrections and predictions that use the \overline{G} scheme instead of the (0) scheme. Moreover, we discussed important aspects of σ_T resummation that may affect significantly the systematic uncertainties in the M_W measurement. Some of our results of these studies of higher-order corrections and theoretical uncertainties are summarized in Table 4.8.54. When comparing with the anticipated experimental uncertainties, we conclude that further theoretical improvements are needed to fully exploit the potential of the LHC for performing high-precision studies of the electroweak gauge bosons. Moreover, more detailed studies of the residual uncertainties of predictions obtained with the available tools are needed, in particular the impact of these effects on the W mass. For instance, our study does not include PDF uncertainties, combined QCD and EW effects, QED/QCD scale uncertainties, and the impact of higher-order EW Sudakov logarithms.

5 Measurement of the W Mass

Contributed by: C. Hays

The m_W measurement in $p\bar{p}$ data uses s -channel resonant W bosons with leptonic decays. The transverse momentum of the decay e or (p_T^\perp) can be measured with high precision and thus provides the bulk of the mass information. Additional information comes from the decay μ transverse momentum (p_T), which is inferred from the measured energy imbalance in the event. Since the lepton energy is well measured, the dominant uncertainty on p_T comes from measuring the hadrons recoiling against the produced W boson. Because the Z boson has a similar mass and production mechanism to the W boson, events with Z bosons can be used to calibrate and model the detector response to hadronic activity.

The best statistical power for measuring m_W is obtained by combining p_T^\perp and p_T into the transverse mass, defined as:

$$m_T = \sqrt{2p_T^\perp p_T (1 - \cos(\theta))} \quad (5.0.49)$$

With precise detector calibration, the lepton momentum can be measured to a few parts in 10,000. However, the hadrons resulting from initial-state radiation are typically measured to a precision of 1%, degrading the resolution of the inferred neutrino momentum. To suppress this degradation, the transverse hadronic momentum (known as the “recoil”) is required to be less than 15 or 20 GeV. Alternatively, the lepton transverse momentum (p_T^\perp) distribution can be used to measure the W boson mass, though this suffers from uncertainties in the theoretical prediction of the W boson p_T^\perp , which has not been modelled from first-principles QCD. In a final analysis, the two fits can be combined to utilize the strengths of each.

5.1 CDF Run 2 Measurement

The Run 2 W mass measurement proceeds by sequentially calibrating the detector response to:

1. Muon momentum
2. Electron energy
3. Hadronic recoil energy

The muon momentum calibration uses low-mass quarkonia decays to dimuons; the electron energy calibration uses the calibrated tracks from W decay electrons; and the hadronic recoil energy calibration uses the measured recoil in $Z \rightarrow \mu\mu$ events.

Track Momentum Calibration

A charged particle’s momentum is measured through its observed curvature in the tracker. Since the momentum is inversely proportional to curvature, the momentum scale is measured as a function of the mean inverse momentum of $\mathcal{J} = \mu$ muons and fit to a line (Fig. 5.1.116). Improper modelling of the muon energy loss in the tracker can lead to a non-zero slope of this line, since high-momentum muons lose a smaller fraction of their energy than low-momentum muons. The amount of material contributing to ionization energy loss is tuned to make the slope equal to zero. At CDF, the tuning is a 6% correction to the known material used in GEANT simulation. To speed up event simulation, a material map based on

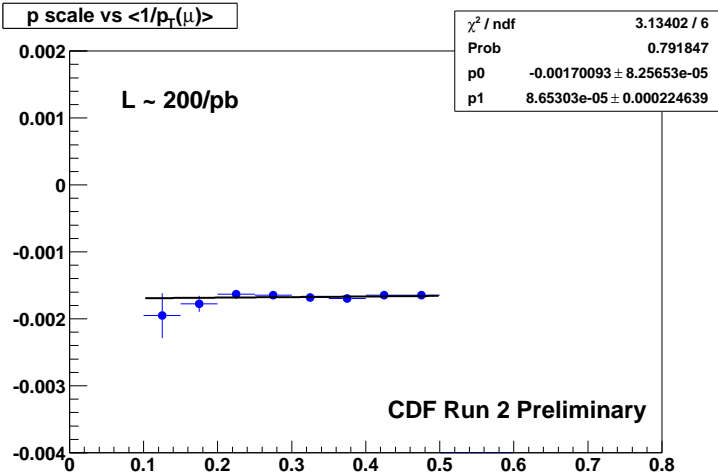


Fig. 5.1.116: The momentum scale correction as a function of mean inverse muon momentum. The correction is determined by comparing the measured $J=$ mass to that of the PDG.

the tracker material is produced and used in place of GEANT. The map contains the material properties necessary for electron and muon simulation: ionization energy loss constants from the Bethe-Bloch equation; and radiation lengths.

To improve momentum resolution, muon tracks from W and Z decays use the transverse beam position as a point in the track fit. This constraint is not applied to $J=$ decays since they can be separated from the beam line. Instead, $J=$ decays are used to verify that the beam constraint produces no bias on the momentum calibration. The $J=$ momentum scale is combined with that of the $J=$'s to reduce the total uncertainty on the momentum scale. As a cross-check, the scale is applied to the $Z \rightarrow \mu\mu$ sample and the extracted Z mass is compared to the LEP measurement of 91.187 GeV.

Aside from the material calibration to model muon energy loss, the simulation of multiple Coulomb scattering is necessary to accurately model the resolution of low-momentum muons (< 10 GeV). The multiple scattering is simulated to have a Gaussian width of:

$$\sigma = 13.6 \text{ MeV} \sqrt{\frac{x_0}{x_0 + P}} \quad (5.1.50)$$

where x_0 is the fraction of radiation lengths of the detector. Additional resolution arises from hard scatters in the tail of the distribution; about 2% of the scatters have a Gaussian width 4 times larger than that of Equation 5.1.50.

At high momentum, additional resolution can result from misalignments in the drift chamber used for track measurement (the central outer tracker, or COT). A detailed alignment procedure based on cosmic rays sets the positions of the wires in the COT. Final curvature corrections, determined using electron calorimeter energy and separating electrons from positrons, are applied to all tracks. The resulting simulation of the resolution is tested using the observed width of the $Z \rightarrow \mu\mu$ resonance. The known hit resolutions and the transverse beam spot size completely determine the resolution of beam-constrained tracks. Any difference between the observed and simulated Z width is removed by tuning the beam spot size in the simulation.

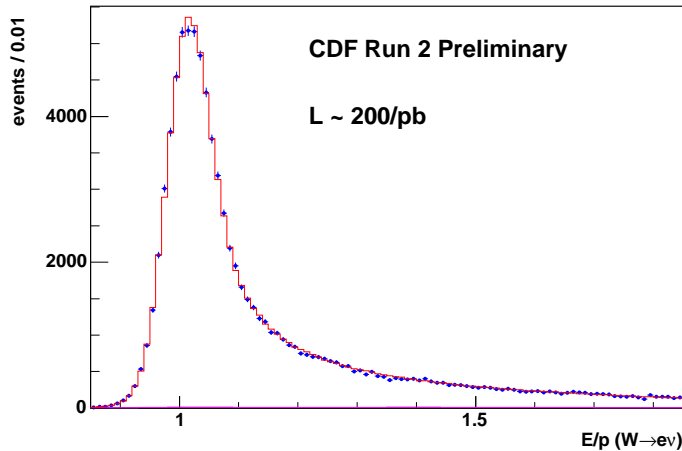


Fig. 5.1.117: The ratio of calorimeter energy to track momentum for electrons from $W \rightarrow e$ decays. The simulated calorimeter energy is scaled to match the data distribution in the peak.

The uncertainties of the momentum scale calibration come from the statistics and systematics of the J/ψ and Z samples ($m_W = 16 \text{ MeV}$), and from possible residual misalignments ($m_W = 6 \text{ MeV}$).

Calorimeter Energy Calibration

Given the momentum calibration, electron tracks from W decays are used to calibrate the electromagnetic calorimeter. The simulated calorimeter energy is scaled such that the ratio of energy to track momentum (E/p) matches that of the data near the peak (Fig. 5.1.117). This calibration requires a detailed simulation of processes affecting the shape and position of the peak. These processes include: electron bremsstrahlung and photon conversion in the tracker; electron and photon energy loss in the solenoid, which sits inside of the calorimeter; and electron and photon energy leakage into the hadronic section of the calorimeter, which is not used in the cluster energy measurement.

The significant amount of material in the silicon tracker moves the peak to larger E/p values, since radiated photons enter the calorimeter cluster but reduce the track momentum. The material model is tested by the shape of the E/p distribution at high values, where harder bremsstrahlung occurs. Figure 5.1.118 shows the difference between simulation and data for each 0.01 bin of E/p , measured in terms of sigma. The events in the region $1.19 < E/p < 1.35$ are divided into two bins and used to tune the amount of material contributing to radiation lengths. This tuning can result in a different correction from the J/ψ material tuning, since ionization energy loss and radiation lengths scale differently with nuclear charge (Z). Thus, to correctly describe both processes *a priori*, one would need to know both the amount and type of material in the tracker.

The CDF calorimeter has a non-linear response as a function of particle energy. A non-linearity correction is taken from the E/p distribution from $W \rightarrow e$ and $Z \rightarrow ee$ decays, separated in bins of E_T (Fig. 5.1.119). This correction is applied to each simulated electron and photon entering the calorimeter.

The total uncertainty on the calorimeter energy scale arises from uncertainties on the material tuning ($m_W = 9 \text{ MeV}$), on the non-linearity correction ($m_W = 23 \text{ MeV}$), on the statistics of the E/p

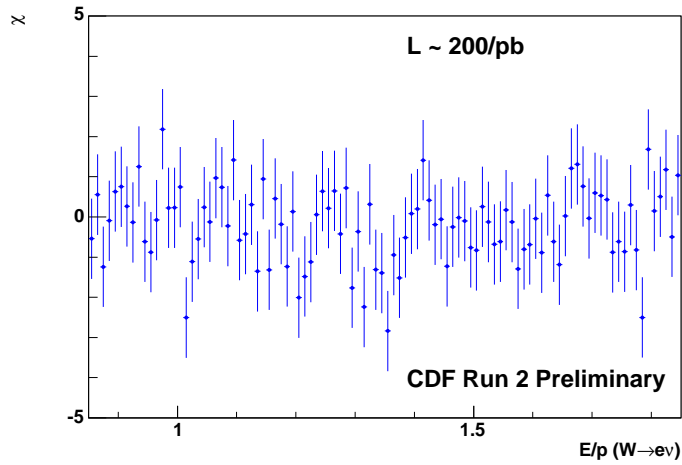


Fig. 5.1.118: The signed χ difference between data and simulation for each bin in the $E = p$ distribution used to extract a calorimeter scale for electrons.

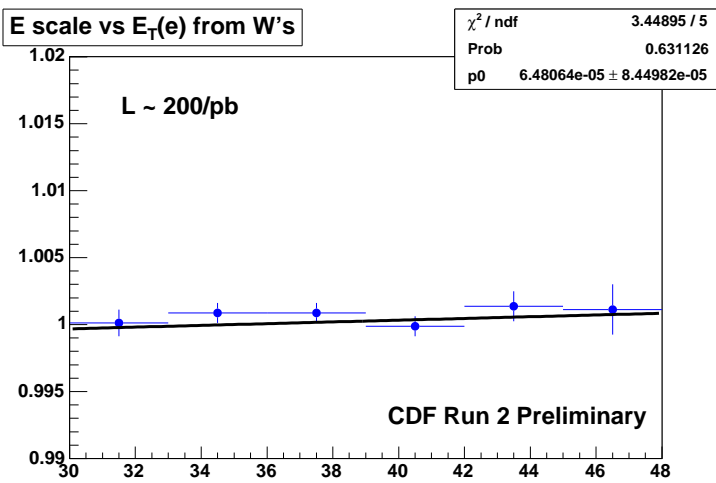


Fig. 5.1.119: The $E = p$ distribution as a function of E_T for electrons from $W \rightarrow e \nu$ decays. The simulated calorimeter response is tuned as a function of E_T to produce zero slope for the combined W and Z sample.

peak ($\sigma_{m_W} = 20 \text{ MeV}$), and on the tracker momentum scale ($\sigma_{m_W} = 17 \text{ MeV}$). This uncertainty is reduced to a total of 30 MeV by incorporating the Z boson mass measurement into the calibration.

Hadronic Recoil Measurement and Simulation

The hadronic recoil energy is measured by vectorially summing all the energy in the calorimeter, excluding that contributed by the lepton. Removing the lepton also removes underlying event energy parallel to the lepton. The amount of removed energy is estimated using calorimeter towers separated in $\Delta\phi$ from the lepton, and a correction is applied to the simulation.

The detector response to the hadronic energy is defined as $R = u_{meas} = u_{true}$, where u_{true} is the recoil momentum of the W boson. The response is measured using $Z \rightarrow ll$ events, since leptons are measured more precisely than the hadronic energy.

The hadronic energy resolution is modelled as having a component from the underlying event (independent of recoil) and a component from the recoiling hadrons. The model parameters are tuned using the resolution of $Z \rightarrow ll$ along the axis bisecting the leptons. This axis is the least susceptible to fluctuations in lepton energy. Figures 5.1.120 and 5.1.121 show the response and resolution in $Z \rightarrow ll$ events after tuning the model parameters.

The underlying event resolution component is parametrized in terms of $\sqrt{E_T}$ in the calorimeter, and incorporated by applying the measured calorimeter resolution as a function of $\sqrt{E_T}$. The simulated $\sqrt{E_T}$ distribution contains the hard interaction producing the W or Z plus additional interactions at a rate that depends on the instantaneous luminosity. The $\sqrt{E_T}$ distribution of the additional interactions is taken from an inelastic scattering sample. The hard interaction distribution is extracted as a deconvolution of the inelastic scattering $\sqrt{E_T}$ distribution. Since generic inelastic scatters have a different Q^2 momentum transfer than W and Z events, a tunable scale factor is applied to the $\sqrt{E_T}$ of the hard interaction. This factor is adjusted to produce the best agreement between simulation and data of the recoil resolution of Z events.

The uncertainties from the recoil simulation arise from the lepton removal ($\sigma_{m_W} = 5 - 8 \text{ MeV}$), response ($\sigma_{m_W} = 9 \text{ MeV}$), and resolution ($\sigma_{m_W} = 7 \text{ MeV}$).

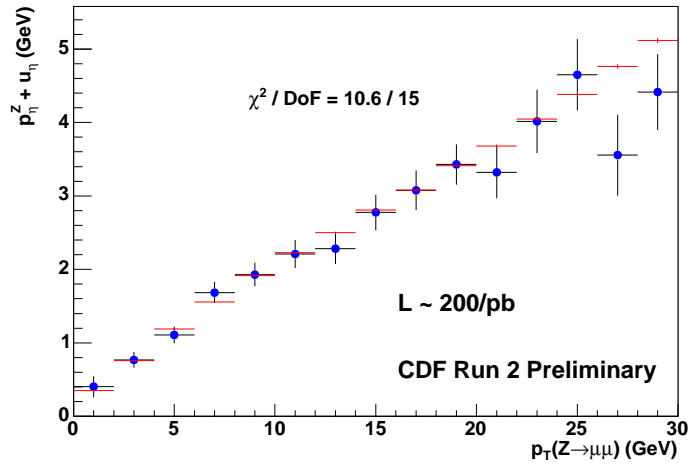


Fig. 5.1.120: The net momentum along the bisecting axis of the muons in $Z \rightarrow \mu\mu$ events, as a function of Z p_T . The calorimeter response to hadronic energy is tuned in the simulation to match the data.

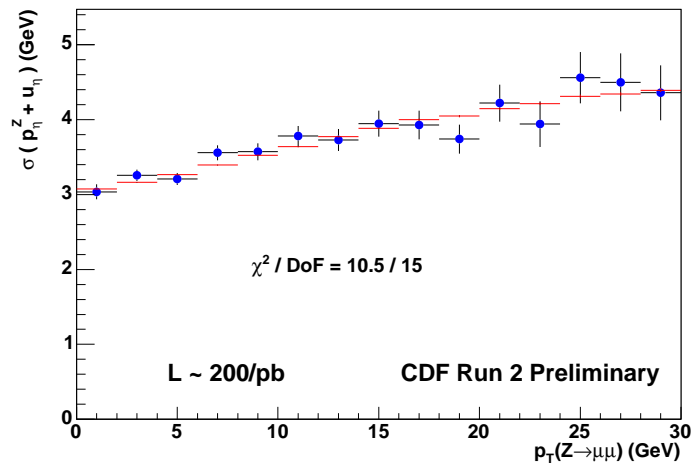


Fig. 5.1.121: The spread of the net momentum along the bisecting axis of the muons in $Z \rightarrow \mu\mu$ events, as a function of Z p_T . The $\sum E_T$ of the hard interaction is tuned to match the simulation spread to that of the data.

6 Measurement of the W Width

Contributed by: J. Zhu

Width of the W boson is a fundamental parameter in the Standard Model. The leptonic partial width for the lepton l can be expressed in terms of the muon decay constant G_F , the W mass and a small ($< 0.5\%$) radiative correction (δ_{SM}) to the Born-level expression as $\Gamma(W \rightarrow l \bar{l}) = G_F^2 M_W^3 \frac{1}{2} [1 + \delta_{SM}]$ [281]. Dividing the partial width by the leptonic branching ratio $\text{Br}(W \rightarrow l \bar{l}) = \frac{1}{3} + \delta_{SM}(M_W) + \mathcal{O}(\frac{\alpha}{s})$, gives the SM prediction for the full decay width $\Gamma_W = 2.090 \pm 0.008 \text{ GeV}$ [282], where the uncertainty is dominated by the experimental M_W precision. Thus a precise measurement of the W width can be used to test the SM calculation and probe the physics beyond SM model since additional particles beyond the SM would increase the W width.

The W width can be measured indirectly using the ratio of the $W \rightarrow l \bar{l}$ and $Z \rightarrow l \bar{l}$ cross sections. Γ_W can also be obtained directly from a precise determination of the W transverse mass (M_T) lineshape. Figure 6.0.122 shows the Monte Carlo simulated M_T spectra for different input W widths. The M_T spectrum has a kinematic upper limit at the value of M_W , and events with $M_T > M_W$ arise due to the combination of the intrinsic W width and the detector resolution. In the region $M_T > 100 \text{ GeV}$, the W width component dominates the detector resolution component. Thus, the transverse mass tail region is sensitive to Γ_W , and the width can be directly extracted from a fit to the region $100 < M_T < 200 \text{ GeV}$. Using this technique, both CDF and D0 experiments have published their results using Run I data [283] [284], preliminary Run II result from D0 has been reported in [285], and the combined result from all Tevatron direct measurements is $\Gamma_W = 2.078 \pm 0.087 \text{ GeV}$ [286].

Due to the rapid falling of the Jacobian peak, only a small fraction of the W events is used in the fitting, and so all previous measurements are limited by the available statistics. At the LHC, after all selection cuts about 60 million W 's are expected in one year of data taking at low luminosity (10 fb^{-1}) [287], the fraction of events in the fitting region (100 - 200 GeV) is roughly 1%, therefore 0.6 million W 's can be used to extract Γ_W . If we scale the statistical uncertainty with $1/\sqrt{N_W}$, the final statistical uncertainty on the width measurement should be smaller than 5 MeV. Γ_W measurements from LHC experiments will all be limited by the systematic uncertainty.

The W width analysis shares most of the issues of W production and decay modelling and the detector response simulation with the W mass analysis, the sources of the systematic uncertainty are therefore similar. Every input parameter in the MC simulation could alter the transverse mass lineshape and cause systematic uncertainty on Γ_W measurement, these parameters are in most cases determined by the $Z \rightarrow l \bar{l}$ data. Although the uncertainties on these smearing parameters are considered as systematic uncertainties for the width measurement, they are really statistical uncertainties which depend on the number of Z events. At LHC, a large collected $Z \rightarrow l \bar{l}$ sample (~ 6 million Z events per channel per experiment) will definitely help to reduce the overall systematic uncertainty. The systematic uncertainty also depends on the fitting region, fitting only the high-end region will have a smaller systematic error since the uncertainties from detector resolution and SM backgrounds will be smaller. With enough W candidates in the tail region at the LHC, using a smaller fitting region like $110 < M_T < 200 \text{ GeV}$ or

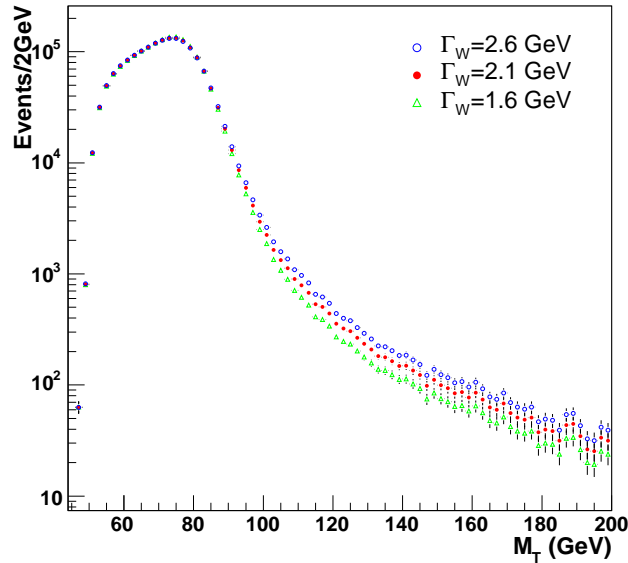


Fig. 6.0.122: Transverse mass spectra from Monte Carlo simulation with different Γ_W widths, normalized to some arbitrary number. The green triangles are for $\Gamma_W = 1.6$ GeV, the red dots are for $\Gamma_W = 2.1$ GeV and the blue circles are for $\Gamma_W = 2.6$ GeV.

$120 < M_T < 200$ GeV will reduce the final systematic uncertainty.

The modelling of the W recoil provided the largest uncertainty in all previous width measurements from Tevatron. The recoil system is mainly composed of soft hadrons from the underlying event and the contribution from the pile-up. $Z \rightarrow \mu\mu$ data is used to measure the detector response and resolution to the underlying event. For the pile-up contribution, fortunately, the mean number of interactions per bunch crossing is about 2 at the low luminosity, which is actually lower than the mean number of interactions per crossing at the Tevatron Run II. This relatively quiet environment, together with the large-size Z samples, will reduce the dominant source of systematic uncertainty. Extrapolating to the LHC data sample, an error of smaller than 15 MeV per channel should be achieved.

At the Tevatron Run I, the absolute lepton scale is known with a precision of about 0.1% and the uncertainty on Γ_W is around 20 MeV. If the lepton scale is known to 0.02% at LHC in order to measure M_W with a precision of better than 20 MeV, the uncertainty due to lepton scale on Γ_W should be less than 5 MeV.

The leptons from the fitting region tend to have higher transverse momenta than leptons near the Jacobian edge, thus the lepton scale non-linearity plays a significant role in the width measurement. The ability to place bounds on the non-linearity using collider data is a limiting source of W mass measurement in Run II; this is also true for the Run II width measurement. In D0 Run Ib measurement,

the test beam results were used and the effect on the width measurement was found to be negligible. At the LHC, with the help of test beam results, this uncertainty should be on the order of 5 MeV.

At the Tevatron, the main sources of backgrounds come from QCD processes, $W \rightarrow \ell \bar{\nu}_\ell$ decays and $Z \rightarrow \ell \bar{\ell}$ decays where one lepton is mismeasured, no new physics processes will contribute to the tail region of M_T spectrum. At the LHC, this may not be the case, non-SM processes may have large contributions to the fitting region. It is very difficult to estimate this uncertainty right now.

For almost all Tevatron measurements, the lepton and recoil resolutions are parameterized as gaussian functions, the effect on the non-gaussian part of the detector resolutions was not carefully estimated. At the LHC, with the extensive studies of the test-beam results and large collected Z samples, the effect on m_W should be less than 5 MeV.

The theoretical uncertainties on the width measurement mostly come from $p_T(W)$ spectrum (due to QCD corrections), PDF and radiative corrections. Currently, the estimated uncertainty on m_W associated with modelling the W boson p_T spectrum is of the order of 30 MeV at the Tevatron. In [288], the authors show that larger QCD corrections are expected at the LHC, and hence the uncertainty will also be larger. On the other hand, as mentioned before, the W boson p_T spectrum can be constrained by $Z \rightarrow \ell \bar{\ell}$ data. With 0.6 million Z events, the uncertainty due to QCD corrections should be controlled to 10 MeV level. Since the boson p_T form is constrained from Z events, it is imperative that all effects that are different for Z and W are included in the generator prescription. The uncertainties from PDF and radiative corrections seem under control for all Tevatron measurements (~ 10 MeV for each), but will need improvements to avoid becoming dominant at the LHC experiments.

The W mass will be measured with a precision of about 30 MeV from the LEP and Tevatron measurements before this measurement [288], the uncertainty of M_W on m_W should be less than 5 MeV. In this high-precision measurement, assuming SM $M_W - m_W$ relation may not be enough.

With an integrated luminosity of 10 fb^{-1} , which should be collected in the first year of LHC's low luminosity run and by considering only one lepton decay channel, a total uncertainty of smaller than 30 MeV should be achieved by each LHC experiment.

7 Summary

This report includes detailed descriptions of experimental methods used to measure the W boson mass, search for single top production, and precision electroweak measurements at hadron colliders. In addition, it includes numerous new theoretical developments in the areas of single top production and precision electroweak measurements. The main conclusions are summarized below. Details of the studies are found in the respective sections of the report and references cited.

Impressive advances have been made to control the systematic uncertainties arising from jet energy calibration in the measurement of the top quark mass, and work is in progress to control the systematic uncertainties arising from b-jets. Tevatron experience has shown that the measurement can be

significantly improved by combining the results from the two experiments, D0 and CDF. It is therefore important to agree on how to classify and apply the uncertainties to allow for a more straightforward combination. A quantitative study of the effects of Color reconnections and other final state interactions is needed to reduce the uncertainties arising from Monte Carlo generation.

Tevatron experiments are using elaborated multi-variate analysis techniques to extract the single top quark signal from the overwhelming $\bar{W} + \text{jets}$ backgrounds. Recently, D0 announced that it observes evidence for single top production when it analyzes about twice the amount of data compared to the one used in the analyses described in this report. We expect the LHC single top samples to have much larger event statistics, especially in the t -channel, which should allow the signal to be extracted using a cut-based analysis. The advanced analysis techniques developed at the Tevatron for the single top searches will be particularly useful for Higgs and beyond the Standard Model searches at the LHC.

The W mass measurements rely on a detailed calibration of the detector that will be more difficult to achieve at the LHC compared to the Tevatron. Recently, the CDF collaboration completed the most precise single measurement of the W mass available to-date, to a stunning precision of 0.06%, following analysis techniques described in this report. Together, the precise measurements of the W boson mass and the top quark mass are constraining the mass of the Higgs boson.

References

- [1] A. Sirlin, Phys. Rev. **D22**, 971 (1980).
- [2] The Tevatron Electroweak Working Group, hep-ex/0507091.
- [3] S. Heinemeyer, W. Hollik and G. Weiglein, Phys. Rept. **425**, 265 (2006), [hep-ph/0412214].
- [4] K. Kondo, J. Phys. Soc. Jap. **57**, 4126 (1988).
- [5] DØ Collaboration, V. M. Abazov *et al.*, Nature **429**, 638 (2004), [hep-ex/0406031].
- [6] CDF Collaboration, F. Canelli, B. Mohr, R. Wallny and J. Hauser, (2006), CDF Note 8151.
- [7] DØ Collaboration, F. Fiedler *et al.*, (2006), DØ Note 5053.
- [8] CDF Collaboration, A. Abulencia *et al.*, Phys. Rev. Lett. **96**, 152002 (2006), [hep-ex/0512070].
- [9] CDF Collaboration, (2006), CDF Note 8090.
- [10] CDF Collaboration, A. Abulencia *et al.*, Phys. Rev. Lett. **96**, 022004 (2006), [hep-ex/0510049].
- [11] DELPHI Collaboration, P. Abreu *et al.*, Eur. Phys. J. **C2**, 581 (1998).
- [12] DELPHI Collaboration, P. Abreu *et al.*, Phys. Lett. **B462**, 410 (1999).
- [13] DELPHI Collaboration, P. Abreu *et al.*, Phys. Lett. **B511**, 159 (2001), [hep-ex/0104047].
- [14] DELPHI Collaboration, M. Mulders, Int. J. Mod. Phys. **A16S1A**, 284 (2001).
- [15] M. P. Mulders, *Direct measurement of the W boson mass in $e^+ e^-$ collisions at LEP*, PhD thesis, University of Amsterdam, 2001.

- [16] DØ Collaboration, B. Abbott *et al.*, Phys. Rev. **D58**, 052001 (1998), [hep-ex/9801025].
- [17] J. Pumplin *et al.*, JHEP **0207**, 012 (2002), [hep-ph/0201195].
- [18] LEP Electroweak Working Group, SLD Electroweak Group, and SLD Heavy Flavour Group, hep-ex/0509008.
- [19] CDF Collaboration, A. Abulencia *et al.*, Phys. Rev. **D73**, 032003 (2006), [hep-ex/0510048].
- [20] A. Bhatti *et al.*, hep-ex/0510047.
- [21] DØ Collaboration, B. Abbott *et al.*, Nucl. Instrum. Meth. **A424**, 352 (1999), [hep-ex/9805009].
- [22] CDF and DØ collaborations and TEVEWWG, hep-ex/0507006.
- [23] L. Lyons, D. Gibaut and P. Clifford, Nucl. Instrum. Meth. **A270**, 110 (1988).
- [24] A. Valassi, Nucl. Instrum. Meth. **A500**, 391 (2003).
- [25] CDF Collaboration, A. Abulencia *et al.*, Phys. Rev. Lett. **96**, 022004 (2006), [hep-ex/0510049].
- [26] CDF Collaboration, A. Abulencia *et al.*, Phys. Rev. Lett. **96**, 152002 (2006), [hep-ex/0512070].
- [27] R. Blair *et al.*, (CDF Collaboration), *The CDF-II Detector Technical Design Report*, Fermilab-Pub-96/390-E (1996).
- [28] Snowmass Working Group on Precision Electroweak measurements, hep-ph/0202001.
- [29] P. Roy, PCCFT0202, PhD Thesis, Blaise Pascal University.
- [30] M. Beneke *et al.*, (2000), [hep-ph/0003033].
- [31] J.-P. Etienne, A.-I. Meyer and J. Schwindling, ATLAS Internal note: ATL-PHYS-INT-2005-002.
- [32] I. Borjanovic *et al.*, Eur.Phys.J **C39S2**, 63 (2005), [hep-ex/0403021].
- [33] L. Sonnenschein, CMS Internal note : CMS-2001-001.
- [34] J. D'Hondt, J. Heyninck and S. Lowette, CMS Note 2006/066.
- [35] I. Efthymiopoulos, ATLAS Internal note : ATL-COM-PHYS-1999-050.
- [36] A. Kharchilava, Phys. Lett. **B476**, 73 (2000).
- [37] R. Chierici and A. Dierlamm, CMS Note 2006/058.
- [38] M. Davids *et al.*, CMS Note 2006/077.
- [39] CDF Collaboration, F. Abe *et al.*, Phys. Rev. Lett. **74**, 2626 (1995), [hep-ex/9503002].
- [40] DØ Collaboration, S. Abachi *et al.*, Phys. Rev. Lett. **74**, 2632 (1995), [hep-ex/9503003].
- [41] S. S. D. Willenbrock and D. A. Dicus, Phys. Rev. **D34**, 155 (1986).

- [42] C.-P. Yuan, Phys. Rev. **D41**, 42 (1990).
- [43] R. K. Ellis and S. J. Parke, Phys. Rev. **D46**, 3785 (1992).
- [44] S. Cortese and R. Petronzio, Phys. Lett. **B253**, 494 (1991).
- [45] T. Stelzer and S. Willenbrock, Phys. Lett. **B357**, 125 (1995), [hep-ph/9505433].
- [46] A. P. Heinson, A. S. Belyaev and E. E. Boos, Phys. Rev. **D56**, 3114 (1997), [hep-ph/9612424].
- [47] T. M. P. Tait, Phys. Rev. **D61**, 034001 (2000), [hep-ph/9909352].
- [48] M. C. Smith and S. Willenbrock, Phys. Rev. **D54**, 6696 (1996), [hep-ph/9604223].
- [49] B. W. Harris, E. Laenen, L. Phaf, Z. Sullivan and S. Weinzierl, Phys. Rev. **D66**, 054024 (2002), [hep-ph/0207055].
- [50] Q.-H. Cao and C. P. Yuan, Phys. Rev. **D71**, 054022 (2005), [hep-ph/0408180].
- [51] Q.-H. Cao, R. Schwienhorst and C. P. Yuan, Phys. Rev. **D71**, 054023 (2005), [hep-ph/0409040].
- [52] Z. Sullivan, Phys. Rev. **D70**, 114012 (2004), [hep-ph/0408049].
- [53] J. Campbell, R. K. Ellis and F. Tramontano, Phys. Rev. **D70**, 094012 (2004), [hep-ph/0408158].
- [54] S. Frixione, E. Laenen, P. Motylinski and B. R. Webber, hep-ph/0512250.
- [55] K. G. Chetyrkin and M. Steinhauser, Phys. Lett. **B502**, 104 (2001), [hep-ph/0012002].
- [56] G. Bordes and B. van Eijk, Nucl. Phys. **B435**, 23 (1995).
- [57] T. Stelzer, Z. Sullivan and S. Willenbrock, Phys. Rev. **D56**, 5919 (1997), [hep-ph/9705398].
- [58] Q.-H. Cao, R. Schwienhorst, J. A. Benitez, R. Brock and C.-P. Yuan, Phys. Rev. **D72**, 094027 (2005), [hep-ph/0504230].
- [59] S. Zhu, Phys. Lett. **B524**, 283 (2002).
- [60] J. Campbell and F. Tramontano, Nucl. Phys. **B726**, 109 (2005), [hep-ph/0506289].
- [61] A. Belyaev and E. Boos, Phys. Rev. **D63**, 034012 (2001), [hep-ph/0003260].
- [62] T. Stelzer, Z. Sullivan and S. Willenbrock, Phys. Rev. **D58**, 094021 (1998), [hep-ph/9807340].
- [63] A. S. Belyaev, E. E. Boos and L. V. Dudko, Phys. Rev. **D59**, 075001 (1999), [hep-ph/9806332].
- [64] Z. Sullivan, Phys. Rev. **D72**, 094034 (2005), [hep-ph/0510224].
- [65] M. T. Bowen, S. D. Ellis and M. J. Strassler, Phys. Rev. **D72**, 074016 (2005), [hep-ph/0412223].
- [66] M. T. Bowen, hep-ph/0503110.
- [67] M. Cacciari, S. Frixione, M. L. Mangano, P. Nason and G. Ridolfi, JHEP **04**, 068 (2004), [hep-ph/0303085].

- [68] CDF Collaboration, D. Acosta *et al.*, Phys. Rev. Lett. **95**, 102002 (2005), [hep-ex/0505091].
- [69] Particle Data Group, S. Eidelman *et al.*, Phys. Lett. **B592**, 1 (2004).
- [70] G. A. Ladinsky and C. P. Yuan, Phys. Rev. **D43**, 789 (1991).
- [71] A. Stange, W. J. Marciano and S. Willenbrock, Phys. Rev. **D50**, 4491 (1994), [hep-ph/9404247].
- [72] S. Moretti, Phys. Rev. **D56**, 7427 (1997), [hep-ph/9705388].
- [73] D. O. Carlson and C. P. Yuan, Phys. Lett. **B306**, 386 (1993).
- [74] G. Mahlon and S. J. Parke, Phys. Rev. **D55**, 7249 (1997), [hep-ph/9611367].
- [75] G. Mahlon and S. J. Parke, Phys. Lett. **B476**, 323 (2000), [hep-ph/9912458].
- [76] D. O. Carlson, E. Malkawi and C. P. Yuan, Phys. Lett. **B337**, 145 (1994), [hep-ph/9405277].
- [77] A. Datta and X. Zhang, Phys. Rev. **D55**, 2530 (1997), [hep-ph/9611247].
- [78] T. Tait and C. P. Yuan, hep-ph/9710372.
- [79] K.-I. Hikasa, K. Whisnant, J. M. Yang and B.-L. Young, Phys. Rev. **D58**, 114003 (1998), [hep-ph/9806401].
- [80] E. Boos, L. Dudko and T. Ohl, Eur. Phys. J. **C11**, 473 (1999), [hep-ph/9903215].
- [81] T. Tait and C.-P. Yuan, Phys. Rev. **D 63**, 014018 (2001).
- [82] C.-R. Chen, F. Larios and C. P. Yuan, Phys. Lett. **B631**, 126 (2005), [hep-ph/0503040].
- [83] D. Atwood, S. Bar-Shalom, G. Eilam and A. Soni, Phys. Rev. **D54**, 5412 (1996), [hep-ph/9605345].
- [84] E. H. Simmons, Phys. Rev. **D55**, 5494 (1997), [hep-ph/9612402].
- [85] C. S. Li, R. J. Oakes and J. M. Yang, Phys. Rev. **D55**, 1672 (1997), [hep-ph/9608460].
- [86] C. S. Li, R. J. Oakes and J. M. Yang, Phys. Rev. **D55**, 5780 (1997), [hep-ph/9611455].
- [87] C.-S. Li, R. J. Oakes, J.-M. Yang and H.-Y. Zhou, Phys. Rev. **D57**, 2009 (1998), [hep-ph/9706412].
- [88] S. Bar-Shalom, D. Atwood and A. Soni, Phys. Rev. **D57**, 1495 (1998), [hep-ph/9708357].
- [89] E. Malkawi and T. Tait, Phys. Rev. **D54**, 5758 (1996), [hep-ph/9511337].
- [90] A. Datta, J. M. Yang, B.-L. Young and X. Zhang, Phys. Rev. **D56**, 3107 (1997), [hep-ph/9704257].
- [91] R. J. Oakes, K. Whisnant, J. M. Yang, B.-L. Young and X. Zhang, Phys. Rev. **D57**, 534 (1998), [hep-ph/9707477].
- [92] T. Han, M. Hosch, K. Whisnant, B.-L. Young and X. Zhang, Phys. Rev. **D58**, 073008 (1998), [hep-ph/9806486].

- [93] A. Datta, P. J. O'Donnell, Z. H. Lin, X. Zhang and T. Huang, Phys. Lett. **B483**, 203 (2000), [hep-ph/0001059].
- [94] R. S. Chivukula, E. H. Simmons and J. Terning, Phys. Rev. **D53**, 5258 (1996), [hep-ph/9506427].
- [95] D. J. Muller and S. Nandi, Phys. Lett. **B383**, 345 (1996), [hep-ph/9602390].
- [96] E. Malkawi, T. Tait and C. P. Yuan, Phys. Lett. **B385**, 304 (1996), [hep-ph/9603349].
- [97] H.-J. He, T. Tait and C. P. Yuan, Phys. Rev. **D62**, 011702 (2000), [hep-ph/9911266].
- [98] P. Batra, A. Delgado, D. E. Kaplan and T. M. P. Tait, JHEP **02**, 043 (2004), [hep-ph/0309149].
- [99] P. Batra, A. Delgado, D. E. Kaplan and T. M. P. Tait, JHEP **06**, 032 (2004), [hep-ph/0404251].
- [100] Z. Sullivan, hep-ph/0306266.
- [101] Z. Sullivan, Phys. Rev. **D66**, 075011 (2002), [hep-ph/0207290].
- [102] W. T. Giele and E. W. N. Glover, Phys. Rev. **D46**, 1980 (1992).
- [103] W. T. Giele, E. W. N. Glover and D. A. Kosower, Nucl. Phys. **B403**, 633 (1993), [hep-ph/9302225].
- [104] S. Keller and E. Laenen, Phys. Rev. **D59**, 114004 (1999), [hep-ph/9812415].
- [105] UA2, J. Alitti *et al.*, Phys. Lett. **B257**, 232 (1991).
- [106] G. Mahlon and S. Parke, Phys. Rev. **D 53**, 4886 (1996).
- [107] S. J. Parke and Y. Shadmi, Phys. Lett. **B387**, 199 (1996), [hep-ph/9606419].
- [108] W. T. Giele, S. Keller and E. Laenen, Phys. Lett. **B372**, 141 (1996), [hep-ph/9511449].
- [109] V. S. Fadin, V. A. Khoze and A. D. Martin, Phys. Lett. **B320**, 141 (1994), [hep-ph/9309234].
- [110] V. S. Fadin, V. A. Khoze and A. D. Martin, Phys. Rev. **D49**, 2247 (1994).
- [111] K. Melnikov and O. I. Yakovlev, Phys. Lett. **B324**, 217 (1994), [hep-ph/9302311].
- [112] R. Pittau, Phys. Lett. **B386**, 397 (1996), [hep-ph/9603265].
- [113] C. Macesanu, Phys. Rev. **D65**, 074036 (2002), [hep-ph/0112142].
- [114] R. K. Ellis, D. A. Ross and A. E. Terrano, Nucl. Phys. **B178**, 421 (1981).
- [115] S. Catani and M. H. Seymour, Phys. Lett. **B378**, 287 (1996), [hep-ph/9602277].
- [116] S. Catani and M. H. Seymour, Nucl. Phys. **B485**, 291 (1997), [hep-ph/9605323].
- [117] S. Catani, S. Dittmaier, M. H. Seymour and Z. Trocsanyi, Nucl. Phys. **B627**, 189 (2002), [hep-ph/0201036].

- [118] Z. Nagy and Z. Trocsanyi, Phys. Rev. **D59**, 014020 (1999), [hep-ph/9806317].
- [119] Z. Nagy, Phys. Rev. **D68**, 094002 (2003), [hep-ph/0307268].
- [120] E. Boos and T. Plehn, Phys. Rev. **D69**, 094005 (2004), [hep-ph/0304034].
- [121] M. Dittmar and H. K. Dreiner, Phys. Rev. **D55**, 167 (1997), [hep-ph/9608317].
- [122] CDF Collaboration, D. Acosta *et al.*, Phys. Rev. **D 65**, 091102 (2002).
- [123] CDF Collaboration, D. Acosta *et al.*, Phys. Rev. **D 69**, 052003 (2004).
- [124] E. Boos, L. Dudko and V. Savrin, (2000).
- [125] CDF Collaboration, D. Acosta *et al.*, Phys. Rev. **D 71**, 012005 (2005).
- [126] DØ Collaboration, V. M. Abazov *et al.*, Phys. Lett. **B622**, 265 (2005), [hep-ex/0505063].
- [127] T. Stelzer and W. F. Long, Comput. Phys. Commun. **81**, 357 (1994), [hep-ph/9401258].
- [128] F. Maltoni and T. Stelzer, JHEP **02**, 027 (2003), [hep-ph/0208156].
- [129] CompHEP, E. Boos *et al.*, Nucl. Instrum. Meth. **A534**, 250 (2004), [hep-ph/0403113].
- [130] J. Lueck, FERMILAB-MASTERS-2006-01; available as Universität Karlsruhe, Institut fuer Experimentelle Kernphysik Report No. IEKP-KA/2006-2, Diploma Thesis.
- [131] T. Sjostrand, L. Lonnblad, S. Mrenna and P. Skands, hep-ph/0308153 (2003), [hep-ph/0308153].
- [132] E. Boos, L. Dudko and V. Savrin, CMS Note 2000/065 (2000), [CMS Note 2000/065].
- [133] E. E. Boos, V. E. Bunichev, L. V. Dudko, V. I. Savrin and A. V. Sherstnev, Phys. Atom. Nucl. **69**, 1317 (2006).
- [134] W.-K. Tung, AIP Conf. Proc. **753**, 15 (2005), [hep-ph/0410139].
- [135] T. Sjostrand *et al.*, Comput. Phys. Commun. **135**, 238 (2001), [hep-ph/0010017].
- [136] G. Marchesini *et al.*, Comput. Phys. Commun. **67**, 465 (1992).
- [137] J. Campbell and R. K. Ellis, Phys. Rev. **D65**, 113007 (2002), [hep-ph/0202176].
- [138] CTEQ, H. L. Lai *et al.*, Eur. Phys. J. **C12**, 375 (2000), [hep-ph/9903282].
- [139] U. Baur, F. Halzen, S. Keller, M. L. Mangano and K. Riesselmann, Phys. Lett. **B318**, 544 (1993), [hep-ph/9308370].
- [140] CDF Collaboration, D. Acosta *et al.*, Phys. Rev. **D72**, 032002 (2005), [hep-ex/0506001].
- [141] DØ Collaboration, V. M. Abazov *et al.*, Phys. Rev. Lett. **94**, 161801 (2005), [hep-ex/0410078].
- [142] J. Campbell, R. K. Ellis, F. Maltoni and S. Willenbrock, Phys. Rev. **D69**, 074021 (2004), [hep-ph/0312024].

- [143] H1 Collaboration, A. Aktas *et al.*, Eur. Phys. J. **C45**, 23 (2006), [hep-ex/0507081].
- [144] H1 Collaboration, A. Aktas *et al.*, Eur. Phys. J. **C40**, 349 (2005), [hep-ex/0411046].
- [145] ZEUS Collaboration, J. Breitweg *et al.*, Eur. Phys. J. **C12**, 35 (2000), [hep-ex/9908012].
- [146] ZEUS Collaboration, S. Chekanov *et al.*, Phys. Rev. **D69**, 012004 (2004), [hep-ex/0308068].
- [147] CDF Collaboration, D. Acosta *et al.*, Phys. Rev. **D71**, 012005 (2005), [hep-ex/0410058].
- [148] M. T. Bowen, S. D. Ellis and M. J. Strassler, Acta Phys. Polon. **B36**, 271 (2005), [hep-ph/0504186].
- [149] ATLAS Collaboration, D. O’Neil, B. Gonzalez-Pineiro and M. Lefebvre, J. Phys. **G28**, 2657 (2002).
- [150] M. Barisonzi, private communication, 2005.
- [151] DØ Collaboration, L. Dudko, (1999), Prepared for VI International Workshop On Artificial Intelligence in High Energy and Nuclear Physics (AIHENP 99), Crete, April, 1999.
- [152] DØ Collaboration, L. Dudko, (2000), Prepared for 7th International Workshop on Advanced Computing and Analysis Techniques in Physics Research (ACAT 2000), Batavia, Illinois, 16-20 Oct 2000.
- [153] E. Boos and L. Dudko, Nucl. Instrum. Meth. **A502**, 486 (2003), [hep-ph/0302088].
- [154] DØ Collaboration, V. M. Abazov *et al.*, Phys. Lett. **B517**, 282 (2001), [hep-ex/0106059].
- [155] DØ Collaboration, B. Abbott *et al.*, Phys. Rev. **D63**, 031101 (2001), [hep-ex/0008024].
- [156] DØ Collaboration, E. Boos and L. Dudko, (1999), DØ Note 3612.
- [157] DØ Collaboration, E. Boos, L. Dudko, A. Heinson and N. Sotnikova, (2000), DØ Note 3856.
- [158] DØ Collaboration, J. Conway, (2000), <http://www.physics.ucdavis.edu/conway/research/software/pgs/pgs.html>.
- [159] C. Peterson, T. Rognvaldsson and L. Lonnblad, Comput. Phys. Commun. **81**, 185 (1994).
- [160] E. E. Boos and A. V. Sherstnev, Phys. Lett. **B534**, 97 (2002), [hep-ph/0201271].
- [161] D0, V. M. Abazov *et al.*, Nucl. Instrum. Meth. **A565**, 463 (2006), [physics/0507191].
- [162] DØ Collaboration, E. Boos and L. Dudko, Nucl. Instrum. Methods A **A 502**, 486 (2003).
- [163] N. Amos *et al.*, prepared for *Computing in high energy physics '95*, Rio de Janeiro 1995.
- [164] J. Schwindling, MLPfit: A Tool For Designing and Using Multi-Layer Perceptrons, see <http://schwind.home.cern.ch/schwind/MLPfit.html>.
- [165] I. Bertram *et al.*, FERMILAB-TM-2104 (2000).

- [166] S. Slabospitsky *et al.*, Comput. Phys. Commun. **148**, 87 (2002), [hep-ph/0201292].
- [167] S. Frixione, B. Weber and P. Nason, JHEP **0308**, 007 (2003), [hep-ph/0305252].
- [168] F. Hubaut *et al.*, Eur.Phys.J. **C44S2**, 13 (2005), [hep-ex/0508061].
- [169] J. Campbell *et al.*, Phys.Rev. **D68**, 094021 (2003), [hep-ph/0308195].
- [170] G. Corcella *et al.*, JHEP **0101**, 010 (2001), [hep-ph/0011363].
- [171] E. Richter-Was *et al.*, ATLAS Note PHYS-98-131 (1998).
- [172] I. Bojanovic *et al.*, Eur. Phys.J **C39s2**, 63 (2005), [hep-ex/0403021].
- [173] J. F. Gunion, H. E. Haber, G. L. Kane and S. Dawson, *The Higgs Hunter's Guide* (Addison-Wesely, 1989), SCIPP-89/13.
- [174] A. Lucotte and F. Chevallier, ATLAS Note ATL-PHYS-COM-2006-0003 , 1 (2005), [published in *Hadron Collider Physics 2005*, Eds. M Campanelli, A. Clark, X. Wu, Springer, ISBN 3-540-32840-8, p.300].
- [175] H. Stenzel, ATLAS Note ATL-PHYS-2001-0003 (2001).
- [176] V. Abramov *et al.*, CMS Note 2006/084 (2006).
- [177] S. Blyth *et al.*, CMS Note 2006/086 (2006).
- [178] CMS Collaboration, CERN-LHCC-2006-01.
- [179] V. S. E. Boos, L. Dudko, CMS Note 2000/065 (2000).
- [180] M. L. Mangano, M. Moretti, F. Piccinini, R. Pittau and A. D. Polosa, JHEP **07**, 001 (2003), [hep-ph/0206293].
- [181] T. Sjostrand, L. Lonnblad and S. Mrenna, hep-ph/0108264.
- [182] S. Abdullin *et al.*, [hep-ph/0605143].
- [183] R. Fisher, Annals of Eugenics **7**, 179 (1936).
- [184] J. Pumplin *et al.*, JHEP **07**, 012 (2002), [hep-ph/0201195].
- [185] ALEPH, DELPHI, L3, OPAL and LEPEWWG, hep-ex/0511027.
- [186] The Snowmass Working Group on Precision Electroweak Measurements, U. Baur *et al.*, hep-ph/0202001.
- [187] M. Dittmar, F. Pauss and D. Zurcher, Phys. Rev. **D56**, 7284 (1997), [hep-ex/9705004].
- [188] M. Dittmar, A.-S. Nicollerat and A. Djouadi, Phys. Lett. **B583**, 111 (2004), [hep-ph/0307020].
- [189] U. Baur and D. Wackerroth, Phys. Rev. **D70**, 073015 (2004), [hep-ph/0405191].

- [190] E. Accomando and A. Kaiser, Phys. Rev. **D73**, 093006 (2006), [hep-ph/0511088].
- [191] F. A. Berends, R. Kleiss, J. P. Revol and J. P. Vialle, Z. Phys. **C27**, 155 (1985).
- [192] D. Wackerroth and W. Hollik, Phys. Rev. **D55**, 6788 (1997), [hep-ph/9606398].
- [193] U. Baur, S. Keller and D. Wackerroth, Phys. Rev. **D59**, 013002 (1999), [hep-ph/9807417].
- [194] C. M. Carloni Calame, G. Montagna, O. Nicrosini and M. Treccani, Phys. Rev. **D69**, 037301 (2004), [hep-ph/0303102].
- [195] CDF Collaboration, F. Abe *et al.*, Phys. Rev. Lett. **75**, 11 (1995), [hep-ex/9503007].
- [196] DØ Collaboration, S. Abachi *et al.*, Phys. Rev. Lett. **77**, 3309 (1996), [hep-ex/9607011].
- [197] Tevatron Electroweak Working Group, hep-ex/0510077.
- [198] CDF Collaboration, V. M. Abazov *et al.*, Phys. Rev. **D70**, 092008 (2004).
- [199] C. Buttar *et al.*, hep-ph/0604120.
- [200] C. Anastasiou, L. J. Dixon, K. Melnikov and F. Petriello, Phys. Rev. **D69**, 094008 (2004), [hep-ph/0312266].
- [201] C. Anastasiou, L. J. Dixon, K. Melnikov and F. Petriello, Phys. Rev. Lett. **91**, 182002 (2003), [hep-ph/0306192].
- [202] K. Melnikov and F. Petriello, Phys. Rev. Lett. **96**, 231803 (2006), [hep-ph/0603182].
- [203] K. Melnikov and F. Petriello, hep-ph/0609070.
- [204] C. Balazs and C. P. Yuan, Phys. Rev. **D56**, 5558 (1997), [hep-ph/9704258].
- [205] R. K. Ellis and S. Veseli, Nucl. Phys. **B511**, 649 (1998), [hep-ph/9706526].
- [206] S. Dittmaier and M. Krämer, Phys. Rev. **D65**, 073007 (2002), [hep-ph/0109062].
- [207] A. Arbuzov *et al.*, Eur. Phys. J. **C46**, 407 (2006), [hep-ph/0506110].
- [208] C. M. Carloni Calame, G. Montagna, O. Nicrosini and A. Vicini, JHEP **12**, 016 (2006), [hep-ph/0609170].
- [209] U. Baur, O. Brein, W. Hollik, C. Schappacher and D. Wackerroth, Phys. Rev. **D65**, 033007 (2002), [hep-ph/0108274].
- [210] W. Placzek and S. Jadach, Eur. Phys. J. **C29**, 325 (2003), [hep-ph/0302065].
- [211] C. M. Carloni Calame, G. Montagna, O. Nicrosini and M. Treccani, JHEP **05**, 019 (2005), [hep-ph/0502218].
- [212] Q.-H. Cao and C. P. Yuan, Phys. Rev. Lett. **93**, 042001 (2004), [hep-ph/0401026].

- [213] A. Andonov *et al.*, *Comput. Phys. Commun.* **174**, 481 (2006), [hep-ph/0411186].
- [214] A. De Rujula, R. Petronzio and A. Savoy-Navarro, *Nucl. Phys.* **B154**, 394 (1979).
- [215] A. D. Martin, R. G. Roberts, W. J. Stirling and R. S. Thorne, *Eur. Phys. J.* **C39**, 155 (2005), [hep-ph/0411040].
- [216] M. Ciafaloni, P. Ciafaloni and D. Comelli, *Phys. Rev. Lett.* **84**, 4810 (2000), [hep-ph/0001142].
- [217] M. Melles, *Phys. Rept.* **375**, 219 (2003), [hep-ph/0104232].
- [218] B. Jantzen, J. H. Kuhn, A. A. Penin and V. A. Smirnov, *Nucl. Phys.* **B731**, 188 (2005), [hep-ph/0509157].
- [219] A. Denner, B. Jantzen and S. Pozzorini, hep-ph/0608326.
- [220] U. Baur, *Phys. Rev.* **D75**, 013005 (2007), [hep-ph/0611241].
- [221] A. V. Konychev and P. M. Nadolsky, *Phys. Lett.* **B633**, 710 (2006), [hep-ph/0506225].
- [222] S. Berge, P. Nadolsky, F. Olness and C. P. Yuan, *Phys. Rev.* **D72**, 033015 (2005), [hep-ph/0410375].
- [223] S. Berge, P. M. Nadolsky and F. I. Olness, *Phys. Rev.* **D73**, 013002 (2006), [hep-ph/0509023].
- [224] C. Carloni Calame, G. Montagna, O. Nicrosini and M. Treccani, *Phys. Rev.* **D69**, 037301 (2004), [hep-ph/0303102].
- [225] C. Carloni Calame, G. Montagna, O. Nicrosini and M. Treccani, *JHEP* **05**, 019 (2005), [hep-ph/0502218].
- [226] C. Carloni Calame, C. Lunardini, G. Montagna, O. Nicrosini and F. Piccinini, *Nucl. Phys.* **B584**, 459 (2000), [hep-ph/0003268].
- [227] C. Carloni Calame, *Phys. Lett.* **B520**, 16 (2001), [hep-ph/0103117].
- [228] C. M. Carloni Calame, S. Jadach, G. Montagna, O. Nicrosini and W. Placzek, *Acta Phys. Polon.* **B35**, 1643 (2004), [hep-ph/0402235].
- [229] E. Barberio, B. van Eijk and Z. Was, *Comput. Phys. Commun.* **66**, 115 (1991).
- [230] E. Barberio and Z. Was, *Comput. Phys. Commun.* **79**, 291 (1994).
- [231] P. Golonka and Z. Was, *Eur. Phys. J.* **C45**, 97 (2006), [hep-ph/0506026].
- [232] P. Golonka *et al.*, *Comput. Phys. Commun.* **174**, 818 (2006), [hep-ph/0312240].
- [233] G. Nanava and Z. Was, *Acta Phys. Polon.* **B34**, 4561 (2003), [hep-ph/0303260].
- [234] P. Golonka, T. Pierzchala and Z. Was, *Comput. Phys. Commun.* **157**, 39 (2004), [hep-ph/0210252].

- [235] P. Golonka, *Computer simulations in high energy physics: a case for PHOTOS, MC-TESTER, TAUOLA, and at2sim*, PhD thesis, Institute of Nuclear Physics, Krakow, 2006, Written under the supervision of Prof. Z. Was.
- [236] P. Golonka and Z. Was, Eur. Phys. J. **C50**, 53 (2007), [hep-ph/0604232].
- [237] G. Nanava and Z. Was, hep-ph/0607019.
- [238] P. Golonka, Photos+ : a c++ implementation of a universal monte carlo algorithm for qed radiative corrections in particle's decays, Master's thesis, Faculty of Nuclear Physics and Techniques, AGH University of Science and Technology, 1999, Written under the supervision of Z. Was, available at <http://cern.ch/Piotr.Golonka/MC/photos>.
- [239] G. P. Lepage, J. Comput. Phys. **27**, 192 (1978).
- [240] H. Baer, J. Ohnemus and J. F. Owens, Phys. Rev. **D42**, 61 (1990).
- [241] B. W. Harris and J. F. Owens, Phys. Rev. **D65**, 094032 (2002), [hep-ph/0102128].
- [242] W. A. Bardeen, A. J. Buras, D. W. Duke and T. Muta, Phys. Rev. **D18**, 3998 (1978).
- [243] J. F. Owens and W.-K. Tung, Ann. Rev. Nucl. Part. Sci. **42**, 291 (1992).
- [244] M. W. Krasny, S. Jadach and W. Placzek, Eur. Phys. J. **C44**, 333 (2005), [hep-ph/0503215].
- [245] S. Jadach and M. Skrzypek, hep-ph/0509178.
- [246] K. P. O. Diener, S. Dittmaier and W. Hollik, Phys. Rev. **D72**, 093002 (2005), [hep-ph/0509084].
- [247] S. Dittmaier, Nucl. Phys. **B565**, 69 (2000), [hep-ph/9904440].
- [248] A. Bredenstein, S. Dittmaier and M. Roth, Eur. Phys. J. **C44**, 27 (2005), [hep-ph/0506005].
- [249] M. Awramik, M. Czakon, A. Freitas and G. Weiglein, Phys. Rev. **D69**, 053006 (2004), [hep-ph/0311148].
- [250] G. Degrossi, P. Gambino, M. Passera and A. Sirlin, Phys. Lett. **B418**, 209 (1998), [hep-ph/9708311].
- [251] A. Ferroglia, G. Ossola, M. Passera and A. Sirlin, Phys. Rev. **D65**, 113002 (2002), [hep-ph/0203224].
- [252] F. Jegerlehner, J. Phys. **G29**, 101 (2003), [hep-ph/0104304].
- [253] A. Denner and T. Sack, Nucl. Phys. **B347**, 203 (1990).
- [254] J. C. Collins, D. E. Soper and G. Sterman, Nucl. Phys. **B250**, 199 (1985).
- [255] J. C. Collins and A. Metz, Phys. Rev. Lett. **93**, 252001 (2004), [hep-ph/0408249].
- [256] X. Ji, J.-P. Ma and F. Yuan, Phys. Rev. **D71**, 034005 (2005).

- [257] X. Ji, J.-P. Ma and F. Yuan, Phys. Lett. **B597**, 299 (2004).
- [258] F. Landry, R. Brock, P. M. Nadolsky and C. P. Yuan, Phys. Rev. **D67**, 073016 (2003), [hep-ph/0212159].
- [259] G. A. Ladinsky and C.-P. Yuan, Phys. Rev. **D50**, 4239 (1994).
- [260] G. P. Korchemsky and G. Sterman, Nucl. Phys. **B437**, 415 (1995).
- [261] S. Tafat, JHEP **05**, 004 (2001), [hep-ph/0102237].
- [262] J.-w. Qiu and X.-f. Zhang, Phys. Rev. **D63**, 114011 (2001), [hep-ph/0012348].
- [263] A. Kulesza, G. Sterman and W. Vogelsang, Phys. Rev. **D66**, 014011 (2002).
- [264] A. Guffanti and G. E. Smye, JHEP **10**, 025 (2000).
- [265] P. Nadolsky, D. R. Stump and C. P. Yuan, Phys. Rev. **D61**, 014003 (2000), [hep-ph/9906280].
- [266] P. M. Nadolsky, D. R. Stump and C. P. Yuan, Phys. Rev. **D64**, 114011 (2001), [hep-ph/0012261].
- [267] J. C. Collins, Phys. Rev. **D58**, 094002 (1998), [hep-ph/9806259].
- [268] M. Krämer, F. I. Olness and D. E. Soper, Phys. Rev. **D62**, 096007 (2000), [hep-ph/0003035].
- [269] P. M. Nadolsky, N. Kidonakis, F. I. Olness and C. P. Yuan, Phys. Rev. **D67**, 074015 (2003), [hep-ph/0210082].
- [270] W. K. Tung *et al.*, hep-ph/0611254.
- [271] CMS Collaboration, CERN/LHCC 2006-021, Volume 2 of the CMS Physics TDR.
- [272] CDF Collaboration, A. Abulencia *et al.*, hep-ex/0508029.
- [273] DØ Collaboration, Measurement of the cross section for inclusive W production in the muon channel at $\sqrt{s} = 1.96$ TeV using the D0 detector, D0note 4750 (2006).
- [274] DØ Collaboration, Measurement of the cross section for inclusive Z production in the di-muon final states at $\sqrt{s} = 1.96$ TeV, D0note 4573 (2006).
- [275] CDF and DØ Collaborations, E. B. James, hep-ex/0701003.
- [276] CDF Collaboration, CDF Run 2 Electroweak Public Results at <http://www-cdf.fnal.gov/physics/ewk>.
- [277] DØ Collaboration, A measurement of the W \rightarrow $\mu\nu$ asymmetry with the D0 detector at $\sqrt{s} = 1.96$ TeV, D0note 5061-CONF (2006).
- [278] A. Tricoli, A. M. Cooper-Sarkar and C. Gwenlan, hep-ex/0509002.
- [279] CDF Collaboration, First measurement of the W boson mass with CDF in RUN II, CDF Note 8665 (2006).

- [280] LEP Electroweak Working Group, 2005, lepewwg.web.cern.ch/LEPEWWG/Welcome.html.
- [281] J. Rosner, M. Worah and T. Takeuchi, *Phys. Rev.* **D49**, 1363 (1994).
- [282] K. Hagiwara *et al.*, *Phys. Rev.* **D66**, 010001 (2002).
- [283] CDF Collaboration, T. Affolder *et al.*, *Phys. Rev. Lett.* **85**, 3347 (2000).
- [284] DØ Collaboration, V. Abazov *et al.*, *Phys. Rev.* **D66**, 032008 (2002).
- [285] DØ Collaboration, Direct Measurement of the W Boson Width in $p\bar{p}$ Collisions at $\sqrt{s} = 1.96$ TeV, D0 Note 7983-CONF, 2004.
- [286] The Tevatron Electroweak Working Group, hep-ex/0510077.
- [287] F. Gianotti, (2006), in *Introduction to LHC physics*, Journal of Physics: conference series 53.
- [288] S. Keller and J. Womersley, *Eur. Phys. J.* **C5**, 249 (1998).